Understanding Phase Transitions of Pharmaceutical Materials

Alexander Lee Morritt

University of East Anglia
School of Pharmacy
September 2020

Thesis submitted to the School of Pharmacy, University of East Anglia
in fulfilment of the requirement for the degree of Doctor of Philosophy.

Dedicated to my family and friends

Acknowledgements

This thesis would without a doubt not exist without the help and guidance of many people. Over the past four years of learning new techniques, acquiring knowledge and making friends there are those who deserve a special mention and thanks.

Those who have put up with me through experiments and writing that require the biggest thanks are my supervisory team, Dr. László Fábián and Prof. Yaroslav Khimyak. They provided me with the opportunity to undertake this PhD and I am grateful to them for choosing me. László has given me time, patience and above all helped me develop my writing ethic and understanding of all-things crystallography. Yaroslav has equipped me with a more questioning nature, has been a solid foundation to my development as a scientist and has made me want to suggest solid-state NMR as technique for just about anything. Both László and Yaroslav have filled countless hours of meetings with philosophical/political debates, excellent restaurant choices, long-winded storytelling and a true scientific scepticism that has really helped me grow as an individual.

A special mention has to go to Karol. With all the time we spent in meetings on Skype, at restaurants, at Warwick or even talking through experiments on messenger. He is quite frankly responsible for helping me understand most of what happened with my PhD and he continues to help even now. He is a true mentor, colleague and friend. Susana and Juan need to be mentioned here as well, as they are the ones who trained me step-by-step to operate and look after our NMRs. I had not expected how complex, technical and difficult solid-state NMR would be, but they helped me through it. Of course, the NMR group or “basement people” as we are also known need a mention. Valeria, Sam, Trey, Iñaki, Matthew and Tom are people I can thank for being there for many a moan, coffee and political discussion in order to procrastinate processing our NMR data.

Many of my friends in Chemistry and Pharmacy need also to be mentioned. Anna for many a coffee break and heart to heart hallway discussions, Sarah for a joint northern attitude on tea, gravy and genuinely caring persona, Mike for so much nerdy talk and mockery that would make anyone external question if we actually like each other and Sion for impromptu coffee time talks where we basically fixed most of the world’s problems (hypothetically of course).

I also want to thank UEA for the opportunity to undertake this PhD, from the scholarship and facilities provided, but also the staff who helped encourage me along the way. Dr. Colin Macdonald for all the advice and training in NMR operation, especially when dealing with power-cuts, unhappy probes and obscure pulse programs. Bertrand Lézé for all the help with PXRD and enjoyable board-game

discussions. I also would like to thank the EPSRC for funding research time at University of Warwick's 850 MHz Solid-State NMR Facility, where I can also thank the facility manager Dinu Iuga for his patience and suggestions.

I want to thank my family, especially my Mum for being there for me and encouraging me to pursue my scientific career. My Dad for many an interesting albeit fruitless debate, but also listening to me talk about my research. My brother for being there in case I needed a break and wanted to chat. I'm grateful for the support you have given to me to get me to where I am today.

And lastly to my greatest supporter, my biggest fan and my whole world. Emily, you have been there for me when it was hard, when it was easy, when things were well and when things weren't exactly going great and I wanted to quit. You are the person who pulled me through and kept me going, who listened to me rant about yet another problem with a magnet or with some data that refused to behave. I am thankful, grateful and above all indebted to the kindness, patience and support you have given me.

Abstract

The effect of confinement on pharmaceuticals is a growing field of interest for drug delivery because of the ability to customise both shapes and sizes of pore space. The pore diameters, volumes and surface areas affect the properties and structural arrangement of pharmaceuticals in ways we cannot currently predict. Nanometre sized pores also provide an interesting landscape for experiments into crystalline/amorphous and polymorphic transitions. However, due to the process of encapsulation, the analysis of these materials presents a challenge. In this work we demonstrate how combined material characterisation techniques such as solid-state NMR, DSC, TGA, PXRD, FT-IR and N_2 sorption can be used in order to gain insight into the properties, structural characteristics and phase transitions of these encapsulated materials. We have also demonstrated how solvent mediated phase transitions can drive the same polymorphic interconversions that can be achieved by thermally dehydrating an API called acyclovir.

A cocrystal of flufenamic acid and nicotinamide, and nicotinamide on its own were chosen as pharmaceuticals to encapsulate in mesoporous silica hosts. At low loadings (<30% wt%) we have shown that FFA/NA remains in an amorphous state inside different mesoporous silica hosts, whereas at high loadings (>40% wt%) in larger pores of silica we have given evidence of crystalline ordering existing. Through the use of variable temperature MAS NMR and the ^{19}F-^{19}F NOESY pulse sequence we were able to distinguish three distinct components with different ordering and dynamics of FFA/NA that existed inside the same pore space. ^{13}C solid state NMR and PXRD of nicotinamide inside pores larger than 6 nm revealed a polymorphic interconversion from form I to a previously unknown form which we later characterised as form δ. Polymorphic conversion of ACV hydrates into anhydrous forms was achieved through slurrying dry solvents with high polarity.

Publications

1. **Solvent driven phase transitions of acyclovir – the role of water and solvent polarity.** K. P. Nartowski, J. Karabin, A. L. Morritt, M. Nowak, L. Fábián, B. Karolewicz and Y. Z. Khimyak, *CrystEngComm*, 2019, **21**, 2180–2192.
2. **Mesoporous Aluminosilicate Nanofibers with a Low Si/Al Ratio as Acidic Catalyst for Hydrodeoxygenation of Phenol**. T. Haynes, T. D'hondt, A. L. Morritt, Y. Z. Khimyak, D. Desmecht, V. Dubois and S. Hermans, *ChemCatChem*, 2019, **11**, 4054–4063.

Presentations

1. **Understanding phase transitions of confined pharmaceuticals.** Oral presentation at 2019 NMR DG Postgraduate meeting at University of York
2. **Controlling crystallisation through the design of supramolecular interactions.** Prize for best oral presentation at 2019 School of Pharmacy Research Colloquium, University of East Anglia
3. **Towards understanding phase transition of confined pharmaceuticals.** Poster Presentation at 31st European Crystallographic Meeting, 2018, Oviedo. Awarded 1st Prize on Nanostructured Materials category
4. **Study of Crystallisation within Mesoporous Silica Particles.** Poster presentation at 34th British Crystallographic Association Conference, 2017, University of Lancaster

List of Abbreviations

ACV	Acyclovir
BET	Brunauer, Emmet and Teller
BJH	Barrett, Joyner and Halenda
CCDC	The Cambridge Crystallographic Data Centre
CSD	Cambridge Structural Database
CP-MAS	Cross Polarisation Magic Angle Spinning
CSA	Chemical Shift Anisotropy
DFT	Density Functional Theory
DSC	Differential Scanning Calorimetry
FFA	Flufenamic Acid
FFA/NA	Flufenanmic Acid/Nicotinamide cocrystal
FID	Free Induced Decay
FT-IR	Fourier Transformed Infrared Spectroscopy
IUPAC	International Union for Pure and Applied Chemistry
LCT	Liquid-Crystal Templating
MAS	Magic Angle Spinning
MCM	Mobil Composition of Matter
MCF	Mesocellular Foam
MSM	Mesoporous Silica Materials
NA	Nicotinamide
NMR	Nuclear Magnetic Resonance
NOESY	Nuclear Overhauser Spectroscopy
PPM	Parts per million

PXRD	Powder X-Ray Diffraction
rf	Radio Frequency
SBA	Santa Barbara Acid
SEM	Scanning Electron Microscopy
TEOS	Tetraethyl Orthosilicate
TEM	Transmission Electron Microscopy
TGA	Thermal Gravimetric Analysis
TMS	Tetramethylsilane
VT	Variable Temperature

Table of Contents

1 Introduction

1.1 Composition of solid materials

Solid materials can categorised through long-range ordering and periodicity into two distinct groups (Figure 1-1).

1. Amorphous materials show no long-range order in their three dimensional structure and lack periodicity[1]. Instead, amorphous forms are more an aggregate of molecules with some short-range ordering. They possess a glass transition temperature (Tg), below which they are referred to as glasses. Tg is the temperature where the more rigid glassy material will undergo a transition towards a more flexible and rubbery state. Continual heating of the rubbery material beyond the melting point (Tm) will convert it to a liquid without a distinct phase transition[2]. The rapid cooling of this liquid can lead back to the amorphous material, however it may lead to spontaneous recrystallisation.
2. Crystalline materials are the other solid category. They are comprised of materials that possess long-range order in all three dimensions. This category has many subsets that divide the materials into single-component and multi-component materials, the latter containing multiple chemical entities in varying ratios in the same phase.

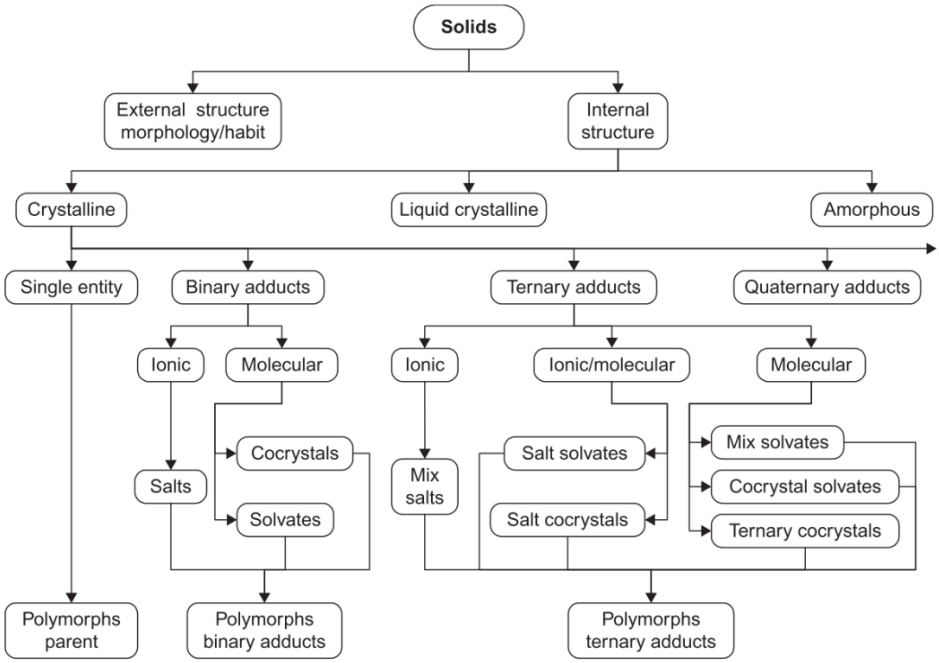

Figure 1-1 A flowchart showing different characterisations of pharmaceutical solids. Adapted from [3]

There are many different solid forms that a particular compound can take on. The simplest subset is that of a crystal consisting of different spatial arrangements of a single entity. When a compound is said to exhibit polymorphism, it means that there are either two or more different structural arrangements. These phases can be different for many reasons, but the essential requirement is that they are made from the same chemical compound. Polymorphs can differ in their packing within the crystalline lattice and exhibit different conformations. Transitions between polymorphs can be brought about through subjecting the crystal to changes in temperature and pressure. It was noted to be of significance within the pharmaceutical industry as early as 1969 by Haleblian *et al*.[4]. Ostwald's rule of stages[5] describes that the first structure that crystallises is the thermodynamically unstable polymorph with the lowest free energy barrier to overcome. After which, recrystallisation occurs into the more thermodynamically stable phases. This means that the metastable form is often the more difficult polymorph to isolate in manufacturing processes.

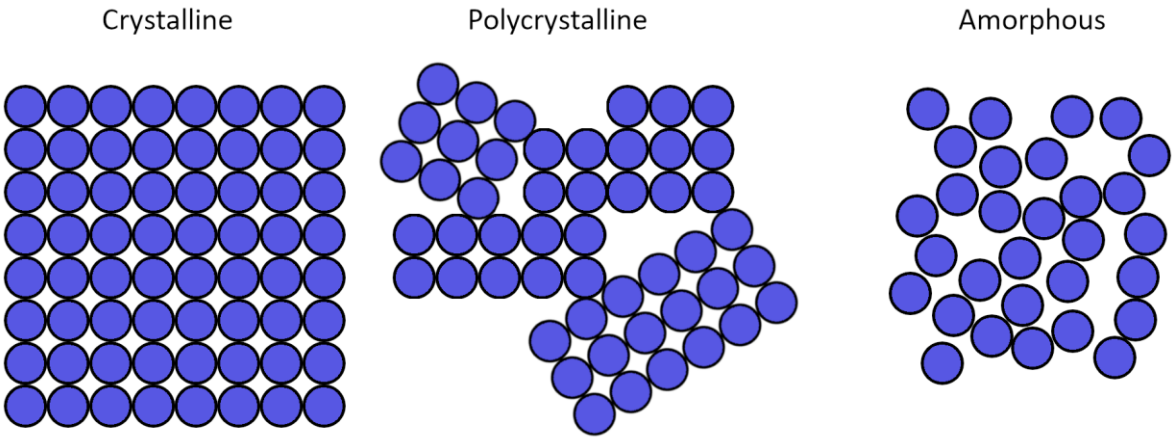

Figure 1-2 The different arrangements of structural order in solid materials

Then there are solid forms that contain adducts of the original material. These can consist of different ratios of the material with another chemical species. As shown Figure 1-1 there are many possibilities of combinations that can occur. These can depend on the bonding type (ionic cation and anion salts/molecular neutral species) and then further depend on the type of additional components added. It is common in the pharmaceutical industry to express the addition of a liquid to crystal structure as a solvate, however if that liquid is water it is referred to as a hydrate. If the additional component is formerly a solid and has formed the adduct it is referred to as a cocrystal. Further details of cocrystals will be discussed later in this chapter.

1.2 Nucleation

The process by which crystal growth occurs is thought to be a well described phenomenon[6]. Molecules or atoms interacting together in an ordered arrangement and then growing from Angstrom scale, to nanoscale, mesoscale until a bulk crystal is formed that can be seen with the naked eye. It can occur with single atoms such a sulphur[7] or with large biomolecules such as proteins[8].

Theoretical models have been developed to describe the kinetics and thermodynamics growth. The confirmation of such models is the challenge that is sought to be solved[9,10] both experimentally in lab, through computer modelling and in an industrial setting[11]. An issue with the experimental confirmation is with the timescale in which the first few building blocks interact and grow. This occurs so rapidly that the species are short-lived and at very low concentrations. Therefore, it is difficult to isolate those critical nuclei as they grow into larger clusters or breakdown back into monomer units.

Hence, the interest in controlling crystallisation of this project. The aim being to investigate this early stage of growth in order to describe structural, phase and energy changes that occur at the nanoscale.

1.2.1 Classical Nucleation

The earliest theory that best described the kinetics and thermodynamics of crystallisation became known as Classical Nucleation Theory[12], (CNT), termed by Volmer[13]. This model began by stating that the formation of a crystalline material was a first order phase transition, whereby the enthalpy of crystallisation ΔH°_{cryst} has a non-zero latent heat value. The phase boundary concentration has a discontinuity feature that results in the boundary between the crystal and solution having non-zero surface free energy. Therefore, if a small area of condensed material forms within a supersaturated solution, the phase boundary that will develop as a result will have a surface energy that is high and unfavourable. As a result of this very few clusters will be able to form within a supersaturated solution, any that do form will have to overcome the free energy barrier by fluctuations within the solution.

The first step in forming the new phase is to overcome this barrier, which in turn determines the kinetics of the system where a number of molecules are present in close proximity to each other that are able to serve as a nucleation point. Many models[14] have different suggestions for the shape of this cluster such as a droplet shape, however the model that will be described here will have this initial cluster as a cubic shape with a side a. When the solute chemical potential of the system is greater than the chemical potential of molecules in the crystal, the solution is described as being supersaturated $\Delta\mu = \mu_{solute} - \mu_{crystal} > 0$. When a cluster develops, there is loss of free energy

equal to $-n\Delta\mu$. However, when the phase boundary develops (with an area and surface tension equal to S and α respectively) there is an increase in free energy $S\alpha$. When the crystal cluster is of cubic shape the area of phase boundary will be equal to $S = 6a^2n^{2/3}$, and the free energy for a given size of cluster will therefore equal and is shown in Figure 1-3:

$$\Delta G(n) = -n\Delta\mu + 6a^2n^{\frac{2}{3}} \ (\mathbf{1})$$

Differentiating (1) we are able to find the critical cluster size $n^*$where a maximum of ΔG passes through ΔG^*, which gives:

$$(2)\ n^* = \frac{64\Omega^2\alpha^3}{\Delta\mu^3} \text{ and } \Delta G^* = \frac{32\Omega^2\alpha^3}{\Delta\mu^2} \ (\mathbf{2})$$

Where Ω is equal to the volume (cube system therefore a^3) the molecule occupies as the crystal.

Crystals may grow from below this point; however, it will be energetically unfavourable and will have to compete with the free energies of the solutes. At the maximum point of n^* there is an equal chance that the critical cluster will grow or decay as the energy difference is the same. This denotes the critical cluster size that every crystalline material has to overcome in order to grow.

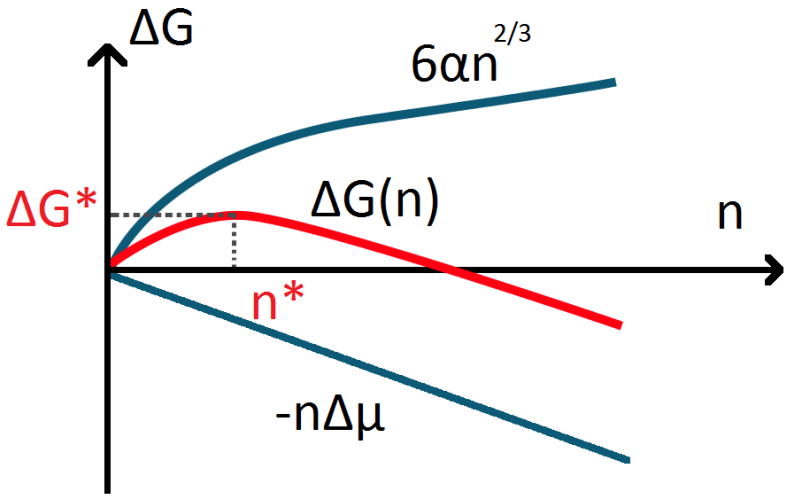

Figure 1-3 Thermodynamics of critical cluster growth, from equation (1) and (2). Adapted from [15]

The rate at which crystallisation occurs, nucleation rate J, is the number of crystalline nuclei formed over time and is expressed as a function of the supersaturation analogous to the Arrhenius equation whereby

$$J = J_0 \exp\left(-\frac{\Delta G^*}{k_B T}\right) \quad (3)$$

In this equation k_B is the Boltzmann constant, T is temperature and ΔG^* is the critical free energy maximum. J_0 can be defined as being the product of the rate of addition of monomer units to the critical nucleus, v^*. The Zeldovich factor, Z, which accounts for the width of ΔG^* at the maxima curve in the $\Delta G(n)$ free energy profile (Figure 1-3). The rate of nucleation has a nonlinear relationship with respect to the supersaturation ratio. Minute fluctuations in supersaturation give huge changes in nucleation rate. Therefore, it is evident that as a cluster grows larger, taking more monomer units out of the system, the supersaturation ratio will lower and drastically reduce the rate of nucleation.

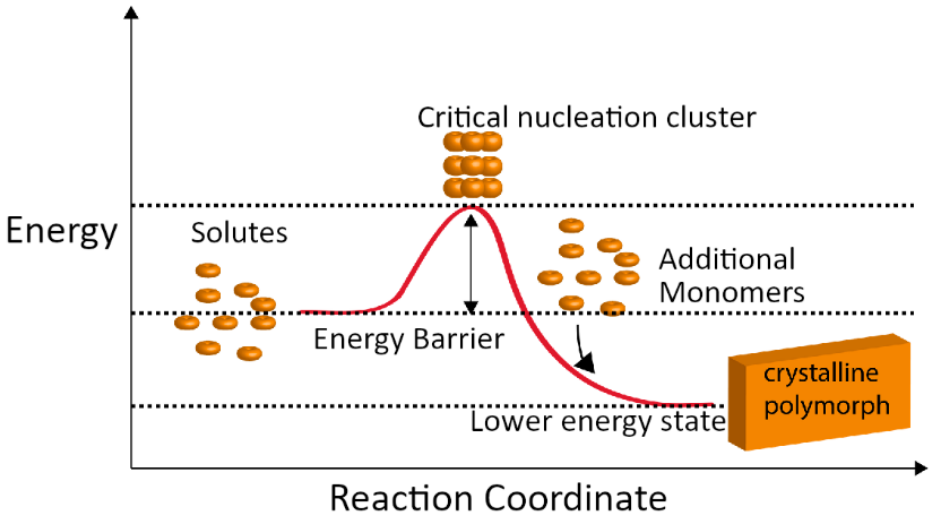

Figure 1-4 Graphical representation of classical nucleation theory. Adapted from [16,17].

1.2.2 Non-classical Nucleation

Following classical nucleation theory, adaptions have been made that add to or better define the initial cluster generating steps. One of these theories is non-classical nucleation[12] (NCN), otherwise known as the two-step mechanism[15] which explores the differences between the crystal and liquid phase layers. Instead of forming a solid crystalline cluster that has systemic order to it, NCN suggests that the cluster is more a dense liquid type phase, lacking order, but is still a cluster of units that have been separated inherently from the solution. The crystalline order that is expected comes later on, after a number of units have been encapsulated by the cluster as a sequential additional to the first couple of molecules that came together. The ordered state will form at the nexus of the cluster as the liquid-like layer of units separate the phases.

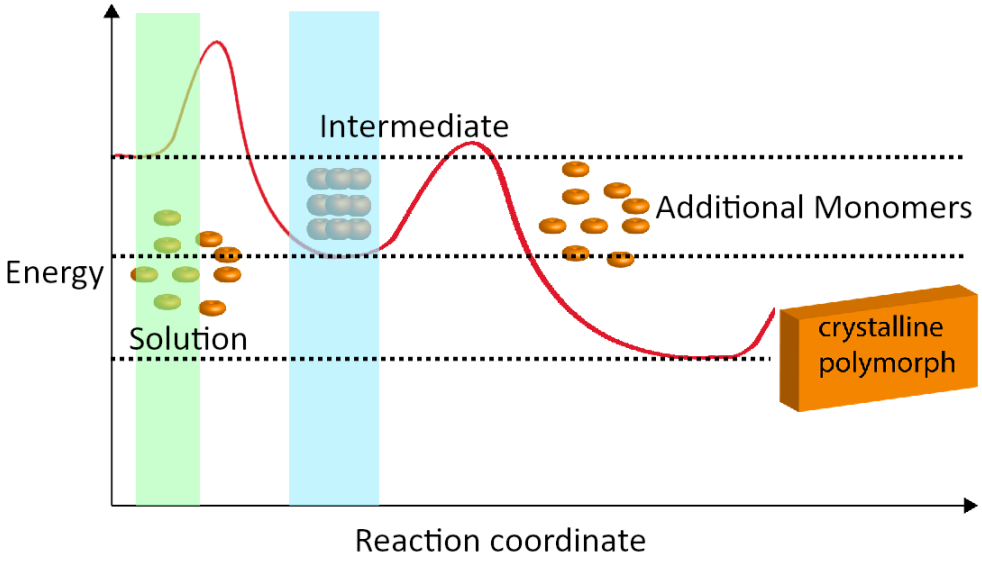

Figure 1-5 Graphical representation of non-classical nucleation pathway. Adapted from [16–18]

The NCN model (shown in Figure 1-5) shows the same endpoint as in the CNT model (Figure 1-4), and still exhibits a critical point at which the free energy can either continue to build or break apart the cluster. The liquid-like intermediate cluster should not be confused with liquid-liquid separation such as oiling out, when the "drops" of condensed units are forming a bulk liquid phase - they have already passed the pre-nucleation phase.

Further work on nucleation is currently occurring, with many studies published in the last 10 years that support the idea of the NCN following the two-step process[19,20]. However, the issue with the research is that the second step is not well described, namely the progressive restructuring of the cluster into a more ordered and compact system at a later aggregation stage. In this two-step process, the faster process is the formation of the metastable intermediate product because the activation energy barrier is lower than that of the ordered nucleus. That nucleus is the rate determining step as it has the larger barrier of activation in order to form.

1.3 Polymorphism in Pharmaceutical Application

Crystallisation itself has become one of the most important sciences for the development and formulation of drug compounds in order to physically produce and administer doses to patients, also is important to the food industry and the fine chemical industry. It is a crucial step that can serve many functions in the production of a compound, two of the most important being the separation and subsequent purification of a material. Within the pharmaceutical industry, separation can be a removal process for intermediate compounds, starting reagents and contaminants from the active

pharmaceutical ingredients (APIs). The scaling up of a novel API from the whiteboard to the lab gives rise to many different solid forms (Figure 1—1) that the finished compound can take. A lot of these forms are poorly soluble and greatly affect the ability of the API to be delivered to its intended target. Therefore, much effort is put into manufacturing materials that have metastable polymorphs or a stable co-crystal to aid its uptake. These forms also try to feature a suitable manufacturing process that has a high yield and purity, otherwise it may not be financially viable for the company to produce.

Polymorphism can result in different forms of the same compound having different chemical and physical properties associated with it. Changes in these can affect how well the compound is able to be solubilised or broken down, in turn affecting the activity of the compound and bioavailability and stability. All of these properties can also be affected by how the drug is formulated with respect to the physical form it takes. The pharmaceutical industry[21] has to take great care when a new lead compound is discovered; developing synthetic methods, small scale lab synthesis for screening, all the way up to large scale plant production – each of these steps can reveal new polymorphs that may be unaccounted for in the final product before separation. The cost of scaling from laboratory to plant production has to be factored, as an expensive reagent or catalyst may not be a viable economic method of production. Computer modelling is good method before large scale production of a compound begins as a number of polymorphs can be predicted and screened[22] given the chemical structure of the lead compound[23].

1.4 Cocrystals

The technical definition of a cocrystal is generally regarded as being a compound consisting of two or more molecules of different compounds that are linked by intermolecular interactions; such as hydrogen bonding or van der Waals forces. The compounds are not covalently bonded to each other, they lie close in space and through these are able to form a unit cell and a repeating lattice crystal structure. One of the more recent developments within the crystallography field is cocrystals and their use in the pharmaceutical industry at increasing bioavailability, stability and solubility. Mechanistically the dissolution and stability have been studied in a range of literature. The dissolution of carbamazepine–salicylic acid cocrystals was described by Cao et al.[24] which were developed as mass transport models. Through applying Fick's law of diffusion and considering the boundary layer of the surfaces of the macroscopic cocrystal. Relative stabilities with regards to pKa of cocrystal components was studied by Bethune et al.[25]. In this study relative terms for cocrystal solubility are derived such as solubility product and the ionisation constants. Through this derivation the findings showed a concordance with the predicted behaviour of a generated pH-solubility curve – the curve estimates

how well a coformer stabilises or will precipitate a cocrystal and thus provides a good guide for selection of a cocrystal without the need to develop a complete phase solubility diagram. Likhitha et al.[26] showed that a combination of nicotinamide and picric acid cocrystal possessed higher melting points than the individual synthon components. Aakeroy et al.[27] made the distinction of whether being a cocrystal or a salt changed potential beneficial pharmaceutical properties of a compound. Through an analysis of over 80 salts and cocrystals they showed that carboxylic acid conversion from an anion to neutral species had significant impact on the structural arrangement of the system. The conversion of anionic salts into cocrystals is an interesting line of research, Nangia et al.[28] were able to successfully convert the zwitterionic drug Sparfloxacin into a neutral species by cocrystallising it. This was achieved through use of a phenol-amine heterosynthon and adjustment of pH and resulted in the neutral species having a better dissolution profile than its zwitterionic counterpart. With the consideration of crystal engineering in mind, Desiraju[29] et al. showed that the synthons could have issues forming due to the interference of interactions between molecular and crystal structures. Hence, the design and choice of two synthons to form a cocrystal should ideally have interactions that favour the pair to bond, but also such that the repeating geometric lattice of the singular molecular component is able to withstand any interference from unfavourable interactions from other parts of the synthons not involved in the molecular cocrystal.

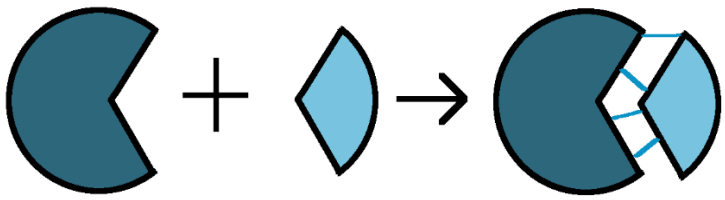

Figure 1-6 Cocrystal intermolecular interactions

Hydrogen bonding is the most widely used method in cocrystal engineering due to the specificity of angles and directions. Also, because most APIs are organic small molecules in nature, they generally will have one or more sites of functionality that are able to hydrogen bond - for example π conjugated rings, carboxylic acids, amides and alcohols. These hydrogen donor/acceptor functionalities have to be matched to form suitable synthons therefore screening is an important tool to use. Some functionalities will possess a stronger capability to hydrogen bond and it is generally accepted that the 'best donor/best acceptor'[30] rule applies when looking at the hydrogen bonding between two different molecules. The resulting supramolecular synthon is that of ordered structural units that have been formed by these intermolecular interactions. The tuning of these interactions has been studied

closely by many groups in order to bring about the engineering of specific crystalline packing that will result in specific properties. Desiraju and Saha[31] showed how it was possible to identify the synthon packing arrangement of the characteristic hydrogen bonding through spectroscopic means. Their described work was as a crystal engineering exercise, however demonstrated that it was possible to both identify synthons which would be suitable to form a particular crystalline packing to give rise to desired properties.

1.4.1 Stability of Cocrystals

The first cocrystal was reported by Friedrich Wöhler[32] in 1844 consisting of quinone and hydroquinone. Since then, many more have been discovered, however it is in the last few decades that cocrystals have become an area of great interest for the pharmaceutical industry. For small molecule drug compounds, cocrystals allow for a flexible way of stabilising the desired APIs as the coformer in the cocrystal can be tailored to match the active compound. Previous work[33] has shown the ability to increase the solubility upwards of a 10,000 fold enhancement (μmol/mL) of a potent ErbB2 inhibitor used in the development of cancer cures. The compound previously had poor solubility of around 0.008 μmol/mL and had limitations with bioavailability. Therefore, multiple acid-base complexes were synthesised in order to enhance the drug delivery profile of the compound.

Another API that has had its solubility increased[34] by formation of a cocrystal was a compound called 2-[4-(4- chloro-2-fluorophenoxy)phenyl]pyrimidine-4-carboxamide. By itself, the compound had low solubility and as a result its permeability to pass through cells could not be measured. It was developed as a candidate for the treatment and prevention of pain caused through surgery, neurological pain and also chronic panic conditions. By forming a cocrystal with glutaric acid, the overall solubility and oral bioavailability was increased significantly.

Enhancement of stability is also a goal for crystal engineers within pharmaceuticals; being able give an API a longer shelf life, stable at changes in humidity and temperatures. Humidity being one of the key areas due to the fact that hydrates of compounds respond differently and decompose faster. Theophylline[35] (a drug used to treat respiratory problems like asthma) was studied extensively and had a number of synthons to pair with in order to form cocrystals due the fact that it interconverts between hydrated and anhydrous forms when the humidity is changed[36]. Because of this reversible behaviour its stability is extremely dependent on the environment it is stored and processed in, presenting the problem of stability. These coformers were oxalic, malonic, maleic and glutaric acids. Of these compounds oxalic acid provided the greatest stability to hydration. Berberine chloride (BBC

– a drug which effects gram positive and negative bacteria) was also a candidate for cocrystallisation stabilisation in order to enhance its stability in humid environments. Yang et al.[37] showed that a cocrystal of BBC with fumaric acid improved stability to temperature, humidity but also increased the solubility of the drug.

The technique of producing a more stable cocrystal against reversible hydration had also been previously employed in 2005 on caffeine[38]. Caffeine exists in three forms; two forms of anhydrous (α which interconverts from β at high temperatures) and a third hydrated form of which the number of waters is nonstoichmetric. A selection of dicarboxylic acids was chosen as coformers to form cocrystals as the structure of caffeine allows for strong hydrogen bonding through the nitrogen and weak hydrogen bonding through the C-H bond present next to the nitrogen on the five membered rings. Cocrystals were formed from oxalic acid, malonic acid, maleic acid and glutaric acid in different stoichmetric ratios (depending on functionality). All cocrystals then exhibited a much higher stability when the relative humidity of the environment was increased, the oxalic acid derivative having the best – stable at 98% RH after 7 weeks.

1.5 Silica as a vehicle of Drug Delivery

1.5.1 Mesoporous silica nanoparticles

A porous material is defined as possessing considerable free internal volume, high surface area and large pore volumes Porous materials are of interest in material science, because they have applicability in many different industries; such as the petroleum industry, zeolite catalysis for cracking oil, zeolite acid catalysis[39], membranes for gas sorption and separation[40], or drug delivery. The International Union of Pure and Applied Chemistry (IUPAC) classifies porous materials into three groups which are based on the pore diameters. These are:

1. Microporous materials – possessing pore diameters smaller than 2 nm, generally known to be metal-organic-frameworks[41–43] (MOFs), zeolites or certain polymers.
2. Mesoporous materials - possessing pore diameters between 2 and 50 nm, generally known to be silica and alumina[44,45] type materials.
3. Macroporous materials – possessing pore diameters exceeding 50 nm, some silica and alumnias, metal oxides[46] and porous glasses[47].

After the discovery of mesoporous silica materials; MCM[48], SBA-15[49], MCF[50] , an avenue of functionalised materials became possible to use as pharmaceutical drug delivery devices. These

materials offer features unique to the nanoscale; possessing a network of pores with diameters between 2 - 50 nm, different order and functionality and high pore volume.

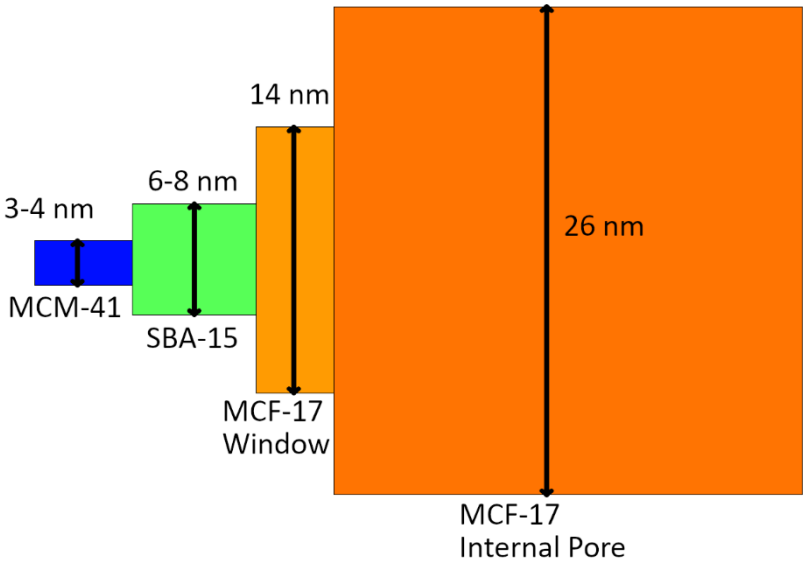

Figure 1-7 Graphical representation of the difference in the pore diameters between MCM-41, SBA-15 and MCF-17 (not to scale).

Mesoporous silicas are generally synthesised using an organic templating agent to influence the size of the desired pores, followed by a calcination step for the removal of the templating agent. MCM-41 was the first of these mesoporous silicas to be described and synthesised by Beck *et al*.[51] and Kresge *et al*.[52] who theorised the liquid crystal templating (LCT) mechanism. This mechanism uses structural directing agents such as cationic surfactants to form micellar type structures when placed in non-neutral pH solutions at room temperature. These surfactants have an alkyl tail that can be altered to then determine the dimensions of the internal pores. To these micellar structures, a silica source is added and in most cases the source is tetraethylorthosilicate (TEOS). This silica source is then hydrolysed in the solution and self-assembles around the micellar templates. After which, heating of the solution results in the condensation of the silicate ion forming a gel. The resulting gel is then calcined in order to remove the organic surfactant leaving the mesoporous silica behind.

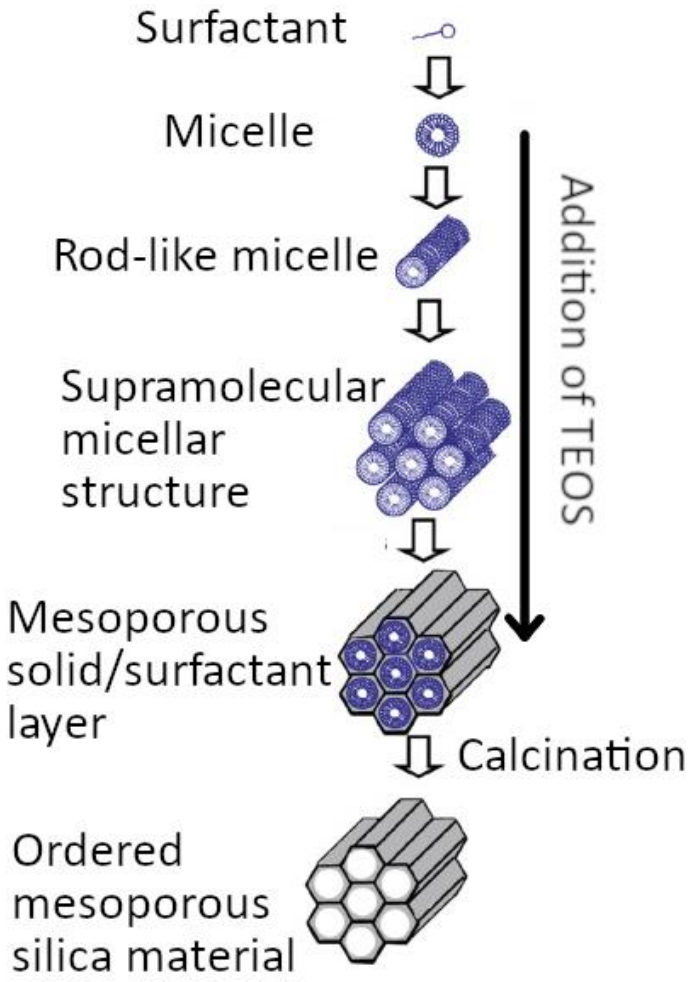

Figure 1-8 Schematic representation of the Liquid Crystal Templating mechanism. Adapted from [53]

Following the discovery of MCM scaffold materials, it was reported by Zhao et al.[54] that a new family of mesoporous silica nanoparticles had been synthesised. Instead of the cationic/anionic surfactants that MCM materials used[51,52] a triblock copolymer of poly(ethylene oxide)-poly(propylene oxide)-poly(ethylene oxide) was used as the source of silica for the template. As with MCM synthesis, a slightly acidic aqueous solution was required to dissolve the copolymer and thus enable the building of the supramolecular micelle templates. The self-assembly of these micelles follows the condensation process of MCM, however the copolymer allowed for the synthesis of highly ordered hexagonal pores ranging from 5 to 30 nm pore diameters. The mechanism of formation of these SBA particles has been studied extensively through different techniques such as EPR[55] and X-ray/neutron scattering experiments[56], the latter of which support the Cooperative Templating mechanism. This mechanism differs in the concentration of the surfactants, being that of much lower concentrations. Here the driving force of assembly is based on interactions between the surfactant ions with the inorganic silica[57]. This pathway has significant impact on the morphology of the resulting mesoporous phase.

The third type of mesoporous silica we will concern ourselves with is called MCF[50] (mesocelluar foam). Its synthesis follows a modification to the SBA-15 procedure where an additional swelling agent, usually 1,3,5-trimethylbenzene (TMB) is added. The result is that the coated micelles swell and form can form much larger silica structures. These structures consist of large spherical cells, ranging from 15 -50 nm, that possess windows to access them between 5-20 nm. They have been referred to as ink-bottle type particles for this structural arrangement. The pores and morphology of particles are able to be controlled through the addition of ammonium fluoride prior to aging.

For the study of crystallisation, it is of interest to attempt to study the early stage of nucleation at the atomic to nanoscale, as this is an area that will enable small scale stacking of molecules but not allow a macromolecular scale structure grow.

1.5.2 Encapsulation of Drugs

Porous materials allow for the encapsulation of guests, more specifically small organic molecules, in an effort to enhance properties of hydrophobic drugs which are notorious for their poor dissolution and oral bioavailability. Mesoporous silica nanoparticles have been shown to improve the oral drug viability of different drugs such as telmisartan[58] and doxorubicin hydrochloride (DOX)[59]. Their evaluation as potential drug delivery vehicles is prevalent in literature due to the stability they offer and their biocompatibility[60–63]. Mesoporous silica nanoparticles also serve the purpose of being a system in which we are able to model the process of crystallisation as it will be the restriction of the size of the pores aiding the understanding of pharmacueticals.[64].

Nartowski et al[65] showed IMC was loaded into SBA-15, MCF and CPG at different ratios of host-guest and then characterised using a variety of methods. One of the methods used to load the IMC into the pores was the melt loading method, by which the host and guest were mixed together then the mixture heated above the melting point of the guest. The molten guest is then drawn into the pores by capillary action. Another method used was the incipient wetness method, where IMC was dissolved into a hot solvent then loaded by dropwise addition of the solution to the silica host.

However, confirming the guest is within the pores is a key area of interest. A range of characterisation techniques are used to corroborate this. Solid state NMR (^{13}C-^{1}H CP-MAS) of the compound before and after loading shows a broadening of the carbon peaks, this is due to the local disorder and possible increase in the mobility of the guest. Differential scanning calorimetry of the host-guest compound at different ratios show different environments of amorphous media within the pores. At lower loading levels there is no glass transition present, indicating an amorphous compound.. However, as loading levels increase in the larger media (CPG host with pore diameter 55 nm) a mixture of polymorphs

become present as the relative size allows for the boundary towards macroporous media to be achieved. Further studies using nitrogen adsorption confirm the guest is physically loaded within the pores and is not just on the surface of the silica particles. Adsorption/desorption isotherms were taken of the pure silica compound and then the different ratio loaded silica-guest materials. The isotherm had Barrett-Jotuner-Halenda method[66] applied to it in order to calculate the total pore volume and as expected as the level of guest increased with respect to the host the overall pore volume decreased showing that the guest eventually completely fills the pores. The combination of these methods allows for insight into the phase transitions that occur on the nanoscale through the confinement of the guest molecule.

^{19}F NMR is an extremely sensitive technique for many reasons; fluorine has a high gyromagnetic ratio giving it good susceptibility to magnetic resonance experiments, the naturally occurring isotope has ½ nuclear spin and 100% abundance. There are a variety of instances where ^{19}F NMR (alongside other materials characterisation techniques) have been used to explore the properties of confined drugs in mesoporous silicas due to these NMR properties. It was used by Egodawatte *et al.*[67] to obtain insight into the loading of 5-fluorouracil (5-FLU) into magnetic MCM-41 systems. The loading and release profile of 5-FLU were explored given a variety of solvent driven release mechanisms and modification of the silica surface through functionalisation. In contrast to use to explore API related properties Bouchoucha *et al.*[68] used ^{19}F NMR to monitor fluorine functionalised mesoporous nanoparticles for use in MRI probes. These probes in bioimaging are a growing area of interest, and the previously mentioned DOX[59] was also encapsulated into ^{19}F functionalised mesoporous silica nanoparticles by Nakamura et al.[69]. ^{19}F MRI allowed the release rate of DOX to be controlled, increasing the release rate of drug by changing the conditions of the environment to be more acidic.

Further exploring the process of crystallisation through the use of the encapsulation of cocrystals is a key step for the pharmaceutical industry. This will allow us to explore the barriers and applicability of mesoporous silica as a candidate for hosting APIs in a cocrystalline form in order to further increase their bioavailability. The loading of cocrystals into mesoporous silicas has been achieved by Skorupska et al.[70,71] with the loading of cocrystals of BA/FBA (benzoic acid/fluorinated benzoic acid) and IBU/NA (ibuprofen/nicotinamide). In each case solid state NMR was the primary tool in order to characterise the structure and dynamics of the drugs inside the pores. 2D NMR correlation techniques such as ^{19}F-^{19}F BABA and ^{1}H-^{19}F HETCOR revealed differences in the rigidity of the loaded BA/FBA material, demonstrating a significant increase in the mobility of the species. IBU/NA was shown to me loaded inside the pores of MCM-41, and also had its release profile characterised for the different racemic structures of the IBU/NA mixtures. They showed that by changing that IBU/NA composition they were

able to control the release rate of the trapped API. This further strengthening mesoporous silicas as a viable drug delivery device due to the possibilities of sustained drug delivery profiles for APIs.

A critical paper for the concern of this thesis is that by Nartowski et al.[72] Use of flufenamic acid (FFA) as a model compound gave us an opportunity to perform ^{19}F NMR as a method of investigating the polymorphic behaviour (Figure 1-9). FFA is known to have many polymorphs and has been investigated thoroughly for its pharmaceutical devleopment[73–75]. FFA was loaded using the melt loading method into multiple hosts as before – MCM-41, SBA-15, and MCF. Confirmation of loading was also completed using PXRD, TGA, nitrogen adsorption/desorption isotherms and DSC thermograms. However, when ^{19}F MAS NMR was performed on the samples the expected signal was a broadening of the single resonance at -60.0 ppm that corresponds to the CF_3 group, in actuality multiple peaks were observed in the spectra showing the existence of multiple phases of FFA within the pores.

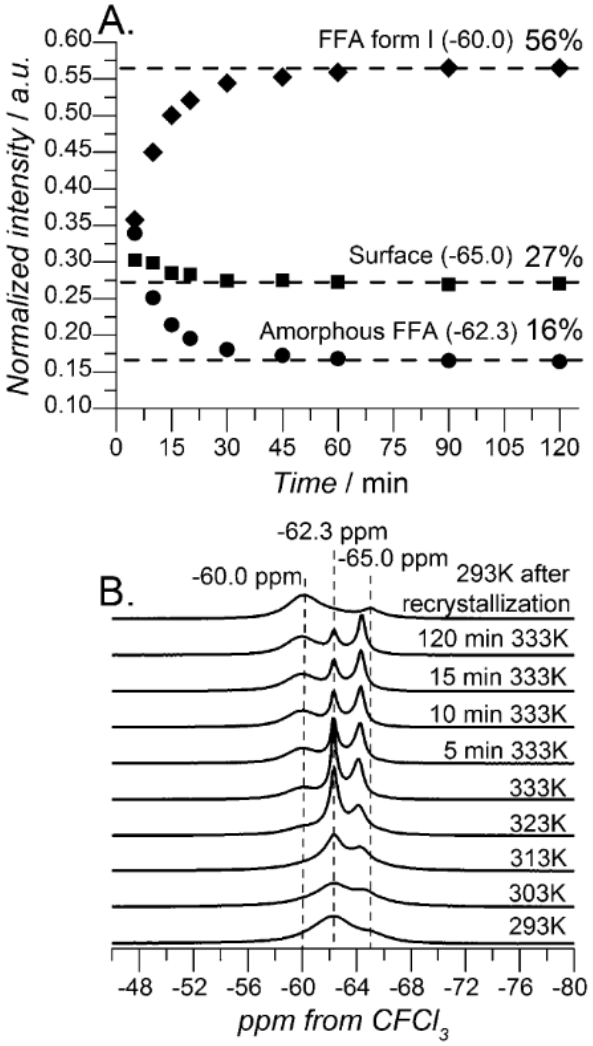

Figure 1-9 A. Kinetics of crystallisation of MCF-FFA 60:40 **B.** Variable-temperature ^{19}F solid-state NMR spectra (9.4 T) of FFA confined within MCF**.** Reproduced from [72]

During a recrystallisation study in MCF-FFA 60:40 there were three populations; one which corresponded with the pure FFA form I peak at -60.0 ppm, a second peak at -65.0 ppm and one in-between at -62.3 ppm. What is interesting about these resonances is that at different loading ratios of FFA the intensity of the crystalline peak decreases, however the secondary peak grows slightly then tails off to the same level as the crystalline as the loading ratio has reached its lowest. This indicates the secondary peak is probably of amorphous nature which was later confirmed through variable temperature ^{19}F spectra, in which recrystallization took place. After heating the loaded MCF-FFA sample to 333K the spectra showed the evolution of a third resonance peak situated in between the crystalline -60.1 ppm peak and the amorphous peak at -65.0 ppm. As the sample was then allowed to cool to room temperature the middle peak that resided at around -62.3 ppm faded to almost no intensity. At this point, as can be seen, there were at least three distinct species within the pores, these phases each possessing different mobility. There is a crystalline phase that is present, and a mobile liquid matter phase that moves along the surface of the silica and then an aggregated species that exists between these two phases. This aggregated phase disappears during recrystallization, implying its molecules have been incorporated into the crystalline phase within the pore. This phenomenon is of interest because it is the direct result of crystallisation occurring from a single molecule type arrangement, into an aggregated system, then into a crystalline-like ordered arrangement. ^{19}F Solid state NMR of the CF_3 giving observable differences in the local environment of nanoscale crystallisation.

1.6 Aims of the Project

Therefore, the aim of the project is to investigate further the different phases of matter possible through encapsulation into silica. The exploration of the phase transitions of pharmaceuticals loaded into the pore space may offer greater insight into the methods by which we can access certain polymorphs or phases of matter. In order to complement the previous studies of FFA[72] we will use a cocrystal of FFA with the well-known coformer nicotinamide (NA)[76] and attempt to explore and probe the boundaries of cocrystalline, coamorphous and mobile species. We will encapsulate FFA/NA cocrystal at various loading levels into three different mesoporous silicas; MCM-41, SBA-15 and MCF. This is in order to explore the landscape of pore diameter size against the ability of an API to recrystallise inside the pores.

Following this we will also load pure NA into the three mesoporous silicas also in order to generate a full picture of the possibilities when loading both the separate components and the cocrystal of FFA/NA. These materials will be made and analysed through a variety of techniques. Nitrogen sorption isotherms of the materials will allow for surface area, pore volume and pore diameter calculations. TGA will allow the direct loading ratio confirmation by decomposition of the organic loaded APIs. DSC will be used to explore any possible amorphous or crystalline material that are able to interconvert, melt or decompose. PXRD will be used in order to show the state of the crystallinity of the API inside (or outside) the silica pores and will be a useful tool in quick phase identification. Solid state NMR will be used heavily in this project as a method of detecting and characterising different polymorphs through distinctive ^{13}C analysis, but also using ^{19}F as a phase identification tool. Within solid state NMR variable temperature experiments will be used to show the impact heating/cooling has upon the mobility and local environment of the API. Lastly computational methods, using the CASTEP[77] code, will be used in conjunction with NMR in order to verify and assist assignments of chemical shifts to specific nuclei.

We also aim to explore the ways in which solution mediated phase transformation can occur within the antiviral drug acyclovir (ACV). This drug possesses two anhydrous forms and two known hydrates which are able to be converted between using thermal dehydration techniques. We will first characterise these known forms using a combination of solid-state NMR, PXRD and DSC in order to understand differences between the structures. We will then use a combination of variable temperature FT-IR studies to monitor the thermal dehydration of the hydrate forms. Following this we will attempt to induce solvent mediated transformations of the ACV polymorphs in order to explore the mechanisms of hydration/dehydration.

2 Characterisation Techniques

2.1 Nuclear Magnetic Resonance

Nuclear Magnetic Resonance (NMR) is a technique that has existed since the 1930s and has become a pillar of spectroscopy since then due to its ability to discern information about the local chemical environment of molecules; their bonding, orientation, coupling and intermolecular interactions with nearby molecules. It was first theorised by Pauli when he discovered the existence of the nuclear spin and first experimentally confirmed in 1937 by Rabi[78] who showed nuclear magnetic resonance by variation of RF fields within a permanent magnetic field. Since then, the evolution of NMR has taken many steps to increase the amount of information that can be interpreted from a spectrum; from increasing the strength of the magnetic field to the invention of Fourier Transform techniques and pulse experiments.

2.1.1 Basic Principles of NMR[79–81]

The basic principle of NMR is that all nuclei possess nuclear spin – quantum mechanics labels this spin I and comes in multiples of ½, which can be positive or negative. The nuclei which possess a nonzero spin quantum number are said to be magnetically active. Their magnetic moment is given the letter μ and is formed as a product of the spin of the nucleus I and the gyromagnetic ratio γ to give:

$$\mu = \gamma I.$$

The spin angular momentum is a vector quantity that can be related through the spin quantum number, where ħ is the Planck's constant (reduced) and $\vec{I}$ is the spin angular momentum:

$$\vec{I}^2 = (I(I+1)\hbar^2)$$

In the presence of an external magnetic field B_0 the nucleus will exist in two spin states (for I=½ nuclei) +½ and -½ along the axis of the magnetic field (conventionally labelled as the *z* axis), where the positive state is aligned with the magnetic field (lower in energy) and the negative state is opposed to the magnetic field (higher in energy). This energy is calculated as the product of magnetic moment $\vec{\mu}$ and

the strength of the magnetic field B_0. When this magnetic field is thus considered to be parallel to the *z* axis of the spin it is possible to quantise the energy where, *m*, the magnetic quantum number follows the selection rules of $\Delta m = \pm 1$ taking integer steps of $2l + 1$ values:

$$E = -\mu_z B_0 = -m\hbar\gamma B_0$$

This causes a splitting of the energy levels associated with nuclear spin which are then proportionally separated through ΔE against the gyromagnetic ratio γ and the applied field B_0. This is called Zeeman splitting an is unique to each nucleus and is shown in Figure 2-2.

$$\Delta E = \hbar\gamma B_0$$

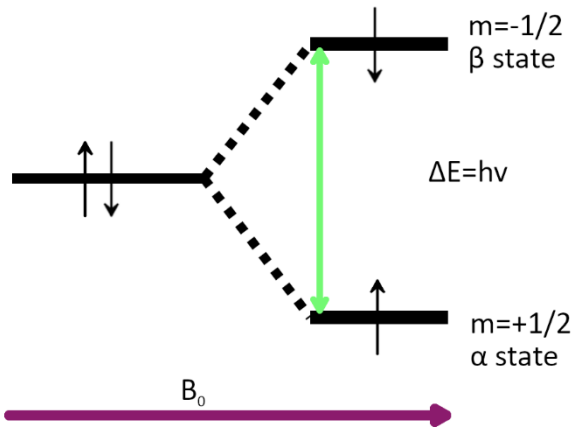

Figure 2-1 Zeeman splitting of relative energy levels between two magnetic spin state ($\boldsymbol{\alpha}$ and $\boldsymbol{\beta}$)

2.1.2 The Larmor precession[79–82]

When a nucleus is placed in a magnetic field, it will experience torque due to the combination of the magnetic moment and angular moment creating a net magnetisation of nuclear spin. The torque experienced by the nucleus will align itself perpendicular to the B_0 field. The rate of this precession within the external magnetic field, B_0, is proportional to the strength of the field and is denoted by:

$$\omega_0 = \gamma B_0$$

Where ω_0 is known as the net angular velocity of the precessing motion. Each nucleus has its own unique motion giving rise to a specific Larmor frequency, v_0, specific to the strength of the field the nucleus is experiencing:

$$v_0 = \left|\frac{\gamma}{2\pi}\right| B_0$$

When the nucleus is subjected to rf energy that is of the same frequency as the precession of the nucleus (the Larmor frequency) perpendicular to the external magnetic field, the nucleus is then able to absorb the energy and change (flip) its magnetic moment from the low energy α state to the higher energy β state.

2.1.3 Bulk magnetisation and Boltzmann distribution[79–83]

The previous theory concerns an isolated nucleus, however in NMR applications we do not deal with a single nucleus nor single type of nuclei. A large number of spins are present in a real sample, each having their own interaction with the applied B_0 external magnetic field continuously. This means that the Boltzman distribution is relevant here, as the occupancy of energy states of the system have a temperature dependence to form thermal equilibrium through:

$$\frac{N_\beta}{N_\alpha} = e^{\frac{-\Delta E}{kT}}$$

Where k is equal to the Boltzmann constant, T is the temperature (measured in Kelvin), ΔE is equal to the energy gap between α and β states and N is the net population of spins existing in those energy states. Using this equation there will be small number of states existing in the higher energy state, and that difference in energy states sums to give an overall magnetisation vector perpendicular to the B_0 field along the *z* axis of the higher energy state. This result is known as bulk magnetisation, M_0.

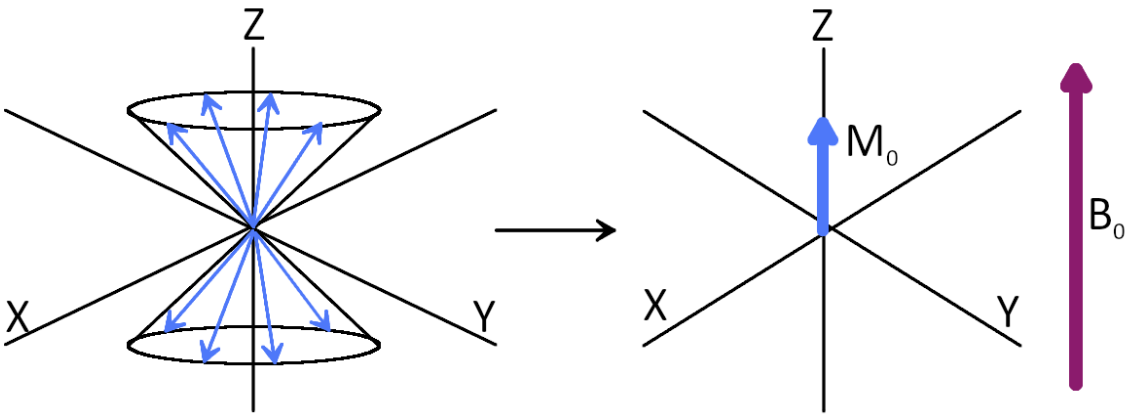

Figure 2-2 Vector model representation. The external magnetic field causes precession of nuclear spins around the *z* axis. An overall difference in populations gives rise to the bulk magnetisation M_0 aligned along the *z* axis to the external magnetic field B_0

Inducing the transition between the spin states α and β is achieved through radiofrequency pulses. These pulses are set to be close to the calculated Larmor frequency of the given nucleus, and are used to make NMR transitions between states occur. A coil that is wrapped around the sample is used as

the vehicle of delivery of the applied rf frequencies. The alternating current in the coil in turn creates a small magnetic field that is denoted as B_1. This second field, B_1, oscillates at the Larmor frequency of the spin at 90° (perpendicular) to the strong external magnetic field, B_0. When considering the appearance and explanation of these magnetisations and rf effects the vector model is replaced with the rotating frame model of reference.

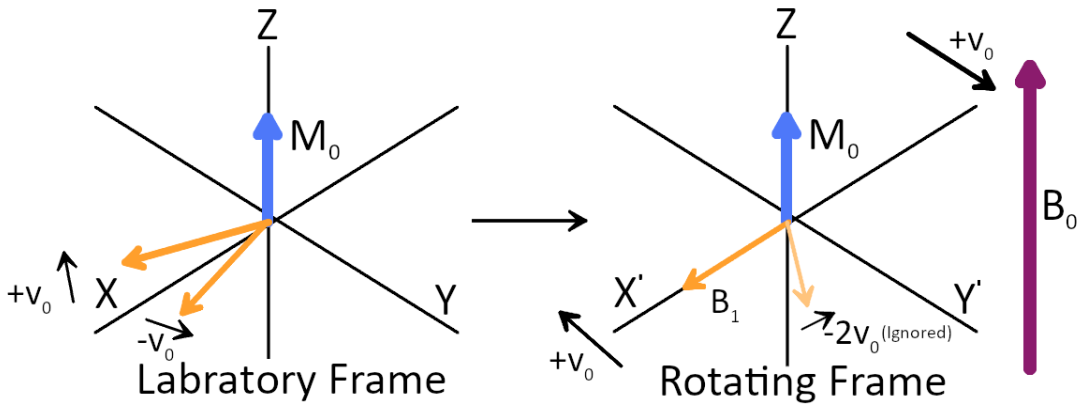

Figure 2-3 Graphical representation of the conversion from laboratory frame to rotating frame of reference

The laboratory frame is primarily described with two vectors, $+v_0$ and $-v_0$, where its coordinates (x, y and z) are static. The *rf* pulse introduces a magnetic field, which subsequently oscillates with nuclear precession (in the transverse plane). This is shown in Figure 2-3 as the $\pm v_0$ vectors and can only occur when the NMR condition is satisfied. In contrast, the rotating frame has coordinates x' and y' which are rotating at the nuclear precession frequency. Also, in the rotating frame, one of the vectors is now static. The second rotates in the opposite direction from the resonance and is able to be ignored ($-2v_0$). The means that, when the rotating frame is considered, the time dependency portion of the *rf* field can be removed and the bulk magnetisation and B_1 can be shown as perpendicular and static to each other.

2.1.4 NMR as a tool of analysis[79–81]

When we consider how to use NMR as an analytical technique, from first appearance if each nucleus only responded to one resonant frequency the technique would be limited to a means of indirect nuclei detection. However, each nucleus in a system experiences the external magnetic field differently due to its local environment and surrounding electrons. This means that a number of frequencies can be observed as a reaction to the applied magnetic field, allowing us to characterise them into different types of functionality.

The electron cloud circulation in their respective orbitals is similar to that of an electrical current. Where there is an electrical current, there is also a magnetic field. Each electron will produce a small, local magnetic field which resides in the opposite direction to that of the applied external field B_0. These secondary fields act to "shield" the nucleus from the external magnetic field, and because of the different electron environment (functionality) each nucleus will then display a different chemical shielding, δ, to that of its neighbour or environment.

When determining the chemical shift of a nucleus in a molecule, considerations such as the different bonding environments, the atom's electronegativity and that of its neighbours or really any interactions that can locally affect the electron cloud and influence the effective magnetic field felt by the nucleus have to be taken into account. Therefore, it serves to experimentally reference this chemical shift to that of a known nucleus. This has led to the development of standardised nuclei for each NMR active nucleus. A good example of this is tetramethylsilane (TMS) which features commonly used ^{1}H and ^{13}C, but also a ^{29}Si.

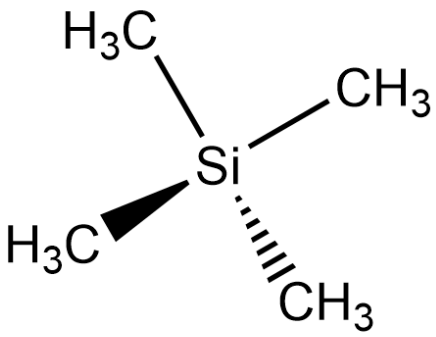

Figure 2-4 Structure of TMS, it is a model compound for referencing as the variation in its chemical shift is minimal and it contains three different nuclei.

2.1.5 Evolution of NMR[84–86]

The first NMR experiments, around 1946, used a methodology known as continuous wave spectroscopy (CW) in order to obtain information about the nucleus. This usually involved having a frequency source fixed to a specific rf frequency at a coil that surrounds the sample within a magnetic field. The sample was spun to eliminate any imperfections in the magnetic field. The emission of rf energy was then monitored as changes to the fixed *rf* on the coil. The spectrum was generated by sweeping the magnetic field over a range of values and observing the rf signal that was emitted by the

sample. Initially this was thought to be the best way to conduct an NMR experiment as it was same way other spectroscopic techniques such as UV-VIS and FTIR worked.

The speed at which we can extract information using CW mode is limited by fundamental considerations. For example, spin $1/2$ nuclei lines are usually quite sharp, meaning that corresponding transition energies vary little from one contributing nucleus to the next. Ideally, we want to take measurements which take advantage of this by discriminating between these closely space lines. For example, if we want to resolve 1 Hz line spacing, this would be equivalent to measuring ΔE of h Joules ($E = hv$). The Uncertainty Principle says $\Delta E \Delta t \sim h$ and therefore $\Delta E = h$, then t our time interval is of the order of 1 s. If we want a 10 ppm width spectrum (a common range for a ^{1}H proton spectrum), which is 1000 Hz, it would take 1000 seconds to sweep the width for 1 complete scan. This equates about 15 minutes per scan.

The sweeping of frequencies in succession took a long time, therefore any larger width spectrum took hours to perform. This technique also suffered poor signal to noise ratio – by combining multiple spectra of the same sample (signal averaging) the signal to noise could be improved at the cost of even more instrument time. We would perhaps want at least 4 scans to double our signal-to-noise ratio to an accepTable level. Requiring one hour for a ^{1}H spectrum, which would still possess a large amount of noise. The resolution benefit from taking longer to scan across means that the experimental times for nuclei with large chemical shift ranges become impractical to perform.

In order to improve experimental times and quality of data Richard R. Ernst[87] pioneered pulse NMR and its subsequent data processing method Fourier transform (FT) NMR. It was discovered that when an intense rf pulse of much shorter timescale (microseconds) is used, it is possible to excite all of the nuclei simultaneously. This generated a complex signal pattern that could only be analysed using FT techniques in order to transform the representation from the complex time domain to the frequency domain. The general FT algorithm is as follows:

$$A(t) = \frac{1}{2\pi}\int_{-\infty}^{\infty} A(\omega)e^{i\omega t}d\omega$$

and

$$A(\omega) = \int_{-\infty}^{\infty} A(t)e^{i\omega t}dt$$

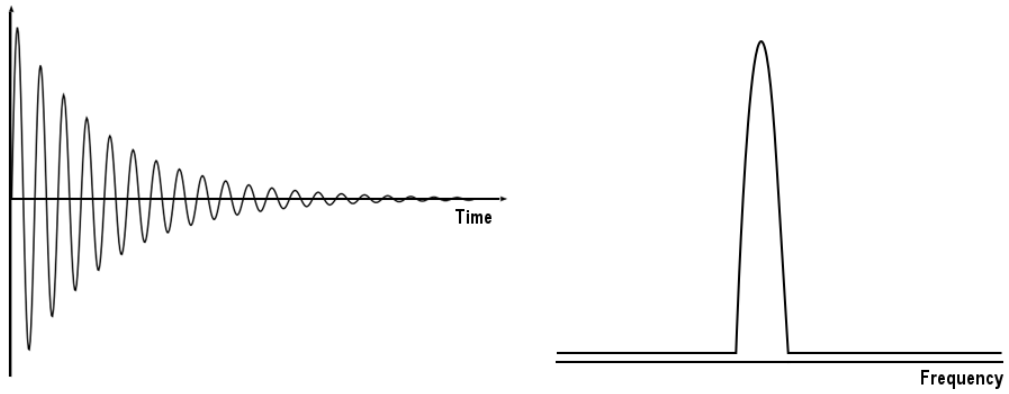

Figure 2-5 Free induction decay in the time domain (left) and its subsequent Fourier transform into the frequency domain (right)

This technique can also use signal averaging in order to increase the strength of the NMR signal by taking many FIDs of multiple pulses and averaging them together. This process of signal averaging has helped to overcome issues with low abundance nuclei such as ^{13}C or ^{15}N by intensifying the overall signal they have and significantly decreasing the overall time required to run an experiment.

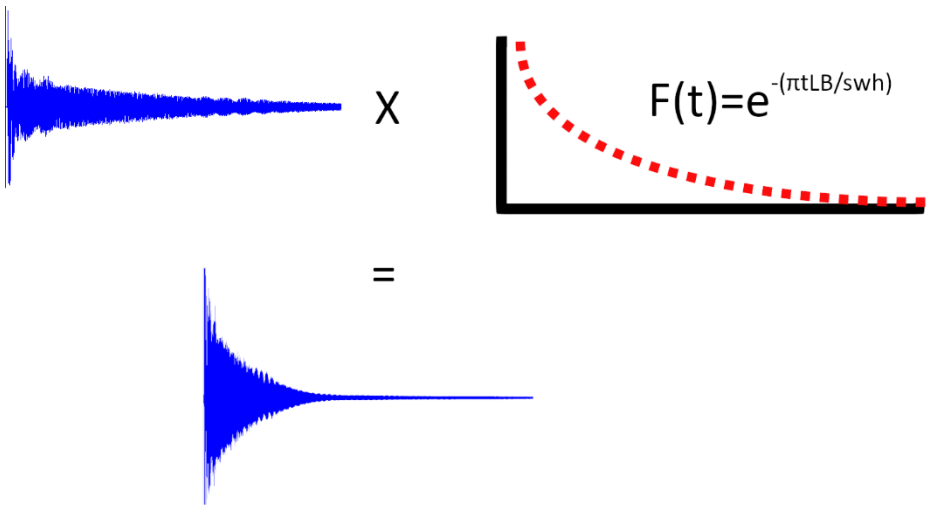

Figure 2-6 Application of a zero-filling window function to an FID

Several modifications have been made to the algorithm over the years in order to increase the quality of data transformation from the time to frequency domain – these involve the manipulation of the FID before transformation. Modifications such as the Window function[88] use the fact that NMR signal decays over the time that it is collected, therefore the amount of noise contributing to the FID that is present at the start and end of the FID is the same. At the end of the FID the noise contribution towards the actual signal is larger, therefore if a decaying exponential function is applied to the FID the tail end

of the FID will have its noise level significantly reduced which will improve the sensitivity in the transformed data. The opposite of this function is the Lorentz-Gauss function. The Windows function causes the FID data to decay faster which will result in a broadening of the linewidths in the spectrum. The Lorentz-Gauss[88] function serves to enhance the resolution of the dataset, by effectively removing the decay at the starting portion of the FID and then exponentials falls to zero in its decay function by the end of the FID. One other manipulation that is useful in data processing is called zero filling that increases the sensitivity of the experiment by applying a zero-value function to the portion of the FID after which all signal has been acquired and all that remains is noise. The size of the FID remains the same, however due to the fact that pure noise has been eliminated, the sensitivity of the spectrum is greatly increased.

2.1.6 Solid-State NMR[89,90]

Solids however are different compared to solution state when measuring NMR spectra. In the solution state the molecule to be analysed has to dissolved into deuterated solvent. The sum effect is that of the nuclear spins of the molecules will interact with the external applied magnetic field while tumbling quickly in the dissolved solvent. This leads to narrowing of the chemical shifts due to the isotropic environment the molecules in solution.

Materials which have crystalline characteristics, rigidity in their solid state or even simple powders show extensive broadening of their signals due decreased molecular motions. The result of this reduction is that the orientation dependent nuclear spin interactions can no longer be averaged the way they are in solution state. Through the Hamiltonian operator ($\hat{H}$) the energies of these different interactions with the nuclear magnetic spin can be shown as the product of the external magnetic field, $\vec{B}$, the orientation dependence of the NMR interaction, A, with respect to the *x, y* and *z* axes:

$$\hat{H} = \vec{I} \cdot A \cdot \vec{B}$$

When describing the quantum mechanical energy of these nuclear spin interactions there are several specific contributions to the increased line widths that can be named. These are; $\hat{H}_z$, the Zeeman interaction Hamiltonian, $\hat{H}_{CS}$, the chemical shift anisotropy Hamiltonian, $\hat{H}_D$, the dipolar coupling Hamiltonian, $\hat{H}_Q$, the quadrupolar coupling Hamiltonian (observed only if I > 1) and $\hat{H}_J$ which is the J-coupling Hamiltonian. These contribute a sum total through:

$$\hat{H}_{TOTAL} = \hat{H}_z + \hat{H}_{CS} + \hat{H}_D + \hat{H}_Q + \hat{H}_J$$

2.1.7 Chemical shift anisotropy and Magic-Angle-Spinning[89–91]

Other magnetic interactions such as chemical shift anisotropy and quadrupolar interactions (for nuclei above $I = ½$) can cause significant line broadening. NMR is already an insensitive tool due to the relative number of nuclei in the raised energy state β at a given temperature, especially for essential nuclei like ^{13}C which occurring naturally have a low isotopic abundance without enrichment or ^{15}N which has a negative gyromagnetic ratio.

The combination of all these factors with inefficient spin-lattice relaxation times creates extremely long experiments that result in broad insensitive signals.

The CSA Hamiltonians consist of two parts that can be written as a product; a spatial component consisting of the variation of interactions of the orientation with respect to the external magnetic field, and a spin component which consists of the angular momentum operators lying parallel to the external magnetic field. For a shielding tensor possessing the axial symmetry, $\delta_{xx} = \delta_{yy}$ the chemical shift Hamiltonian can be expressed as:

$$\widehat{H}_{CS} = \gamma B_0 I_z \left[\delta_{iso} + \frac{1}{2}\delta_{CSA}(3cos^2\theta - 1)\right]$$

Here the δ_{iso} represents the isotropic shielding parameter which can be expressed by:

$$\delta_{iso} = \frac{1}{3}(\delta_{xx} + \delta_{yy} + \delta_{zz})$$

And the chemical shift anisotropy term, δ_{CSA}, is expressed through:

$$\delta_{CSA} = \delta_{zz} - \delta_{iso}$$

As a result of molecular motion and constant tumbling, the Hamiltonian in solution state averages out for the orientation of all spins, however when the sample is solid it is relatively slow moving. By applying motion to the sample, it is possible to change the spatial portion of the Hamiltonian. Through mechanical rotation of the sample at extreme speeds, the tumbling motion of solutions can be simulated. This has to be done at an angle incline to the B_0 field (Figure 2-7). This so-called "magic angle" of inclination is about 54.7° and as a result will scale the anisotropic component of the Hamiltonian $(3\cos^2\theta - 1)$ to a value of zero, leaving the isotropic part. Spinning speeds of up to 126 kHz can be reached with modern probe setups[92].

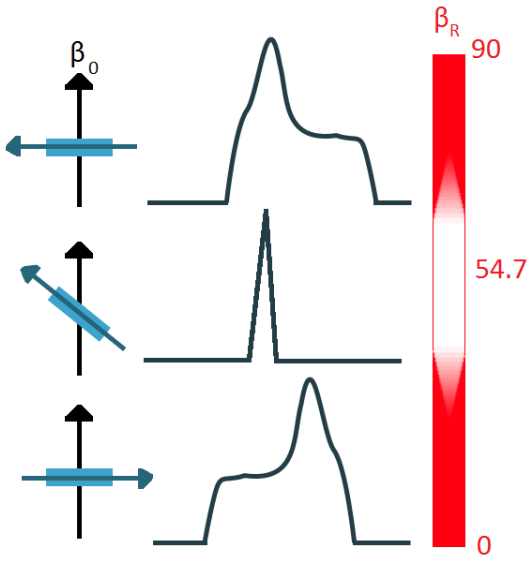

Figure 2-7 Orientation of a rotor inside an NMR with respect to the alignment of the B_0 field and orientation dependence the optimal MAS angle setup of 54.7° has on the line shape of an NMR spectrum

2.1.8 Cross Polarisation[89,90,93–95]

As stated previously some nuclei have a low natural abundance that we wish to study in NMR, such as ^{13}C (1.1 %) and ^{15}N (0.0037 %). They can also have low gyromagnetic ratios. This presents a problem with the sensitivity of signal. Another problem frequently found with the acquisition of low natural abundance nuclei is extremely long relaxation times requiring very long recycle delays (all these factors contribute to decreased sensitivity of the measurements). For instance, ^{29}Si has multiple minute relaxation times when in certain frameworks, which over the course of the analysis of the nuclei extends the experimental time significantly. This means that a high number of scans is required to acquire a good quality spectrum and the recycle delay in between experiments is effectively dead time.

Sensitivity itself has two direct means of improvement; increasing the level of magnetisation using polarisation transfer mechanisms from nuclei with higher gyromagnetic ratios or increasing the number of sequential scans to allow more signal averaging.

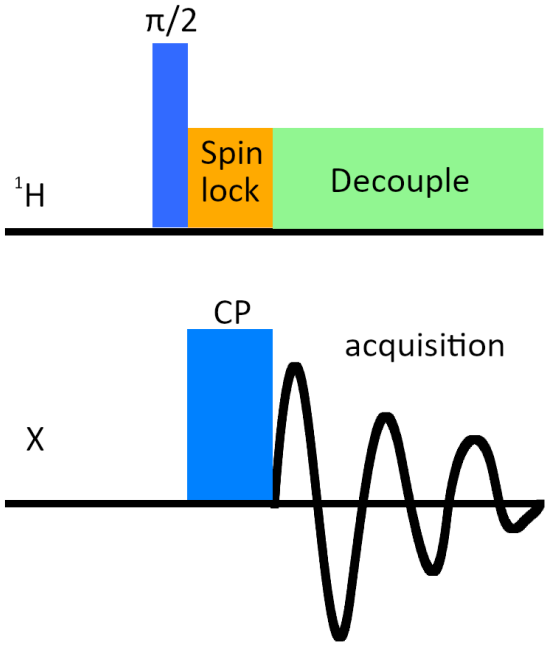

Figure 2-8 Graphical representation of the cross-polarisation pulse sequence. A 90° pulse is first applied to the high spin nuclei (in this case ^{1}H). This brings the magnetisation of proton into the *xy* plane. Then a spin lock on proton magnetisation is enabled through a phase shift by 90°. At the same a *rf* pulse is applied on the low spin nuclei (^{13}C, ^{15}N, ^{29}Si etc) which matches the Hartmann-Hahn condition. This enables the transfer of polarisation from the high spin nuclei to the low spin nuclei. After a time, the Hartmann-Hahn pulse is turned off and the low spin nuclei FID acquisition begins while the high spin nuclei pulse is left on to decouple.

This allowed for the development of cross-polarisation[96] magic-angle-spinning (CP-MAS Figure 2-8) solid-state NMR experiments where nuclei such as protons, which possess a large gyromagnetic ratio, can be used to polarise low gyromagnetic ratio nuclei such as ^{13}C or ^{15}N. The transfer of magnetisation from protons to these nuclei is driven through the dipolar couplings between them. We can explain the principle of the mechanism of the cross-polarisation experiment using the doubly rotating frame model. The first frame of this model shows two spin systems, *I* and *S*, which are precessing at their Larmor frequencies about the external magnetic field, B_0.

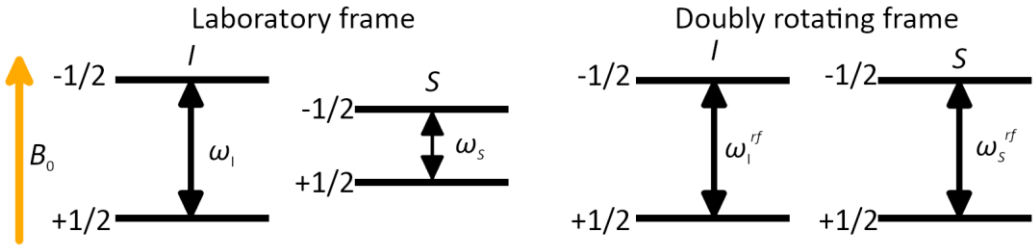

Figure 2-9 Energy differences between the gaps of spins *I* and *S* in the laboratory frame (left) and doubly rotating frame (right). This shows the equalisation of energy gaps when the Hartmann-Hahn condition is achieved.

This works by establishing the Hartmann-Hahn[97] condition which ensures that the contact between the two spins of the nuclei is allowed. When this energy gap is met both spins will be precessing at the same rate in the doubly rotating frame. The spins effectively heat each other up, resulting in the low gyromagnetic ratio spin having enhanced magnetisation with respect to the magnetic field. This occurs dependent on the condition of strong heteronuclear dipolar couplings between the two spin systems, any motions that are able to disrupt this coupling will decrease the efficiency of the transfer of magnetisation, which in turn leads to a decrease in the NMR signal given off by the receiving nuclei. After which proton decoupling is turned on and the signal from the low gyromagnetic ratio nuclei would be acquired.

2.2 X-Ray Diffraction[98–100]

2.2.1 Crystalline Materials

In order to fully understand the structure of a crystalline organic material, accurate information is needed regarding the nature of the intermolecular interactions. However, during the synthesis of a number of compounds, large single crystals with minimal imperfections are extremely difficult to obtain. A crystalline compound is a material containing a repeating periodic internal structure. This repetition will have periodicity across the three geometric directions, *xyz*, and possess characteristic angles to create a series of cells. The unit cell can be described as being the smallest unit that repeats and possesses the full symmetry information of the crystal structure. While the asymmetric unit is the smallest fraction of that unit cell that can be both translated and rotated in order to build one complete unit cell. Combined with the symmetry information it is possible to grow the whole structure (i.e. the crystalline lattice) by repeating this unit in all directions to form

Classification of different symmetries of these lattices falls into the geometrically defined 14 Bravais lattices. These lattices are able to be generated by combining one of the seven crystal systems (Table

2-1) with one of the four centering types. These are based around the number of lattice points, further dividing into four distinct groups; primitive, base-centred, body-centred and face-centred. In order to discover which system a crystal belongs to we use X-ray diffraction. This allows us to classify and arrange crystals made from singular atoms, ionic components or entire molecules.

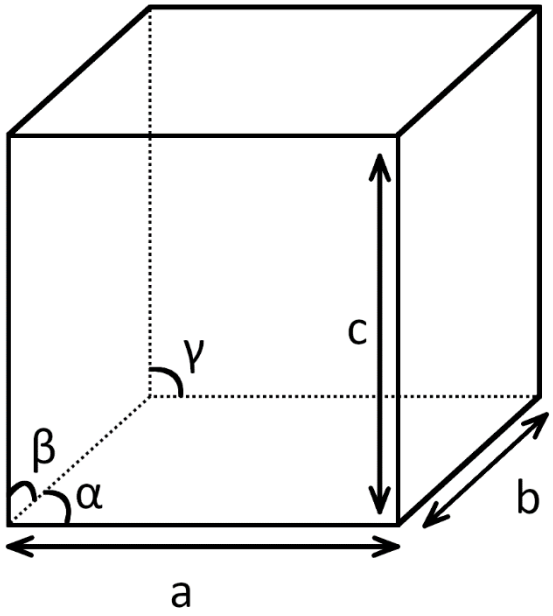

Figure 2-10 Diagram of crystallographic parameters of lengths and angles

Table 2-1 List of all seven crystallographic systems and cell parameters

Crystal System	Cell Lengths	Cell Angles
Cubic	$a = b = c$	$\alpha = \beta = \gamma = 90°$
Tetragonal	$a = b \neq c$	$\alpha = \beta = \gamma = 90°$
Orthorhombic	$a \neq b \neq c$	$\alpha = \beta = \gamma = 90°$
Monoclinic	$a \neq b \neq c$	$\alpha = \gamma = 90° \neq \beta > 90°$
Triclinic	$a \neq b \neq c$	$\alpha \neq \beta \neq \gamma \neq 90°$
Hexagonal	$a = b \neq c$	$\alpha = 120° \;\; \beta = \gamma = 90°$
Rhombohedral	$a = b = c$	$\alpha = \beta = \gamma \neq 90°$

2.2.2 X-Ray Diffraction Methodologies

Each crystalline system will be made up of a different arrangement of atoms and will therefore possess a unique diffraction pattern that is characteristic of that system. Through the use of XRD there are two main routes to accessing the structural information about a crystalline system: powder X-ray diffraction (PXRD) and single crystal X-ray diffraction (SCXRD). In the case of the latter, SCXRD can only be used when a crystal is able to grow perfectly to a certain size between 50-250 microns. SCXRD allows for precise information regarding the unit cell parameters, atomic positions, electron densities, bonding lengths and angles. Once this information is obtained experimentally, a structural solution can be proposed that has good agreement with the data.

The second technique, which will be used primarily in this thesis, is PXRD. Sometimes the only product obtained is a micro-crystalline powder, therefore SCXRD is not possible due to the limitations of the technique. This is accomplished by measurement of the x-ray intensity as the function of the scattering angle (2θ). This allows for a fingerprint style pattern to be generated based on the crystal structure and allows the easy comparison in a database (such as the PDF-4 database[101]) for both inorganic and organic compounds. PXRD gives valuable information regarding the unit cell, space group and initial reflections. Which when combined with further computational techniques such as CSP can allow a set of model systems to be computed, however these require significant refinement in order to categorically state the structure of the compound with any degree of accuracy.[102,103]

2.2.3 X-Ray generation and energy levels

An X-ray is generated when a high energy electron bombards an inner shell electron of a nucleus. The resulting collision causes the generation of two characteristic types of X-ray known as K_α and K_β (Figure 2-11). In addition to these, X-rays that have a continuous distribution of their energy are also produced. These X-rays are called Bremsstrahlung (braking radiation) because the radiation comes from electrons that are being decelerated from being fired at a metal object. The energy they subsequently give off due to this braking is sufficiently high to be in the X-ray electromagnetic spectrum.

The mechanism by which K_α and K_β X-rays are produced comes as a result of an electron being ejected from a core shell and the subsequent emitting of an X-ray photon of energy from the electron dropping down to fill a lower shell. The two types of X-ray that are subsequently generated differ by how far the electrons descend. K_α radiation comes from any electron descending from the L shell, whereas K_β radiation comes from any electron descending from the M shell. In order to generate the initial high energy electrons, a filament (usually made from tungsten) is heated which produces high energy

thermal electrons. These thermal electrons are then accelerated towards the target by a high potential voltage difference from 5-400 kV, but typically in the range of 30-60 kV for most applications. The anode itself is commonly made from copper or molybdenum (Cu/Mo) and in practice have different uses depending on the type of sample. When done in practice, both of the K_α and K_β radiation sources are detected as doublets (named $K_{\alpha 1}, K_{\alpha 2}, K_{\beta 1}$ and $K_{\beta 2}$ respectively). These doublets are not usually resolved in the diffraction patterns. These occur due to small a splitting of the different energy levels of the L shell where the electron descends from.

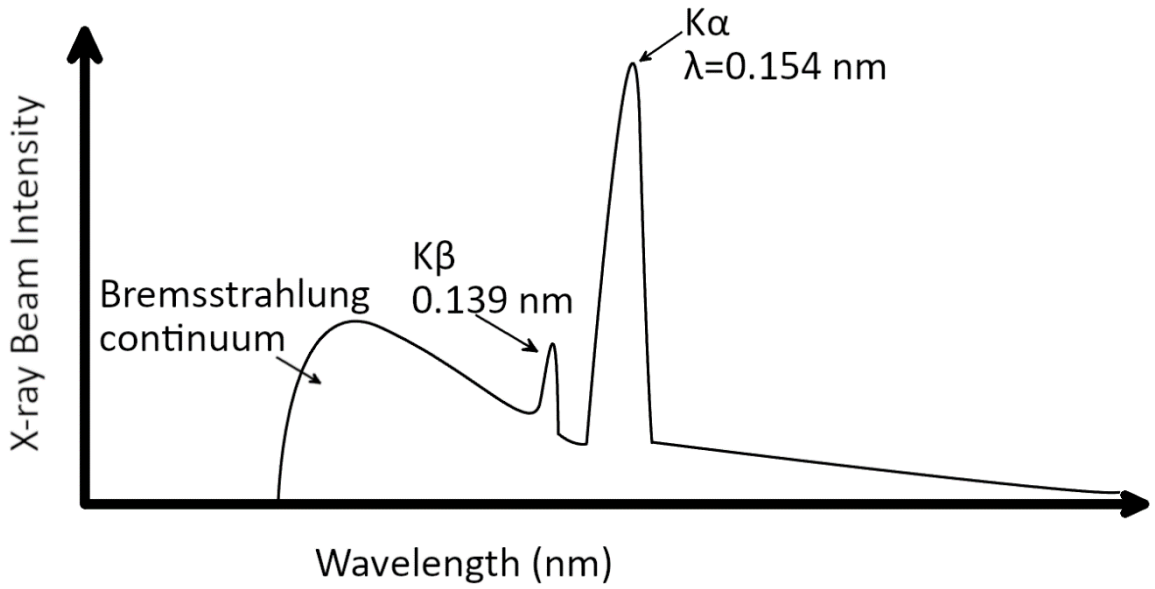

Figure 2-11 X-ray emission spectrum obtained from Cu target featuring characteristic K$\boldsymbol{\alpha}$ and K$\boldsymbol{\beta}$ wavelengths

2.2.4 Bragg's Law[104]

By treating a crystal system as a product of planar surfaces that are arranged symmetrically at intersecting characteristic angles, it is possible to characterise these crystallographic planes by Miller indices using the notation system, *hkl*. When these planes are parallel, they will subsequently possess the same Miller index and will also be equally space by a distance d_{hkl}.

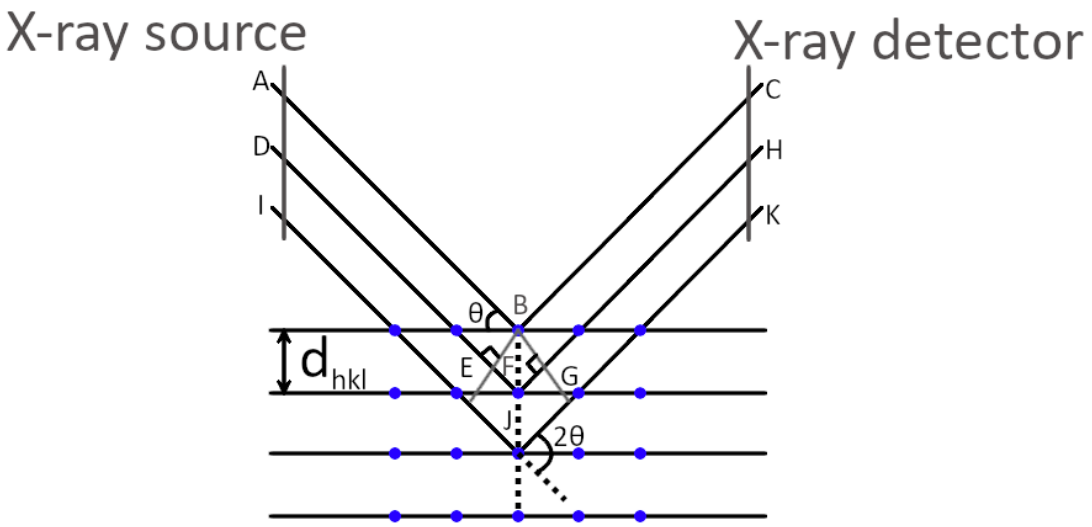

Figure 2-12 Bragg's equation example of x-ray diffraction at an angle of $\boldsymbol{\theta}$ adapted from [98]

Figure 2-12 is an illustration of the reflection of X-rays by a crystal structure which show the Bragg condition. The blue dots which are arranged in an array represent the repeating structure of a crystal. The parallel lines which cut through that structure are indicative of parallel planes (with Miller indices *hkl*) and are spaced by the interplanar spacing of d_{hkl}. The Figure shows the X-ray source produces a parallel set of monochromatic X-rays (A, D, I) at the crystal which are at an angle of θ_{hkl}. When the incident beam *A* hits the atom at point *B* a reflected beam *C* emerges. The same is true for *D* and its reflection *H*. When these reflected beams emerge from the crystal they will reinforce or arrive in the same phase as one another. If the distance of the path between these X-rays is equal to a integer multiple of the wavelength of that X-ray, then the X-rays are amplified – this is called constructive interference. This can then be plotted as a function of the 2θ to form the diffractogram If the resultant X-rays arrive at different points along the wavelength the opposite occurs, the amplifications cancel each other out – resulting in destructive interference and no diffraction peak present. As illustrated in Figure 2-12, atoms *BE* and *BG* are drawn at right angles to each other. This means that the difference between the path lengths of the two beams can be calculated by:

$$Difference = EF + FG$$

Given that our spacing is equal to d_{hkl} can be written also as:

$$EF = FG = d_{hkl} sin\theta_{hkl}$$

Equating to find that difference between *BE* and *BG*:

$$Difference = 2d_{hkl} sin\theta_{hkl}$$

This equates to the Bragg Equation where the relation between the crystalline planes d_{hkl} at a given angle of diffraction θ where we can observe the reflections of these planes. At the start of the equation n refers to the diffraction order which must be a integer ($n = 1$ for first order, $n = 2$ for second order etc…):

$$n\lambda = 2d_{hkl}sin\theta_{hkl}$$

2.3 Thermal Analysis[105,106]

2.3.1 Differential Scanning Calorimetry[107]

One of the two thermal techniques used in this thesis is Differential Scanning Calorimetry. DSC is capable of measuring the thermal uptake or release of energy in a system. This is achieved by measuring the heat of the sample system against a reference system as a function of temperature. This allows thermal transitions related to the state of the sample to be measured and quantified. The phenomena of interest include the melting of a solid, polymorphic interconversion, crystallisation, glass transition or thermal decomposition.

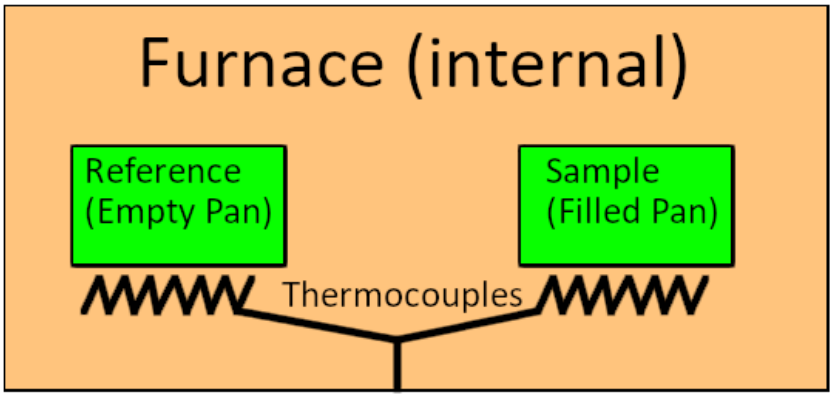

Figure 2-13 DSC Oven (internal) diagram showing thermocouples connected to reference and sample areas

Typically, a metal crucible of known thermal properties, such as aluminium, is used as a vessel for a sample (T_s) and a second crucible that is empty is used as a reference (T_r). These are sealed with a lid made from the same metal and then placed into a highly accurate furnace possessing two heating blocks designed to hold the pans. The temperature of the heating blocks is then raised at a linear rate, specified by the user (5-20 °C per/min usually), heating up the sample and reference. Due to the fact that a sample is present, that possesses a specific heat capacity (C_p), it will be heated more slowly

when compared the reference pan which is empty. When an exothermic or endothermic event takes place the C_p of the sample will change. This will result in amount of heating/cooling required to keep both sample and reference the same will change resulting in a differential signal ΔT between the sample and the reference ($\Delta T = T_s - T_r$). For a crystalline solid, in typical DSC thermogram where the *y* axis represents heat flow (J/s), an endothermic event such as melting (T_m) is represented by a dipped peak. Integrating the area of this peak gives the enthalpy in J/g.

The use of this technique allows the investigation of polymorphic forms through accurate melting points which is commonly used for pharmaceutical identification. It also allows the ability to gain insight into amorphous polymer materials by looking into their thermal properties.

2.3.2 Thermal Gravimetric Analysis[108]

The second thermal technique used in this thesis is thermal gravimetric analysis (TGA). This technique continuously measures the weight of a given sample over a period that the sample is heated. This is used to detect the mass change and any physical/chemical changes in the material like desolvation, dehydration or decomposition.

In this technique a sample is placed in a metal (aluminium or platinum) or ceramic hanging crucible that is placed on an extremely accurate microbalance. The balance is then enclosed by a furnace to seal it from the external environment and purged with nitrogen gas. Typically, a linear heating program that exceeds the materials decomposition temperature will be used to investigate at what point a material decomposes. Although isothermal studies, where a particular temperature is held and the subsequent change of mass is investigated are also possible.

In practice TGA has many applications in the pharmaceutics, i.e. measurement of the loss of water from drug hydrate and studies of the thermal stability of pharmaceuticals. It also allows for the quantification of the stoichiometry of a particular hydrate or solvate, which is helpful for insight into particular stepwise desolvation or desorption processes that occur upon heating. Primarily it used in this thesis in under to quantify the organic components of encapsulated silica materials.

2.4 Nitrogen Sorption Isotherms[109–112]

Liquid nitrogen boils at 77 K and is used extensively as cryogenic liquid in commercial, industrial and academic institutions as a method of cooling way below temperatures of freezing water or dry ice. Due to the fact it does not require pressurisation and its low density (90 g/ 100 ml) it can readily be transported and is easy and cheap to produce. It is also non-reactive so will not react with solids it comes into contact with. These factors allow it to be used as a vehicle to analyse porous solids.

Nitrogen gas allows a range of information on the pore to be attained, for example the pore volume and available surface area, and also the pore diameter and its adsorption capabilities. An alternative gas that could be used is argon (boiling at 87 K) which is more inert and is able to offer advantages in the analysis of micropores, however due to cost it was not chosen. In this thesis, measurements of pore volume are an essential analytical tool for ascertaining if encapsulated drugs are within the pore system of the host.

2.4.1 Methodology

Prior to the analysis a sample is degassed under high vacuum and temperature in order to desorb any solvent or water attached to the surface of the porous material. Many porous materials are extremely hygroscopic and will readily adsorb water from the atmosphere. This water has to be desorbed in order to conduct a precise measurement of the properties of the pore. Solvents may be used in the synthesis of the porous solid and will have the same effect. After degassing, the container with the sample is generally backfilled with nitrogen gas in order to minimise water adsorption in between transfer from the degas station to the analysis station. Adsorption measurements are generally performed through a volumetric determination approach, where a known quantity of nitrogen gas is admitted into the sample in the analysis station. The sample is kept at a constant temperature of 77 K and the nitrogen gas that is admitted to the container will eventually adsorb to the material surface causing a reduction in pressure until an equilibrium in reached. The amount of adsorbed gas at a particular partial pressure is thus determined as being the difference between the amount of nitrogen gas allowed into the sample area against the amount of nitrogen gas that is needed to fill the space around the sample. Due to this a precise weighing of the sample is required in order to calculate its textural properties after the experiment.

2.4.2 Isotherm types

There are many different isotherm types that confer to specific features of the material that is being investigated. The IUPAC[109] (Figure 2-14) names eight different physisorption (not chemisorption) types that materials can be classified into. Of these types, we are concerned with type IV as they are the most commonly representative of silica type mesoporous materials.

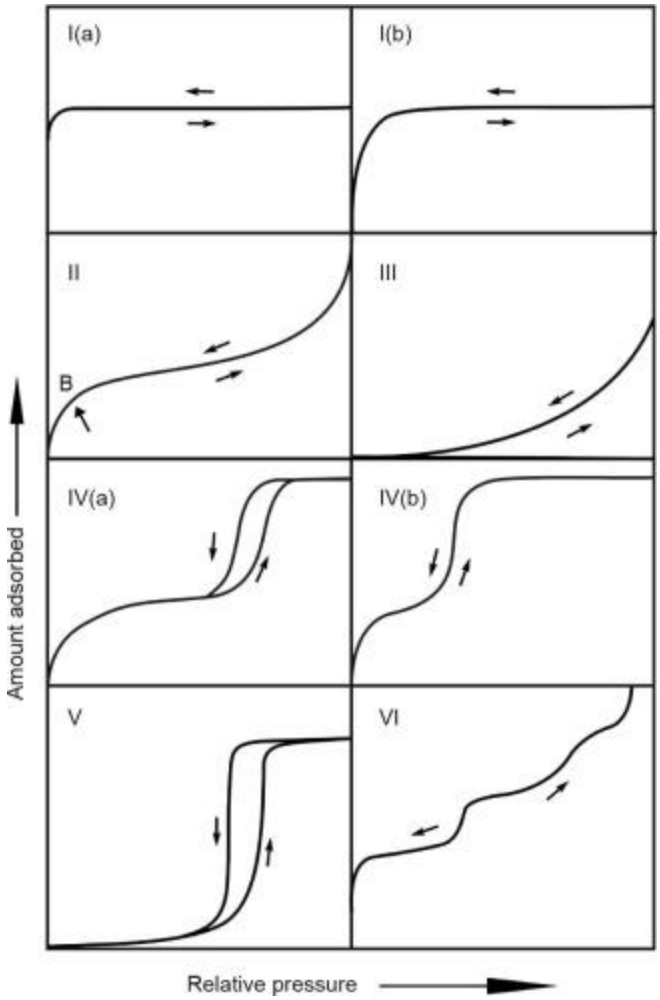

Figure 2-14 The eight types of physisorption hysteresis loops displayed by nitrogen adsorption as proposed by IUPAC[109]

Isotherms of a type I variety are generally given by solids that are microporous and possess relatively small external surface area, such as activated carbons or molecular zeolite sieves. As shown in the Figure above the isotherm follows horizontally across the axis, showing that there is an absolute value the amount of nitrogen that is adsorbed to the available surface area. The initial steep incline in the graph is due to greater number of interactions of the nitrogen gas with the microporous material concluding with the relatively fast filling of the narrow accessible pores. Micropores of this nature are generally found to have pores with widths around less than 1 nm[113].

Type II are associated with nonporous or macroporous solids and they are reversible. A type II isotherm gives an unrestricted layer of both mono-layer and multilayer adsorption in the material up to high partial pressures. The monolayer filling is shown up to point *B* on the graph of this isotherm. The long region after the initial steep incline on the graph where multilayer filling is occurring.

However, in a type III material there is no initial monolayer formation that is visible as indicated by the long exponential growth type curve. This indicates that the molecules of gas are more clustered in to favourable areas of adsorption on the material. This material only fills and condenses when the partial pressure becomes extremely high.

Type IV isotherms are what concern the content of this thesis. They are characteristic of mesoporous materials such as the silica scaffolds discussed previously. At low partial pressures they follow an initial type II behaviour with monolayer/multilayer adsorption of nitrogen gas to the walls of the pores. As the partial pressure then increases, and the multilayer is extremely large, they will fully condense the nitrogen from the gas to a liquid-like condensate that exists at lower pressure than that of pure liquid nitrogen. They will then show a hysteresis behaviour on their desorption isotherm if their pores are wider than around 4 nm (IVa type), or will be simply fully reversible for pores smaller than 4 nm (IVb type).

Type V possesses some similarity to type III, its shape coming from much weaker interactions of the adsorbed gas with the material. At significantly higher partial pressures the filling of pores occurs as a steep increase in the level of adsorbed gas.

Type VI isotherms show a characteristic called layer-by-layer adsorption which presents as a distinct set of step-wise filling in the isotherm profile. This material usually consists of a highly uniform and nonporous type surface. Each of the steps represents a specific capacity of adsorption for that particular layer and the steepness of the step has a dependency related specific material and temperature.

2.4.3 Hysteresis in mesoporous materials

There are several types of hysteresis behaviour that have been reported, showing the different types of reversible adsorption and desorption behaviours which can subsequently be related the adsorbate's pore diameter and shape. The six characteristic types as classified by IUPAC[109] are shown in the Figure 2-15.

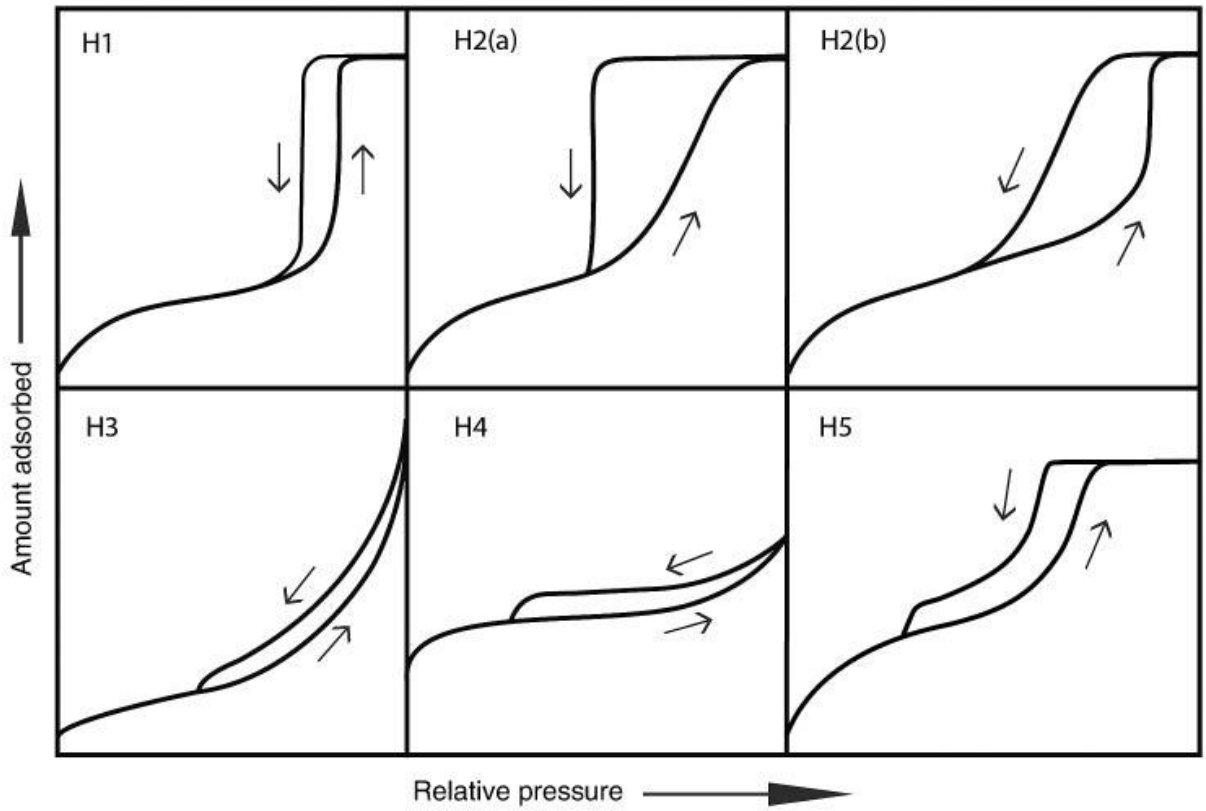

Figure 2-15 Types of hysteresis in nitrogen sorption isotherms of mesoporous materials. This is based in the IUPAC classification. Type H1 and H2(b) are of interest in this thesis. Adapted from [109]

Type H1 isotherms are generally found in porous materials which show a narrow range of mesopores that are uniform in nature. Concerned in this thesis, materials such as MCM-41 and SBA-15 show this type of hysteresis behaviour. The narrow loop shown in H1 isotherms is a distinct property of the adsorption branch possessing delayed condensation. However, these loops can also be found in ink-bottle type mesopores, for which the window into the pore is of similar size to that of the internal pore.

H2 isotherms consist of two subtypes, H2*a* and H2*b*, and are more consistent with a higher degree of complexity with regards to the structure of the pores. Generally, these are found in pores that are interconnected and are found in ink-bottle type mesopores. In type H2*a* a sharp desorption branch can be noted which comes from either pore-blocking or percolation in narrow areas of the pore necks or can come from cavitation-induced evaporation of the adsorbate. Generally, H2*a* type isotherms are associated with silica-gels, some porous glass materials or SBA-16/KIT-5 materials. The H2*b* type isotherm is associated with mesocellular silica foams and are usually materials possessing a wide range of pore neck sizes.

Type H3 loops possess two distinct characteristics, the first being that the adsorption branch of the loop is similar to that of a type II isotherm and the second being that the desorption branches' lower limit is located where at the cavitation-induced partial pressure. Type H3 loops generally belong to non-rigid aggregate type particles which are consistent with clay materials, however can be labelled H3 also if the pore system is that of a macropore variant that is not completely filled with the condensate gas.

The H4 type loop is similar to that of H3 with the primary difference being the adsorption branch. In a type H4 loop, the adsorption branch is a composite of the type I and II isotherms. The uptake at lower partial pressures is more pronounced and associated with the filling of a microporous material.

A type 5 hysteresis loop is associated with materials which possess fewer uniform structures, with both open and partially blocked mesopores being present in the material.

2.4.4 Analysis of isotherms; BET surface area, pore volumes and diameters

In order to analyse the surface area of a material, Brunauer, Emmet and Teller (BET)[114] developed a method based on the available theoretical model of the mechanism of adsorption. There are certain assumptions that have to be taken in to account with this method which are: (1) the heat of adsorption remains constant in the first monolayer, (2) interaction of the adsorbed molecules laterally is negligible, (3) any molecules that become adsorbed can thus become a new adsorption surface and that subsequent monolayers possess the same heat of adsorption (but different to the first layer).

$$A_s = \left(\frac{V_m}{22{,}414\ cm^3/mol}\right) N_A \sigma$$

The surface area (A_S) can be determined by using the volume coverage of the monolayer (V_m) Avogadro's number (N_A) and the accepted area (σ) covered by one nitrogen molecule (0.162 nm^2) and the molar volume of a gas under standard conditions (22,414 cm^3/mol). V_m can be estimated using BET equation with three separate parameters; where V_{ads} (dependent on partial pressure, P/P_0, of the system) is equal to the adsorbed volume:

$$V_{ads} = V_m \frac{c\frac{P}{P_0}}{1-\frac{P}{P_0}} \quad \frac{1-(n+1)\left(\frac{P}{P_0}\right)^n + n\left(\frac{P}{P_0}\right)^{n+1}}{1+(c-1)\left(\frac{P}{P_0}\right) - c\left(\frac{P}{P_0}\right)^{n+1}}$$

In this equation the parameter *c* depends on the first monolayer's heat of adsorption and *n* describes the number of layers which are able to be adsorbed to the surface of the material. When *n* increases and therefore tends to infinity to show complete coverage, the equation is simplified to:

$$V_{ads} = V_m \frac{c\frac{P}{P_0}}{\left(1-\frac{P}{P_0}\right)\left(1+(c-1)\frac{P}{P_0}\right)}$$

When put into application, the BET equation is only valid in the linear region at the start of the isotherm adsorption step. This is due to the difference between mono and multilayer filling of the surface area of the pores. This range is usually described as being at partial pressures less than 0.3.

The determination of the pore volume comes from the whole isotherm using the Kelvin equation; where r_p is the pore radius, t_c is equal to the thickness of the adsorbed layer, γ is equal to the surface tension of the bulk liquid (in this case nitrogen) and V_m is equal to the molar liquid volume: This equation applies to mesoporous materials which are able to adsorb a finite amount of gas at partial pressures is approximately equal to 1 - when the pores are considered to be completely filled of the condensed liquid.

$$ln\frac{P}{P_0} = -\frac{2\gamma V_m}{RT(r_p - t_c)}$$

Several models exist in order to determine the size of pore diameters for a variety of materials. The method that will be primarily used in this thesis is based on Barret, Joyner and Halenda (also known as the BJH method)[115]. This method is only valid at partial pressures greater than 0.4. The basis for this method is the change in the gas to liquid phase transition when a fluid is confined relative to when it exists as a bulk liquid.

For materials possessing pore diameters of less than 10 nm this equation is no longer valid as it is more appropriate for macroscopic materials where the adsorption mechanics do not follow type I isotherm behaviour. It has been shown that when used it can severely underestimate pore diameters by up to 30%, experimentally confirmed through TEM and PXRD methods. These materials require the use of DFT methodologies which are based on the molecular simulation of the systems. Small pores such as MCM-41 use these methods such as the NLDFT[116,117] model.

3 Experimental Methods

3.1 Materials

Flufenamic acid (FFA), nicotinamide (NA), Pluronic P-123 copolymer, n-hexadecyltrimethylammonium bromide 1,2,3-trimethylbenzene, tetraethylorthosilicate (TEOS), ammonium fluoride, sodium chloride, 37 wt. % hydrochloric acid, methanol, anhydrous methanol, ethanol were purchased from Sigma-Aldrich and used without further purification.

3.2 Synthesis

3.2.1 Cocrystal FFA/NA

FFA/NA cocrystal were made using the method reported by Fabian *et al*.[118]. Typically, 100 mg of a stoichmetric ratio (1:1) of FFA and NA was placed in a grinding jar and placed in a ball mill. 25 μl of acetone was added to the jar and the mixture was ground for 30 minutes at a frequency of 30 Hz.

3.2.2 MCM-41 silica host

The MCM-41 host, a mesoporous silica host possessing pores around 3 nm, were produced in accordance with the method by Grün *et al.*[119]. Typically, 2.5 g of n-hexadecyltrimethylammonium bromide was dissolved into distilled water (miliQ quality), then a solution of ammonia (37 wt. %, 13.2 g) and ethanol (60 g) was mixed in. The solution was then stirred for 15 minutes, after which 4.7 g of TEOS was added. After 2 hours of subsequent stirring, a precipitate formed which was then filtered and washed with methanol and distilled water. The material was dried in an oven overnight at 363 K then calcined in a furnace (in air) at 823 K for around 5 hours.

3.2.3 SBA-15 silica host

The SBA-15 host, a mesoporous silica host possessing pores around 6-7 nm, were produced in accordance with the method described by Zhao *et al*.[54] which included the addition of sodium chloride added for stability and to produce a highly ordered species as detailed by Li *et al.*[49]. P-123 triblock copolymer (2.0 g) was dissolved in 2M HCl (62.5 mL) at 298 K. A clear colourless solution was obtained. TEOS (4.23 mL) was added to this dropwise, before being stirred for 20 hours at 313 K. The resulting mixture was then aged in an oven at 363 K for 24 hours, filtered, washed with distilled water and then dried. The white solid that resulted was then calcined in a furnace at 823 K for 6 hours in air.

3.2.4 MCF silica host

The MCF host, a mesoporous ink-bottle type silica host possessing pores of 26 nm and windows of 14 nm, were produced using the methodology published by Han *et al.*[50]. Typically, P-123 triblock copolymer (4 g) was dissolved in 1.5 M HCl (75 mL) at 298 K. After which 1,3,5-trimethylbenzene (4 g), a swelling agent, was added and the resulting solution placed in a water bath to be heated to 313 K and stirred vigorously for 2 hours. Then TEOES (9.2 mL) was added dropwise to the solution and stirred for around 5 minutes. The mixture was then aged in an oven at 313 K for 20 hours. After which NH_4F (46 mg) was added, stirred in, then aged again in an oven at 373 K for 24 hours. The resulting white precipitate was then filtered, washed with ethanol and distilled water, then dried in an oven at 313 K for 24 hours. The resulting powder was then calcined in a furnace at 1173 K for 10 hours in air.

3.3 Melt loading of drugs

3.3.1 FFA/NA

Typically, the silica host (MCM-41, SBA-15 and MCF) were preheated in a glass vial in an oven at 393 K to desorb as much water as possible. The silica was then gently mixed with the FFA/NA cocrystal in a vial in ratios of 85:15, 80:20, 75:25, 70:30, 60:40, 50:50 as a wt. $wt.^{-1}$ ratio. The vials were then heated up to 419 K (10 K above FFA/NA's melting point) on a hotplate inside an aluminium heating block. The vials were then gently mixed with a spatula for 10 minutes while at this temperature. The vial was then subsequently cooled to room temperature in ambient air, capped and placed in a desiccator prior to analysis.

3.3.2 NA

Typically, the silica host (MCM-41, SBA-15 and MCF) were preheated in a glass vial in an oven at 393 K to desorb as much water as possible. The silica was then gently mixed with the crystalline NA in a vial in ratios of 85:15, 80:20, 75:25, 70:30, 60:40, 50:50 as a wt. $wt.^{-1}$ ratio. The vials were then heated up to 412 K (10 K above NA's melting point) on a hotplate inside an aluminium heating block. The vials were then gently mixed with a spatula for 10 minutes while at this temperature. The vial was then subsequently cooled to room temperature in ambient air, capped and placed in a desiccator prior to analysis.

3.4 Preparation of ACV forms

3.4.1.1 ACV form I

Anhydrous ACV form I was produced according to the method previously used by Lutker *et al*.[120]. ACV form V (4.5 g) was placed in a glass vial, and heated using an oven to 180 °C at a rate of 5 °C per minute from room temperature. The heated material was then left at 180 °C for 30 minutes before being taken out to cool at room temperature.

3.4.1.2 ACV form II

Anhydrous ACV form II was produced in two ways. The first was using a slurry experiment by taking ACV form V with DMSO for a period of one week. It could also be produced by slurrying ACV form I in methanol, NNDMF or DMSO for a period of four weeks. Both resulted in a gel containing crystalline ACV form II.

3.4.1.3 ACV form V

The 3:2 hydrate form V of ACV was bought as a commercially available sample. Crystalline product was produced by recrystallisation of ACV form V in water. ACV form V (100 mg) was placed into distilled water (40 mL) and left at 37 °C until recrystallisation occurred after a period of 24 hours.

3.4.1.4 ACV form VI

The 1:1 hydrate form VI of ACV was prepared through hydration of ACV form I. ACV form I (150 mg) was placed in a glass vial and mixed gently with distilled water (1 mL) in order to let the water, cover the surface of the powder. The vial was left at room temperature for 72 hours. The resulting material was then dried using filter paper prior to analysis.

3.4.1.5 Organic solvents for slurry preparation

The Table below lists the solvent and properties used in the slurry experiments of ACV.

Table 3-1 Solvent parameters

Solvent	Formula	$\Sigma\alpha^1$	$\Sigma\beta^2$	Dielectric constant	Dipole momentum[3]	δD^4	δP^4	δH^4
Water	H_2O	1.17	0.47	78.36	1.87	15.5	16.0	42.3
Methanol	CH_3OH	0.43	0.47	32.61	1.70	14.7	12.3	22.3
Ethanol	C_2H_5OH	0.37	0.48	24.85	1.69	15.8	8.8	19.4
n-Propanol	C_3H_7OH	0.37	0.48	20.52	1.55	16.0	6.8	17.4
Iso-propanol	C_3H_7OH	0.33	0.56	19.26	1.56	15.8	6.1	16.4
n-Butanol	C_4H_9OH	0.37	0.48	17.33	1.66	16.0	5.7	15.8
Acetone	CH_3COCH_3	0.04	0.49	20.49	2.88	15.5	10.4	7.0
Acetonitrile	CH_3CN	0.07	0.32	35.69	3.92	15.3	18.0	6.1
Dimethylformamide	$(CH_3)_2NCHO$	0.00	0.74	37.22	3.82	17.4	13.7	11.3
Dimethyl sulfoxide	CH_3SOCH_3	0.00	0.88	46.83	1.80	18.4	16.4	10.2
Acetic acid	CH_3COOH	0.61	0.44	6.25	1.70	14.5	8.0	13.5
Ethyl acetate	$CH_3COOC_2H_5$	0.00	0.45	5.99	1.78	15.8	5.3	7.2
Toluene	$C_6H_5CH_3$	0.00	0.14	2.37	0.38	18.0	1.4	2.0
Dichloromethane	CH_2Cl_2	0.10	0.05	8.93	1.60	17.0	7.3	7.1
Chloroform	$CHCl_3$	0.15	0.02	4.71	1.04	17.8	3.1	5.7

1. – Abraham's[121] hydrogen bond acidity (Abraham's notation $\Sigma\alpha_2^H$), **2.** – Abraham's[121] hydrogen bond basicity (Abraham's notation $\Sigma\beta_2^H$), **3.** – Dipole moment in the unit of Debye; **4.** - Hansen solubility parameter values accounting for dispersion forces (δD), dipolar intermolecular forces (δP) and hydrogen bonds between molecules(δH) in the unit of $MPa^{0.5}$

3.5 CASTEP Computational Parameters

All computations were performed using the CASTEP code (ver. 8.0) and on the fly ultrasoft pseudopotentials.[77] Calculations were performed for the crystal structures of FFA/NA (structure code:EXAQAW[118]), crystal structures of NA form I and II (structure codes:NICOAM01 and NICOAM04), crystal structures of ACV form I, II, V and VI (structure codes: MECWIC01, MECWIC03, CEHTAK10 and WOZPAE[120,122]) reported in CSD.

Geometry optimisations were undertaken using the Perdew-Burke-Ernzerhof (PBE) generalised gradient approximation (GGA) exchange-correlation density functional[123], ultrasoft pseudopotentials[124], a Monkhorst-Pack grid of k-points with a spacing of 0.05 $Å^{-1}$ and a cut-off energy

of 800 eV. Geometry optimisation was run with constrained cell dimensions and positions of all heavy atoms.

Calculations of the NMR chemical shieldings were performed using the gauge including projector augmented wave approach (GIPAW) and on the fly pseudopotentials as implemented in CASTEP code.[125,126]

The isotropic shieldings generated through this (σ_{calc}) were then adapted into chemical shifts (δ_{calc}) using the equation, where σ_{ref} is equal to the shielding constant taken from the zero-intercept plot fit of the calculated chemical shifts against the experimental chemical shifts:

$$\delta_{calc} = \sigma_{ref} - \sigma_{calc}$$

3.6 Characterisation Methods and Conditions

3.6.1 Differential Scanning Calorimetry

DSC measurements were taken using a Q 2000 MTDSC instrument or a Discovery DSC 2500 (TA Instruments, New Castle, DE, U.S). The change in instrument was due to a fire destroying the first. The same parameters were used in both for consistency. Samples were weighed out into TA 100 μL aluminium crimped pans and sealed with a lid. Samples were weighed to between 1-2 mg. Calibration of temperature and energy was completed with indium, tin and n-octadecane. Heating rates varied between 5-20 K min^{-1} depending on sample. An empty pan made from the same material as the sample pan was used as reference. Results were analysed with TA Instruments UA 2000 software for the Q 2000 MTDSC or with Trios Software v5.1.1 for the Discovery DSC 2500 (TA Instruments-Waters LLC).

3.6.2 Thermal Gravimetric Analysis

Materials were placed into a TQ 500 thermogravimetric analyser, or a TGA 5500 (TA Instruments, New Castle, DE, U.S.). The change in instrument was due to a fire destroying the first. The same parameters were used in both for consistency. Samples of around 5-10 mg were loaded into platinum pans and heated to 383 K to remove any water present. The samples were then heated to 873 K with varying heating rates, 5-30 K min^{-1}, and left at 873 K to completely thermally decompose. Samples were then cooled to room temperature. A nitrogen purge flow for the sample of 10/25 mL min^{-1} was used. Results were analysed with TA Instruments UA 2000 software for the TQ 500 thermogravimetric analyser or with Trios Software v5.1.1 for the TGA 5500 (TA Instruments-Waters LLC).

3.6.3 Powder X-ray Diffraction

Powder X-ray diffraction patterns were taken using an ARL™ X'TRA Powder Diffractometer (Thermo Fisher Scientific Inc., Waltham, MA, U.S.) employing Cu Kα radiation source (λ = 0.1540562 nm) in Bragg-Brentano geometry. Samples were ground with a pestle and mortar prior to loading onto a low background holder. Soller slits of 2.5° were used with a 0.2 mm divergence slit. The tube voltage and current were 45 kv and 40 mA respectively. A step size of 0.01° was applied between the 2θ range of 5-36° with a scanning rate of 2 seconds per step.

3.6.4 Nitrogen Physisorption

Adsorption-desorption isotherms of nitrogen were obtained using a Nova 2200e Surface Area and Pore Size Analyzer attachment, and later an Autosorb iQ with Pore Size Analyzer attachment (Quantachrome, Hook, UK) at 77 K. The change in instrument was due to an upgrade due to a fire destroying the first. The same parameters were used in both for consistency. The available BET surface area was calculated with the use of molecular nitrogen (0.162 nm^2) between the relative partial pressure ranges of 0.05 to 0.20, with the assumption of monolayer coverage of the material in this linear region. Pore diameter sizes were calculated either using NLDFT[116,117] (MCM-41) or the Barrett-Joyner-Halenda method[115] (SBA-15, MCF). For MCF the adsorption branch was used to estimate the internal larger pore size, while the desorption branch was used to estimate the window size. Pore volume was calculated at a partial pressure close to 1 using the Kelvin equation as described in chapter 2.4.4. Isotherm measurements are repeated for each point until a stable measurement can be achieved to a factor of ±10%.

3.6.5 Scanning Electron Microscopy and Transmission Electron Microscopy

The use of SEM and TEM have historically used as a characterisation method of silicas in order to contribute towards the nitrogen adsorption isotherms. Information such as the pore diameters can found from these experiments. It was decided not to perform these measurements on samples made as this characterisation had been previously completed in our research group previously, and the protocols used to make the silicas were not changed. The availability, cost and time for these measurements on samples prior and post loading was not feasible and the nitrogen physisorption technique served as a characterisation method to verify the properties of the samples.

3.6.6 VT FT-IR

VT FT-IR were performed on a Bruker Vertex 70 spectrometer using a Specac High Temperature Golden Gate Controller between 30 to 250 °C in attenuated total reflection mode (ATR). Typically, the wavelength range of 4000-400 cm^{-1} were analysed at a resolution of 4 cm^{-1}. 32 scans were acquired for each temperature point.

3.6.7 Solid State NMR

Low field measurements of ^{1}H, ^{19}F, ^{13}C and ^{15}N were taken using a 400 MHz Bruker AVANCE III solid state NMR spectrometer with a triple resonance MAS probe. The operating frequencies were; 400.23 MHz for ^{1}H; 376.57 MHz for ^{19}F, 100.64 MHz for ^{13}C and 40. 57 MHz for ^{15}N. Materials were packed into 4 mm zirconia rotors, and capped with either Kel-F or Vesper caps. Samples were rotated using dry air from a compressor. ^{1}H and ^{13}C chemical shifts are given with reference to TMS, ^{19}F chemical shifts were given with respect to $CFCl_3$ and ^{15}N chemical shifts were referenced to labelled glycine at 33.4 ppm. MAS rates of 10 KHz were used.

High field measurements of ^{1}H, ^{19}F, and ^{13}C and were taken using a 850 MHz Bruker AVANCE III solid state NMR spectrometer with a triple resonance MAS probe. The operating frequencies were; 850.22 MHz for ^{1}H, 799.94 for ^{19}F and 213.81 for ^{13}C. ^{1}H and ^{19}F experiments were recorded using either 2.5 mm zirconia rotors or 1.3 mm zirconia rotors where the materials were packed into and capped on both ends. MAS rates of 25-30 KHz were used for 2.5 mm rotors, whereas 55-60 KHz were used for the 1.3 mm rotors. For ^{13}C experiments 4 mm zirconia rotors were used spinning at a MAS rate of 10 KHz.

3.6.7.1 One dimensional single pulse sequence for MAS

Pulse program of 1D MAS experiments, single 90° pulse followed by FID acquisition.

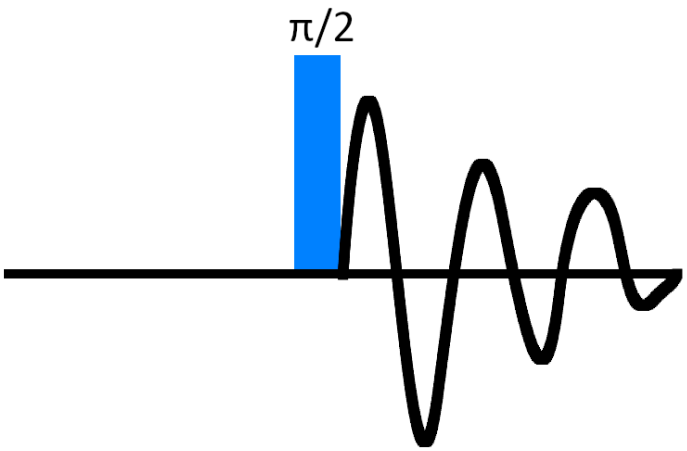

Figure 3-1 1D single pulse MAS experiment

^{1}H MAS NMR spectra were acquired using a ^{1}H π/2 pulse length of 2.6 µs at an MAS rate of 10 kHz, ^{1}H π/2 pulse length of 3.2 µs at an MAS rate of 30 kHz or a ^{1}H π/2 pulse length of 1.5 µs at an MAS rate of 55 kHz.

^{19}F MAS NMR spectra were acquired using a ^{19}F π/2 pulse length of 3.6 µs at an MAS rate of 10 kHz, a ^{19}F π/2 pulse length of 3.2 µs at an MAS rate of 30 kHz and a recycle delay of 10 s or a ^{19}F π/2 pulse length of 2.5 µs at an MAS rate of 55 kHz and a recycle delay of 10 s

3.6.7.2 Single ^{13}C pulse with High-Power-Decoupling (HDPEC)

^{13}C{^{1}H} MAS NMR spectra were acquired using a ^{13}C π/2 pulse length of 4.5 µs at an MAS rate of 10 kHz and varying recycle delays using SPINAL64[127] heteronuclear ^{1}H decoupling during acquisition with a *rf* field of 89 kHz. Typically, a recycle delay of 30 seconds was used, however in mobility experiments of CLASSIC a low recycle delay of 2 seconds and 256 scans were used.

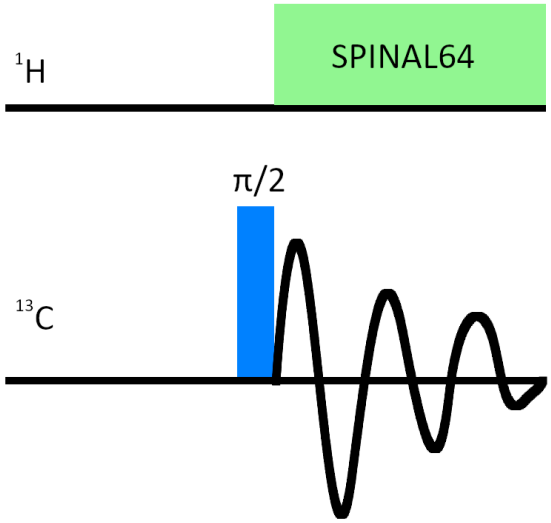

Figure 3-2 High power decoupled $^{13}C\{^{1}H\}$ pulse program representation (MAS NMR)

3.6.7.3 Cross-polarisation MAS (^{1}H-X)

^{1}H-X CP-MAS NMR experiments were acquired using ramped amplitude on the ^{1}H channel during the contact of the Hartmann-Hann condition step. As in HPDEC, the SPINAL64[127] heteronuclear dipolar decoupling was used during acquisition to decouple ^{1}H signal.

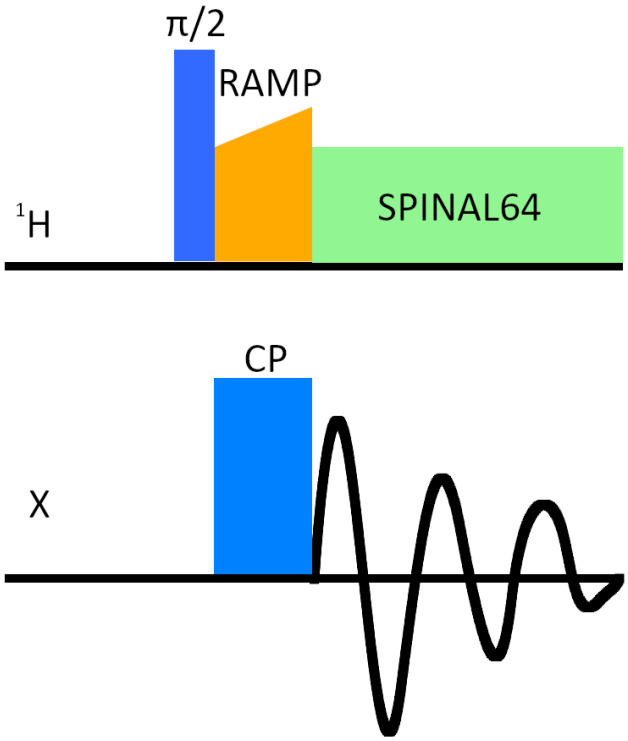

Figure 3-3 Cross polarisation experiment for ^{1}H-X on two channels represented

^{1}H-^{13}C CP/MAS NMR spectra were acquired using a ^{1}H π/2 pulse length of 4.5 μs and a CP contact time of 2000 μs using a MAS rate of 10 kHz. The Hartman–Hahn conditions were set using HMB. A recycle delay of 20 seconds was used.

^{1}H-^{15}N CP/MAS NMR spectra were acquired using a ^{1}H π/2 pulse length of 3.5 µs and a CP contact time of 2000 μs at an MAS rate of 10 kHz. The Hartmann–Hahn match was set with ^{15}N labelled glycine. A recycle delay of 30 seconds was used.

3.6.7.4 Cross-polarised non-quaternary suppression (CPNQS)

Suppression of non-quaternary carbons can be achieved through a form of spectral editing during the standard ^{1}H-^{13}C CP-MAS experiment. By adding a dephasing step between the CP/RAMP step and the FID acquisition it is possible to phase out CH and CH_2 functional groups. This is due to those groups losing magnetisation more rapidly than quaternary groups because of strong heteronuclear dipolar interactions. The peaks belonging to CH_3 functional groups do not lose their intensity due the fast movement of the methyl group which is less effected by heteronuclear dipolar interactions. A dephasing delay (DD) of 25 μs was used.

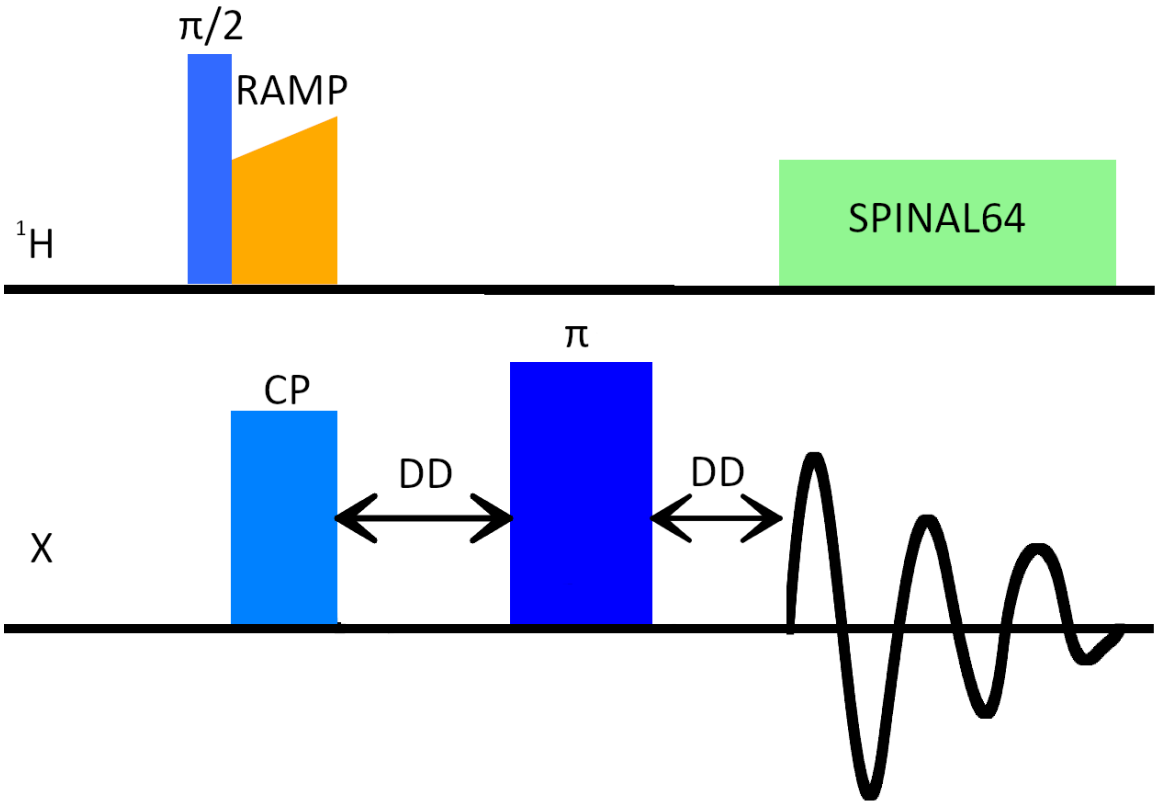

Figure 3-4 CPNQS representation on proton and X channel with a dephasing delay indicated (DD)

3.6.7.5 Two dimensional ^{19}F-^{19}F NOESY (Nuclear Overhauser Effect Spectroscopy)

2D -^{19}F-^{19}F NOESY MAS NMR experiments were recorded a high field (850 MHz) using a 1.3 mm probe spinning at 55 KHz. The pulse length of 2.1 μs was used. The chemical shift was allowed to involve in the evolution period, t_1. Variable mixing times from 10-600 ms were used before acquisition of the FID. The technique is used in solid state NMR to see the interaction of different species containing the ^{19}F functionality as cross-peaks of exchange of magnetisation on the resulting 2D spectra.

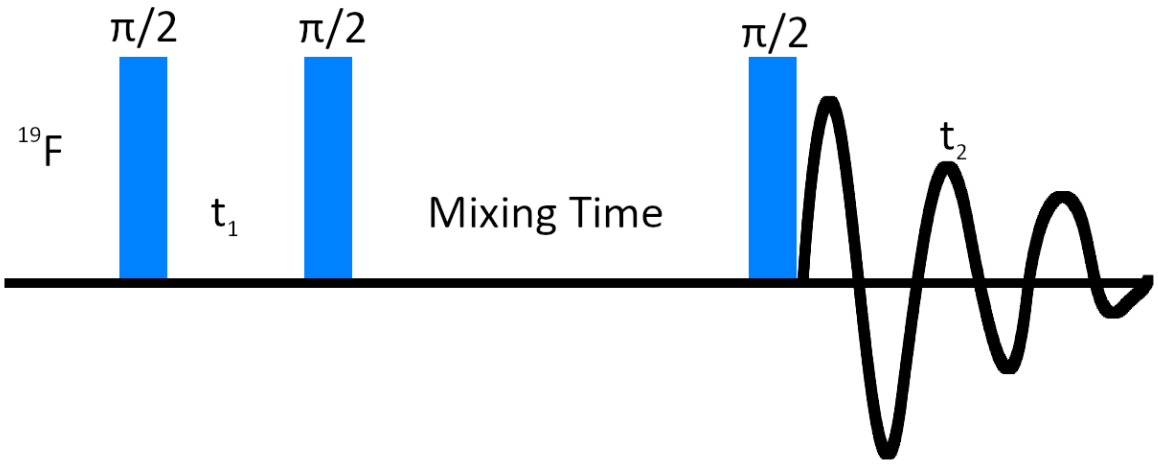

Figure 3-5 NOESY representation of the pulse sequence for 2D ^{19}F-^{19}F homonuclear studies.

3.6.7.6 Data Processing

Data processing was acquired using the Topspin software. Versions varied from 3.1.7, 3.5pl7, 3.6 and 4.0.2. Deconvolution of NMR was performed using Origin Pro 2016 64 bit.

4 A study on the crystallinity of Flufenamic Acid/Nicotinamide Cocrystal in confined environments

4.1 Introduction

From previous successful loading[72] of the well-known polymorph of flufenamic acid form I (FFA) into the pore space and discovering the existence of several different components when the pore size was varied, we decided to attempt to load a cocrystal using FFA as one of the components. A cocrystal of FFA with the well-known coformer nicotinamide (NA) was selected due to previous experience within the Khimyak/Fabian Research group at synthesising the species. NA is a very attractive model compound for assembling cocrystals due to its simple hydrogen bonding capabilities with carboxylic acid and amide functionality, common within the pharmaceutical industry. The cocrystal (FFA/NA) has a high melting point at 136.8 °C (Figure 4-2) as opposed to other cocrystals of fenamic acids with NA and is reported to be stable in water[118]. These properties make the cocrystal an ideal candidate for study when being loaded into the pores using melting methods, but also because it is known that silicas are extremely hygroscopic therefore water stability is a good property to possess.

There are multiple ways of synthesising the FFA/NA cocrystal. However, due to the larger quantity of compound needed to load it in the pore system, the best method to make sufficiently large batches high purity was by Liquid-Assisted-Grinding (LAG) using a ball-mill. LAG methodology allowed around 200 mg batches of cocrystal to be produced in around half an hour, which were in a powdered crystalline homogenous state rather than heterogeneous chunks of crystal. This method also had the benefit of not producing any solvates from impurities from recrystallisation methods, which may interfere with loading capabilities.

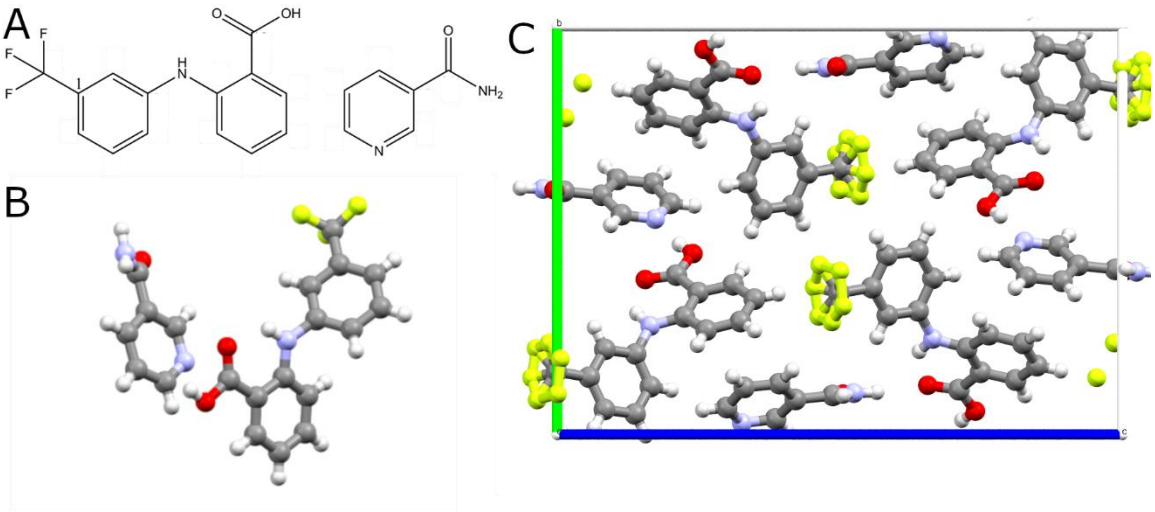

Figure 4-1 A. Structure of FFA and NA. **B.** Orientation of asymmetric unit of FFA/NA, grey indicates carbon atoms, white hydrogen atoms, red oxygen atoms, blue nitrogen atoms, yellow fluorine atoms **C.** Packing of a unit cell of cocrystal FFA/NA viewed along the *a* axis, CCDC reference EXAQAW[118]

The FFA/NA cocrystal is monoclinic with $P2_1/c$ symmetry and a unit cell volume of 1802.4 $Å^3$ (Figure 4-1). It has a relatively large unit cell, with axis lengths of 0.5, 1.5 and 2.21 nm. This is an important consideration when it is being loaded into the different porous silicas described in this chapter. There are three silicas chosen for loading: MCM-41[51,52], SBA-15[54] and MCF[50]. MCM-41 and SBA-15 have pore dimensions of *ca*. 3 nm and *ca.* 6 nm respectively, however MCF has a different pore structure. It features pore windows and internal cavities, these measuring 17.0 nm and 29.4 nm. The ability for multiple unit cells to be able to stack in all three dimensions is what will determine the crystallisation capacity inside the silica pores.

When the cocrystal is loaded into the pore space, the cocrystal first is physically mixed with dried silica powder at the weighted loading ratio desired. Then the mixture is heated above the melting point of the cocrystal, in this case 136°C, in order to melt the cocrystal. Figure 4-2 shows the melting points of each the cocrystal and its starting components. The mechanism of loading is then believed to be capillary action, where the pores of the silica particle take in the liquid cocrystal. The mixture is then able to cool down and crystallise to what extent is possible.

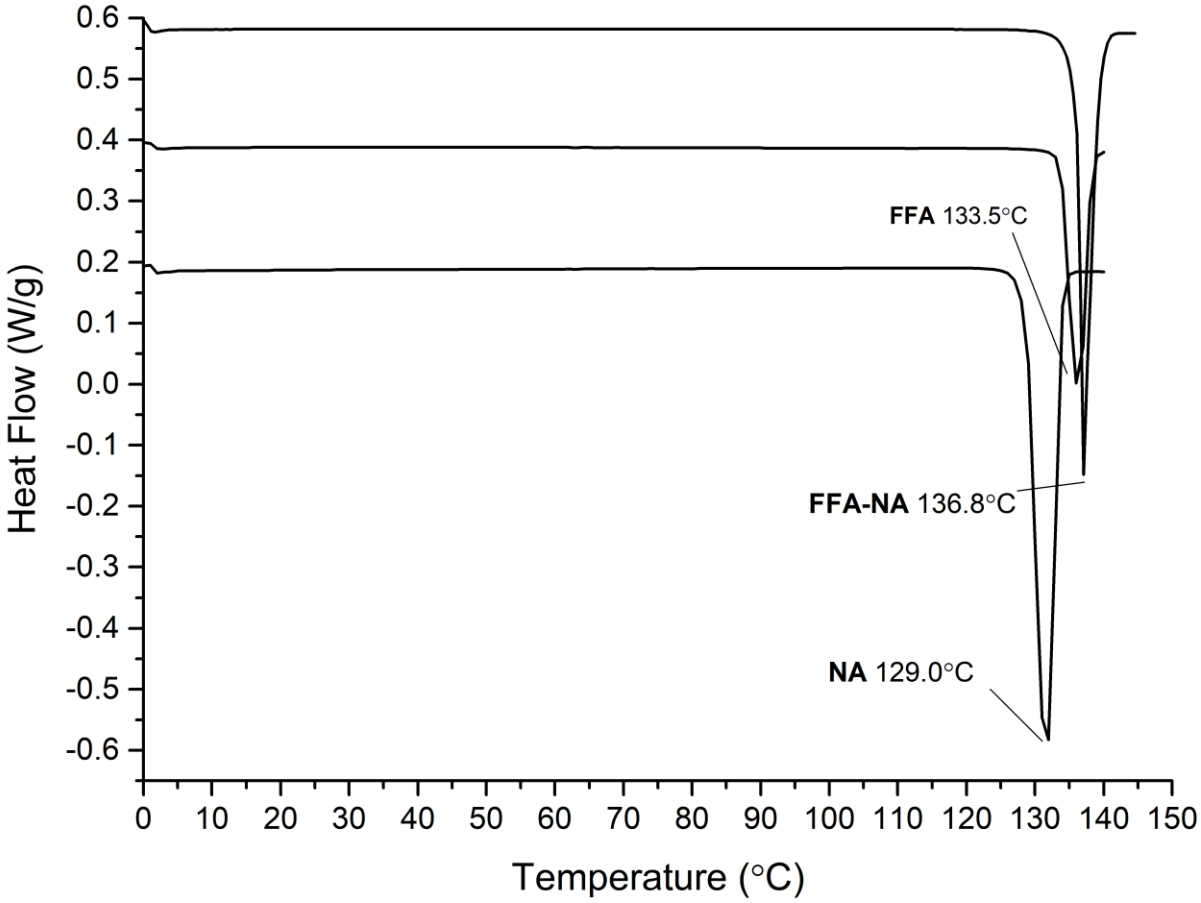

Figure 4-2 DSC Thermogram of FFA/NA and its constituent components that are used to make it - FFA form I and NA form I

The capability to amorphise a crystalline system in a controlled way is one of the other objectives of this work due to the importance of solubility and bioavailability an amorphous system brings to drug delivery. Scale of the system and lack of long-range ordering means that the describing an amorphous system accurately is a difficult task. The example we show in this chapter being the cocrystal FFA/NA. There are a few possibilities when a cocrystal system is amorphised that we have explored and will attempt to be describe.

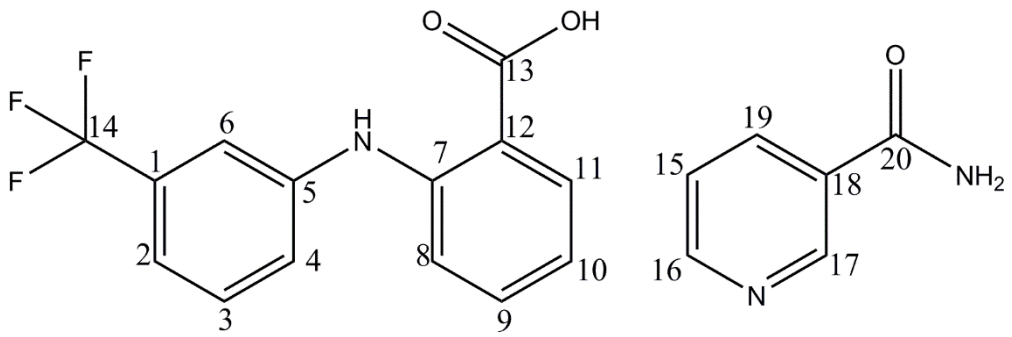

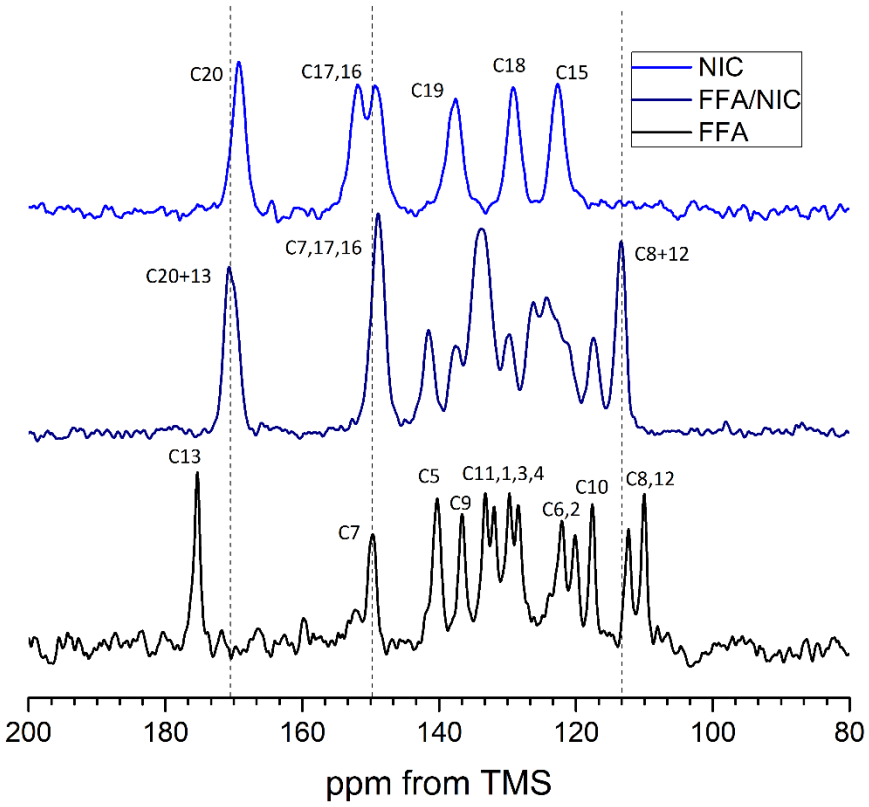

Figure 4-3 From top: ^{1}H-^{13}C CP/MAS solid-state NMR spectra of NA, FFA/NA cocrystal and FFA form I. Spectra acquired at 10 kHz (9.4 T). Dotted lines indicate similar chemical shift in C20 (left), C7/C16/C17 middle and C8/C12 right

As the prospect of multiple amorphous forms and mixtures of varying ratios are a possibility, solid-state NMR will be the primary tool used to characterise these forms, because of its ability to distinguish between crystalline and amorphous forms. In Figure 4-3 the spectra of the forms of the individual coformers that are used to produce the cocrystal are shown alongside the spectrum of pure cocrystal. It is quite obvious to see that the spectrum of the cocrystal is not simply the amalgamation of the two and has become more complicated, Figure 4-3 demonstrates how much more complex a cocrystal system is in terms of carbon chemical shifts. A combined computational and experimental approach was required in order to identify and label the ^{13}C sites of FFA/NA. Therefore, using the CASTEP code, calculations were performed on the crystal structure of FFA/NA (CSD structure reference: EXAQAW). Following a geometry optimisation of the structure the NMR chemical shieldings were calculated and converted to chemical shifts. Figure 4-4 A. shows the assignment of FFA/NA and

Figure 4-4 B. shows the agreement of experiment chemical shifts to calculated chemical shifts. These shifts are also listed in the Table below.

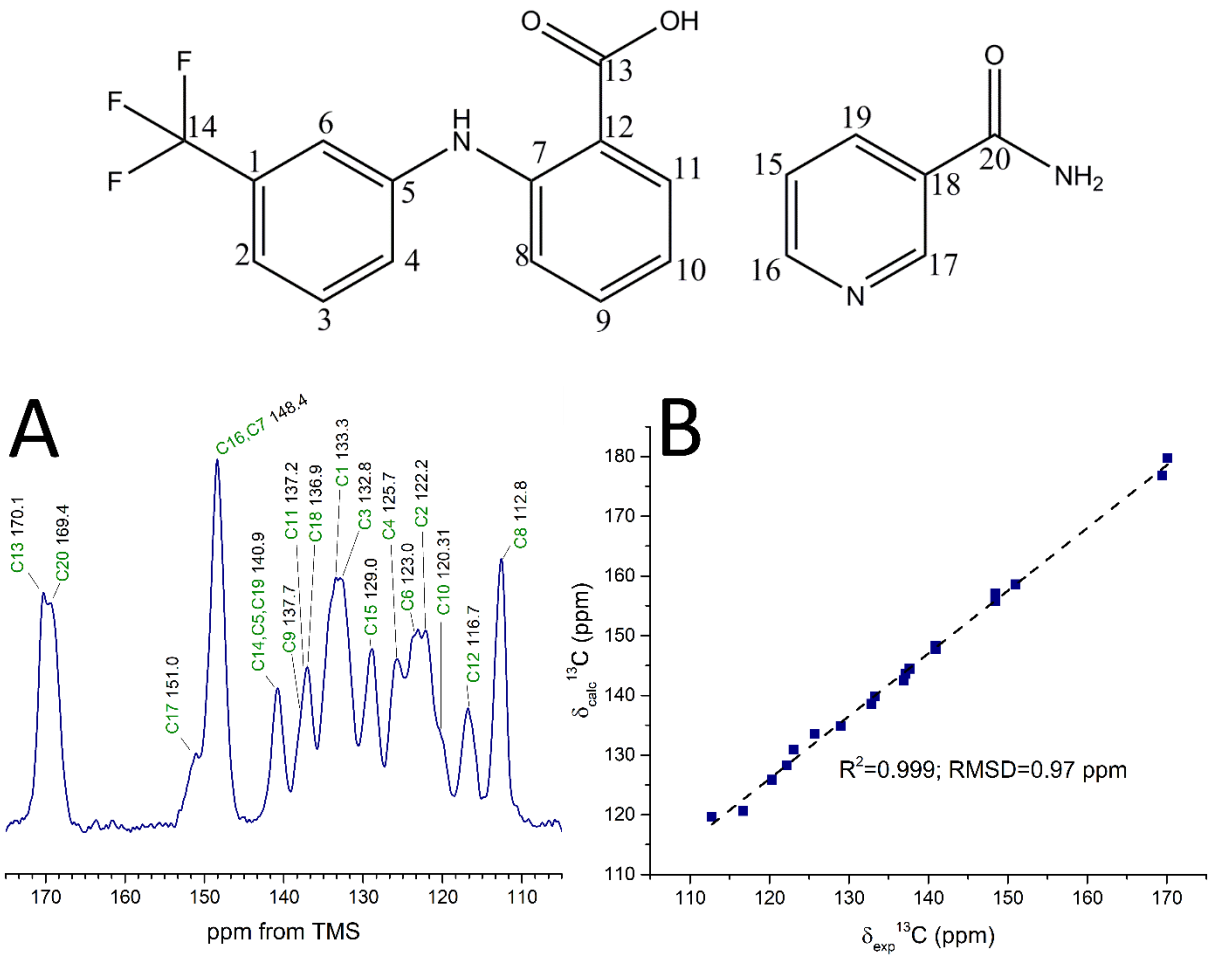

Figure 4-4 A. ^{1}H-^{13}C CP/MAS solid-state NMR spectrum of FFA/NA cocrystal with assignment based on CASTEP prediction. **B.** Comparison of experimental and CASTEP calculated ^{13}C chemical shifts.

Table 4-1 Comparison of the experimental and calculated ^{13}C chemical shifts of FFA/NA. Carbons belonging to FFA are highlighted in blue and carbons belonging to NA are highlighted in red. $\boldsymbol{\sigma_{ref}}$ was calculated to be 178.68 ppm.

^{13}C Site	FFA/NA Cocrystal	
	δ_{exp}	δ_{calc}
C1	133.3	139.8
C2	122.2	128.2
C3	132.8	138.6
C4	125.7	133.6
C5	140.9	148.2
C6	123.0	131.0
C7	148.4	155.8
C8	112.8	119.7
C9	137.6	144.5
C10	120.3	125.9
C11	137.2	143.6
C12	116.7	120.6
C13	170.1	179.8
C14	140.9	148.3
C15	129.0	134.9
C16	148.4	157.1
C17	151.0	158.6
C18	136.9	142.5
C19	140.9	147.8
C20	169.4	176.8

In order to be able to distinguish multiple polymorphic forms with a high level of certainty we turn to ^{19}F solid-state NMR. The sensitivity ^{19}F possesses allows for good insight into kinetics but also allowed us to distinguish different FFA species in our previous work[72]. Fluorine-19 has a high gyromagnetic ratio of 251.662 $10^6\ rad \cdot s^{-1} \cdot T^{-1}$ (close to ^1H at 267.52210$^6\ rad \cdot s^{-1} \cdot T^{-1}$), is spin $I = 1/2$ and is 100% naturally the occurring isotope. FFA has a CF_3 group in its structure. This site is represented

by a single resonance in the ^{19}F NMR spectrum of pure cocrystal (Z'=1 system) at -61.0 ppm. The commercial form I of FFA is used to make the cocrystal. ^{19}F solid-state NMR spectrum of FFA form I shows a single peak at -60.2 ppm, which is an important distinction to know whether separation of the cocrystal components has occurred. The other polymorph to consider is FFA form III, with a single ^{19}F peak at -62 ppm. The transformation of form I into III occurs slowly over time as form III is the most thermodynamically stable form.

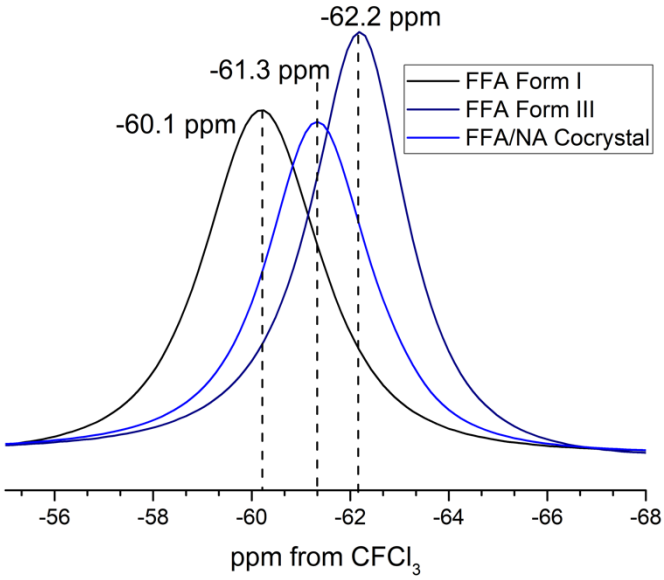

Figure 4-5 $^{19}F\{^{1}H\}$ solid-state MAS NMR spectra (9.4 T) of FFA Form I, FFA Form III and FFA/NA Cocrystal

Figure 4-6 shows a representation of the possibilities that could occur upon loading FFA/NA into the confined pore space. After the molten liquid has cooled below its T_m of 136.8°C there are many different pathways the system could follow, and it is possible that more than one could be followed over the lifetime of the components inside the pores. There are two main factors that will affect the products, the first being the interaction of FFA/NA molecules with the surface of the silica which consists of silanol protons created a high-energy environment that will favour the hydrophilic components of the FFA and NA. This may cause some specific orientations due to the need to minimise unfavourable interactions with the surface such as that of the fluorine atoms of FFA. The second factor that will affect the products is the size of the pore and the amount of space available to pack molecules of FFA/NA in the specific crystallographic directions. The most obvious possibility in Figure 4-6 is a recrystallisation of molten FFA/NA back into crystalline FFA/NA, which would depend on their being enough space within the pore for stacking of FFA/NA molecules into a long range ordered system.

There is also the possibility that the FFA/NA amorphises due to insufficient crystallographic packing. This possibility could be then called a coamorphous state in which aggregates of FFA/NA are found inside the pore space. The final possibility of combines the principles of the previous two possibility but implies that FFA/NA cocrystal separates into its component parts FFA and NA. These again could recrystallise into specific clusters or amorphise into aggregates. The forms of which could also be different to the form I FFA and form I NA that were used to make the cocrystal. The possibility of these systems interchanging with each other is present also, as we will show that the effect of temperature, loading ratio and addition of solvent greatly affects the capability of a system to become crystalline.

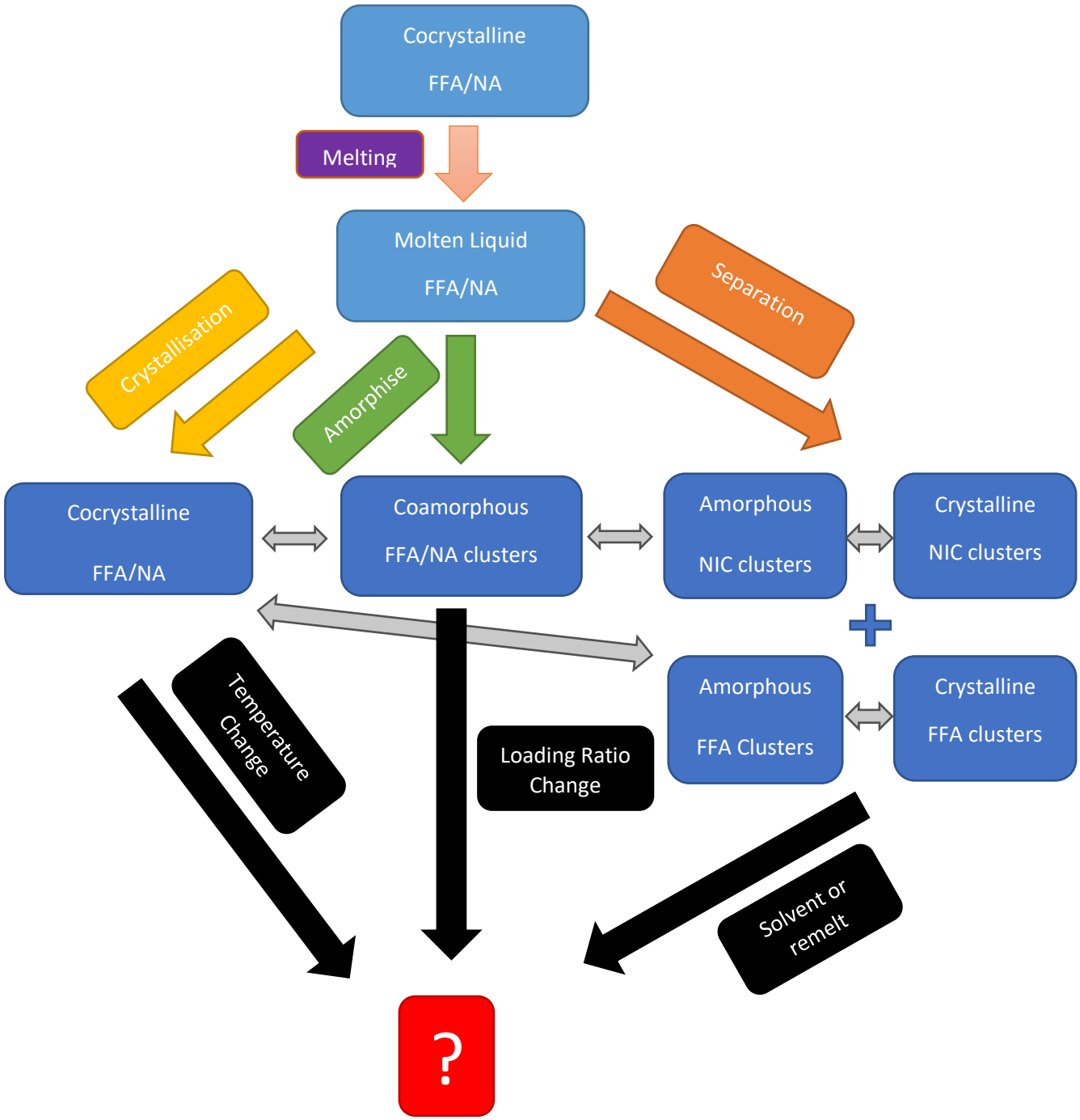

Figure 4-6 Flowchart of the possibilities of interconversions between different forms of cocrystalline, coamorphous and separated materials after loading into pore space

4.2 Loading of FFA/NA into Silicas

When considering the loading of the guest into the silica hosts the physical weight ratio must be considered. Our previous protocol involved set weight percent ratios from 15% up to 60% weight of the guest[65,72] when loading FFA and indomethacin into select silica hosts. The loading weights allows for a broad range of pore filling to occur with each silica host. In our previous practise we have found that over 50% of the loading of the guest usually results an excess of material that exceeds the loading capacity of the silica host. Pure FFA/NA cocrystal degrades at ca. 250°C. These weight loss in TGA is in good agreement with the loading level expected from the adopted melt-loading protocols. This is measured in these graphs as a function of mass against temperature. The loading ratios for each silica are 15%, 20%, 25%, 30%, 40% and 50% guest to host by mass and their weight loss from TGA is shown the Table below. Figure 4-7 shows the TGA curves for each silica host that has been loaded with FFA/NA.

Table 4-2 Percentage weight loss of FFA/NA after complete thermal decompisition compared to the expected loading percentages.

Expected Loading Percentage of FFA/NA	**TGA Weight Loss of FFA/NA % from Silica Host**		
	MCM-41	**SBA-15**	**MCF**
15	16.267	16.594	15.335
20	21.066	21.785	20.232
25	25.362	26.720	24.622
30	31.717	30.574	29.395
40	40.501	40.591	39.119
50	48.541	50.767	49.211
60	N/A	N/A	60.05

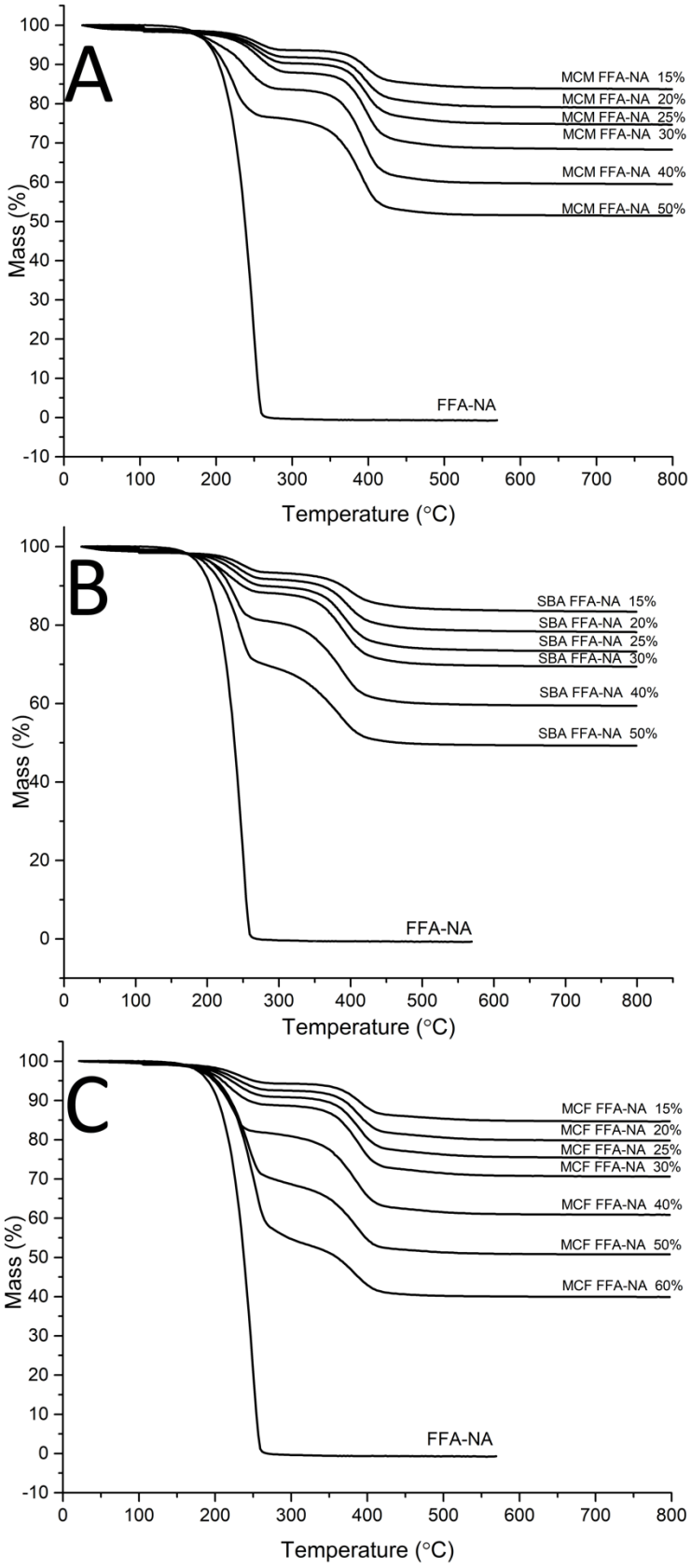

Figure 4-7 TG curves of **A.** MCM-FFA-NA, **B.** SBA-FFA-NA and **C.** MCF-FFA-NA loaded materials. Loading levels indicated as wt% of silica to FFA/NA cocrystal.

From the melt-loading method of encapsulating the guests into the hosts there is concern that simply melting the cocrystal will cause it to deposit over the surface of individual silica particles instead of entering the pores on those surfaces. There is also the concern that the resulting powder remains a physical mixture of small-recrystallized cocrystal and silica particles and that no loading into the pores has taken place.

The way that we have solved this issue is to perform nitrogen physisorption on all samples as a way of determining how much pore volume is available. This serves as an indicator towards how much space has been taken up inside the pore by our loaded cocrystal. It however does not conclusively determine if there is guest that is loaded outside the pore on the surface of the silica particles, for this further analysis by methods such as DSC and XRD is required and will be discussed further sections on a per silica basis.

The Figure 4-9-B below shows the measure of the total pore volume available after loading the guest for each sample, including completely empty silicas as a reference. For the larger pore space in MCF there is a distinct filling of the pores above 30% loading ratio whereby the pore volume decreases in a linear fashion. Whereas in the smaller pores of SBA-15 and MCM-41 the trend in the decrease in pore volume is more linear with respect to the loading ratio, except in MCM-41 where is appears to be completely full from the 40%-50% loading ratio. The BET surface plot, Figure 4-9-A, shows a correlation that as the amount of loaded drug increases, the BET surface area decreases. This implies the drug has been successfully loaded into the pore space. Figure 4-8 features the adsorption and desorption isotherms of the each of the silicas with all drug-loaded ratios, the isotherms have been scaled so that each is visible. Also, in Figure 4-8 is the pore diameter analysis for each silica. For MCM-41, DFT methods[128] were used to calculate the pore diameters, whereas the BJH (Barrett-Joyner-Halenda)[66] method was used for the determination of SBA-15 and MCF pore diameters.

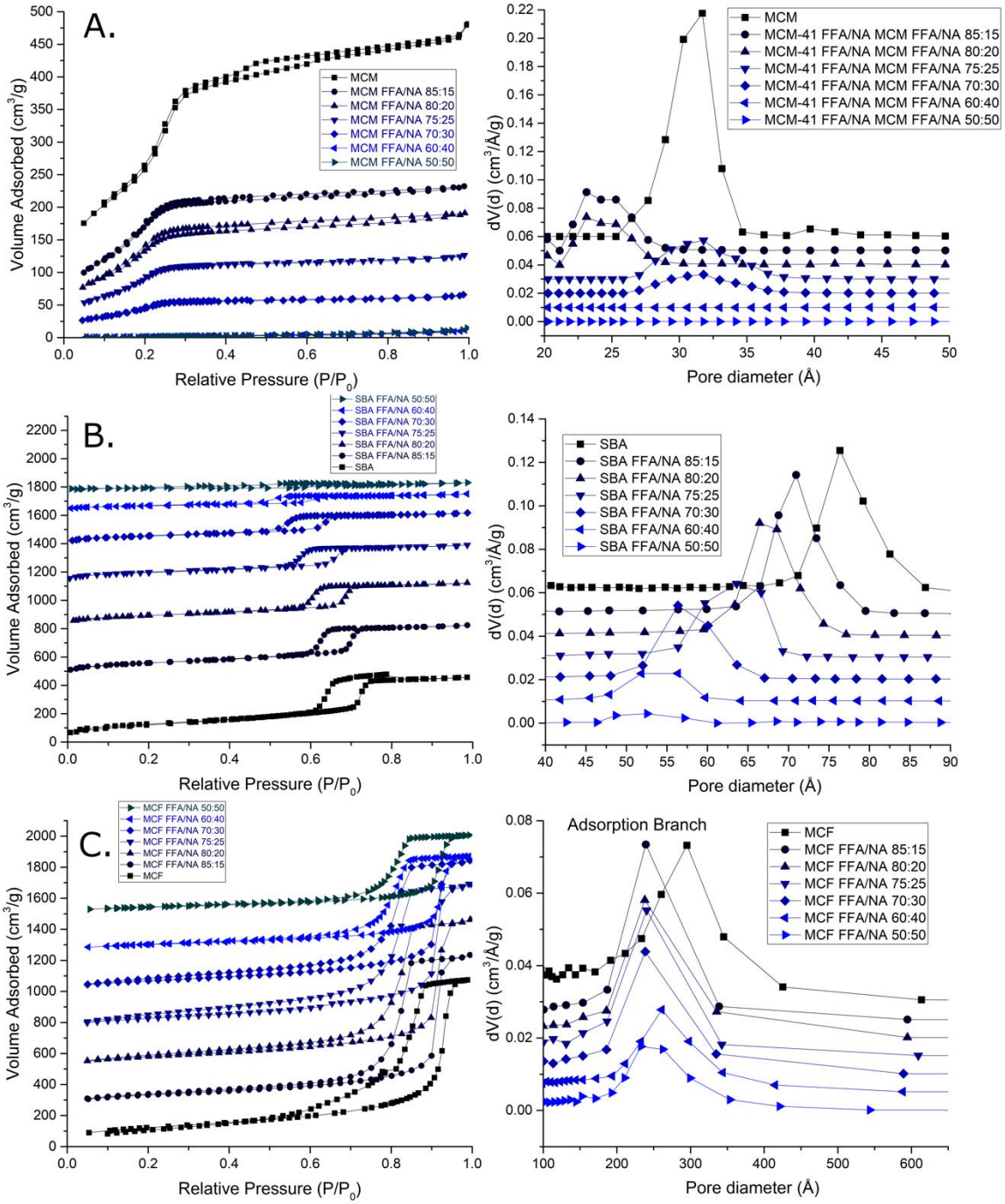

Figure 4-8 Nitrogen adsorption/desorption isotherms and pore size distribution curves for **A.** MCM, **B.** SBA-15, **C.** MCF at different host:guest FFA/NA loadings. SBA 15 isotherms are offset by 8% gap and MCF isotherms are offset by 250 $cm^3\ g^{-1}$.

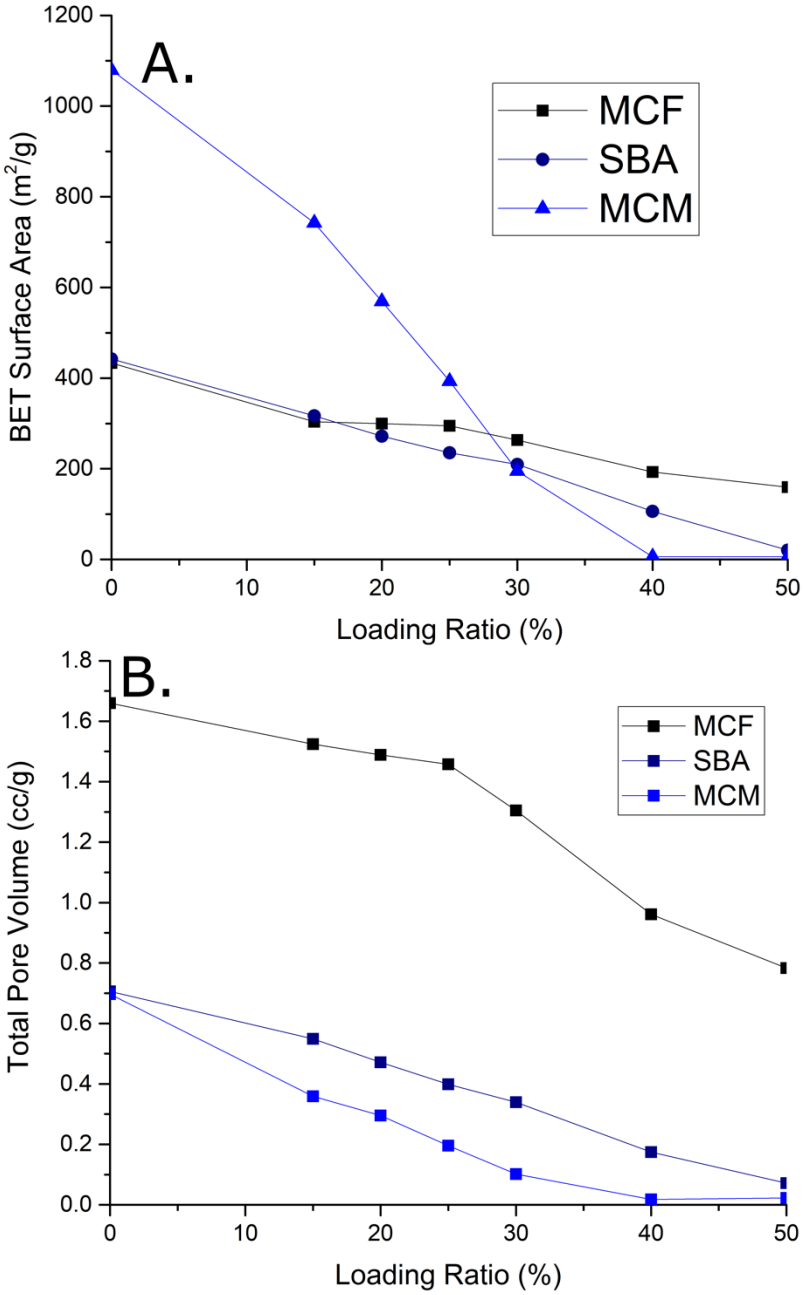

Figure 4-9 A. BET surface area (calculated as a multi-point BET in the linear region of the isotherms) **B.** Pore Volume (calculated at *P/P_0 of 0.99)*

4.3 Incorporation of FFA/NA into MCM-41 mesoporous silica

Of the mesoporous silicas, MCM-41 has the smallest pore dimensions at ca. 3 nm in diameter. From previous work with FFA loading inside the pore space[65,72], we predicted that it would be difficult to crystallise the FFA/NA cocrystal inside this limited space. Therefore, it was predicted that the loading

of cocrystal into the pores would result in an amorphous guest in the pores. The DSC thermogram (Figure 4-12) shows that at 50% loading level there are multiple melting peaks of materials. It is difficult to assign these peaks without other data. It is known from our previous studies with FFA that the loading of material generally results in a melting point depression at all loading levels. The large broad peak in the thermogram could refer to the presence of water inside the silica. Due to the high hygroscopic properties, there will be a certain percentage of adsorbed water inside the pores, this will be desorbed first before any melting of any components does. At 40 wt.% loading level, there is a small melting onset at 116.9°C indicating the presence of some crystallinity; though it is not possible to say whether this belongs to FFA, NA or FFA/NA. The onset at 116.9°C has also shifted to a lower temperature when compared to the peak at 50% at 120.1°C, which is consistent with loss of bulk crystallinity we see with depressed melting points. The crystallinity is noticeably absent also at the 30% loading ratio and below, with no detectable sharp melting point above 100°C. A broad component, beginning around 20-30°C and ending at 80-90°C, is present in all of the thermograms with loaded compound inside the pores. This greatest intensity at the 30% loading ratio compared to the higher ratios at 40-50%. This broad component becomes less significant as the ratio of drug to silica decreases to the 15 wt. %. This is most likely water that is being desorbed from the silica surface as the temperature in increasing and the amount of space is increasing.

This is also hinted by the results of PXRD analysis. Both the individual components of the cocrystal FFA/NA and the co-crystal have characteristic diffraction peaks. Out of all loading ratios, only the 50% loading ratio has some indication of crystallinity. This crystallinity also appears to match that of the diffraction patterns of the cocrystal with some separated forms of FFA form I and NA form I. As shown in the Figure by different coloured lines, there are mostly peaks matching cocrystal, however there are some peaks that fit to both FFA and NA separately. This implies that there has been partial separation of cocrystal. Now when the DSC thermogram of 50% loaded material is consulted we can infer that there is a small amount of crystalline FFA in the sample from the corresponding melting point peak at 133.5 °C which matches with the melting point of form I. The large melting peak with a maximum at 127 °C is most likely to be that of the FFA/NA as a depressed melting peak. Finally, the peak at 120.1 °C would correspond to an equal amount of NA form I to FFA form I that instead of being crystalline features a depressed peak not corresponding to it standard melting point of 129 °C. Below that loading, at 40% and lower, there appears to be only a broad amorphous component to the PXRD patterns. In the DSC of the 40% loaded sample, there was a small melting peak at 116.9 °C however this small portion of crystallinity is not able to be seen its corresponding PXRD pattern.

However, the point to highlight is such that the pores at 50% are fully loaded with FFA/NA material to the point where it is likely the material overloaded and outside the pore structure. This crystallinity falls off rapidly, when we consult the DSC and PXRD data of 40% loading. Lack of diffraction peaks at 40% loading and an extremely small melting point on the DSC show that we have lost clusters that possess long-range order. This implies that part of the crystallinity that we see at high loadings of 50% could be the result of two conclusions. From the calculations performed on the sorption isotherms we know that at loadings of 40-50% the BET surface area and total pore volume are extremely low. This implies that the pore space is completely filled at a level of 40% or higher. We only see evidence of some form of crystallinity at 50% loading however, when we know the pores are most likely overloaded with material. Therefore, any excess crystalline material will be outside the pores, either coating the outside of the silica particles or existing as small clusters in the physical mixture with silica powder.

Table 4-10 BET surface area (calculated as a multi-point BET in the linear region of the isotherms) and Pore Volume (calculated at *P/P_0 of 0.99)*, Pore Diameters calculated from DFT model of isotherm

Loading Ratio (% weight to MCM-41 weight)	BET Surface Area(m^2/g)	Total Pore Volume (cm^3/g)	Pore Diameter (nm)
0	1079	0.697	3.169
15	742	0.359	2.313
20	569	0.296	2.313
25	393	0.196	3.179
30	195	0.102	3.179
40	5.8	0.018	N/A
50	6.1	0.022	N/A

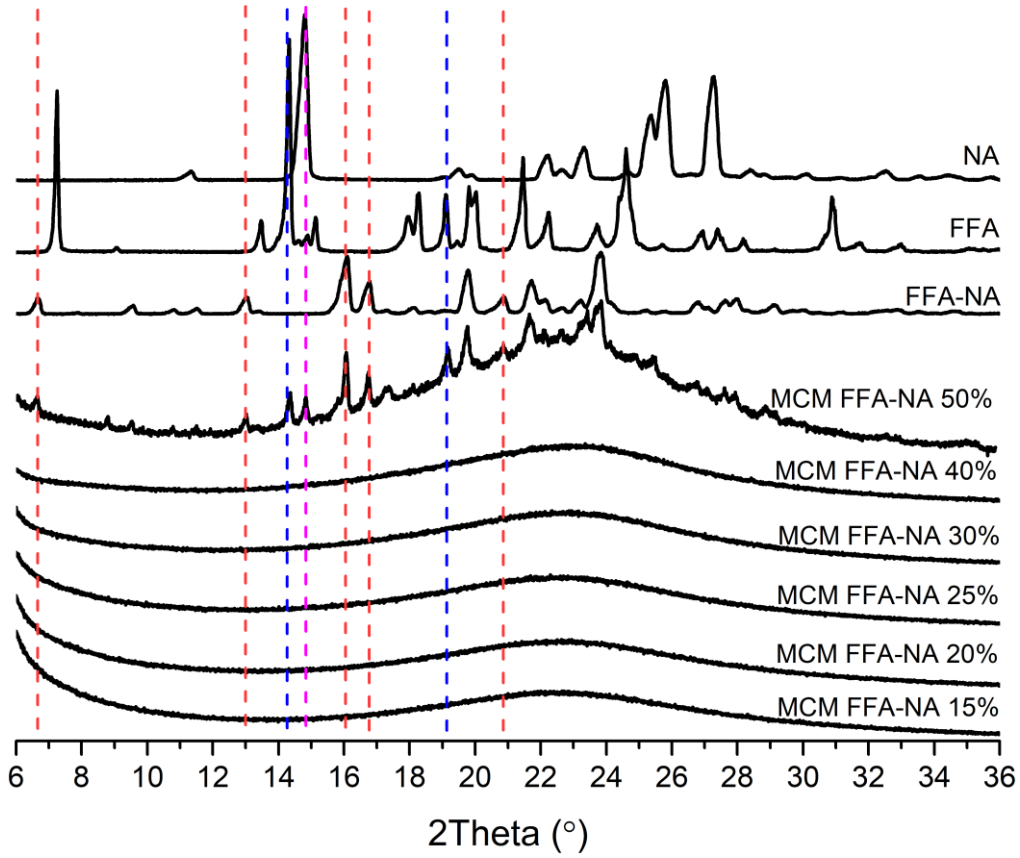

Figure 4-11 PXRD patterns of MCM-41 silica loaded with FFA/NA at various loading levels (red lines indicate matching FFA/NA, blue lines matching NA form I and pink lines match FFA form I host:guest (in wt%)

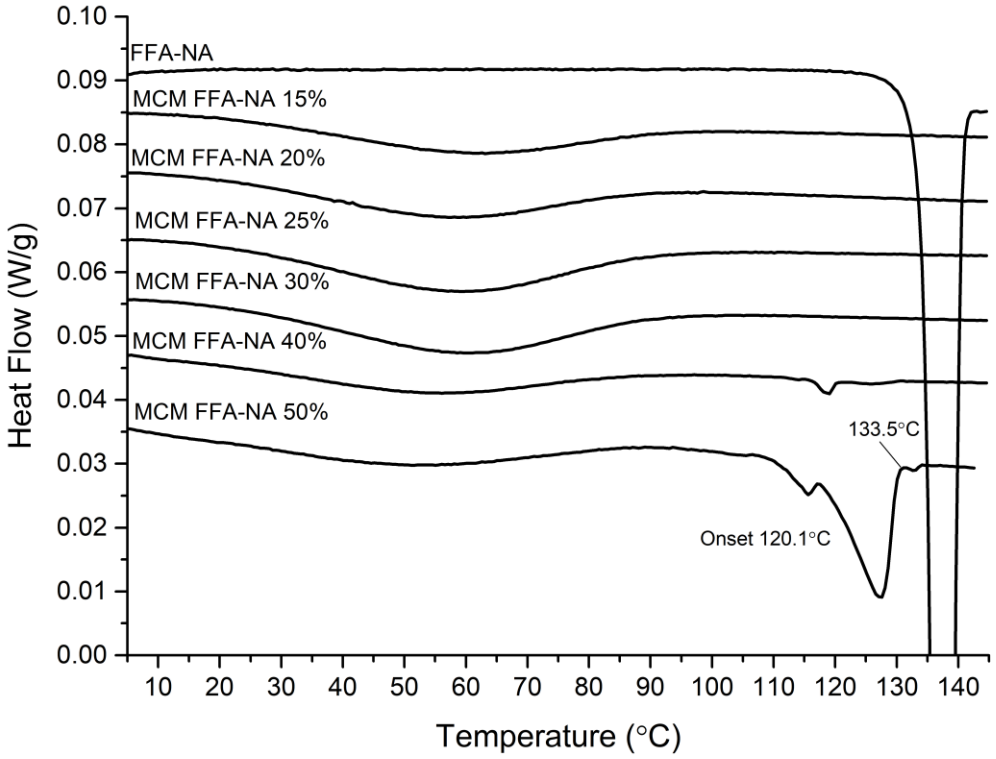

Figure 4-12 DSC thermogram of MCM-41 loaded with FFA-NA loading ratios (silica weight %/ FFA-NA weight).

There is also the consideration of dimensions of the pore in relation to the unit cell of the cocrystal system. MCM-41 has pores with *ca*. 3 nm diameters, while the cocrystal unit cell (*abc*) is 0.5, 1.5 and 2.21 nm. Considering the longest dimension of the FFA/NA unit cell being its *c* axis and the silica pores being 3 nm – if we attempt to orient molecules of FFA/NA such that the *c* crystallographic direction was parallel to the pore walls, the *ab* plane could be only be packed in such a way that up to a few molecules could be stacked onto each other across the cylindrical pore space available. The issue with the model being that it is not yet defined in literature how many repeated unit cells is required to form a semblance of crystallinity, it is simply assumed that crystallinity occurs at some point on the nanoscale and continues onto the macroscale world of bulk materials. Figure 4-13 below is an assumed model based on a fully loaded pore structure.

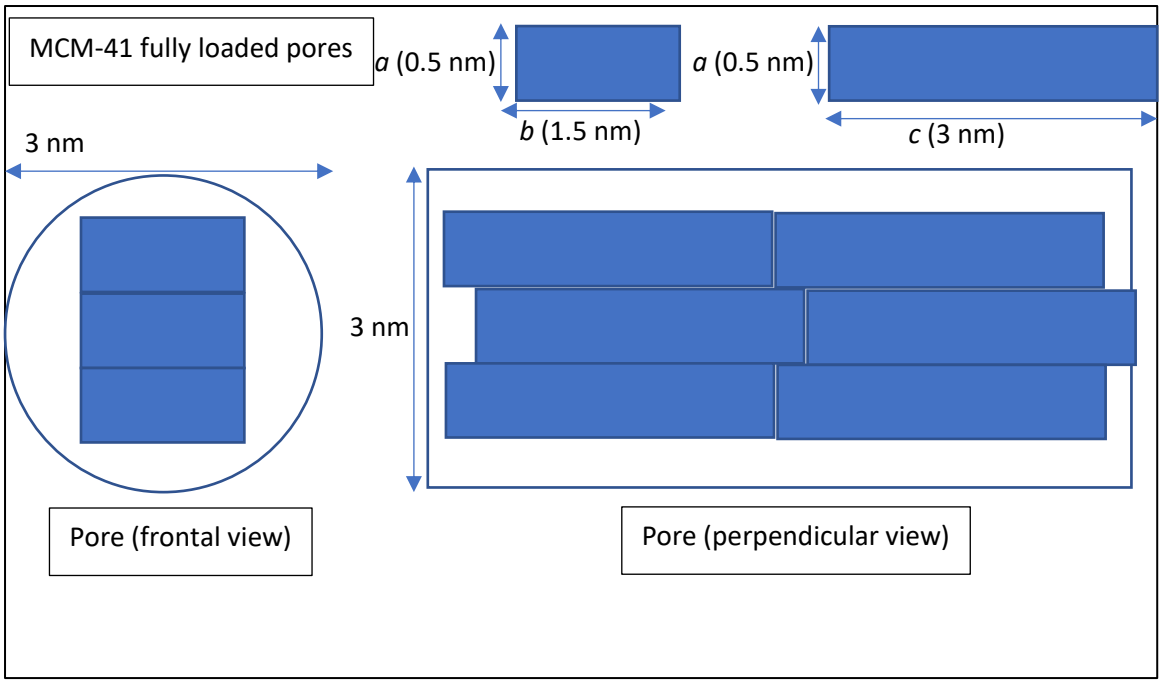

Figure 4-13 MCM-41 Fully Loaded Pore diagram of frontal and perpendicular view of pore space. Blue rectangles represent FFA/NA unit cells to scale with the pore dimensions.

When the loading of cocrystal inside MCM-41 is at 30% or lower we can safely assume that we have an absence of material inside the pores – the pores are not fully loaded. The space created gives way to mobility of the materials inside the pores. If nitrogen gas is able to penetrate the pores and adsorb to the walls, then the materials in the system must be moving fluidly or have formed small plugs in specific areas inside the pores.

The FFA/NA aggregates will interact with the hydrophilic walls of the silica, due to presence of surface silanol groups. The expectation is that this interaction with the surface will be favoured over the interaction with other FFA/NA molecules. Due to the increased mobility of these molecules also means that adjacent molecules of FFA/NA may not have the strongest intermolecular interactions with each other in order to be able maintain a repeated long-range order in a particular direction. This may also be the reason that at lower loadings we do not see any evidence of long-range order.

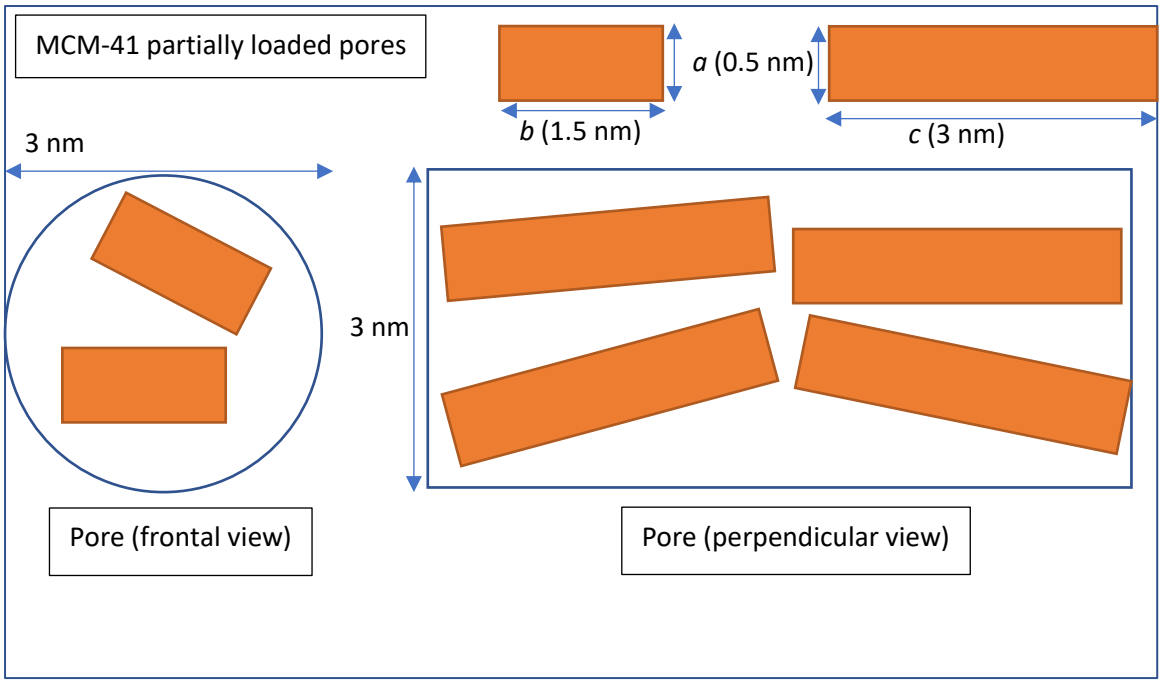

Figure 4-14 MCM-41 Partially loaded pore diagram of frontal and perpendicular view of pore space. Orange rectangles represent FFA/NA unit cells to scale with the pore dimensions.

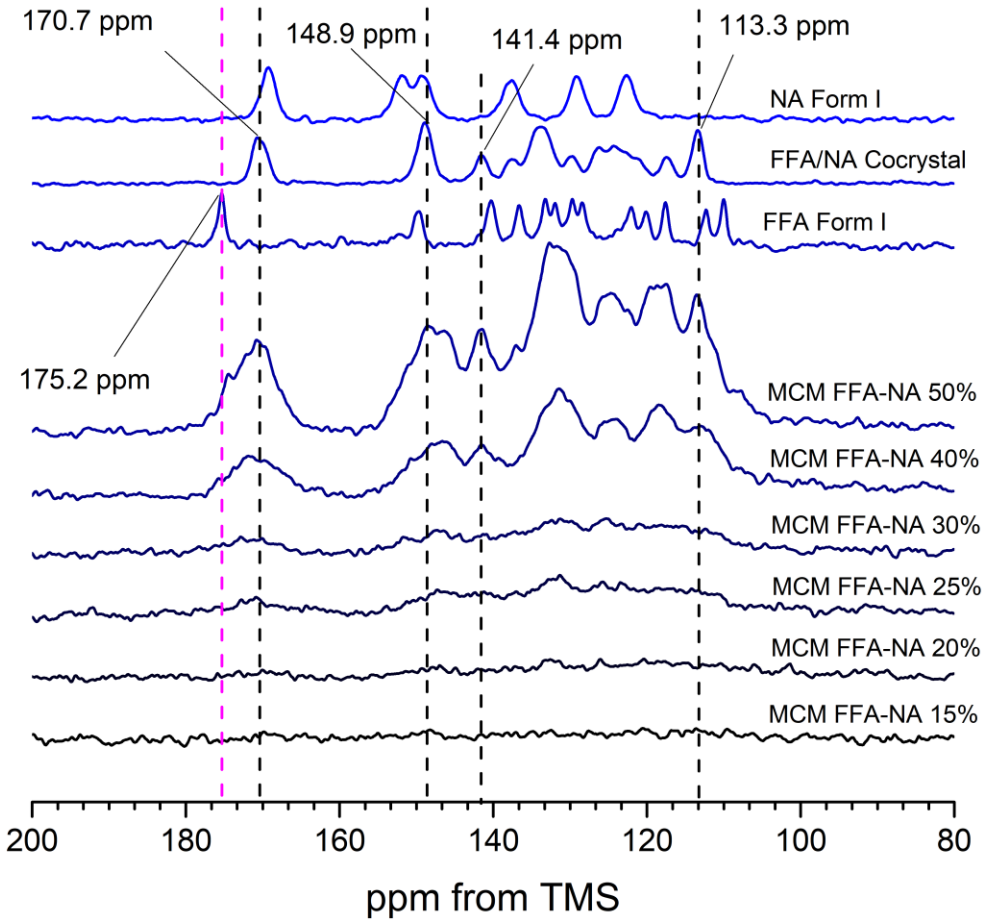

Figure 4-15 ^{1}H-^{13}C CP/MAS solid-state NMR spectra of MCM-41 loaded with FFA/NA cocrystal at 298 K at various loaded levels indicated by the percentage of loading of FFA/NA. Peak matching FFA form I in pink, peaks matching FFA/NA in black where appropriate

The ^{1}H-^{13}C CP/MAS NMR spectra of MCM-41 silica loaded with FFA/NA show that temperature has an interesting effect on the state of the species of FFA/NA inside the pore space. At room temperature (Figure 4-15), there are peaks that correspond with the FFA/NA peaks in 50% and 40% loadings at 170.7, 148.9, 141.4 and 113.3 ppm. There is also a shifted small peak of FFA form I at 175.2 ppm in the 50% loaded material. The difference in peak intensity follows the loading level of pores as the spectra have each been recorded using the same recycle delay and number of scans. The intensity of the spectra at 40% almost has half the intensity of the 50% loaded material. Then when we progress to the 30% and lower loadings at room temperature there is little to no intensity in peaks is observed. This implies that the FFA/NA molecules are not arranged as much a manner exhibiting long range and that it is possible that they are much more mobile inside the pore space. If the FFA/NA is more mobile due to rapid isotropic movement of individual molecules, then the efficiency of the CP transfer will be

significantly reduced. Particles of FFA/NA therefore appear to become more liquid-like as the loading ratio is reduced.

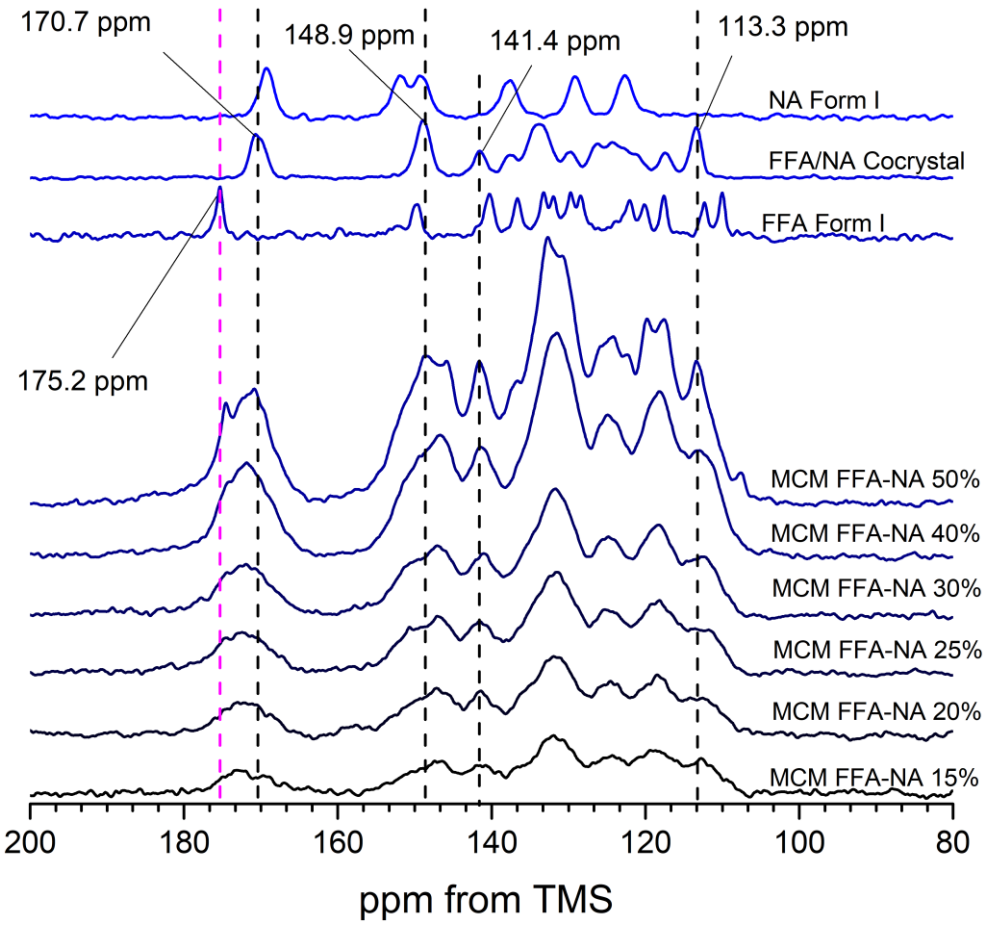

Figure 4-16 ^{1}H-^{13}C CP/MAS solid-state NMR spectra of MCM-41 loaded with FFA/NA cocrystal at 223 K at various loaded levels indicated by the percentage of loading of FFA/NA. Peak matching FFA form I in pink, peaks matching FFA/NA in black where appropriate

The same ^{1}H-^{13}C CP/MAS experiments then performed at 233 K show that the low loading of materials, ca. 30%, is present and detectable. From the Figure 4-16, signal can be seen of each loading ratio even at the lowest loading of 15%. These spectra have been recorded with the same number of scans and recycle delay as their room temperature counter-parts for comparison. The presence of signal intensity now at lower loading can be explained by the considerable reduction of mobility of the encapsulated species at lower temperature, and thus the enhanced ^{1}H-^{13}C CP efficiency. In contrast, the spectra recorded at room temperature show little to no intensity below 30% loading level of the guest. Part of the enhancement of signal will have been due to the increase in rigidity of the system.

The signal intensity that we now see as a result of cooling down the components within the pores shows that the state of FFA/NA inside the pores is very dependent on the temperature of the system.

^{1}H NMR spectra are difficult to assign to individual components. FFA and NA both have a large number of aromatic protons. MAS rate of 10 KHz is not effective in achieving sufficient resolution. The room temperature spectra (Figure 4-18) show broad resonances spanning 5-10 ppm which encompass the twelve aromatic protons across FFA and NA and the amide environment on the NA. The carboxylic acid proton of FFA is expected to be much higher but is not visibly present. As the loading level of the FFA/NA decreases, the intensity of the broad resonance decreases while the peak shifts upfield slightly. This is most likely due to ^{1}H sites from the silanol environments[129] dominating the spectra and the physical amount of drug has decreased. The environments that exist below 5 ppm are those of silanol groups in three different environments that can be distinguished currently (Figure 4-17). These are a single silanol group by itself is at 1 ppm, a silanol group that is hydrogen bonding with an adjacent silanol group or a water molecule hydrogen bonding via the oxygen of water to the proton of the silanol at 2 ppm, and finally a silanol group hydrogen bonding to water via the proton of the water and the oxygen of the silanol group at 3.4 ppm.

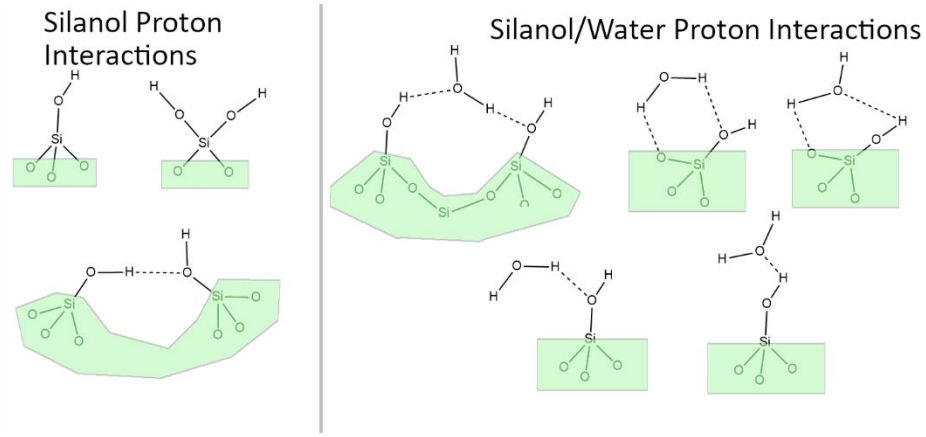

Figure 4-17 Different possible silanol interactions with water that produce ^{1}H NMR signals. Green indicates bulk area of silica where majority of Si-O exists as oppose to the exposed surface where silanol groups are located.

The growth of these peaks as the amount of loaded cocrystal is decreased is due to the available pore space becoming host to water molecules from the air due to hygroscopic nature of MCM-41 host. These environments are less abundant at 40-50% loadings due to complete filling of the pore space. By firstly pre-heating the silica at above 100 °C for a couple of hours beforehand will remove adsorbed water by evaporation, then adding the FFA/NA above the melting point of the cocrystal (136°C) will

minimize the amount of water present. After the samples have cooled down to room temperature, water from the air will eventually fill some of the space left in the lower loaded samples. There will also be silanol groups on the surface of the individual MCM-41 particles which are not protected by the cocrystal and these will also adsorb a small percentage of water to the surface.

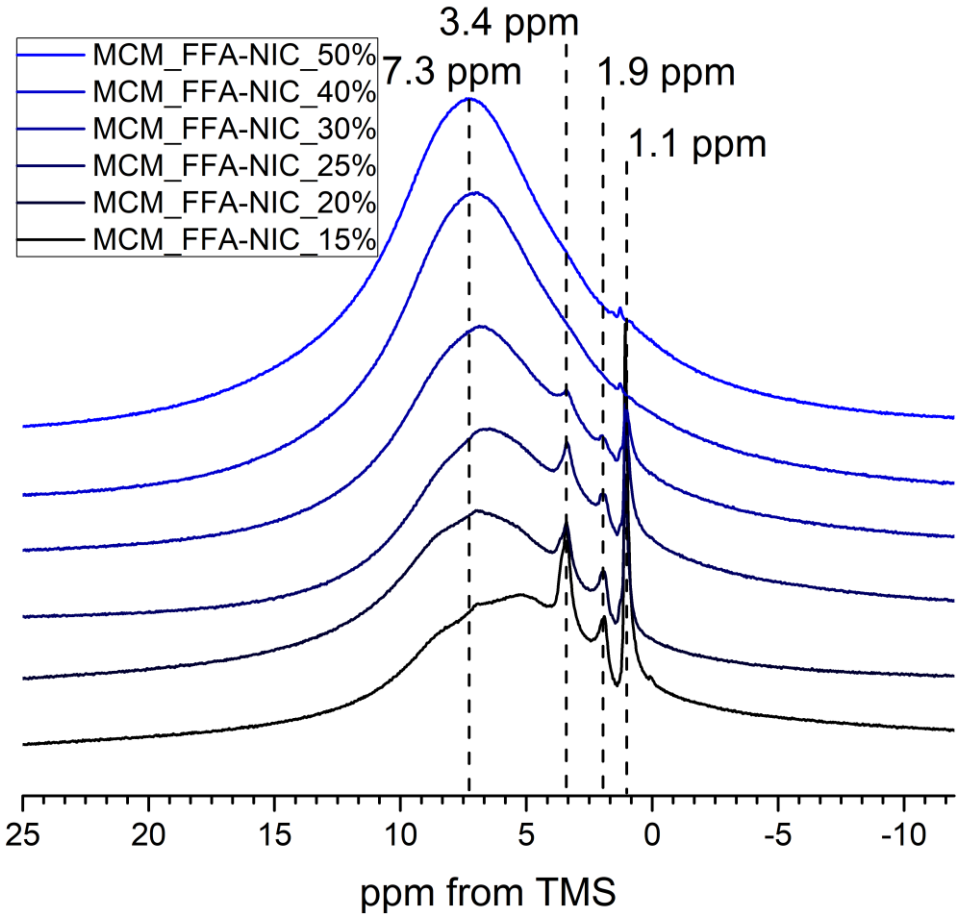

Figure 4-18 ^{1}H MAS solid-state NMR spectra of MCM-41 loaded with FFA/NA cocrystal at 298 K at various loaded levels indicated by the percentage of loading in the legend

As the temperature is lowered to 233 K (Figure 4-19) any water molecules that existed in a liquid phase will freeze inside the pores. This will also as slow down the mobility of any cocrystal inside the pores that is able to freely move – namely in the samples at 30% loading and lower. The effect of cooling the samples results in the chemical shifts belonging to FFA/NA to broaden further when compared to the room temperature spectra, most likely due to the freezing and locking of more conformations comparative to the mobile room temperature samples. There is also a reduction in the intensity of the silanol peaks compared to the room temperature samples.

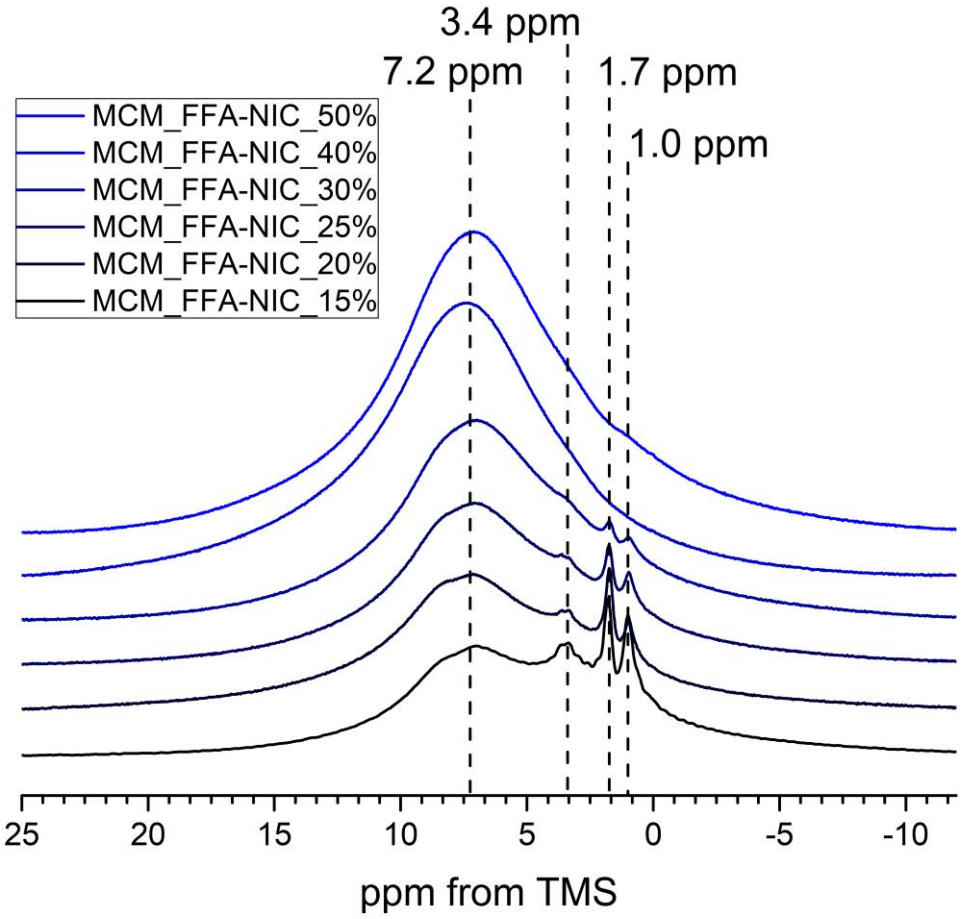

Figure 4-19 ^{1}H MAS solid-state NMR spectra of MCM-41 loaded with FFA/NA cocrystal at 223 K at various loaded levels indicated by the percentage of loading in the legend

The ^{19}F MAS NMR spectra of MCM FFA/NA (Figure 4-20) recorded at room temperature shows ^{19}F resonance centred at -62.3 ppm at the highest FFA/NA loading levels of 50% and 40%. At the loading level of 30% and lower, the ^{19}F peaks have shifted further upfield to -63.2 ppm along with the development of a shoulder at ca. -65 ppm. At the highest loading of 50% PXRD we know that there has been a small separation at the 50% loading ratio of FFA/NA into FFA form I and NA form I. There are no peaks in the PXRD patterns that match crystalline FFA/NA cocrystal at loadings below 40%. (Figure 4-5). The resonances present in the ^{19}F NMR are extremely broad and have shifted upfield which would suggest a less ordered state of matter for the FFA/NA that is inside the pores.

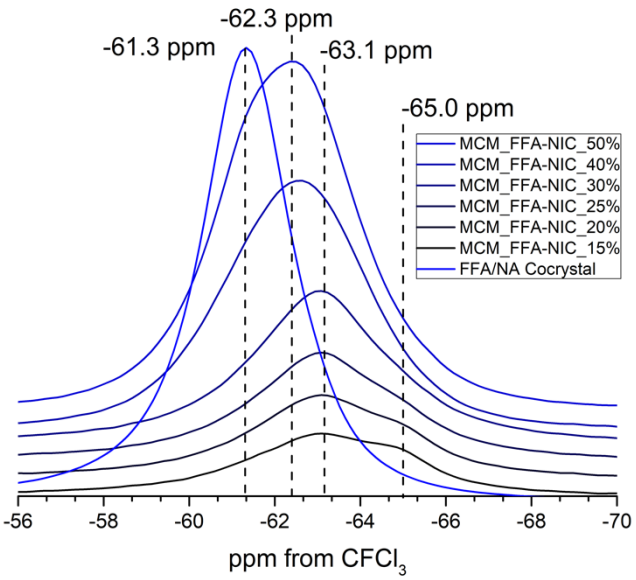

Figure 4-20 ^{19}F MAS solid-state NMR spectra of MCM-41 loaded with FFA/NA cocrystal at 298 K at various loaded levels indicated by the percentage of loading in the legend and pure FFA/NA cocrystal for comparison

The development of a fluorine environment at -63.1 ppm at the 30% loading ratio is at the point at which there is available space for the particles to move freely from the pore volume calculations performed on the sorption isotherms. The shifting of the population at -62.3 ppm at 40% loading to -63.1 ppm at 30% loading coinciding with gaining of space within the pores suggests that the environment belongs to that of a more mobile species. The shoulder at -65 ppm would then imply a species that exists with greater mobility and probably liquid-like in nature. This kind of molecular mobility is common with drug systems loaded in MSMs. Studies with aspirin[130] and naproxen[131] show the increased molecular mobility of drug loaded in pore space, but also that the surface chemistry of the silica (modified or unmodified) can greatly affect the drugs' interactions.

The ^{19}F spectra recorded at 233 K (Figure 4-21) are much broader, hence this shoulder is not resolved. The lowering of the temperature is effectively freezing the motions of the molecules. We can therefore infer the size of the aggregate of FFA/NA molecules at -63.1 ppm is much larger than that of the shoulder at -65 ppm. The latter most likely being more liquid-like and mobile molecules of FFA/NA. The process of cooling down the sample stops mobility afforded to the FFA/NA molecules at room temperature. These cooled FFA/NA molecules are then more likely to attach themselves to others inside the pores forming small aggregates.

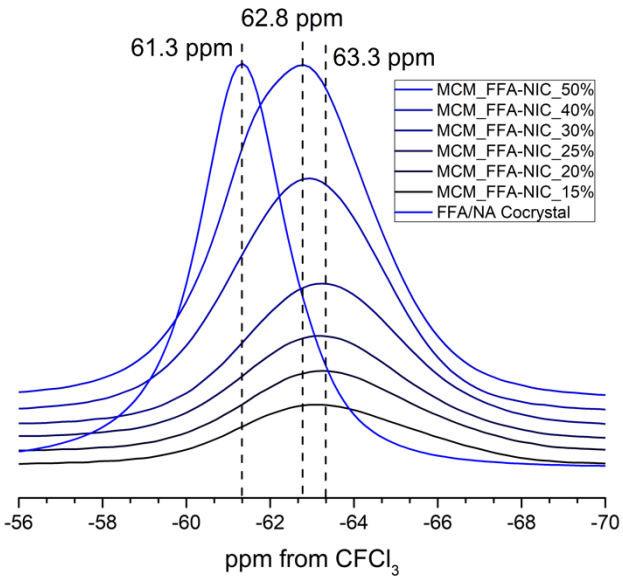

Figure 4-21 ^{19}F MAS solid-state NMR spectra of MCM-41 loaded with FFA/NA cocrystal at 223 K at various loaded levels indicated by the percentage of loading in the legend and pure FFA/NA cocrystal for comparison

The effect of both fast MAS rate and high field (19.96T) enabled us to distinguish the different species within the pore system with much better resolution. As seen in the Figure 4-22 below there is a distinct separation of two types of ^{19}F populations at 50% loading: -60.9 ppm and -62.2 ppm. The peak at -60.9 ppm in the ^{19}F spectrum can be assigned to pure FFA/NA cocrystal as evident from the match in PXRD. There is however no peak matching that of what is believed to be the separated FFA form I present which would be at around -60.1 ppm. Considering that 40-50% loading is effectively filling the pore space completely, the population at -60.9 ppm would then refer to FFA/NA molecules that are outside of the pore space in small clusters. The second peak of in the spectrum of 50% loading at -62.2 ppm would on first glance be assigned to FFA form III, however there is no evidence of this form in the PXRD. We believe represents aggregates of FFA/NA molecules inside the pores. This is also apparent for the 40% loaded material and below where the peak at -62.2 ppm remains. The reason we believe it is not FFA form I inside the pores is from our previous work on FFA loaded into MCM-41[72]. In that published work, FFA form I has a small presence at -60.1 ppm indicative of effective loading outside the pores. There was also no presence of form III in any of the PXRD for this material. This would again confer with our hypothesis of a completely filled pore space of aggregates of FFA/NA material due to the size limitations of the pore dimensions. Following trend at low field, the ^{19}F peaks in the samples with loading level below 30% levels shift upfield to -62.5 ppm at 30% and -62.7 ppm at loadings of 25%.

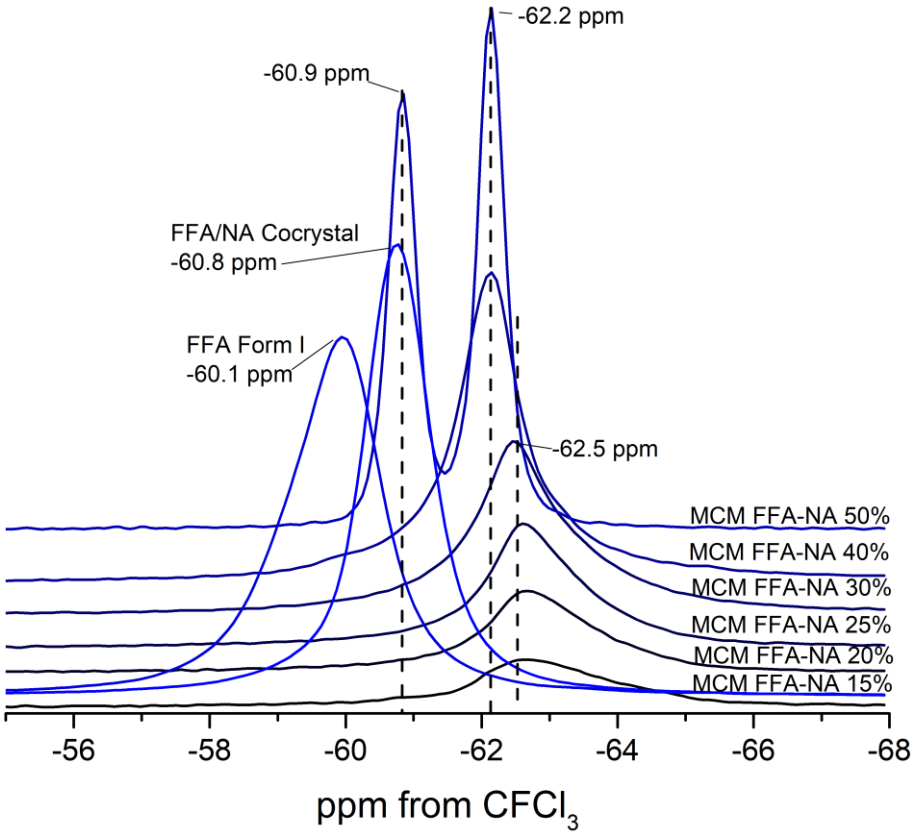

Figure 4-22 High field ^{19}F MAS NMR spectra of MCM-FFA/NA composites recorded at 19.96 T and 55 KHz MAS rate. Samples are labelled according to their host:guest ratio (in %weight). For reference FFA/NA cocrystal and FFA form I were added to the Figure, recorded at 19.96 T at 35 KHz MAS rate.

Our data on FFA/NA in MCM-41 indicate the guest species inside the pore are present as an aggregate form FFA/NA that does not represent a crystalline drug. It is clear that the pores can also be overloaded to the point either where particles exist on the surface of MCM-41 particles. Importantly, the mobility of loaded FFA/NA is also dependent on the loading ratio. Loadings of 30% and lower appear to create space inside the pore network allowing FFA/NA molecules to behave in a more liquid-like manner. Upon cooling the mobility of the system has been reduced, which in turn enhances the intensity of the ^{1}H-^{13}C CP we are able to acquire. In this case defining the mobility of the system and how has more relevance than stating the degree of crystallinity, as it appears the only crystalline clusters of material are located outside the pore space. Figure 4-23 below summarises this hypothesis as an arrangement of how we believe the FFA/NA have been arranged inside the pores dependent on the spatial composition and loading ratio.

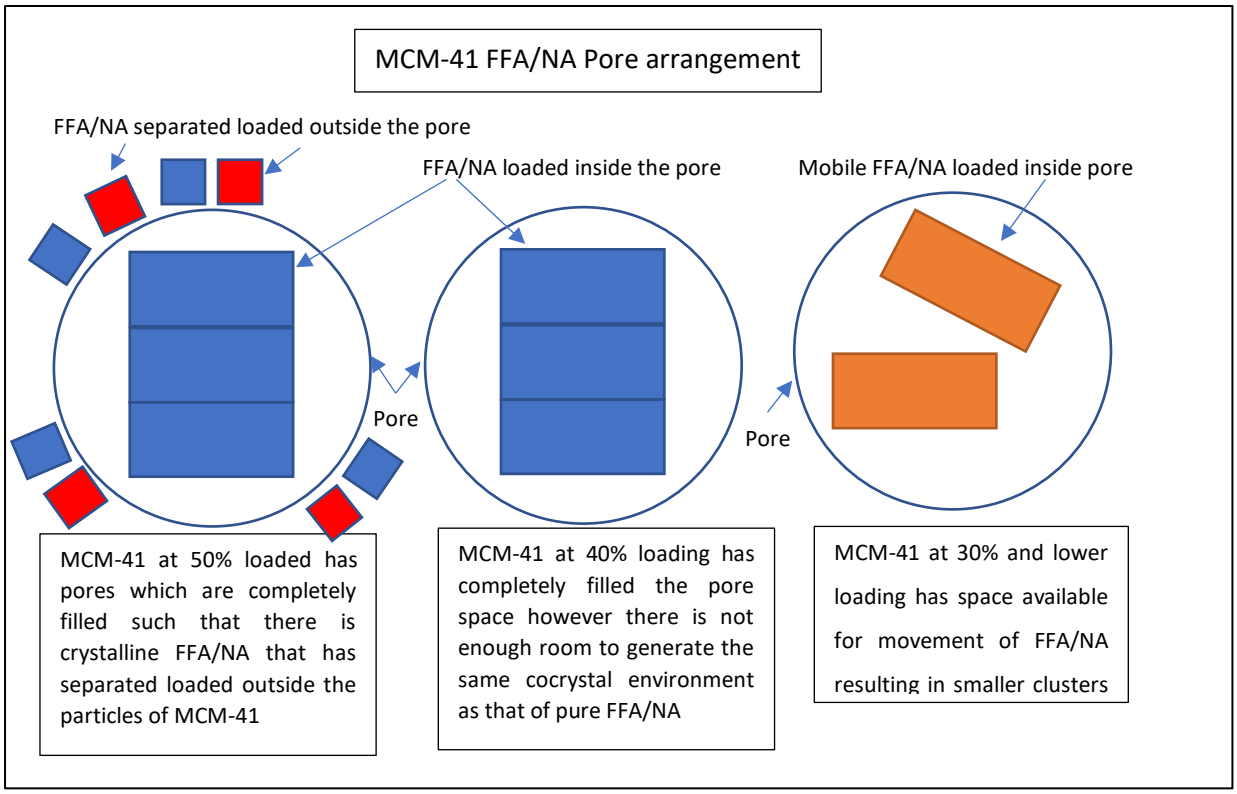

Figure 4-23 Pore arrangement hypothesis of FFA/NA in MCM-41 at fully loaded and partially loaded ratios

4.4 Incorporation of FFA/NA into SBA-15 mesoporous silica

SBA-15 mesoporous silica has pores that range from 6-7 nm in diameter. At approximately double to size of MCM-41 the possibility of forming an encapsulated phase that possesses more stability and long-range order is a possibility.

Following the results of the DSC (Figure 4-24), it can be seen that at the highest loading of 50% there is a slightly depressed melting point of *ca*. 129°C compared to the melting point of pure FFA/NA cocrystal at 136.6°C. Following previous hypothesises we would assume that the melting point in SBA-FFA/NA 50% loaded material refers to either components existing outside the pore space, or due to the larger pore space this could imply the presence of a crystalline phase of FFA/NA existing inside the pores. In this case it can also be considered that the 129°C could refer to pure NA form I which has a melting point of 129°C that has separated from the FFA/NA cocrystal. Form I of NA however is not likely due to the absence of a secondary melt in reference to pure FFA form I. There is also a small

water component to all the loading ratios of SBA-15; between 30-70°C at 50-25% loadings, then at 20-15% loadings the same component shifts slightly to between 40-80°C.

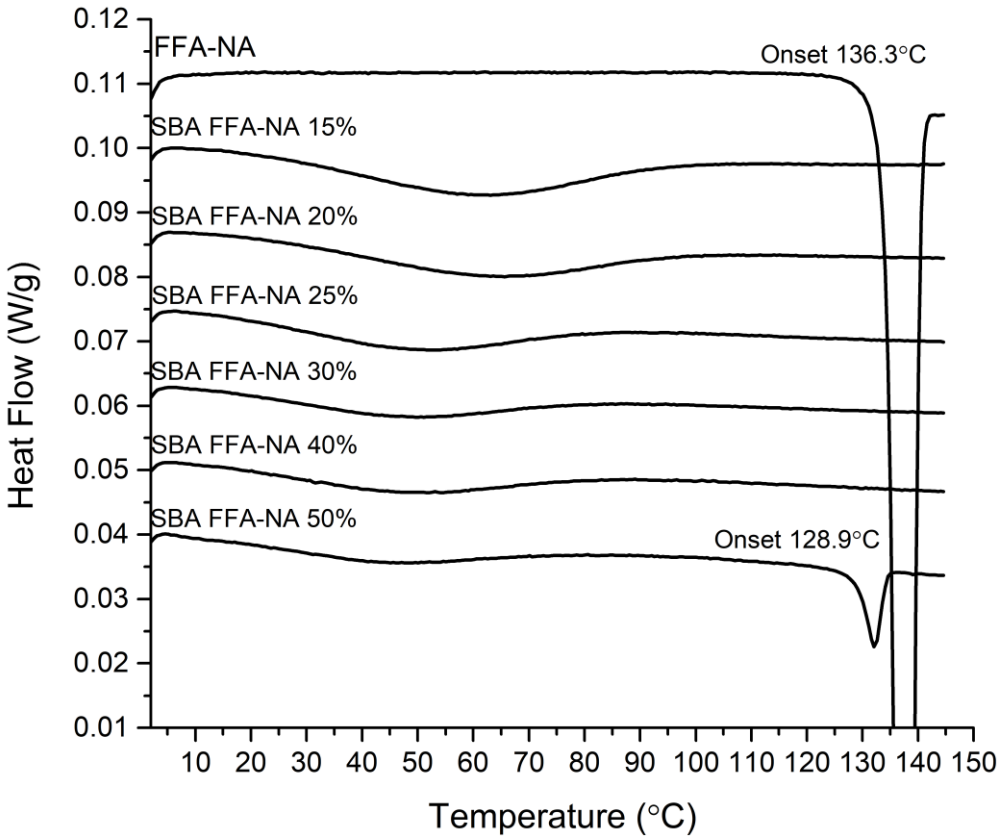

Figure 4-24 DSC thermogram of SBA-15 loaded with FFA-NA loading ratios (silica weight %/ FFA-NA weight).

This can also be seen in the PXRD data (Figure 4-25), where at the highest loading of 50% that are peaks that align with pure FFA/NA cocrystal. The other loadings of 40% and lower have a broad amorphous component consistent with SBA-15. These two techniques suggest that for this silica with larger pores, there is only a phase present at the highest FFA/NA loading ratio of 50 wt%.

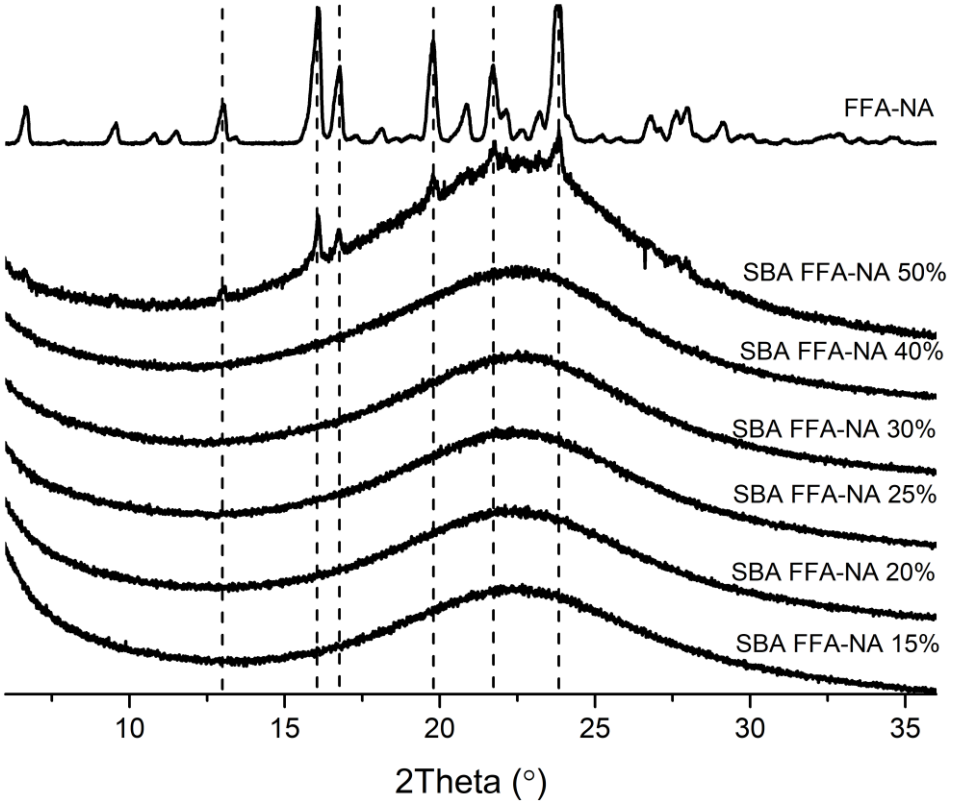

Figure 4-25 PXRD patterns of SBA-15 silica loaded with FFA/NA at various loading levels, host:guest (in wt%)

Turning to the results of nitrogen sorption (Table 4-3), SBA FFA/NA materials show a linear decrease of both BET surface area and calculated Pore Volumes with the increased loading level of FFA/NA. As the amount of loaded cocrystal is increased the available BET surface area decreases down to 20.4 m^2/g at 50% loading, but does not appear to go lower as in MCM-41 at 50% which had a BET surface area of around 5 m^2/g. Pore volume also follows the linear trend, declining from 0.707 to 0.072 cm^3/g. Pore diameter as calculated from BJH method also decreases upon loading level of FFA/NA increasing.

Table 4-3 BET surface area (calculated as a multi-point BET in the linear region of the isotherms) and Pore Volume (calculated at *P/P_0 of 0.99)*, Pore Diameters for SBA-15 calculated using the BJH method from the adsorption branch of the isotherm

Loading Ratio (% weight to SBA-15 weight)	BET Surface Area(m^2/g)	Total Pore Volume (cm^3/g)	Pore Diameter (nm)
0	442.1	0.707	7.64
15	316.9	0.549	7.10
20	271.9	0.472	6.64
25	235.2	0.399	6.64
30	209.7	0.339	5.64
40	105.9	0.174	5.64
50	20.4	0.072	5.26

TGA of the samples have confirmed that the loading ratios agreed with the initial amount of the FFA/NA guest. The sorption data implies that there is space available in the pores at loading below 40%, therefore the existence of aggregates and liquid-like forms is likely similarly to the case of MCM-41. At 50% loading it is difficult to say whether the pores are filled completely and the melting point is from a species inside pores of SBA-15 or whether the pores are completely filled yet the melting point is from material loaded outside the pores.

When the dimensions of SBA-15's pores are considered, the possibility of formation of crystalline FFA/NA material inside the pores becomes more realistic compared to MCM-41. SBA-15, having an average pore diameter of 6 nm, would allow for many molecules of FFA/NA to stack in the longitudinal direction of the pore network. When accounting for defects and connections to other pores within the SBA-15, there could be stacks of around 8-9 units of FFA/NA if the pore is presumed to be fully loaded with material. The pore diameter being the limiting factor of growth, however being double to size of the previous pore dimensions, shows that a sufficiently large cluster of FFA/NA could be physically arranged inside demonstrating the possibility of long-range order. However, this would also

assume a perfect, optimal arrangement of the molecules within the pore network, and such an arrangement would require enough lattice energy in order to hold together.

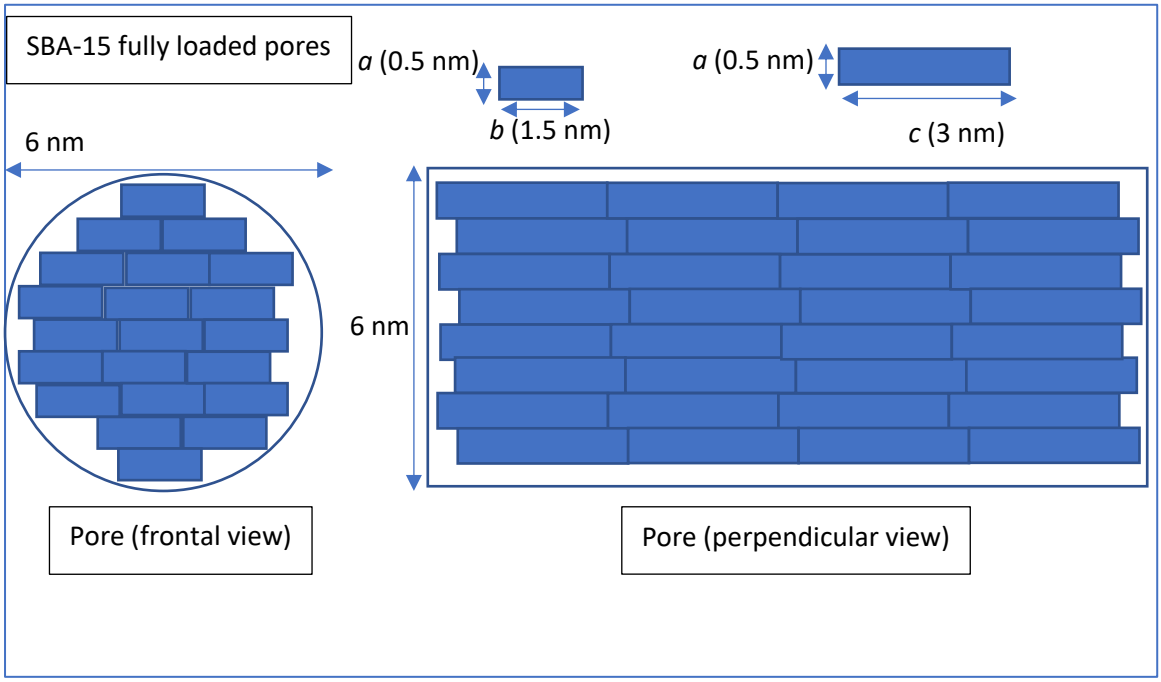

Figure 4-26 SBA-15 Fully Loaded Pore diagram of frontal and perpendicular view of pore space. Blue rectangles represent FFA/NA molecules to scale with the pore dimensions.

Unlike in MCM-41 where 30% loading resulted in space being created in the pore network, from both the DSC data and adsorption data we can assume that, in SBA-15, at 40% and lower loading ratios there is space for movement of FFA/NA molecules. The difference in behaviour between MCM-41 and SBA-15 is in the ability for more molecules of FFA/NA to stack and arrange themselves into a system that has a more order to it. The effective doubling of the diameter of the pores could also allow for stacking to occur along more than one plane. The possibility of rotating the molecules of FFA/NA (*abc* = 0.5 x 1.5 x 2.21 nm) such that the *ac* plane of the unit cell is perpendicular to the walls of the cell could occur. This would not allow many species to stack and fill the height of the pore, however from the movement that is implied at 40% loading and lower, means that any semblance of order could be disrupted should a small space form to allow rotation of FFA/NA molecules.

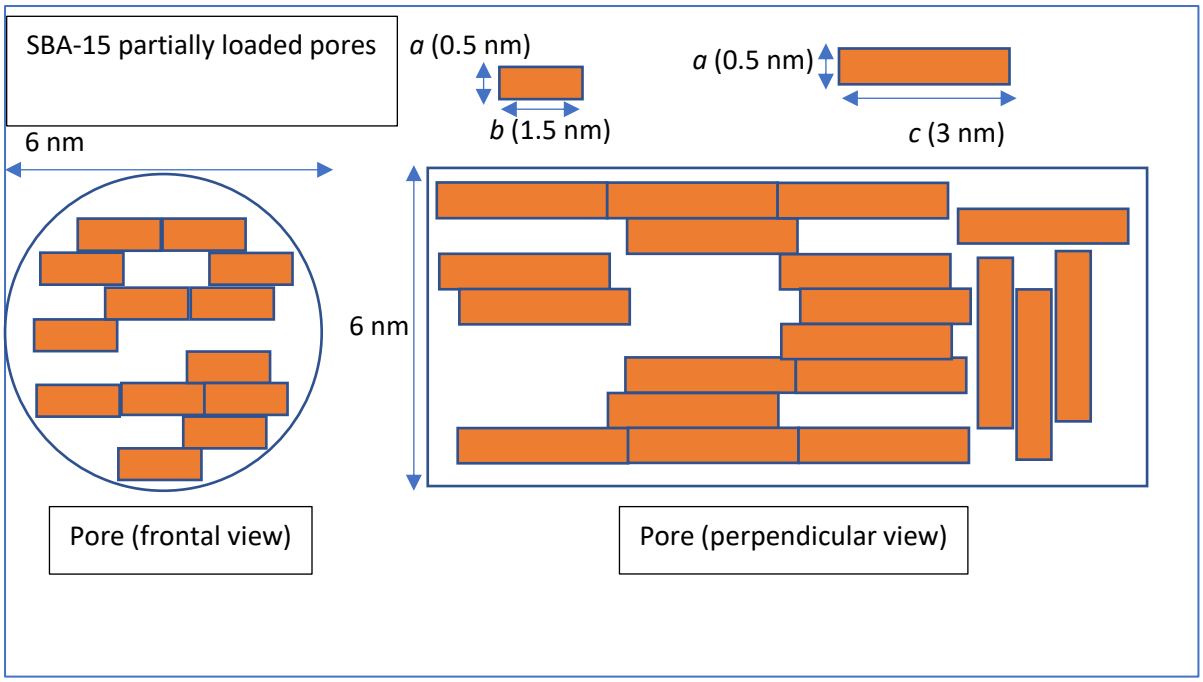

Figure 4-27 SBA-15 Partially loaded pore diagram of frontal and perpendicular view of pore space. Orange rectangles represent FFA/NA unit cells to scale with the pore dimensions.

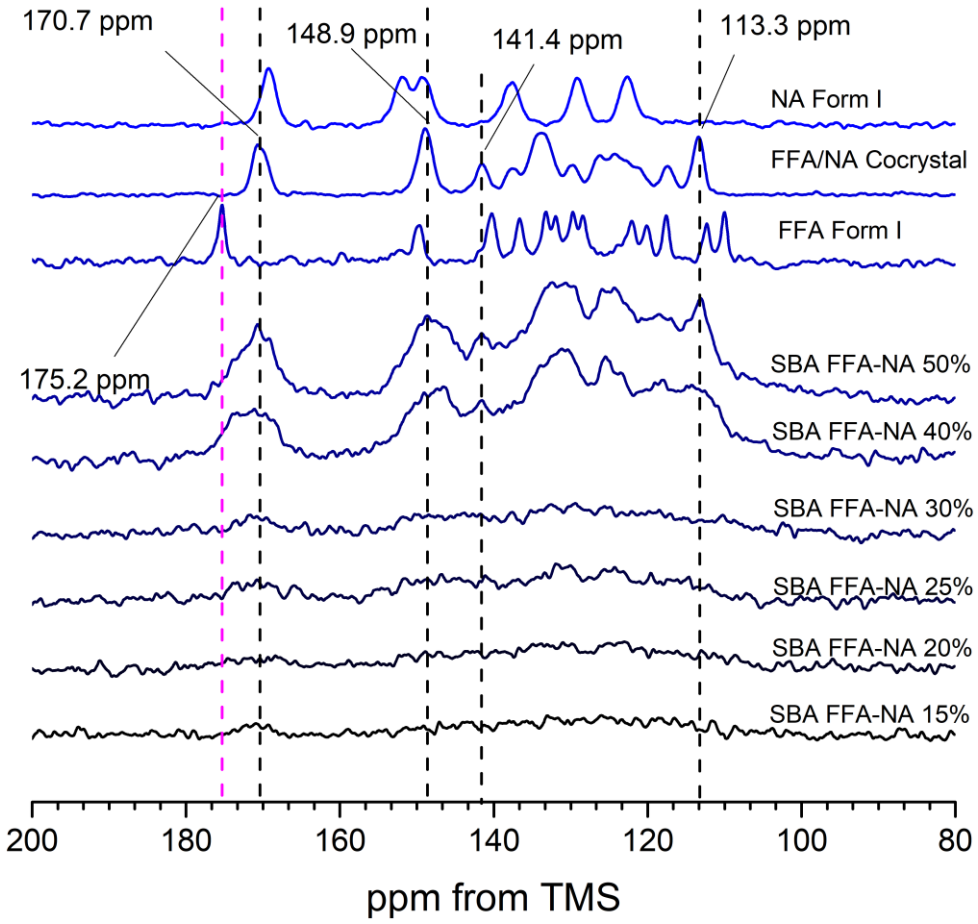

Figure 4-28 ^{1}H-^{13}C CP/MAS solid-state NMR spectra of SBA-15 loaded with FFA/NA cocrystal at 298 K at various loaded levels indicated by the percentage of loading in the legend

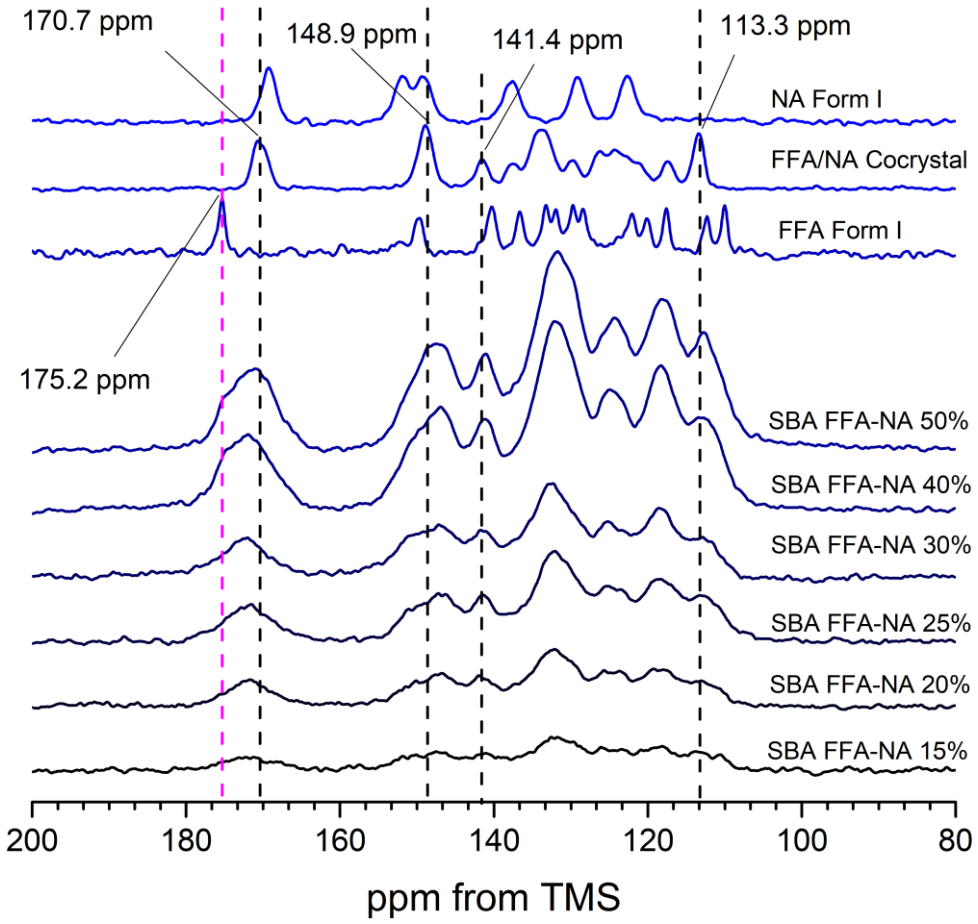

Figure 4-29 ^{1}H-^{13}C CP/MAS solid-state NMR spectra of SBA-15 loaded with FFA/NA cocrystal at 233 K at various loaded levels indicated by the percentage of loading in the legend

The ^{1}H-^{13}C CP/MAS NMR spectra of SBA-15-FFA/NA materials recorded at room temperature (Figure 4-28) show little to no intensity up to 30% loading. Freezing to 233 K (Figure 4-29) allowed us to detect the encapsulated material to be detected even at loadings of 15 wt.%. Comparatively the behaviour is like that of MCM-41 in terms of the temperatures and where the signal disappears. As before, when the loading ratio decreases it appears that arrangement of the molecules in the pores will begin to become less static due to space created and hence the decrease in CP intensity. Partial pockets and orientations of molecules will result in the forming and breaking of hydrogen bonding capable to sustain some order required to show a CP intensity. However, the results shown are that of the sum of the average of the entire pore of FFA/NA. The effect of cooling the system down will slow down the movement of the molecules, freezing any water in the system, but also creating the opportunity for more aggregated species to exist in the timeframe of our experiment hence be detected through CP transfer.

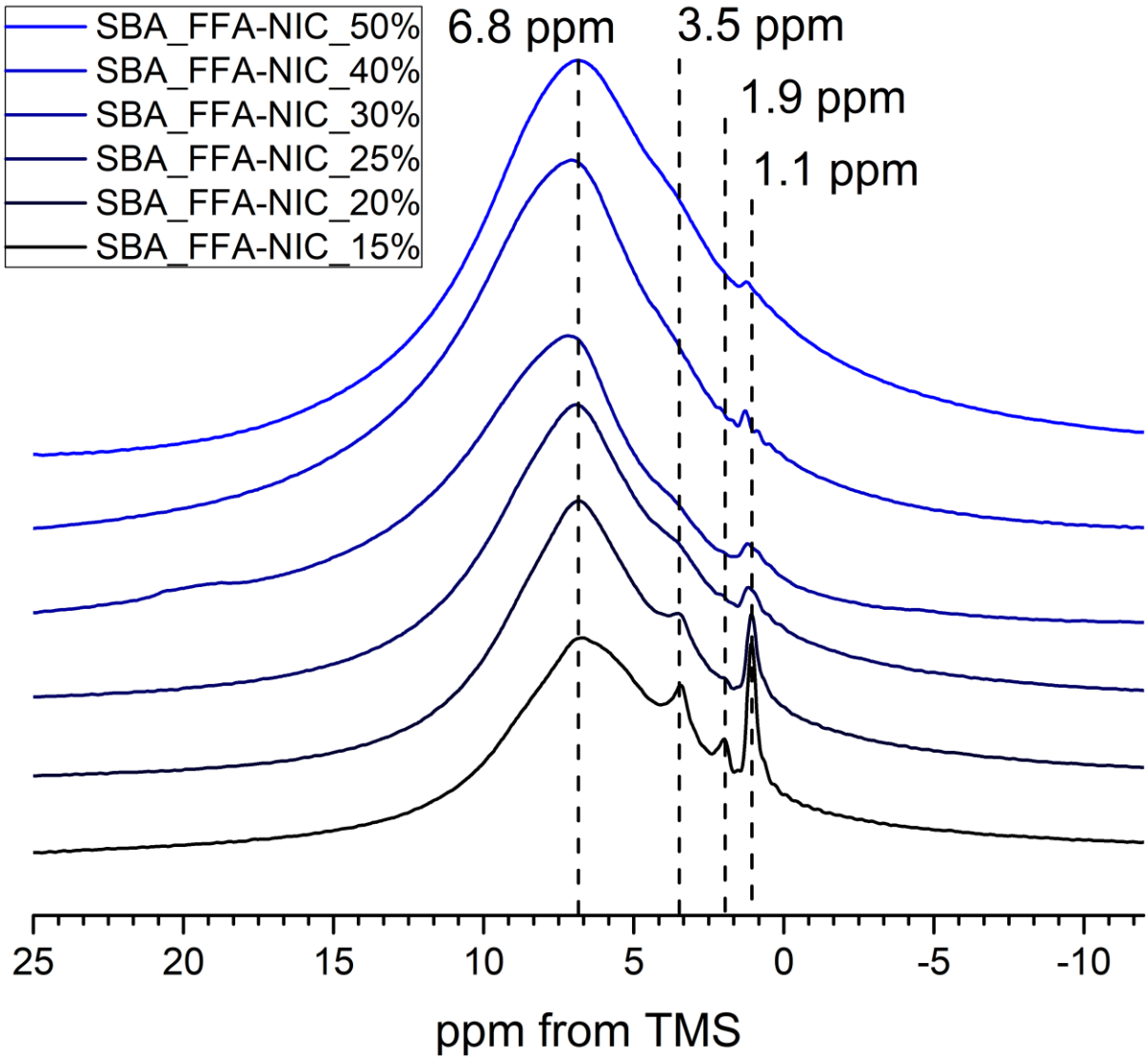

Figure 4-30 ^{1}H MAS solid-state NMR spectra of SBA-15 loaded with FFA/NA cocrystal at 298 K at various loaded levels indicated by the percentage of loading in the legend

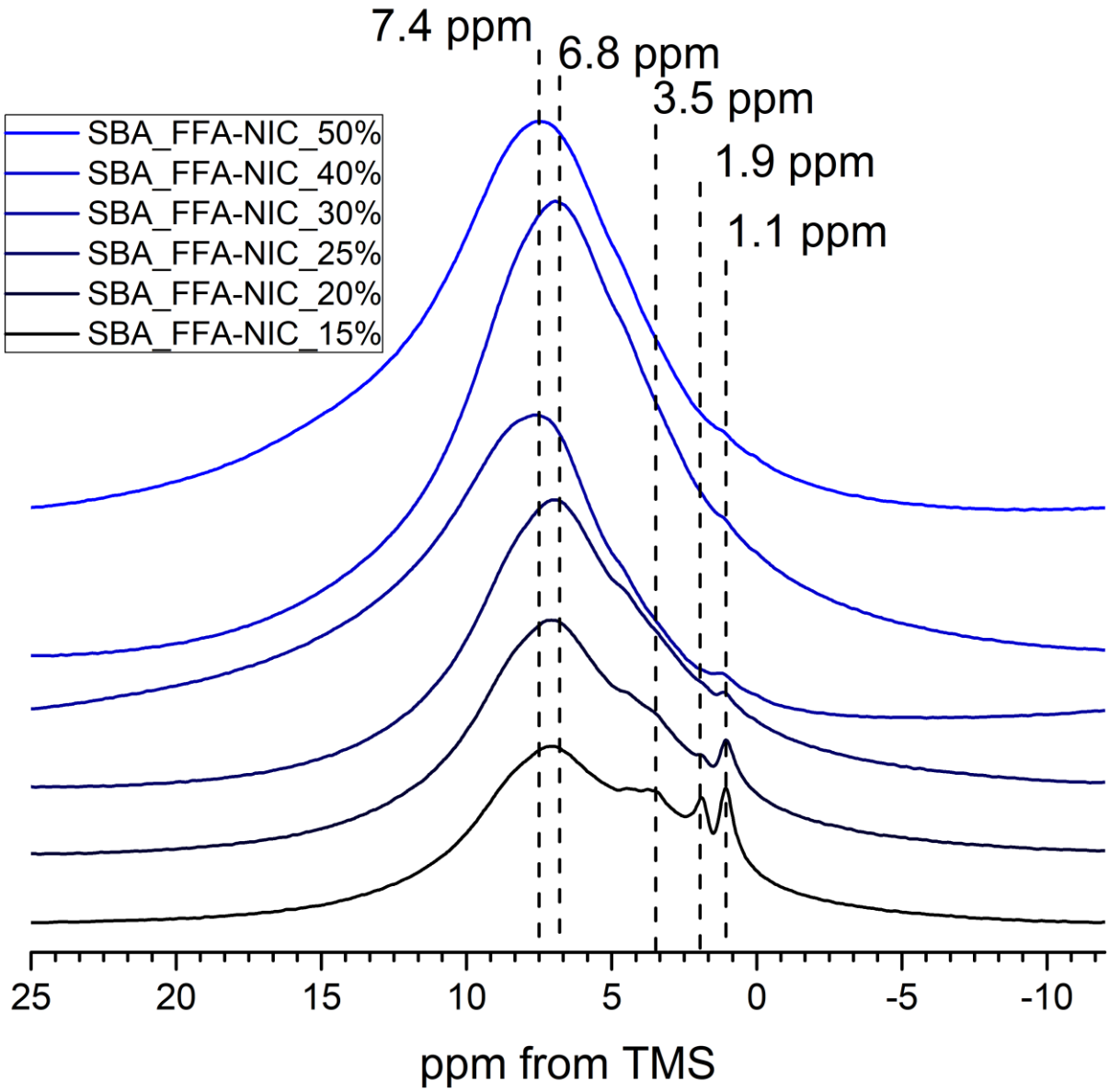

Figure 4-31 ^{1}H MAS solid-state NMR spectra of SBA-15 loaded with FFA/NA cocrystal at 223 K at various loaded levels indicated by the percentage of loading in the legend

^{1}H MAS NMR spectra of the SBA FFA-NA (room temperature Figure 4-30, low temperature Figure 4-31) series are very similar to those recorded for the MCM-41 series. The primary peaks at *ca.* 6 ppm are assigned to aromatic protons. As before, we can assume that the appearance of the peak roughly at 1 ppm is that of silanol protons on the surface SBA-15[129,132]. The peaks at 2 and 3.5 ppm are due to different hydrogen bonds with water at the surface of the silica walls as stated in the MCM-41 section (Figure 4-17). The same relationship appears apparent with SBA-15 with regards to these populations, as the loading ratio of FFA-NA is decreased these populations become a more prominent part of the

resulting spectrum. When considering completely emptied silica materials, MCM-41 in this case possesses over double the available BET surface area of SBA-15 (1079 vs 442 m^2/g). Therefore, the number of available silanol groups will be significantly higher in MCM-41 which is why a decrease in the overall intensity of those silanol groups is observed in SBA-15 loaded materials.

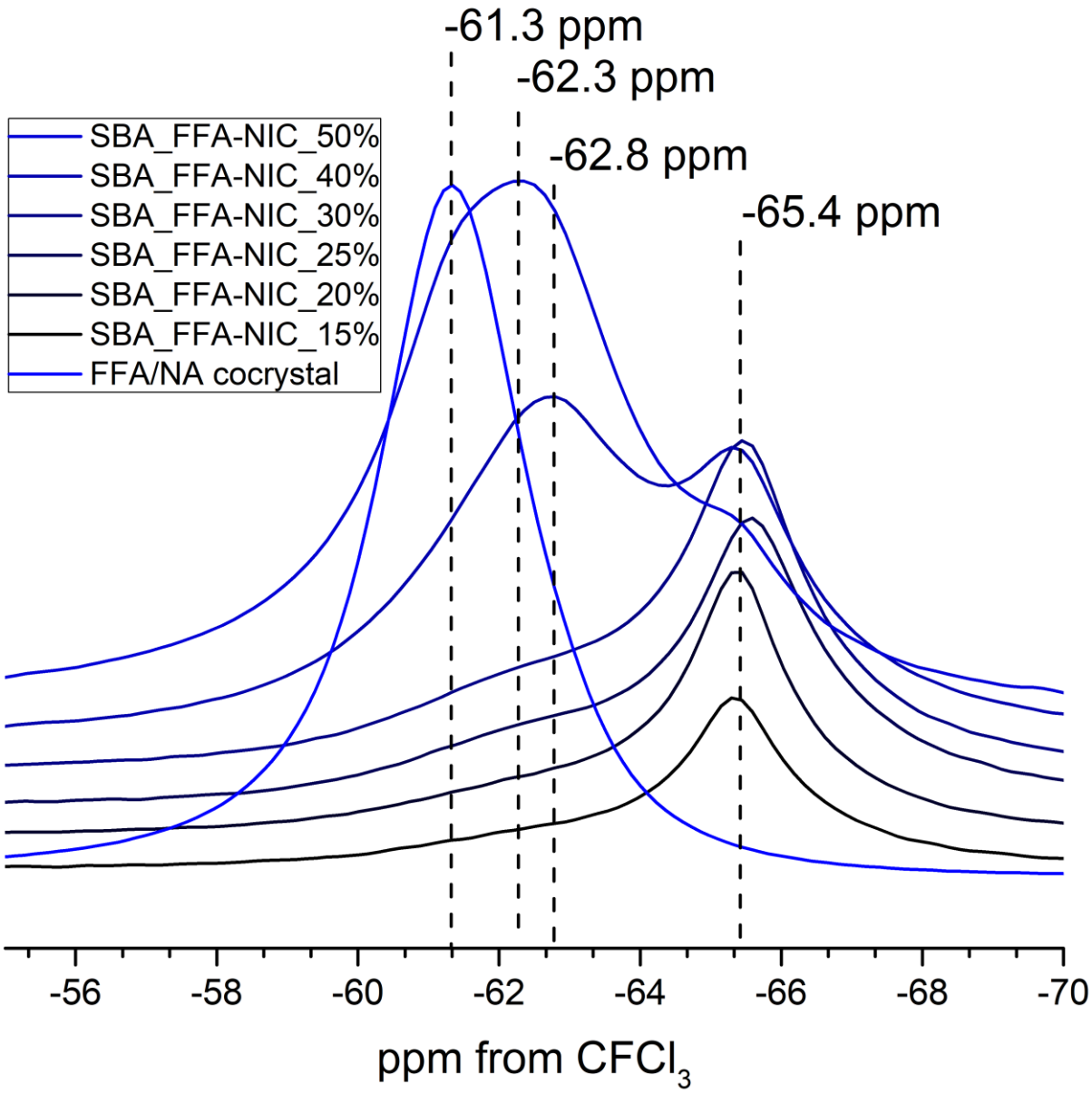

Figure 4-32 ^{19}F MAS solid-state NMR spectra of SBA-15 loaded with FFA/NA cocrystal at 298 K at various loaded levels indicated by the percentage of loading in the legend and pure FFA/NA cocrystal for comparison

^{19}F MAS NMR spectra of SBA FFA/NA at 9.4 T series show the presence of two populations of the CF_3 group at room temperature (Figure 4-32). The population represented by a peak at -62.3 ppm is

observed in the materials with the high loading of FFA/NA. The other population at-65.4 ppm dominates the spectra of the materials with loading level below 30 wt%.

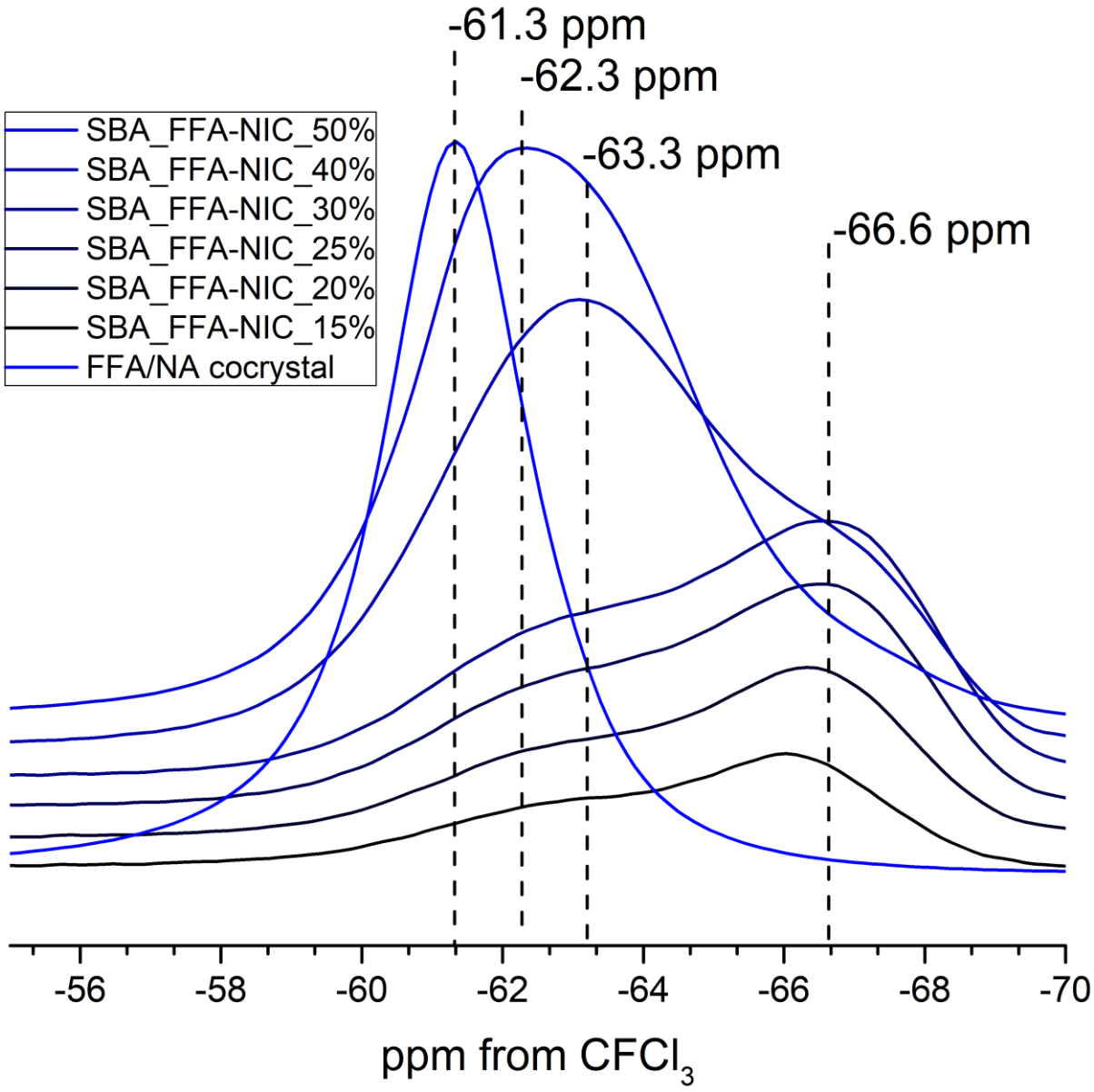

Figure 4-33 ^{19}F MAS solid-state NMR spectra of SBA-15 loaded with FFA/NA cocrystal at 223 K at various loaded levels indicated by the percentage of loading in the legend and pure FFA/NA cocrystal for comparison

The ^{19}F chemical shift of -62.3 ppm does not directly match that of pure FFA/NA cocrystal which is slightly downfield at 61.3 ppm. However, the peak at -62.3 ppm most likely does belong to a form of FFA/NA when the PXRD is consulted (Figure 4-25), peaks matching the FFA/NA are present at the

highest loading of 50%. As in MCM-41 even though the peak at -62.3 ppm is similar to that of FFA form III, it most likely does not belong to that form as there is no evidence of it in the PXRD diffraction pattern at 50% loading. The implication is similar to that of MCM-41 in that there has been an increase in the disorder of FFA/NA inside SBA-15, associated with the downfield shift in the peak centre. As the loading ratio decreases further to 30% it can be seen that the intensity of this population at -62 ppm has decreased significantly. A shoulder is still present, but the population at -65 ppm dominates the spectrum. This trend continues as the loading ratio is decreased further with intensity falling off as the loading ratio decreases to 15%. Also as seen in the low temperature data of MCM-41, a similar trend of broadening occurs on all populations and is very apparent on the 50-40% loading ratios. The effect of freezing is present, which is causing less movement of material within the pores. The shoulders present in 30-15% loading are much more pronounced, implying that the population of aggregated FFA/NA is larger at lower temperatures which would make sense due to material being able to attach to one other due to less mobility in the system. The population at -65 ppm is still present however, when compared to room temperature is much broader.

^{19}F MAS spectra of the samples were recorded at 19.94 T, and also at higher MAS rate (Figure 4-34). This resulted in much better resolution of the population at -62.2 ppm, as a peak at -60.9 ppm can be detected. The latter peak can be ascribed to FFA/NA material that is most likely located outside the pores of SBA-15 host when loaded at 50% loading ratio. From the adsorption data, it is known that at 50% loading level there is little to no pore volume left in order to pack material into the pore (S_{BET} = 20.4 m^2/g and V_{total} = 0.072 cm^3/g).

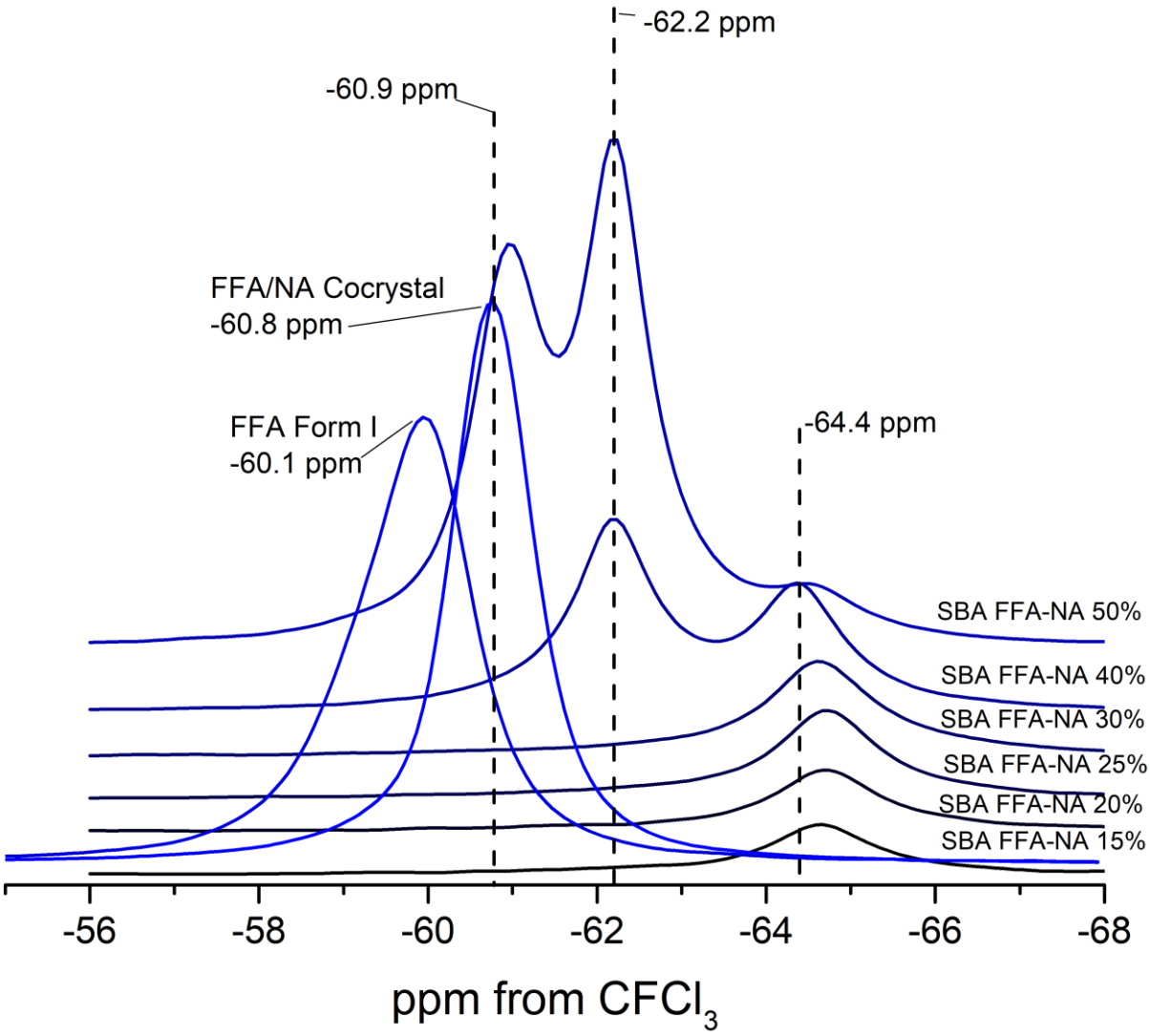

Figure 4-34 High field ^{19}F MAS NMR spectra of SBA-FFA/NA composites recorded at 19.94 T and 35 KHz MAS rate. Samples are labelled according to their host:guest ratio (in %weight). Pure sample of FFA/NA cocrystal and FFA form I have been added for comparison

The spectra with lower level of loading (Figure 4-34) than 50% show to peaks at -62.2 ppm and -64.4 ppm, the former disappearing to a small shoulder when the loading ratio is dropped to 30%. When considering the decrease in FFA/NA material and then the increase in the amount of pore volume to be filled, we can attribute the loss of the -62.2 ppm population as being to be the loss of volume of material that would allow some aggregates of FFA/NA to exist inside the pores. Primarily the FFA/NA material at lower ratios would instead be more liquid-like and coating the walls of the pores, which corresponds to the population at -64.4 ppm.

A lot of the conclusions that have been drawn thus far suggest to the existence of different species of FFA/NA inside SBA. These species vary in their population depending on the loading level. However,

we have not shown that these species exist within the same area of the pore space, mainly that they exist discretely as an averaged-out sample of data. Therefore, we decided to use a ^{19}F-^{19}F NOESY 2D NMR experiment in order to probe whether these species are close enough in space to exchange magnetisation. Any interactions between the populations that generate a ^{19}F-^{19}F crosspeak would indicate the species are exchanging magnetisation with each other at a space of 3 Å or less. In order to average out the dipolar interactions further this NOESY was performed in a 1.3 mm probe spinning at 55 KHz. Due to time constraints only one sample in this series was studied. The sample we chose was SBA loaded at 40% with FFA/NA. This was because at 50% loading SBA possessed FFA/NA material that was located outside the pore space. The sample at 40% loading, from our previous data at 35 KHz MAS rate (Figure 4-34) had the highest intensity of the two peaks at -62.2 ppm and -64.5 ppm as evidenced in the Figure 4-35. The effect of faster MAS rate serves to sharpen the individual peaks due to the reduction in dipolar couplings.

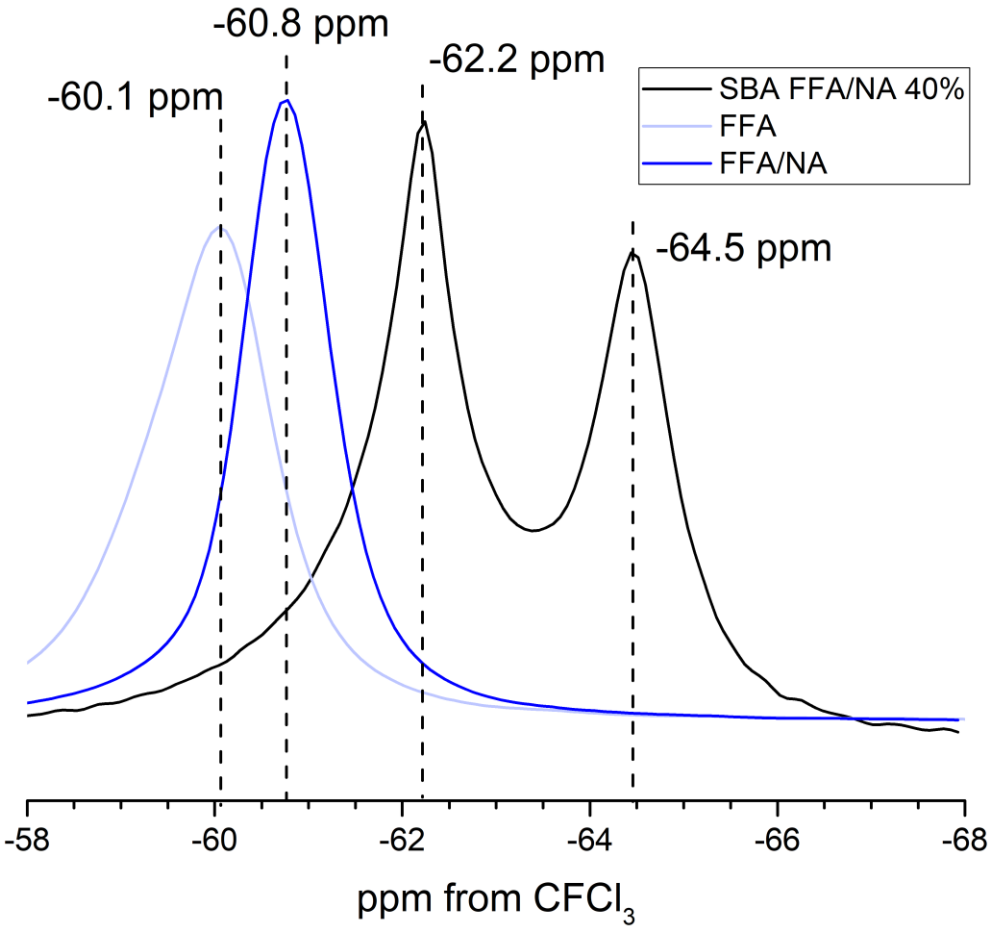

Figure 4-35 ^{19}F spectra of SBA-15 loaded with FFA/NA at 40% acquired at 19.96 T at an MAS rate of 55 KHz, compared to FFA form I and pure FFA/NA cocrystal.

Figure (4-36) shows the NOESY spectra recorded of the 40% loaded sample at multiple mixing times from 50 ms to 150 ms. In the diagonal populations at -62.2 and -64.5 ppm are present their relevant cross-peaks are also present. It can be seen that with the increasing the mixing time from 50 ms to 100 ms the intensity of the crosspeak increases massively, after which the intensity then falls at 150 ms. The initial increase in intensity is most likely due to the length of time the two species are allowed to exchange magnetisation being increased. The subsequent falloff in the intensity at 150 ms would then maybe be due to more relaxation mechanisms coming into effect. Prior to the NOESY data it was assumed that the species seen at -62.2 and -64.5 ppm within the sample were macroscopic representation of the entire collection of FFA/NA molecules inside the pores of SBA. The fact that there is a crosspeak linking both populations, within a narrow spectral window, means that both species must be within the same space as each other as the exchange of magnetisation crosspeaks indicate that they must be within 3 Å of each other.

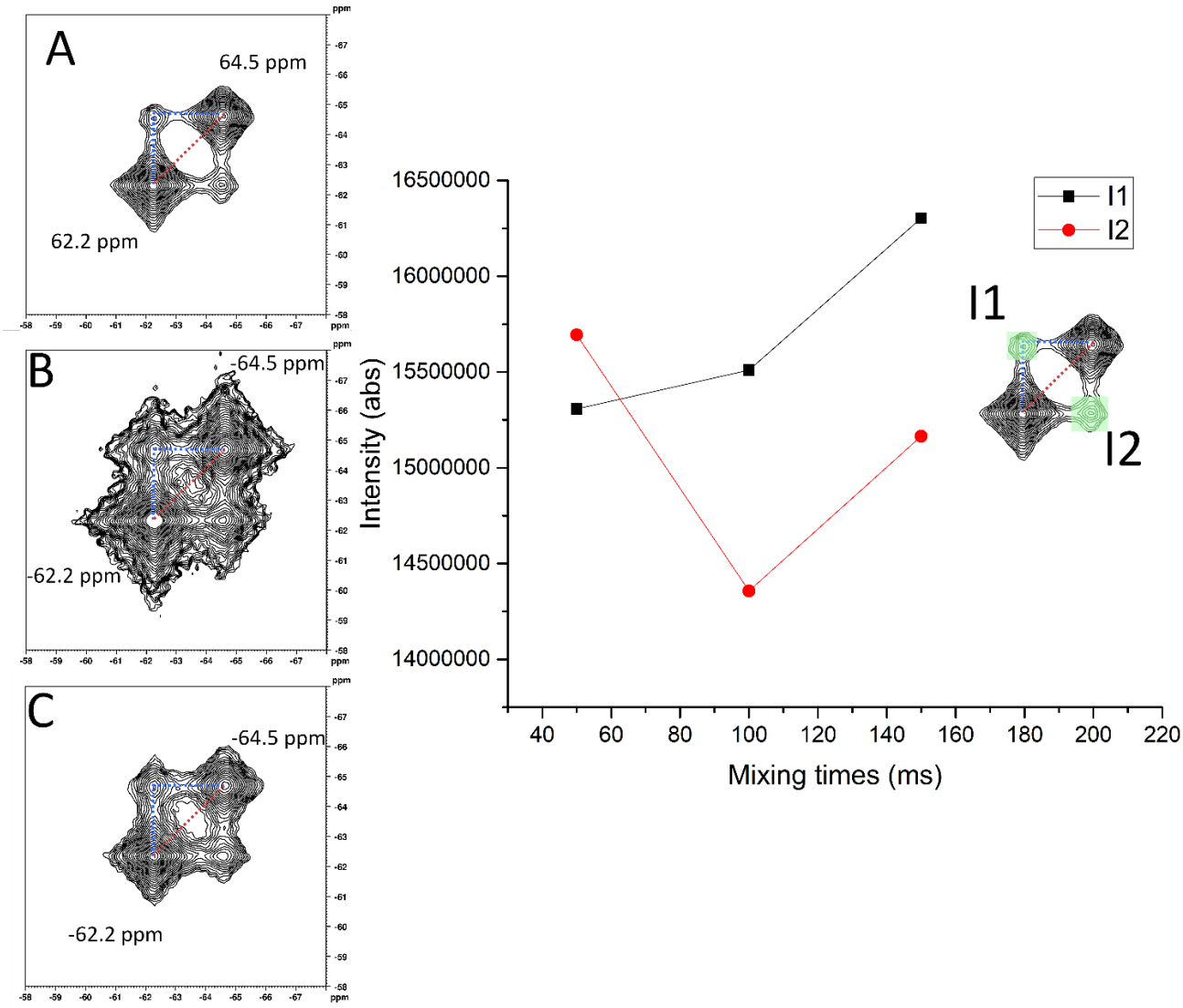

Figure 4-36 ^{19}F-^{19}F NOESY spectrum of SBA-15 loaded with FFA/NA at 40% with various mixing times; **A.** 50 ms, **B**. 100 ms, **C.** 150 ms. Spectra acquired at 19.96 T at a MAS rate of 55 KHz. Absolute integrations are shown on the right with regions I1 and I2 for the three mixing times.

From these data the assumptions that have been made regarding the state of the FFA/NA within the pores can be legitimised further. The pores of SBA-15 are able to be overloaded with FFA/NA material that is located outside of the SBA-15 particles, this occurs at 50% loading. At 40% loading there are two distinct species of FFA/NA within SBA-15. Of these two species one is more mobile than the other as we have shown the influence of temperature on these species. Considering the space inside the pore, the presence of amorphous aggregate would be most likely over something crystalline in nature. The second species is present in all SBA-15 samples made, most likely located as a liquid-like species along the walls of the internal pore network. The two species present inside the pore network are able

to interact with each other therefore they are in the same pore space and not located in different parts of the SBA-15 particles separate from each other. As in MCM-41 temperature changes the ratios of populations due to the freezing effect of mobility of the FFA/NA within the SBA-15 particles.

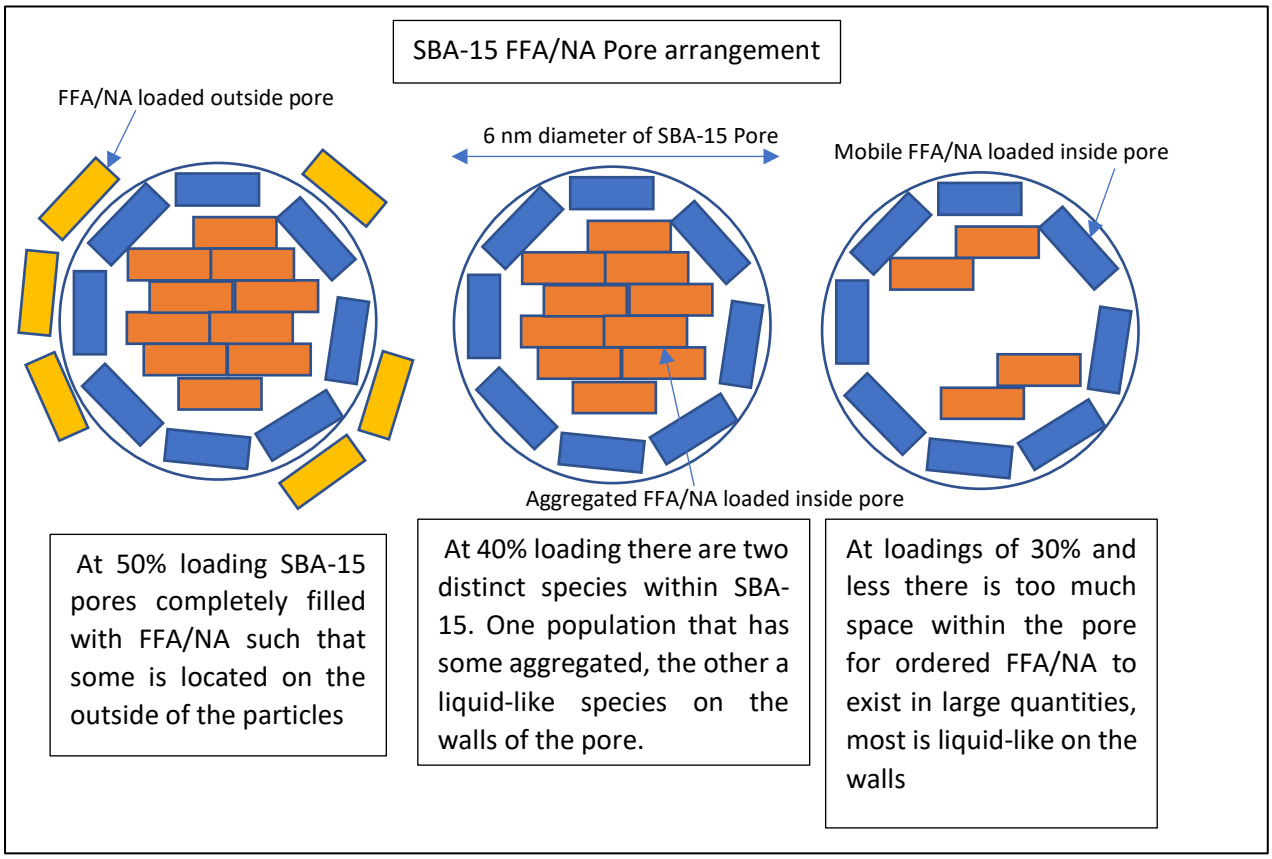

Figure 4-37 Pore arrangement hypothesis of FFA/NA in SBA-15 at fully loaded and partially loaded ratios

4.5 Incorporation of FFA/NA into MCF mesoporous silica

The third silica chosen for loading of FFA/NA was MCF. These particles have a different pore structure to that of MCM-41 and SBA-15. While MCM-41 and SBA-15 have defined cylindrical pores of constant diameter and shape, MCF is a network comprised of smaller windows that lead to larger internal pores. There are several variants of MCF that can be synthesised which allow for tuning the size of the windows and internal pore. The chosen material we have has windows of around 14 nm and internal pores of around 26 nm as calculated using the BJH method[50,115] (adsorption branch for internal pore, desorption branch for windows). A much larger pore diameter than that of MCM-41 and SBA-15 would hypothetically allow MCF to host many more molecules of FFA/NA to stack within the pore.

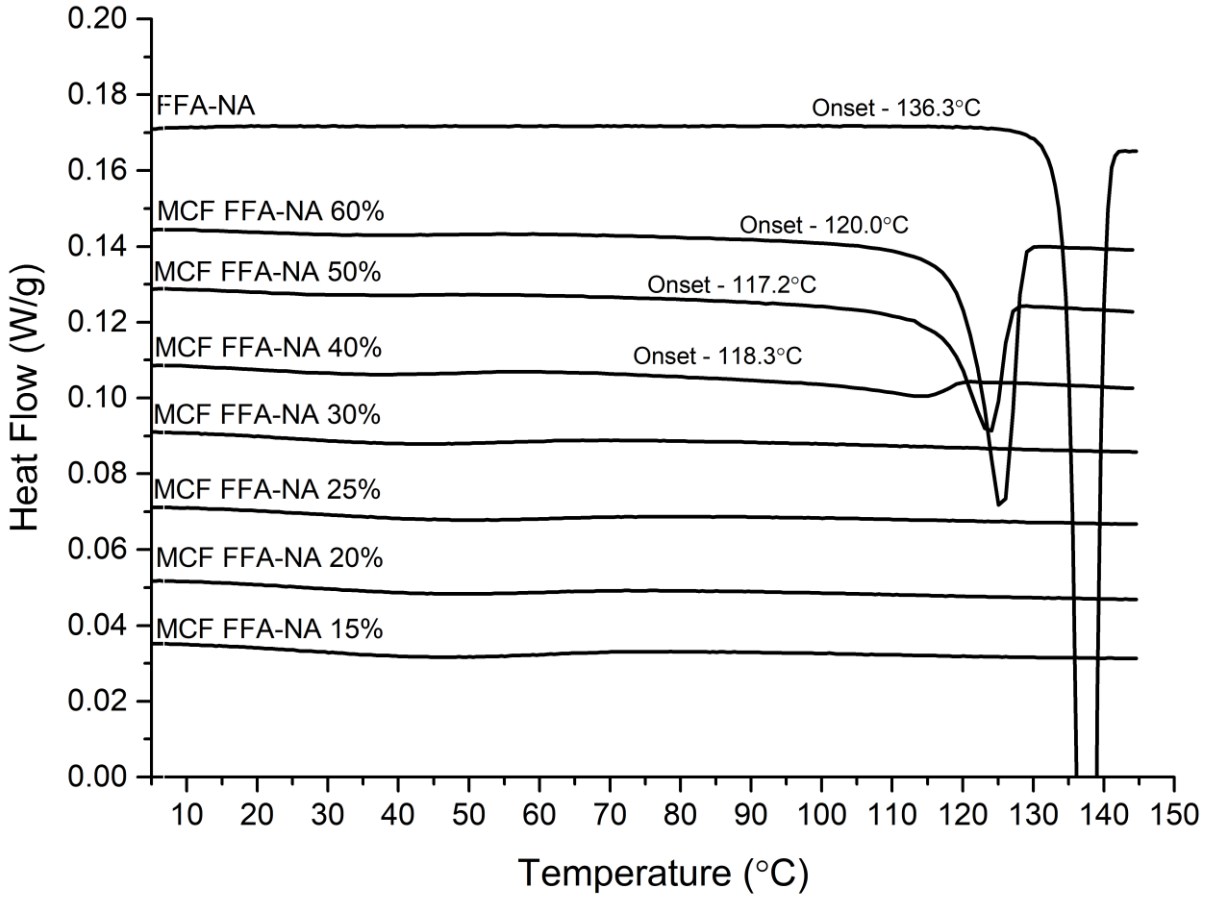

Figure 4-38 DSC thermogram of MCF loaded with FFA-NA loading ratios (silica weight %/ FFA-NA weight).

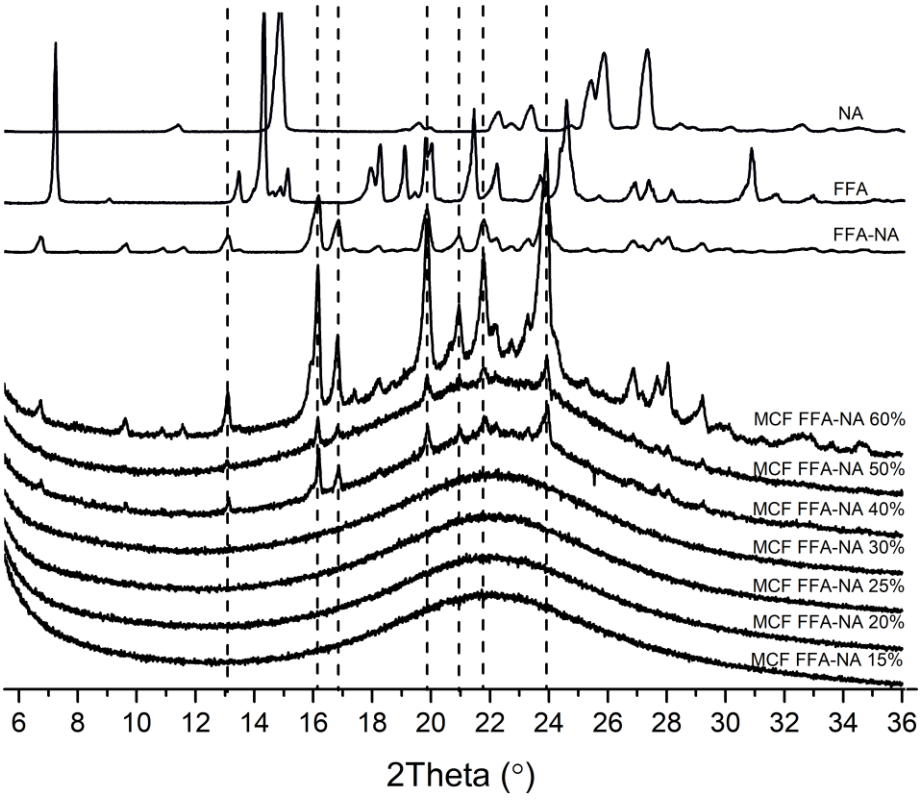

Figure 4-39 PXRD patterns of MCF silica loaded with FFA/NA at various loading levels, host:guest (in wt%)

As in previous DSC data there a depression in the melting point of the material inside the pores. Pure FFA/NA material for comparison can be seen to melt at 136.3°C, at the highest loading of 50% the onset melting point has dropped to 117.2°C and as the loading ratio is decreased to 40% there is a small onset that is difficult to see in the baseline, however a small peak temperature can be isolated at around 115°C. The shift of the melting point and the broadening of the melting peaks imply that the quantity of macroscopic crystalline material is decreasing. No enthalpic events are observed for MCF-FFA/NA < 30%, confirming the loss of long-range order.

These results can be corroborated by the PXRD patterns. The diffraction patterns of MCF-FFA/NA-40 and MCF-FFA/NA-50 show peaks that match with pure FFA/NA cocrystal. This confirms that melt-loading resulted in the formation of cocrystalline FFA/NA in the pores rather than separate crystalline FFA or NA. There is a heavy background present in the PXRD patterns that comes as a result of the MCF material.

Comparatively MCF has a similar surface area to that of SBA however the overall pore volume is double that of both SBA and MCM. As shown previously there is a mostly linear relationship between the various loading ratios, however, the main difference is that at the highest level of loading there is still

some surface area accessible and unoccupied pore volume. Therefore, we can imply that unlike at 50% loading in SBA and MCM, where the pores were completely filled and there is most likely some FFA/NA material coated on the outside of the individual silica particles, 50% loading in MCF has not completely filled the pores with material.

Table 4-4 BET surface area (calculated as a multi-point BET in the linear region of the isotherms) and Pore Volume (calculated at P/P_0 *of 0.99)*, Pore Diameters for internal for MCF calculated using the BJH method from the adsorption branch of the isotherm, values in brackets indicate the pore windows calculated using BJH method from the desorption branch of the isotherm

Loading Ratio (% weight to MCF weight)	**BET Surface Area(m^2/g)**	**Total Pore Volume (cm^3/g)**	**Pore Diameter (nm)**
0	433.2	1.660	29.508 (13.957)
15	303.6	1.524	23.936 (13.154)
20	299.9	1.489	23.7914 (13.153)
25	294.7	1.457	24.0484 (11.385)
30	263.5	1.305	23.858 (11.351)
40	192.9	0.961	26.082 (11.126)
50	159.5	0.783	23.265 (11.701)

When the size of the internal pore of MCF is considered, there is a significant increase in the pore diameter which in turn allows for a greater number of FFA/NA units to be able to stack and arrange into a moiety which possesses the long-range order that could be expected of a crystalline material. The Figure below shows a schematic representation of the possibility of stacking those cells within the internal pore of MCF. When only considering the internal pores (not the windows to these pores) it is possible to stack about 50 units of FFA/NA at the longest point of the cylindrical pore. This is assuming perfect orientation and filling of pore such that the *a* direction of the cell is perpendicular to the diameter of the pore. The filling of pores at levels of 40-50% loading of FFA/NA would be predicted as in MCM and SBA to take on a similar arrangement of filling, however there may still be some space left in the pore for movement in between pores via the windows present in MCF.

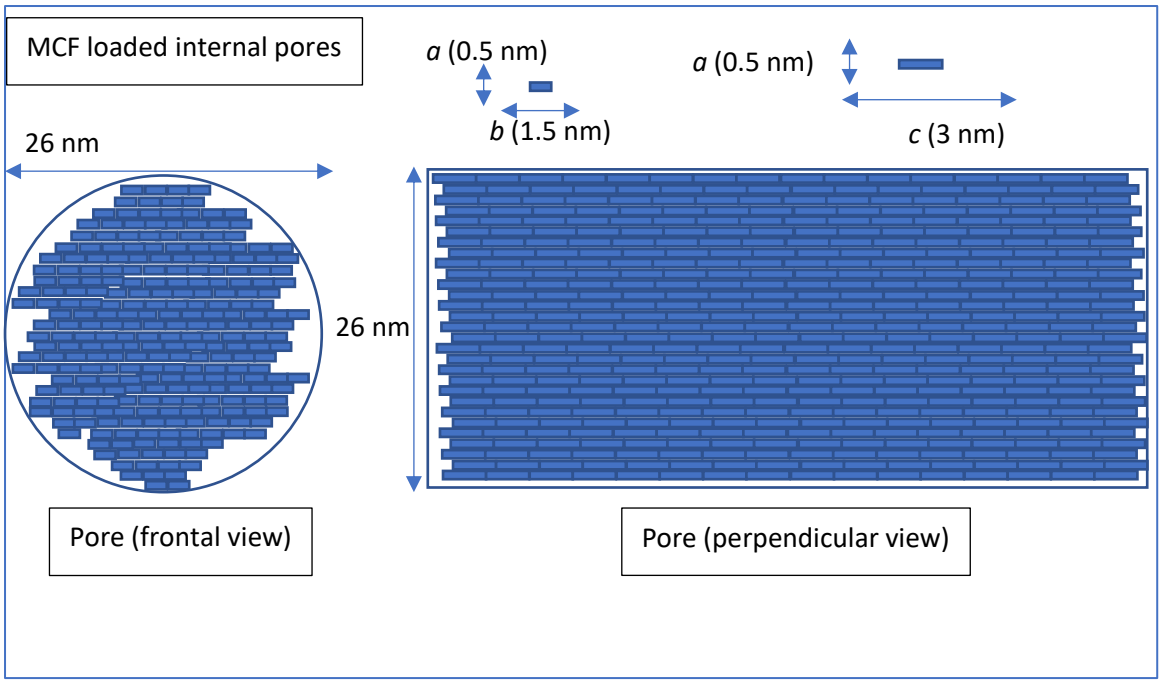

Figure 4-40 MCF Fully Loaded Pore diagram of frontal and perpendicular view of pore space. Blue rectangles represent FFA/NA unit cells to scale with the pore dimensions.

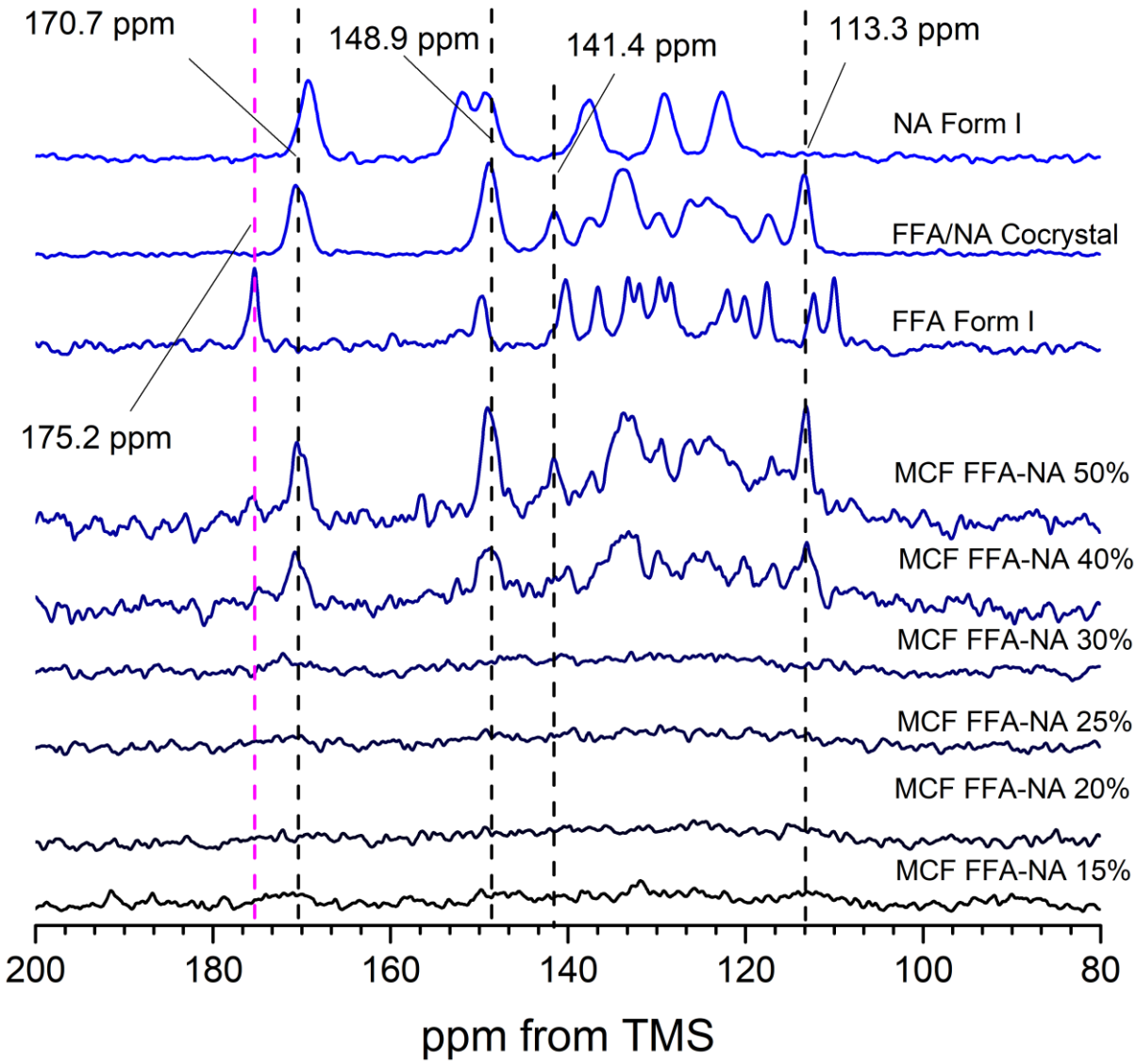

Figure 4-41 ^{1}H-^{13}C CP/MAS solid-state NMR spectra of MCF loaded with FFA/NA cocrystal at 298 K at various loaded levels indicated by the percentage of loading in the legend

From the ^{1}H-^{13}C CP/MAS NMR spectra (Figure 4-41) there is a distinct similarity at 298 K (room temperature) to the spectra of loaded MCM-41 and SBA-15. The spectra of the materials with loading ratios of 50 and 40% show some peaks that can be associated with FFA/NA, for example the peak at 170.7, 148.9 and113.3 ppm – all of which clearly are present at 50-40% loading. As the loading ratio drops to 30% there is a clear loss of any discernible signal above the background.

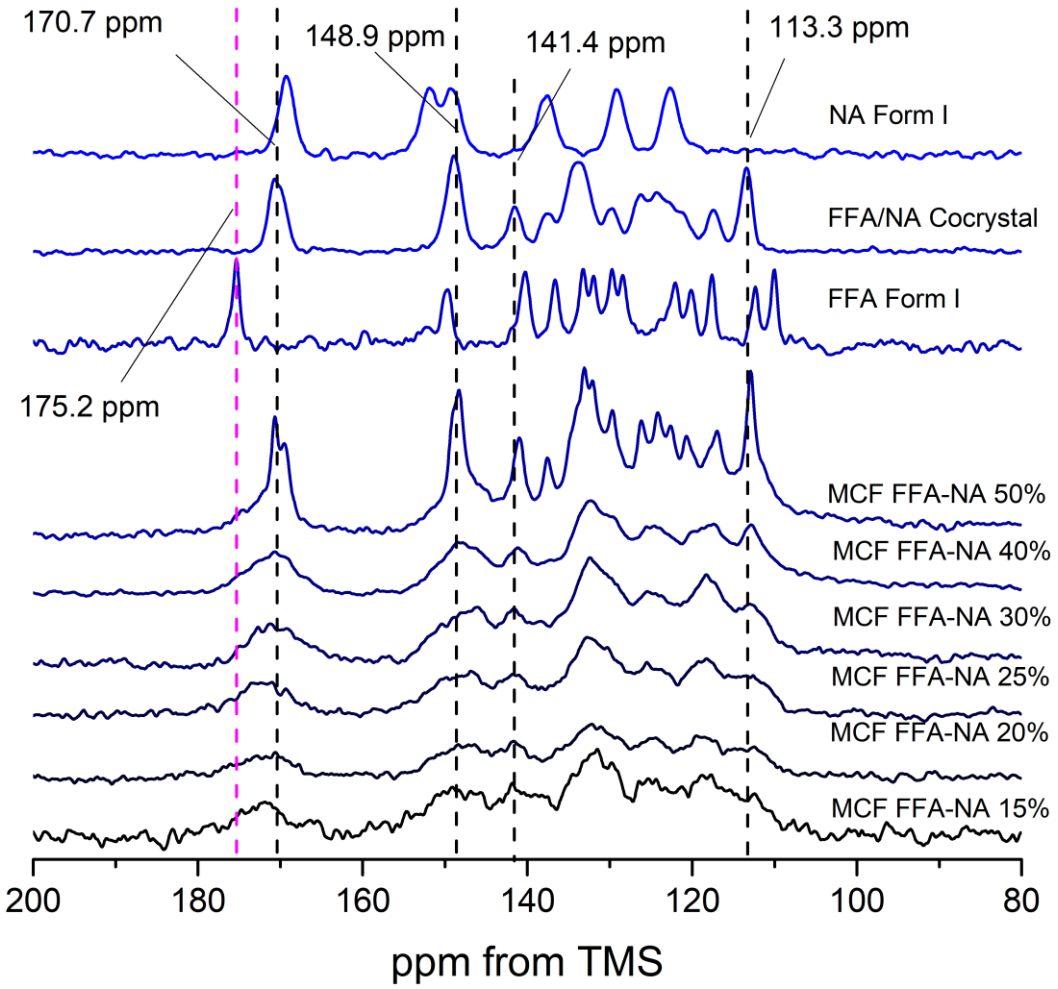

Figure 4-42 ^{1}H-^{13}C CP/MAS solid-state NMR spectra of MCF loaded with FFA/NA cocrystal at 233 K at various loaded levels indicated by the percentage of loading in the legend

As shown before, the effect of lowering the temperature greatly enhances the signal from each sample (Figure 4-42). However, at 50% loading the signal is clearly much more defined than of any other sample, both when compared to other loading ratios of MCF and when compared to the other silica when loaded at 50%. When the samples are cooled there is a significant increase in signal at all loading levels. This is due to the process of CP requiring rigid bonds to allow transfer of polarisation from proton to carbon. The high mobility at room temperature makes this transfer less effective, and lowering the temperature greatly reduces the mobility of the system to allow for the more effective mechanism of polarisation transfer to occur. The broadness of the peaks will be due to the more conformations of FFA/NA being locked into place and therefore producing a broader signal from the greater range of chemical shift for each carbon atom.

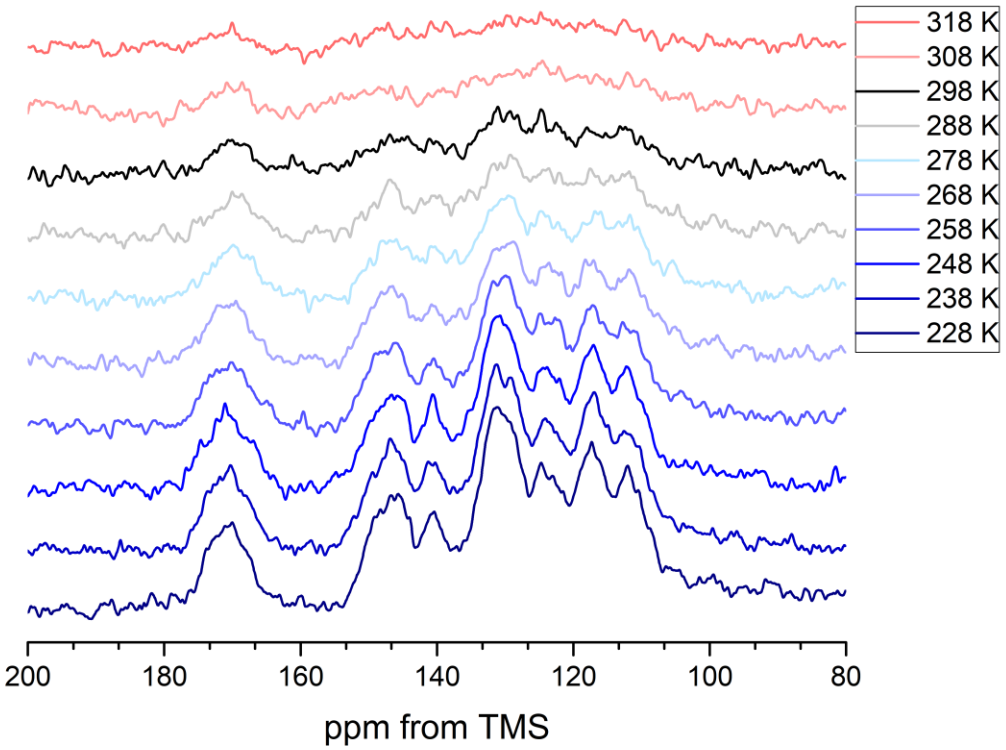

Figure 4-43 ^{1}H-^{13}C CP/MAS solid-state NMR spectra of MCF loaded with FFA/NA cocrystal at 35% loading over variable temperatures (228-318 K)

Based on the ^{1}H-^{13}C CP/MAS NMR data for MCF-FFA/NA materials with different levels of loading, it had become apparent that materials with 30-40 % loading ratio featured some long-range order. We have studied the effect of temperature on the appearance of the spectra for MCFFFA/NA at 35% loading in the range of 228-318 K (Figure 4-43). As expected, as the sample is cooled from room temperature, there is a gradual increase in the intensity of the peaks, until all the carbon environments are defined at *ca*. 248 K. Further cooling results in slight narrowing of the broad peaks, which can be observed most at the peak at 170 ppm. Upon heating the sample to 318 K, small peaks that were present just above the baseline at 170 ppm are mostly eliminated into noise. This further validates the hypothesis of high mobility of FFA/NA material within the pores. As the sample is heated the ability for molecules of FFA/NA to move and break apart increases, therefore the rigid network of bonds to allow for efficient CP and the long-range order associated are disrupted. The sample was not heated beyond 318 K due to the technical limitations of the probe and rotor being used.

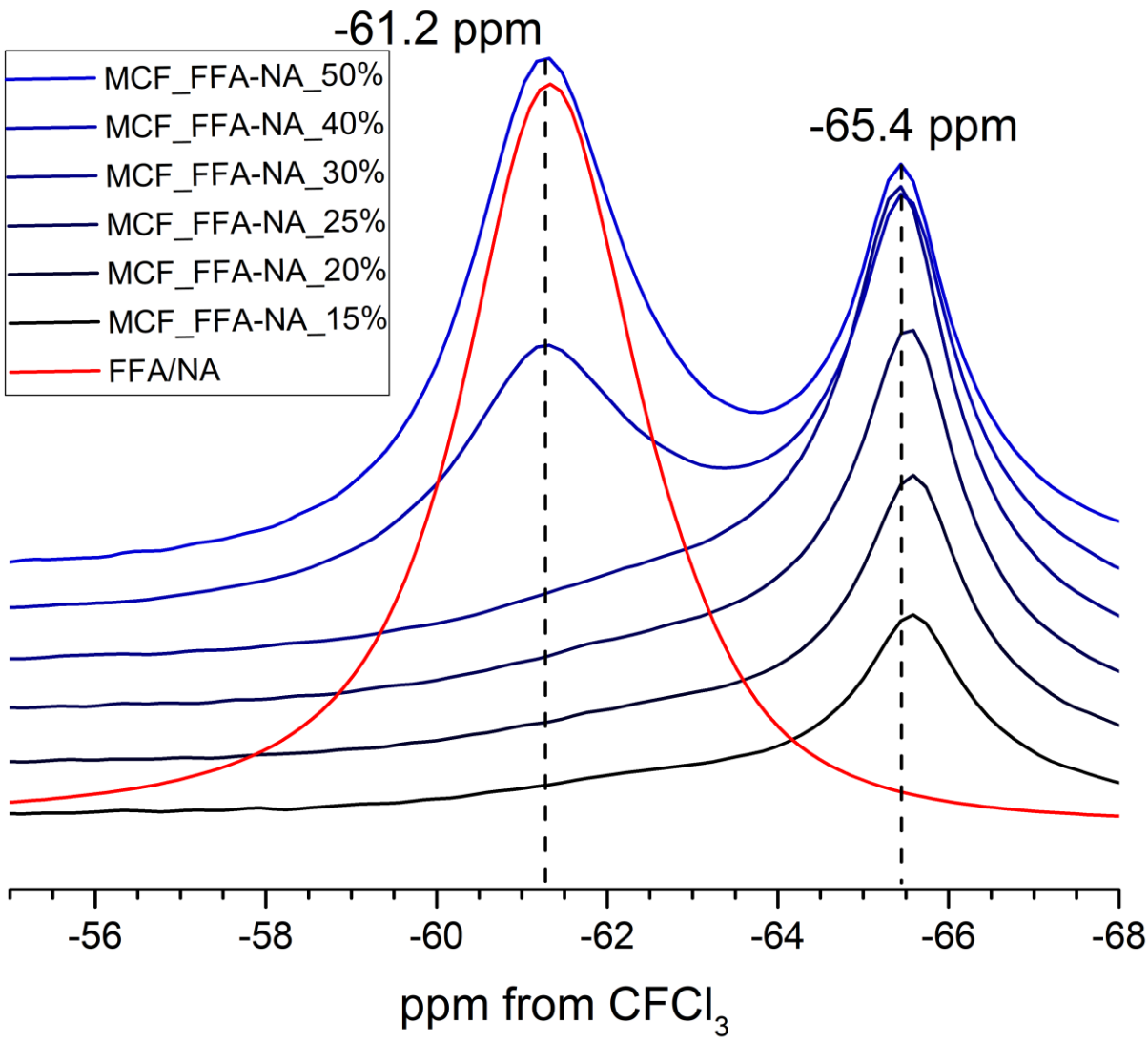

Figure 4-44 $^{19}F\{^{1}H\}$ MAS solid-state NMR spectra of MCF loaded with FFA/NA cocrystal at 298 K at various loaded levels indicated by the percentage of loading in the legend and pure FFA/NA cocrystal for comparison

^{19}F MAS NMR spectra for MCF loaded with FFA/NA at different ratios (Figure 4-44) at 9.4 T are similar to those of SBA-15 composites. MCF with FFA/NA at 50 and 40% show the presence of two ^{19}F populations at -61.2 and at -65.4 ppm. The peak present at -61.2 ppm does appear to match that of pure FFA/NA cocrystal, implying that at loading levels of 40% and greater there is a crystalline component present. As the loading ratio decreases to 30% the population at -61.2 ppm disappears into a small shoulder that is a small component of the remaining peak at -65.4 ppm. At room temperature, this behaviour follows that of the FFA/NA incorporated in MCM-41 and SBA-15, where the loading ratio falls and the lack of a peak at -61.2 ppm implies that the species present is that of either a more aggregate amorphous phase or similar to a liquid-like mobile species at lower loadings.

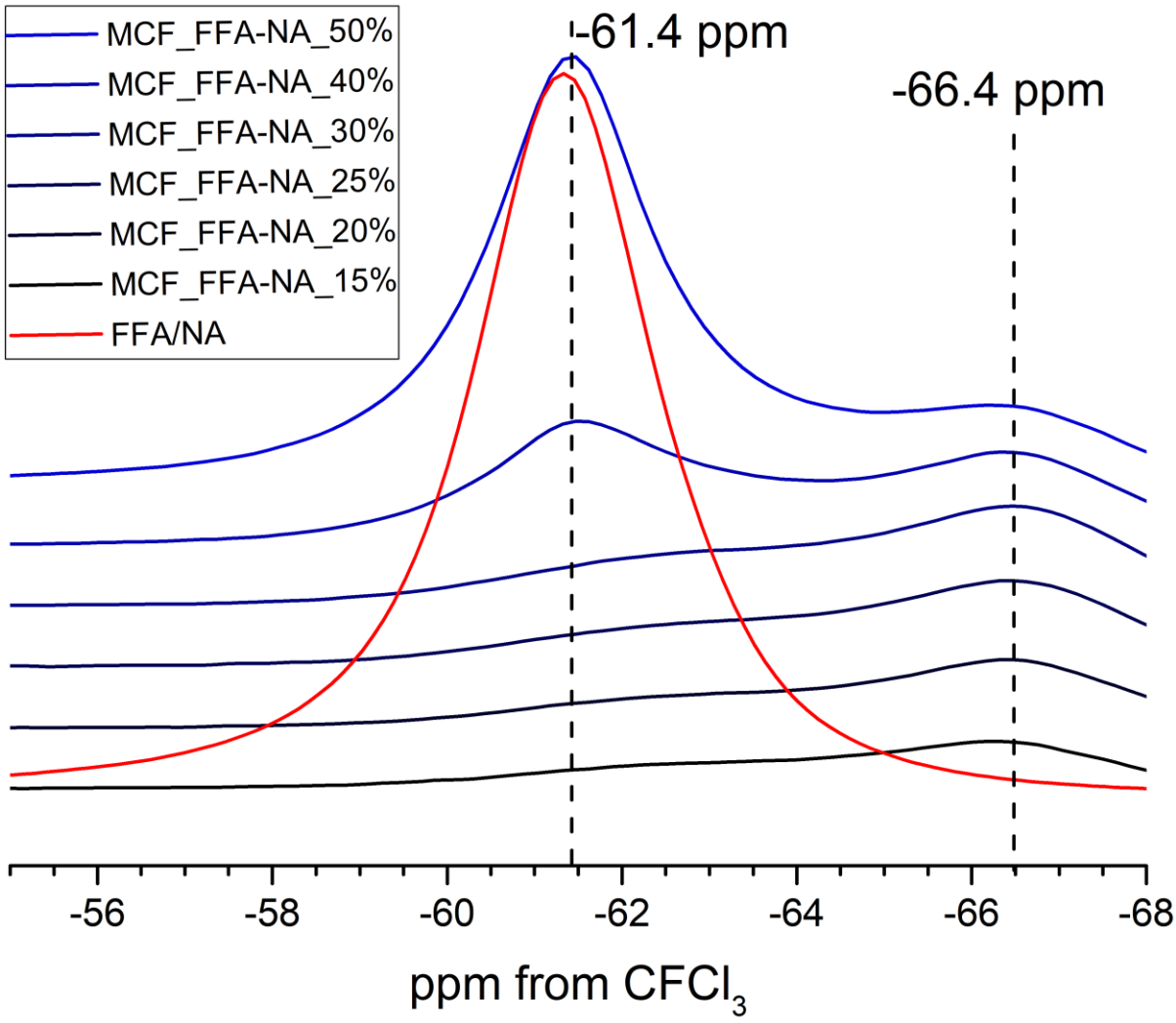

Figure 4-45 $^{19}F\{^{1}H\}$ MAS solid-state NMR spectra of MCF loaded with FFA/NA cocrystal at 223 K at various loaded levels indicated by the percentage of loading in the legend and pure FFA/NA cocrystal for comparison

When the temperature is lowered to 223 K (Figure 4-45) there is a significant increase in the size of the population at -61.4 ppm at all loading ratios. The shoulder at -61.4 ppm that was only slightly present at room temperature can now be seen to form a more defined population at loading ratios of 30% and lower. The implication as that, as in SBA-15, there are at least two forms of FFA/NA material within the MCF pore. One of these forms has a similar chemical shift to that of pure FFA/NA and the other is shifted too far downfield to be FFA form III that has separated from cocrystal material, also there is no evidence of FFA form III in the PXRD of these materials (Figure 4-40). The component with the peak at -66.4 ppm will belong to a more liquid-like species within the pores. The intensity of the peak at -.66.4 ppm could have fallen for one of two reasons, either because of a population decrease

and hence the increase of the crystalline population at -61.4 ppm. The second possibility is that the peak has broadened because these liquid-like molecules have had their mobility reduced and therefore taking on more conformations along the pore walls resulting in a broader peak.

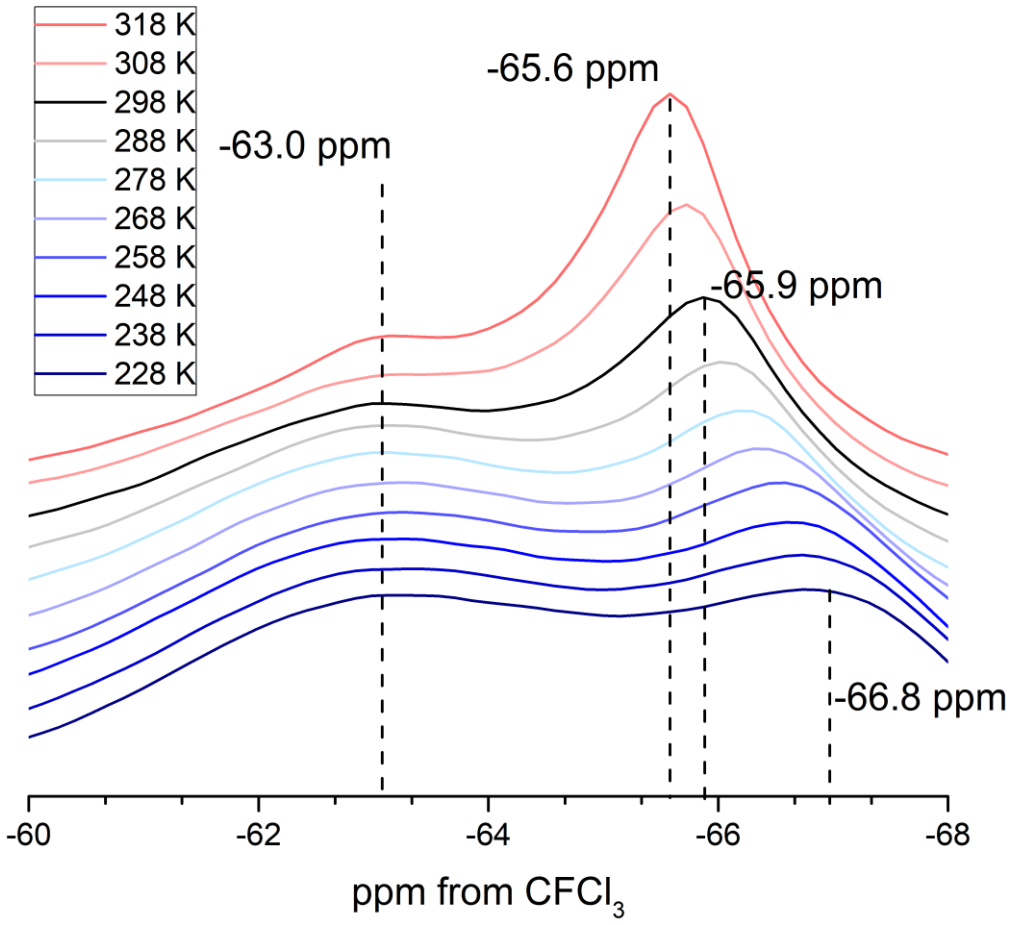

Figure 4-46 $^{19}F\{^{1}H\}$ MAS solid-state NMR spectra of MCF loaded with FFA/NA cocrystal at 298 K at 35% loading at variable temperatures (228-318 K)

After each CP spectrum was recorded of MCF loaded at 35% with FFA/NA a ^{19}F spectrum (Figure 4-46) was recorded also to observe the effect of the temperature variation of the ^{19}F chemical shifts. This material lies between what we see a crystalline component in at 40% and where we do not see a crystalline component at 30% loadings. In this material there does appear to be a lack of a crystalline component present. However, the peak at -65.9 ppm which we have begun to associate with a more liquid-like species shifts downfield as the temperature decreases, until it settles on just below -66.8 ppm. The increase in temperature appears to sharpen that species and shifts it upfield to -65.6 ppm. When considering the loading ratio and the effect of cooling this shift could be explained by how mobility is being affected by the temperature change. We are seeing the liquid-like species being

heated up and becoming more mobile, therefore it will appear more isotropic and will exist in less conformations along the wall of the pores.

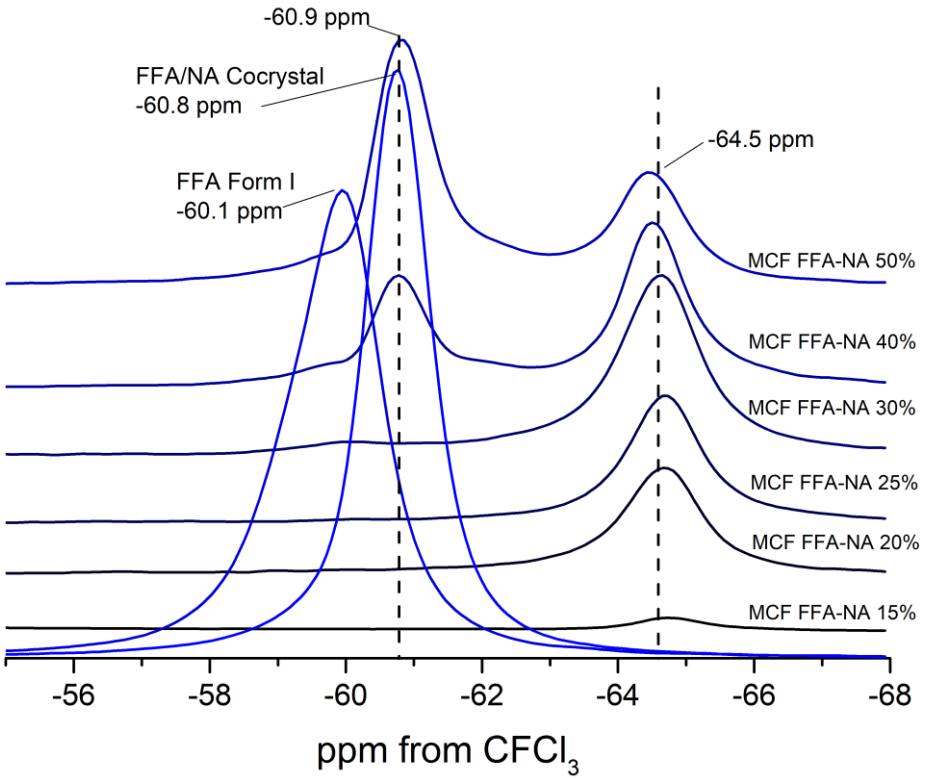

Figure 4-47 $^{19}F\{^{1}H\}$ MAS solid-state NMR spectra of MCF loaded with FFA/NA cocrystal at 298 K at various loaded levels indicated by the percentage of loading in the legend and pure FFA/NA cocrystal and FFA form I for comparison at high field (19.96 T) at a MAS rate of 35 KHz.

The MCF samples were taken to higher field 19.96 T for greater resolution and a faster MAS rate of 35 KHz (Figure 4-47) to help distinguish and separate populations as done with the MCM-41 and SBA-15 samples. The crystalline portion of the material that had a similar chemical shift to pure FFA/NA was able to be fully resolved and separated from the liquid-like portion of the spectra in each case where it was present (40% and higher loading ratios). The peak corresponding to liquid-like population is observed -64.5 ppm. As before when the loading ratio of FFA/NA in MCF is at 30% and lower, there is no population present at -61 ppm to correspond to pure FFA/NA. The absence of a peak at -62.2 ppm in Figure 4-47, which was present in SBA-15, implies that there two types of FFA/NA within MCF pores – one of these types, -64.5 ppm, matching the secondary population that exists in SBA-15. The other being a more rigid and ordered arrangement of FFA/NA that retains similarities to pure cocrystal.

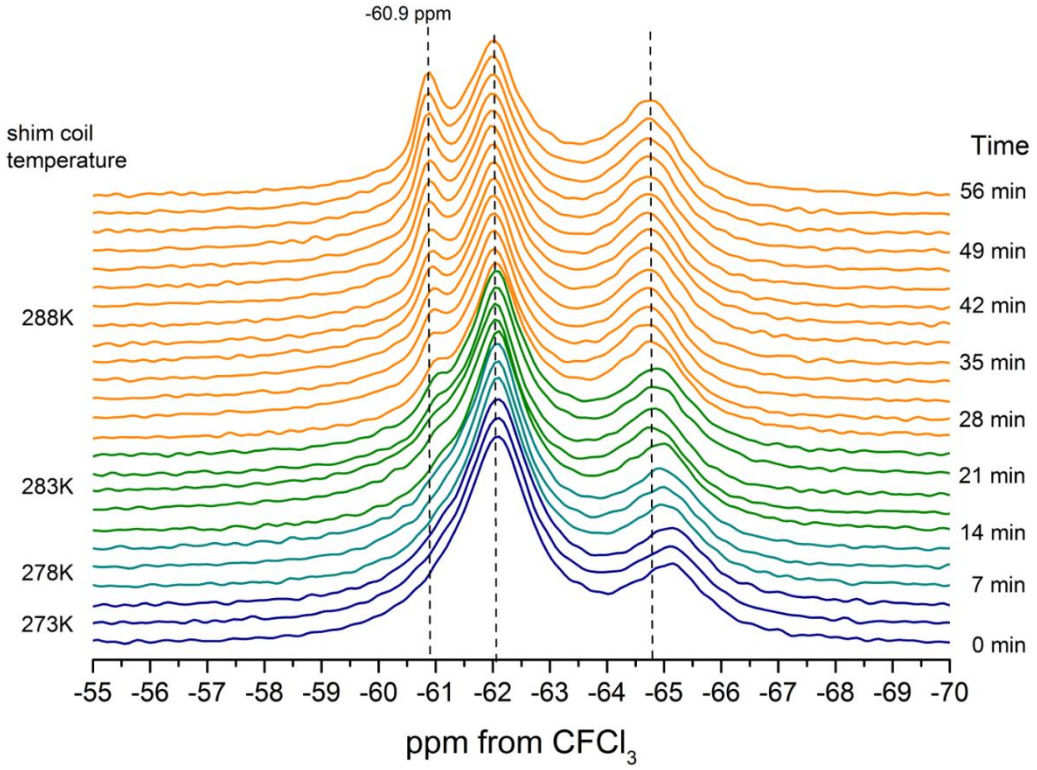

Figure 4-48 In situ ^{19}F MAS NMR spectra of MCF loaded with FFA/NA at 50% loading to monitor crystallisation. The spectra are recorded at 19.96 T using 1.3 mm rotor and MAS rate of 55 KHz

In order to explore the mechanism of formation of the species within MCF an in-situ crystallisation study was performed using a 1.3 mm rotor setup. The methodology for loading FFA/NA into the pores has been described before in the experimental section. In order to allow the sample time to recrystallize after melting the sample is usually left for 24-48 hours. To investigate the crystallisation mechanism in-situ; a fresh sample was prepared, loaded into the rotor and ^{19}F spectra were acquired in regular intervals over the space of an hour (Figure 4-48). Initially two peaks were present, one -65 ppm which we associated with the surface liquid-like species and the second centred at -62 ppm similar to that of the population found in SBA – that of an aggregate type species of FFA/NA. This second species did not match that of pure FFA/NA cocrystal as had been discovered before, however overtime a third species began to evolve at -60.9 ppm. As shown in the Figure above this evolution began after 20 minutes. As the peak of crystalline component grew the peak at -62 ppm decreased in intensity but did not disappear, leaving the final spectrum with three distinct environments of FFA/NA. This experiment has shown that the recrystallization of FFA/NA is possible to monitor using ^{19}F NMR, and that within MCF is most likely a mixture of material possessing similar order to that of pure FFA/NA

cocrystal (-60.9 ppm), an aggregate structure like that found in SBA-15 (-62.2 ppm) and a liquid-like species along the pore wall existing in all three silicas (at around -65 ppm).

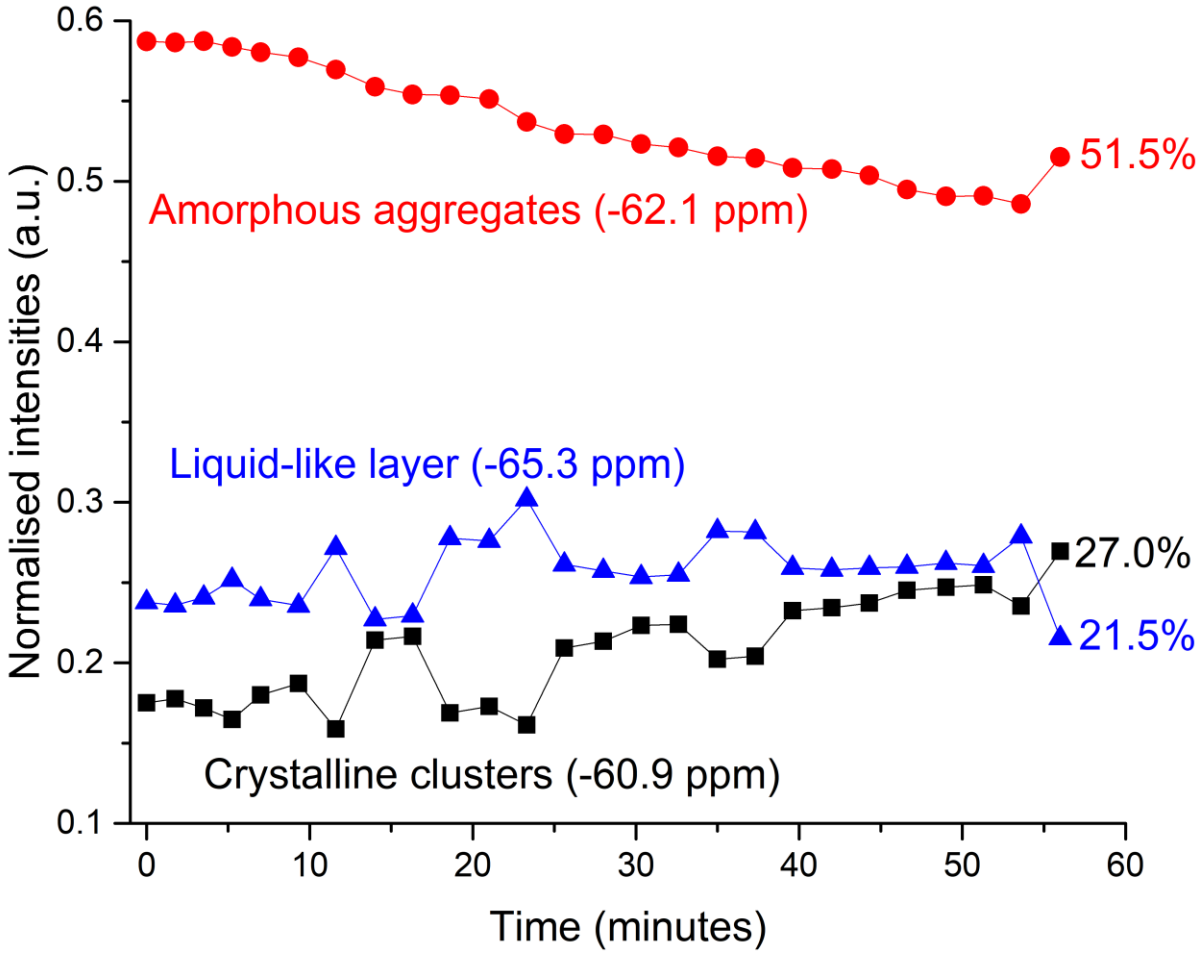

Figure 4-49 Kinetics of the confined in-situ crystallization of FFA/NA in MCF at 50% loading ratio

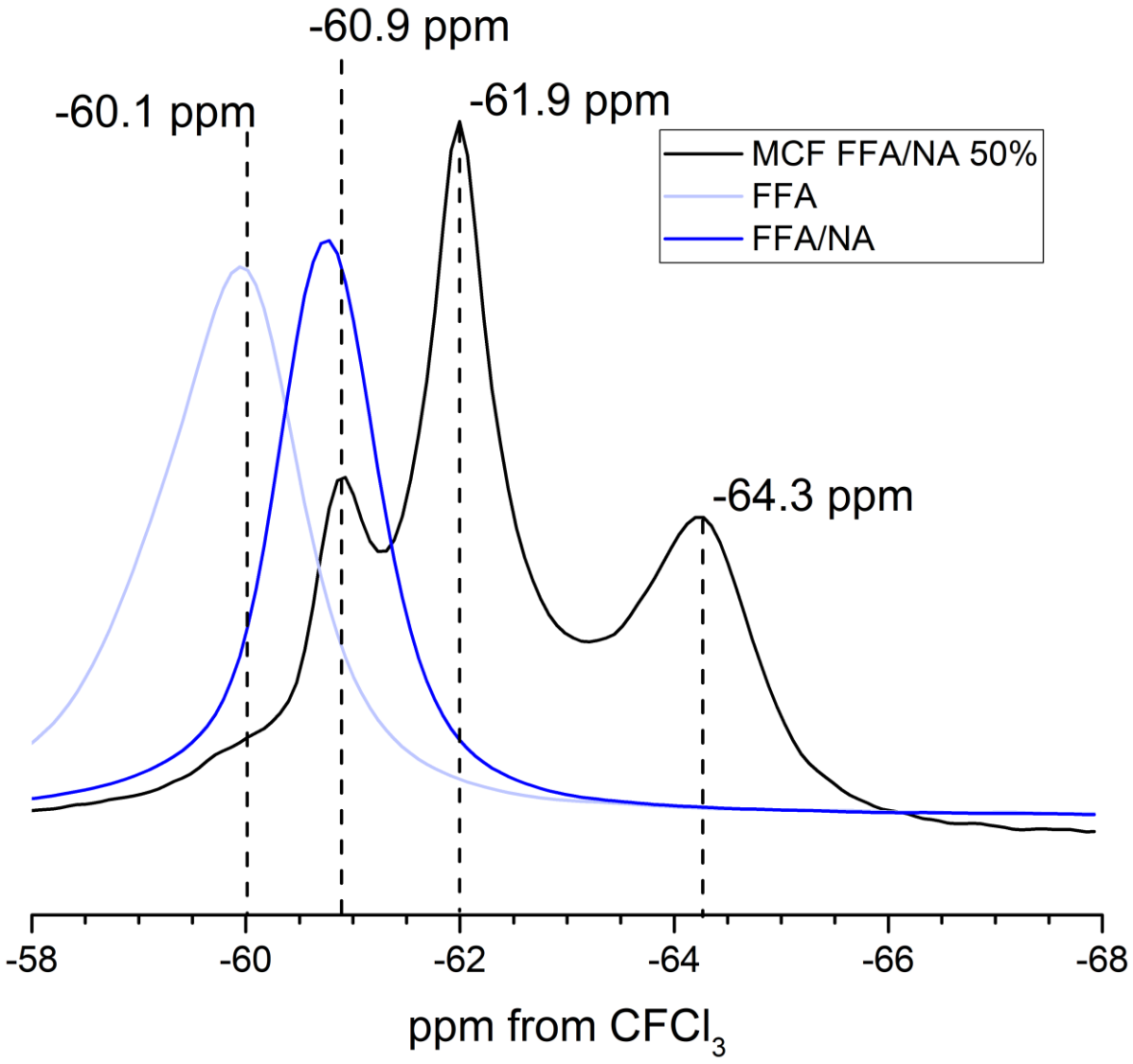

Figure 4-50 ^{19}F MAS NMR spectra of MCF loaded with FFA/NA at 50% loading. The spectra are recorded at 19.96 T using 1.3 mm rotor and MAS rate of 55 KHz. Comparison of FFA form I and FFA/NA cocrystal are also present (35 KHz MAS rate).

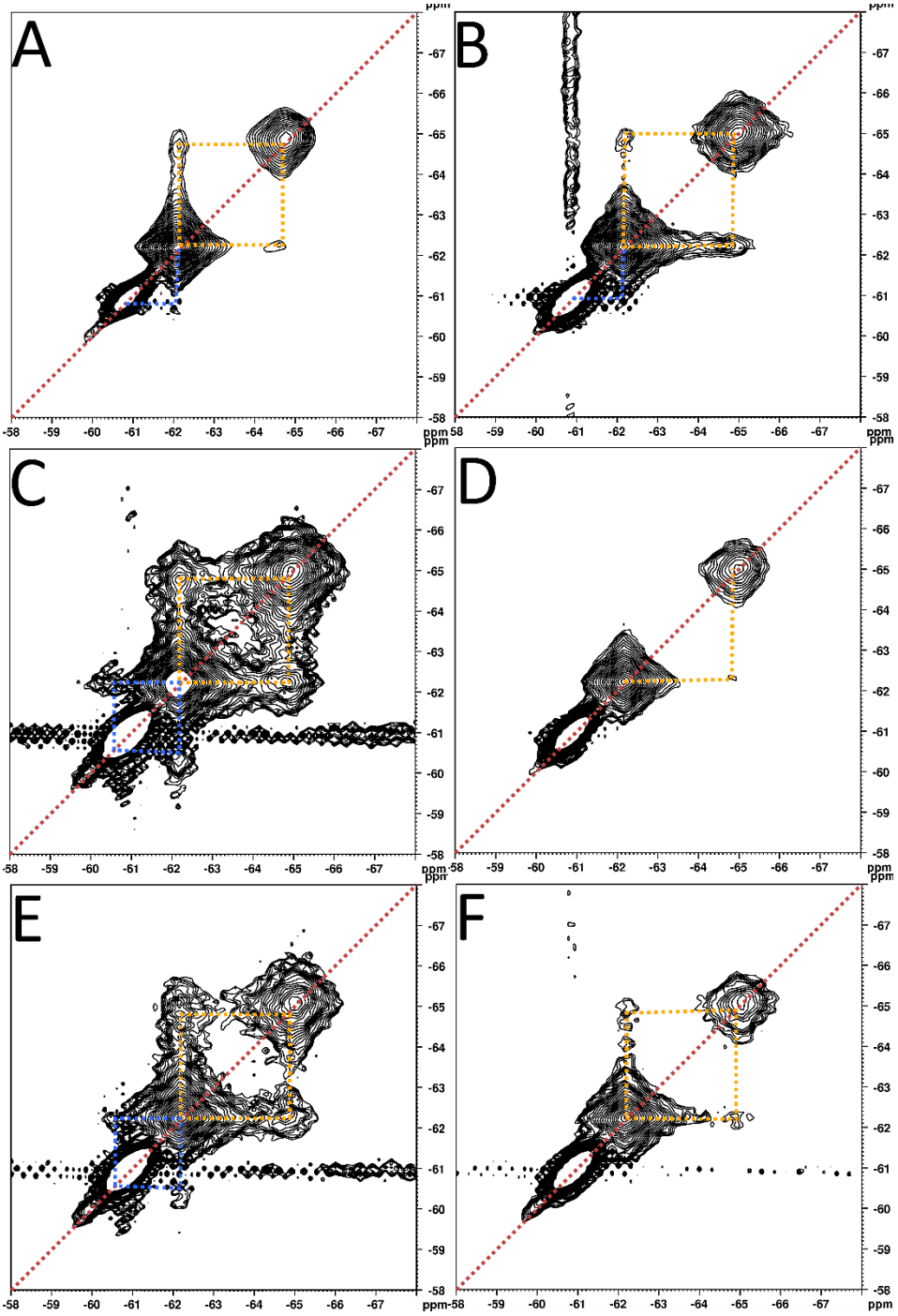

Figure 4-51 ^{19}F-^{19}F NOESY spectrum of MCF loaded with FFA/NA at 50% with various mixing times; **A.** 50 ms, **B**. 100 ms, **C.** 150 ms, **D.** 200 ms, **E.** 400 ms, **F.** 600 ms. Spectra acquired at 19.96 T at a MAS rate of 55 KHz.

This experiment shows that there is the possibility of at least two of the populations existing within the same pore space. However, it cannot be assumed without evidence that all three populations are spatially close to each other. Following the recrystallisation study on the sample, a series of ^{19}F-^{19}F

NOESY spectra were recorded at varying mixing times (Figure 4-51) in order to discern if the populations of material exist within the same pore space. There is a cross peak between the populations at -62 and -65 ppm. There is also a smaller cross peak between the population at -61 and -62 ppm. However, there is no evidence, at any mixing time we performed, of a cross peak between —61 and -65 ppm. Across the three populations there are cross peaks from the central population at —62 ppm linking the other two. NOESY cross peaks occur when an exchange of magnetisation happens in the order of about 3 Å. This implies that within the larger pores of MCF these three populations are located sufficiently close in space so that they are able to exchange magnetisation. Structurally it is assumed the peak at -61 ppm is the most ordered and therefore the most crystalline. Following that logic our population shifts downfield correlate to that of a decrease in the degree of order.

The hypothetical model (Figure 4-52) we have developed follows this basis of three different species of FFA/NA inside MCF at high loading. There must be clusters of FFA/NA that are attached to the surface (-65 ppm), the surface has extreme hydrophilicity and will be able to adsorb the plentiful hydrogen bonding capabilities creating a liquid-like layer. This population would be mobile along the surface as the strength of intermolecular interactions are not enough to hold the molecules to the surface. This population of FFA/NA would possess the lowest degree of ordering and be the most fluid-like of the three populations. The population at -61 ppm, the most ordered, therefore it would require the most space in order to stack and repeat the molecules of FFA/NA. Inside a confined pore structure this would best be found as a cylindrical core that is connected to other pores. The centre of the core being the most ordered and the outer molecules of FFA/NA that form the surface of the crystalline core would most likely have molecules that break off and reattach in places. The population at -62 ppm we hypothesise to consist of aggregated molecules of FFA/NA. However, the high intensity of the cross peak between the aggregate FFA/NA molecules (-62 ppm) and liquid-like populations (-65 ppm) indicates that the there is a greater volume of exchange of magnetisation between these two species at the mixing time shown.

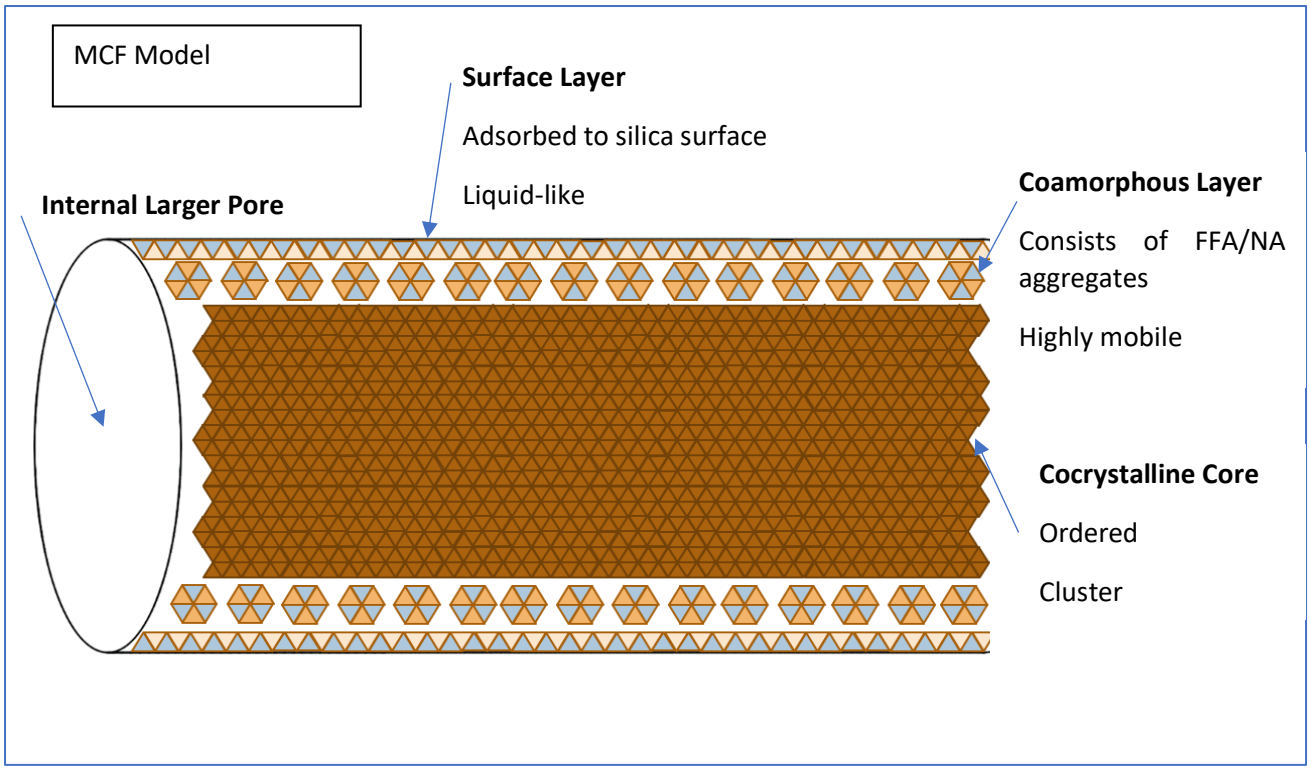

Figure 4-52 Pore arrangement hypothesis of FFA/NA in MCF. Figure indicates the three hypothesised structures of FFA/NA and their spatial arrangement inside the pores

4.6 Comparison of Encapsulation of FFA/NA in Mesoporous Silicas – Summary

In this work we demonstrated how ^{19}F NMR can be used as effective tool in order to probe the environments of encapsulated multicomponent pharmaceuticals within silica hosts. We have stated a hypothesis what we believe is the distinct separation of three species in our largest pore, each possessing different mobilities and but able to interact with each other. We have shown the temperature dependence of these different mobilities, and how heating/cooling a sample can drastically change the populations of each species. We have demonstrated the presence of some of these species in silicas with smaller pores. We have observed liquid-like population of encapsulated guest that flows along the edge of walls of the pore space. This is followed by co-amorphous aggregates. When the pores have sufficient free space, this is followed a component that resembles an encapsulated crystalline material. We have demonstrated the interactions between these populations and proposed a model of encapsulation of FFA/NA in mesoporous materials with different pore diameters.

5 Nicotinamide and its behaviour when encapsulated into mesoporous silica materials

5.1 Introduction

Looking at the previous results, the loading of nicotinamide (NA) into the pore space was the next logical step. Previously in the group we have loaded FFA[72] into silica, and in the previous chapter we loaded a cocrystal of FFA and NA. This gave us an interesting insight into coamorphous/cocrystalline boundaries that are possible when loading APIs into a limited pore space. However, we realized that NA would have to be loaded by itself into each of the silicas; MCM-41[51,52], SBA-15[54] and MCF[50]. Therefore, in order to explain any possibilities, we had not already covered of our loading hypothesis of size-dependent relationship of pore diameter to the crystallinity.

Nicotinamide is a member of the vitamin B family, exists in many food products and is on the World Health Organisation's List of Essential Medicines[133,134]. Nicotinamide has two known polymorphs in the Cambridge Structural Database, form I (CSD code: NICOAM, NICOAM01-03, NICOAM05-09,) and II (CSD code: NICOAM04). The commercially available and most common is polymorph I which crystallises in the monoclinic system ($P2_1/c$). Its unit cell volume is 578.9 $Å^3$, approximately three times smaller than that of cocrystal FFA/NA's unit cell (CSD code: EXAQAW[118]). Form I has a unit cell with dimensions (*abc*) of 0.4, 1.5 and 0.9 nm. Form I also has only one molecule of NA in its asymmetric unit. Within the cell volume there are four separate molecules of NA present. There is hydrogen bonding between the carbonyl oxygen and the subsequent amide proton of the next NA molecule approximately 2.1 Å away.

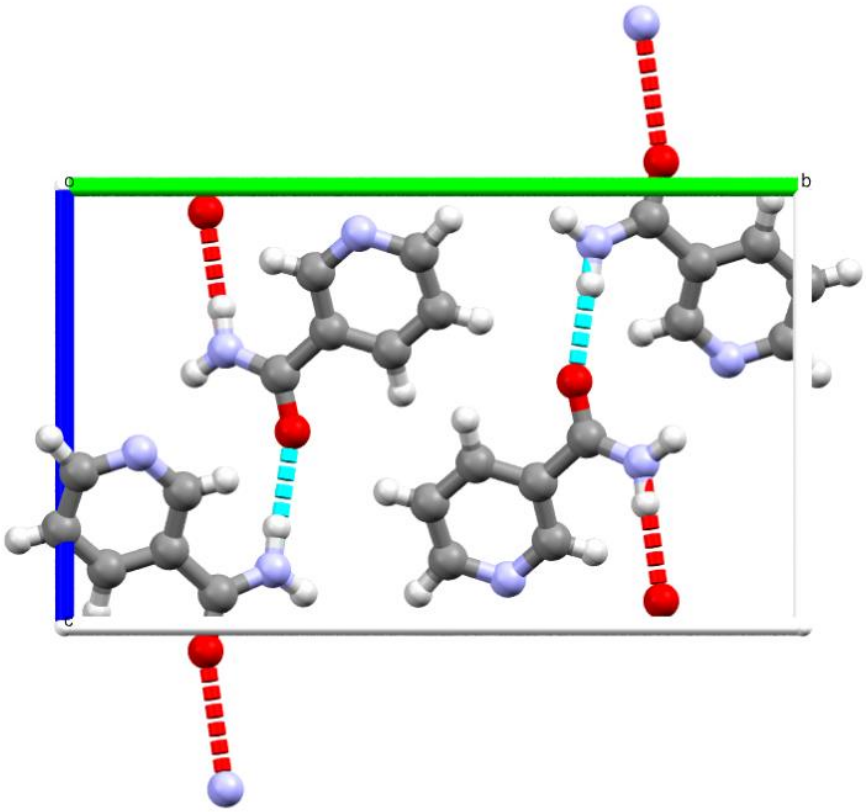

Figure 5-1 Nicotinamide Form I (left) crystal packing diagram viewed along *a*-axis. Blue dotted lines indicate hydrogen bonding from the carbonyl oxygen to the proton of the next adjacent molecule's amide group

The discovery of form II by Li *et al.*[135] was by accident when trying to prepare cocrystals of NA with a antitubercular drug called Tiocarlide, N,N'-[4-(3-methylbutoxy)-phenyl]thiourea. Crystals were recovered from the mother liquor where a mixture of form I the new form II were found. Form II is also monoclinic (*P*2/*n*). Compared to form I this polymorph has a significantly larger unit cell volume of 2395.21 $Å^3$, almost five times the size of form I and slightly under half the size of FFA/NA unit cell volume. This form has four symmetry independent molecules of NA within its unit cell giving a Z' of 4, and there are sixteen molecules packed into a singular unit cell. Comparative to form I, three of the four (NA molecules **2**, **3** and **4** in Figure 5-2) molecules in the asymmetric unit have hydrogen bonding of the carbonyl/amide to opposing carbonyl/amide groups, with H…O distances ranging between 2.046 and 2.123 Å. The fourth (NA molecule **1** in Figure 5-2) in the asymmetric unit shares an amide hydrogen bond with a carbonyl group, the other hydrogen of the amide of this unit forming a hydrogen bond with a nitrogen of pyridine of an adjacent NA unit.

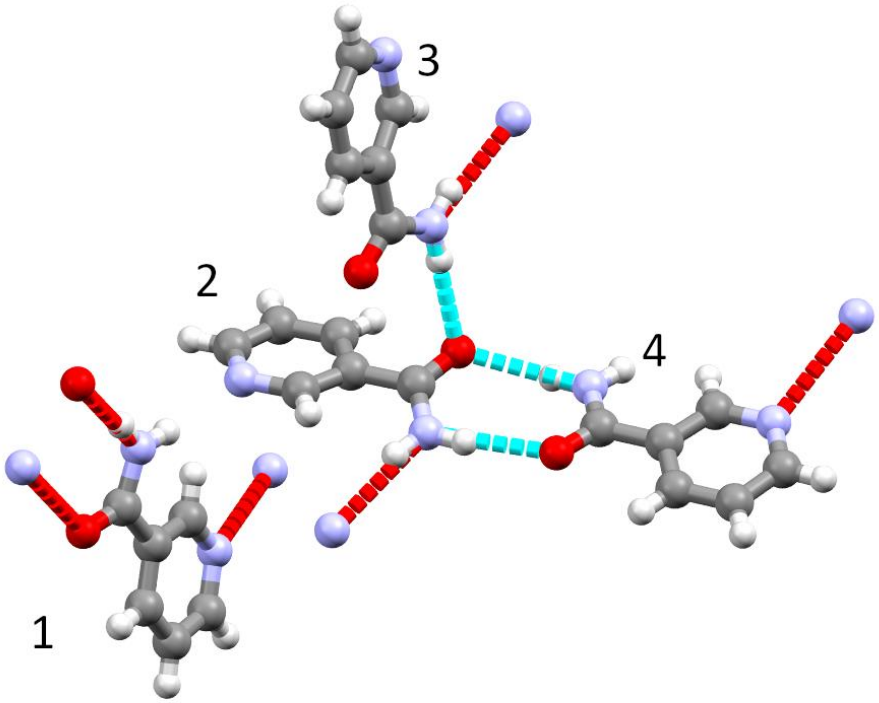

Figure 5-2 Nicotinamide Form II crystal packing of asymmetric unit. Blue dotted lines indicate hydrogen bonding from the carbonyl oxygen to the proton of the next adjacent molecule's amide group

Figure 5-4 below shows the ^{1}H-^{13}C spectrum of nicotinamide form I. This form has an extremely long recycle delay of 200 seconds, however after a number of scans a clear spectrum has been obtained showing the individual carbon environments of the polymorph. There has been no recorded solid state NMR of form II as the authors have stated that reproducibility was problematic and the outcomes were random and unpredictable. As such the predicted NMR has been calculated using the CASTEP code, firstly by a geometry optimization of the crystal system (CSD code: NICOAM04), chemical shift calculations were subsequently performed with gauge including projector augmented wave approach (GIPAW).

Form I has six clear carbon environments for each carbon in the asymmetric unit, whereas the form II has twenty-four carbons that all have different chemical shifts in a very narrow window of chemical shift. From computational assignment however we can assign these peaks , regarding form II and estimated ^{13}C spectrum has been generated and assigned using the crystal structure provided by Li *et al.*[135] on the CSD. In comparison, the CASTEP calculated chemical shifts of form I are in good agreement with the experimentally collected data.

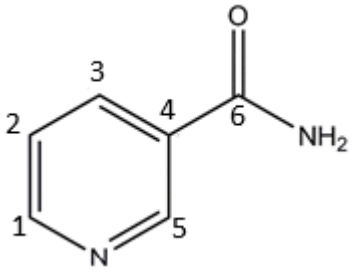

Figure 5-3 Assignment of carbons in nicotinamide molecule for form I

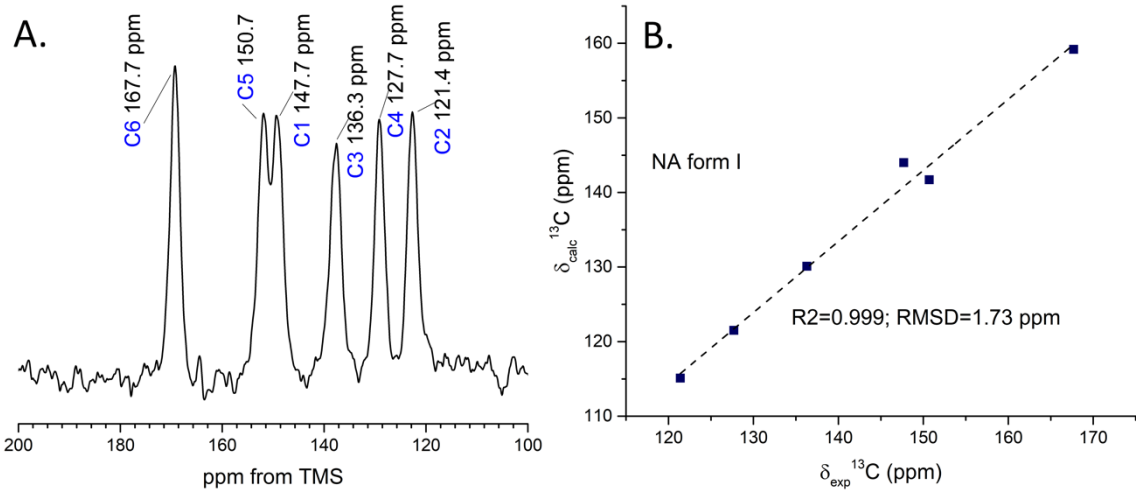

Figure 5-4 A. ^{1}H-^{13}C CP/MAS solid-state NMR spectrum of NA form I with assignment based on CASTEP prediction. **B.** Comparison of experimental and CASTEP calculated ^{13}C chemical shifts.

Table 5-1 Comparison of the experimental and calculated ^{13}C chemical shifts of NA. $\boldsymbol{\sigma_{ref}}$ was calculated to be 169.11

^{13}C Site	**NA Form I**	
	δ_{exp}	**δ_{calc}**
C1	147.7	144.0
C2	121.4	115.1
C3	136.3	130.1
C4	127.7	121.5
C5	150.7	141.7
C6	167.7	159.2

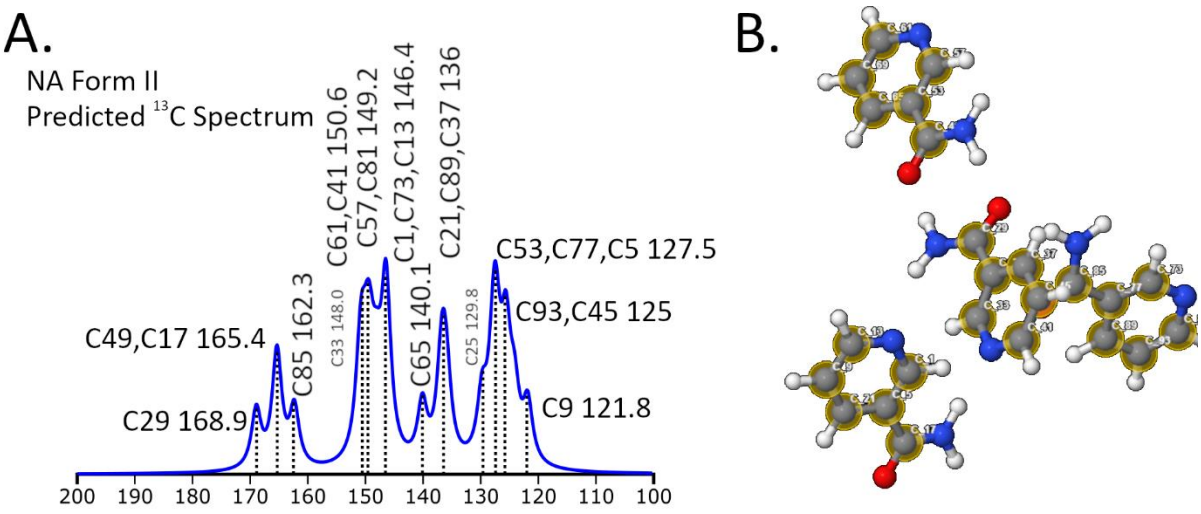

Figure 5-5 A. Predicted ^{13}C spectrum of NA form II with line broadening set to 1 ppm, many carbons overlap and are not visible **B.** Carbon labelling of the four units of NA within asymmetric unit

Table 5-2 Estimation of ^{13}C chemical shifts of NA form II based on CASTEP structure. σ_{ref} was was used from previous CASTEP calculation on form I and was 169.11

^{13}C Site	Estimated chemical shift (ppm)
C29	168.9
C49	165.4
C17	165.3
C85	162.3
C61	150.9
C41	150.6
C57	149.6
C81	149.2
C33	148.0
C1	146.5
C73	146.4
C13	146.4
C65	140.1
C21	136.9
C89	136.5
C37	135.9
C25	129.8
C53	127.8
C77	127.6
C5	127.2
C69	125.7
C93	125.6
C45	124.1
C9	121.8

Differential scanning calorimetry of both nicotinamide polymorphs (Figure 5-6) shows single endotherms, with no interconversions between the two. Form I exhibits a melting endotherm at 129°C whereas the reported melting point for form II is at 108°C.

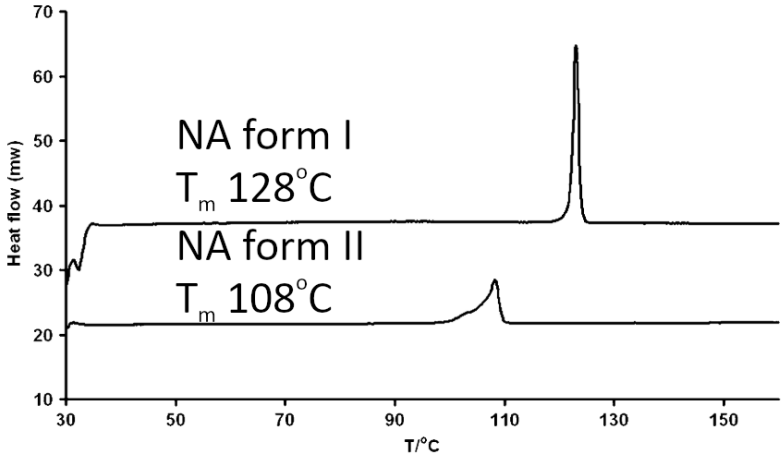

Figure 5-6 DSC thermograms of NA form I and NA form II, adapted from Li *et al*.[135]

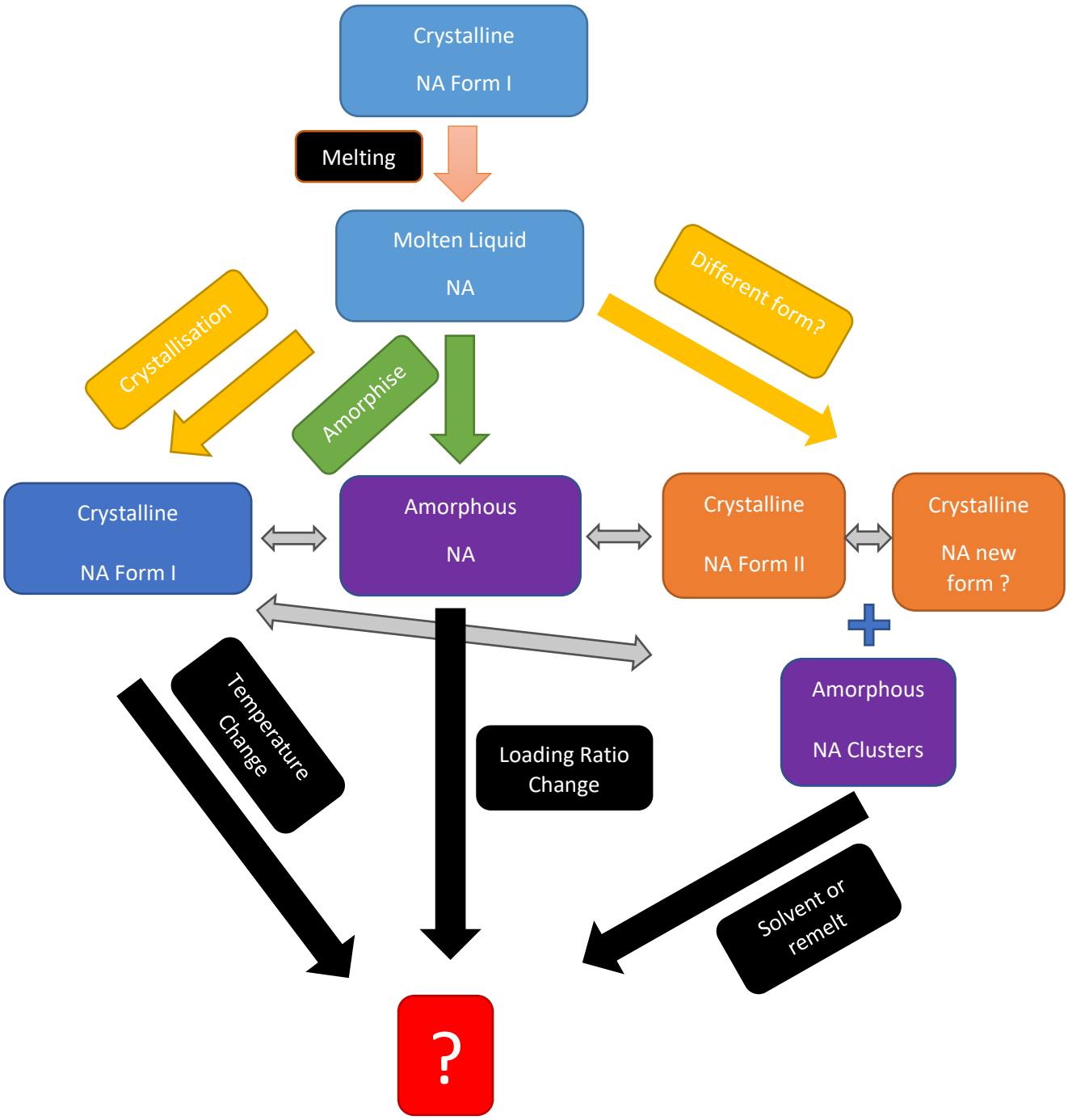

Figure 5-8 Flowchart of the possibilities of interconversions between different forms of crystalline, amorphous and separated materials after loading into pore space

5.2 Loading of NA into Silicas

As detailed in the previous chapter with FFA/NA we consider a physical weight ratio when loading material into the pore space. As in our previous protocol we chose loading ratios of NA ranging from 15% up to 50%. The TGA curves (Figure 5-9) show the loading of each silica at each loading ratio. As NA is an organic material, in each case as the temperature reaches around 280-290 °C full decomposition occurs leaving each silica. There is a gradual decline at the start of each TGA curve, most likely coming from bound water on the surface of the silica particles and inside the pores.

Table 5-3 Percentage weight loss of FFA/NA after complete thermal decompisition compared to the expected loading percentages.

Expected Loading Percentage of NA	**TGA Weight Loss of NA % from Silica Host**		
	MCM	**SBA-15**	**MCF**
15	17.6	17.6	14.9
20	21.8	22.8	19.9
25	27.1	27.3	24.4
30	32	32.7	30.1
40	41.6	42.5	40.4
50	50.5	52	50.3

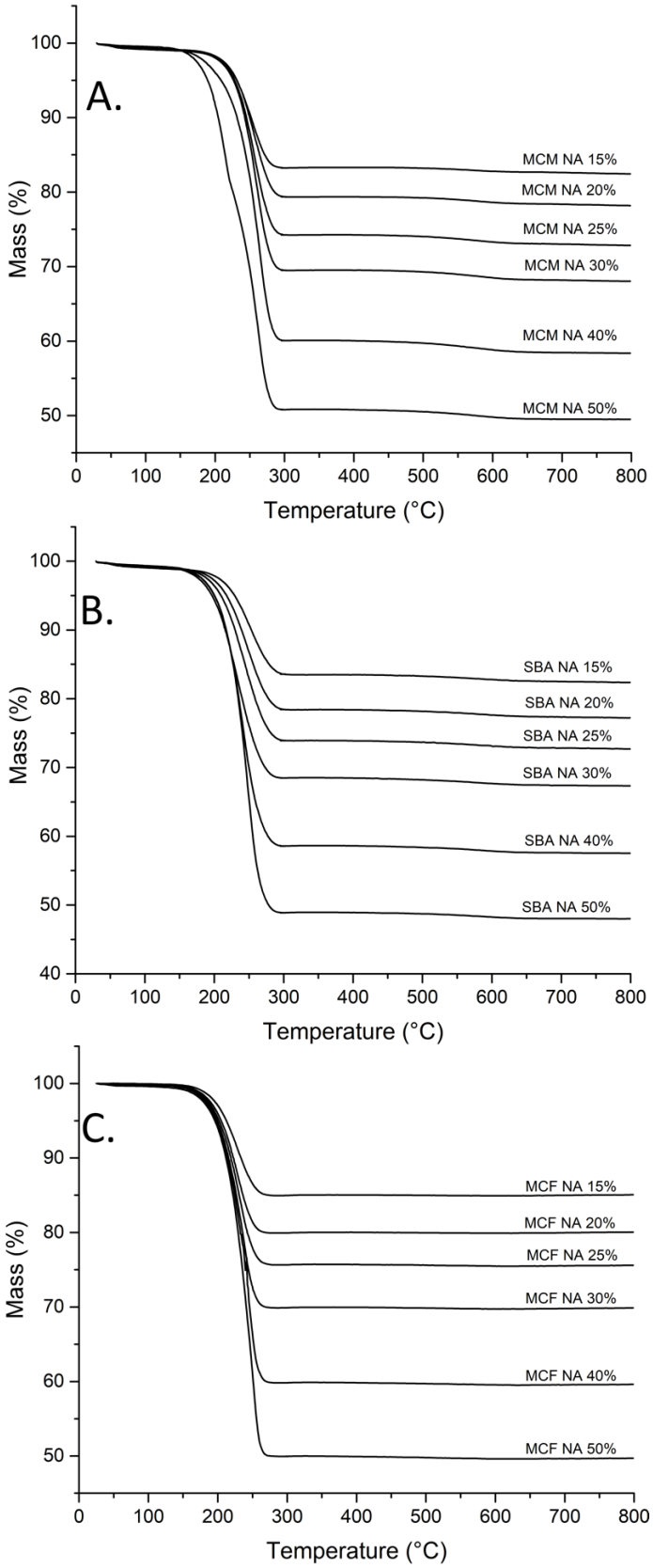

Figure 5-9 TG curves of **A.** MCM-NA, **B.** SBA-NA and **C.** MCF-NA loaded materials. Loading levels indicated as wt% of silica to NA cocrystal.

Figure 5-10 show the adsorption/desorption isotherms for each of the loaded silicas. The hysteresis loop for each silica shows a type IV reversible isotherm of both the loaded and unloaded materials. This isotherm is characteristic of mesoporous silicas showing a large multilayer adsorption of nitrogen gas that is steadily desorbed on the desorption branch after condensation. As the amount of material inside the pores increases the isotherm loop can be seen to decrease in size. MCF and SBA show an approximate linear decrease in the hysteresis loop from unloaded to 50% loading, however MCM has a significant decrease in BET surface area to the point where at 40% loading and higher are difficult to distinguish, implying a fully loaded material. The calculated pore volumes for MCM also agree with this, dropping down to around 10 m^2/g. In Figure 5-11 is the pore diameter analysis for each silica loaded with NA. For MCM-41, DFT methods[128] were used to calculate the pore diameters, whereas the BJH (Barrett-Joyner-Halenda)[66] method was used for the determination of SBA-15 and MCF pore diameters. MCF being an ink-bottle type mesoporous silica has two measurements, one for the window and one for the internal pore. The window diameter is taken from the desorption branch of the isotherm and the internal pore is taken from the adsorption branch[50].

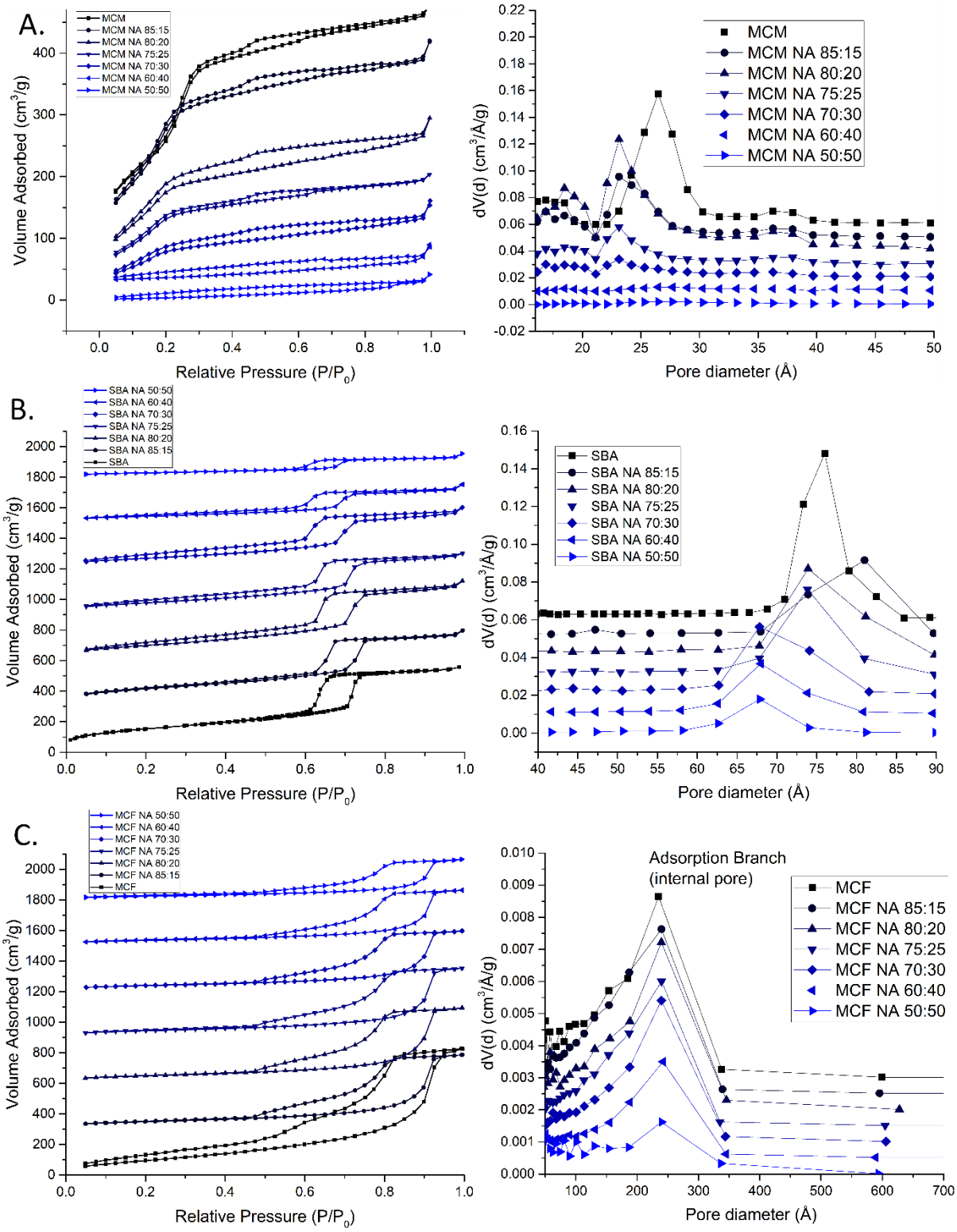

Figure 5-10 Nitrogen adsorption/desorption isotherms and pore size distribution curves for **A.** MCM-41, **B.** SBA-15, **C.** MCF at different host:guest NA loadings

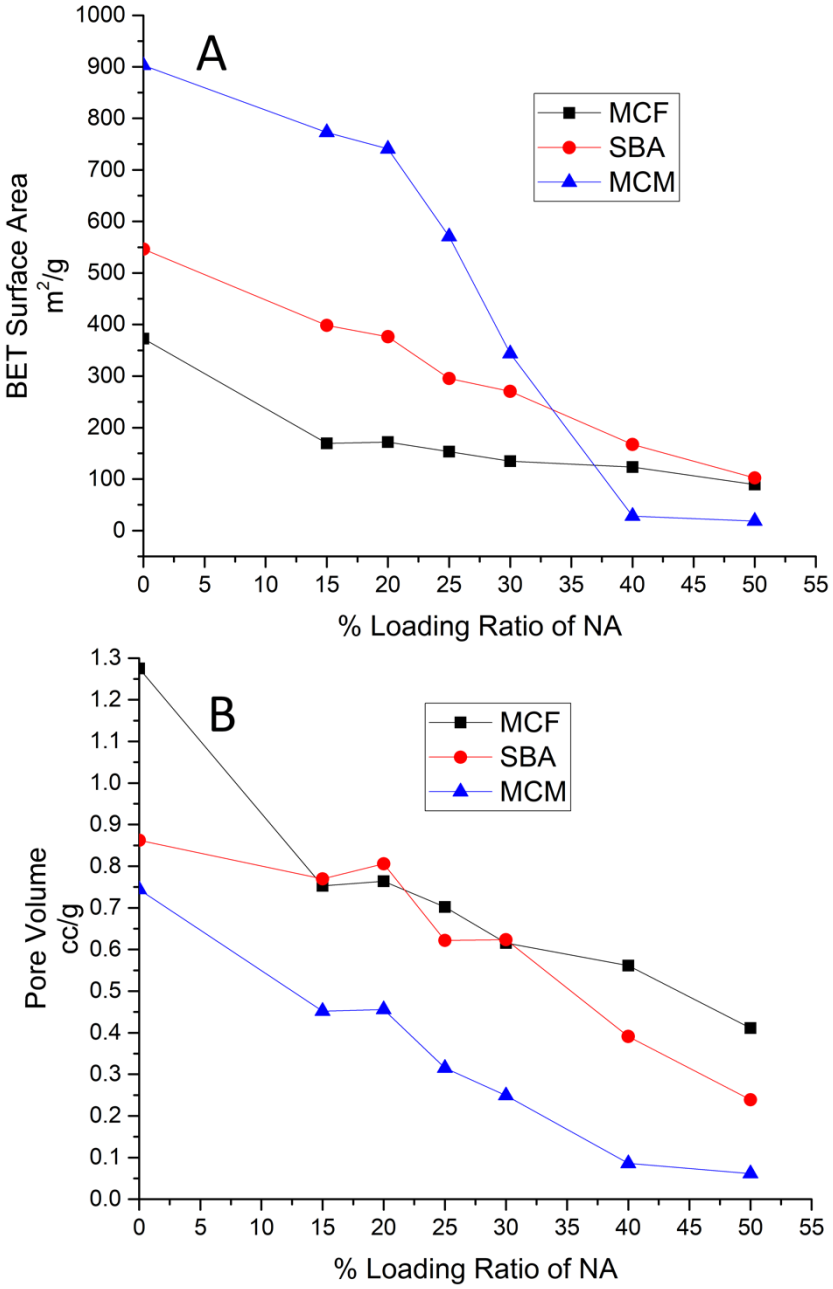

Figure 5-11 A. BET surface area (calculated as a multi-point BET in the linear region of the isotherms) **B.** Pore Volume (calculated at *P/P_0 of 0.99)*

Previously ^{19}F solid state NMR allowed us to clearly distinguish different mobilities and degrees of order within the pores with FFA/NA cocrystal, however there is no ^{19}F functionality present with NA. With NA we are limited to ^{13}C and ^{1}H NMR as our primary NMR nuclei of characterization. The two nuclei not discussed currently are ^{17}O and $^{14/15}N$. ^{17}O would be prohibitively difficult to detect being only 0.038% at natural abundance level, while ^{17}O also being quadrupolar would mean our signal would be extremely broad. In addition, the cost of buying enriched ^{17}O is very high and then chemically

exchanging the carbonyl oxygen would be difficult. Therefore, we identified that ^{13}C NMR is the best way to identify any polymorphic changes to NA as we are able to distinguish each individual carbon site, we are able to enhance our signal of these populations by using cross-polarization NMR, which we already know has worked well with loaded molecules[65,72].

5.3 Incorporation of NA into MCM-41 mesoporous silica

As highlighted previously, MCM-41 possess the smallest pores of the silicas we synthesised for these loading experiments. Possessing pore dimensions of around 3-4 nm and the greatest available surface area of the silicas of around 1000 m^2/g gives MCM-41 excellent adsorption properties, for example in CO_2 adsorption and purification[117,136,137]. More recently it has become an ideal model mesoporous silica for surface analysis of molecules in a confined space[138,139]. When we consider form I of NA in reference to MCM-41, we note two particular properties that may affect its ability to load and crystallise in the pore space. Firstly, the reduction in the unit cell volume when compared to FFA/NA, being three times smaller, should allow a greater number of molecules to stack and arrange themselves inside the pore. Secondly the greater number of orientations in which NA would be able to stack itself when compared to FFA/NA, again due to the reduced unit cell dimensions. The CF_3 group on FFA will limit the orientation in which the cocrystal would stack, being hydrophobic would mean that preferentially would stack away from the surface silanol groups of the silica. NA on the other hand is a lot more hydrophilic and is able to hydrogen bond extremely well to silanol groups with both its amide group and the pyridine nitrogen on its ring, reducing high energy interactions.

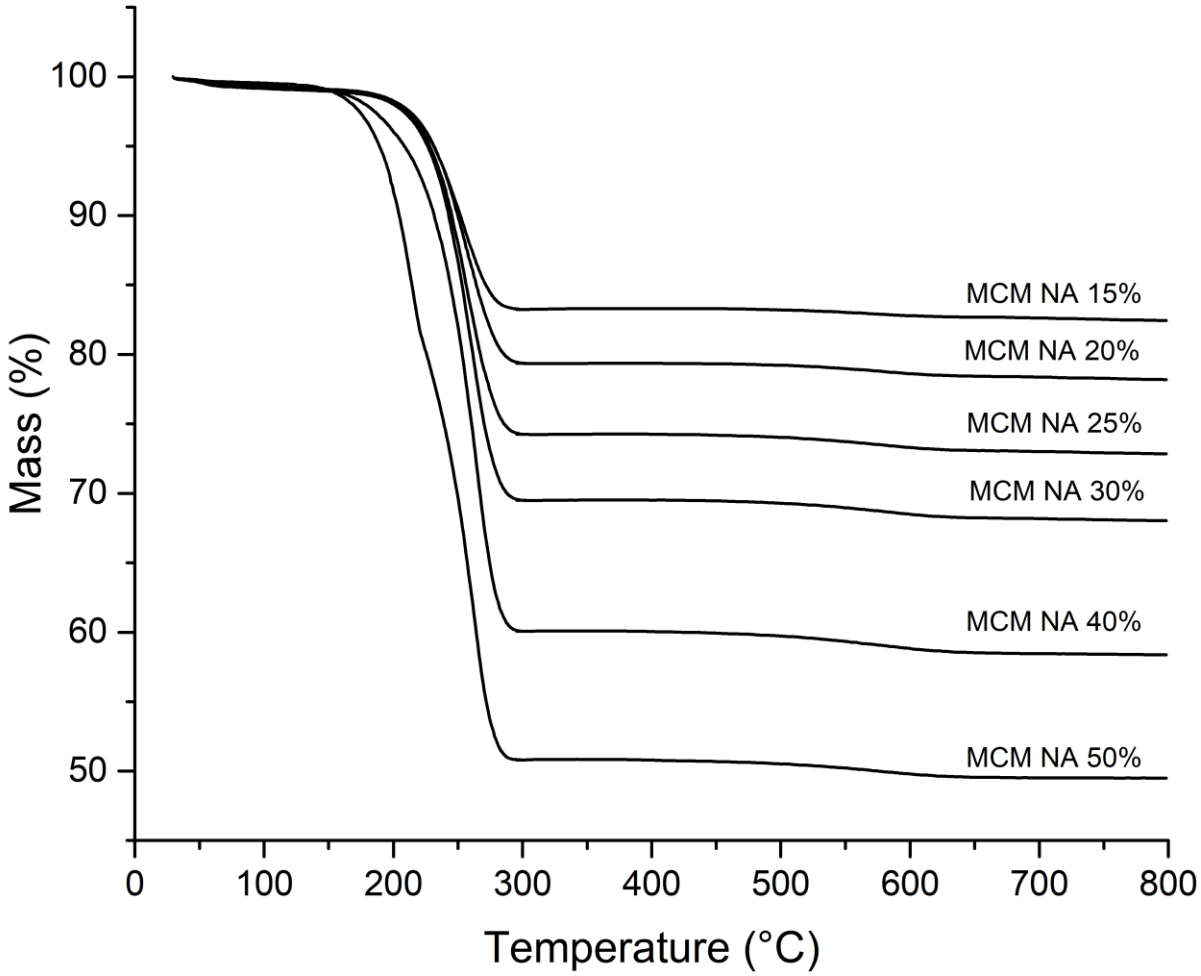

Figure 5-12 TG curves of MCM-NA loaded materials. Loading levels indicated as wt% of silica to NA cocrystal.

The Table 5-6 shows the available BET surface area and pore volume calculated from the isotherms of MCM loaded materials. The linear decrease in surface area is apparent as the loading ratio is increased, and when compared to FFA/NA drops suddenly at the 40% loading mark (Table 5-6). This also correlates with the pore volume that has been calculated at this loading level implying that by the 40% loading ratio the pores are completely saturated or blocked with NA molecules. This would then imply that above 40% loading there is a significant number of molecules of NA located outside the pores. When the DSC thermograms are consulted there is a significant melting peak for 50% loaded material that perfectly matches the melting point of NA form I at 129°C as indicated on the DSC curve (Figure 5-14). For loading ratios at 40% and below there is no melting peak present in the thermogram, and from the sorption data we know that the pores are loaded with NA material at 40% and 50% ratios. When the PXRD of these materials is also considered (Figure 5-13) there is a clear indication that the form of NA is form I as it possesses characteristic peaks. There are no matching peaks towards

to the form II diffraction pattern. There are no apparent peaks below 40% loading implying a complete absence of crystallinity. Therefore, we can conclude that at these ratios the content of NA within the pores does not possess the long-range order expected of a crystalline material and is likely to be amorphized. In each thermogram there is a broad component between 40-60 °C, which is most likely caused by the evaporation of water that is adsorbed to the surface of the pores.

Table 5-4 BET surface area (calculated as a multi-point BET in the linear region of the isotherms) and Pore Volume (calculated at *P/P_0 of 0.99)*, Pore Diameters calculated from DFT model of isotherm

Loading Ratio (% weight to MCM-41 weight)	**BET Surface Area(m^2/g)**	**Total Pore Volume (cm^3/g)**	**Pore Diameter (nm)**
0	902.823	0.7441	2.65
15	772.589	0.4518	2.31
20	740.812	0.4558	2.31
25	570.816	0.3153	2.31
30	343.747	0.2489	2.31
40	28.014	0.08625	2.77
50	18.589	0.06142	2.65

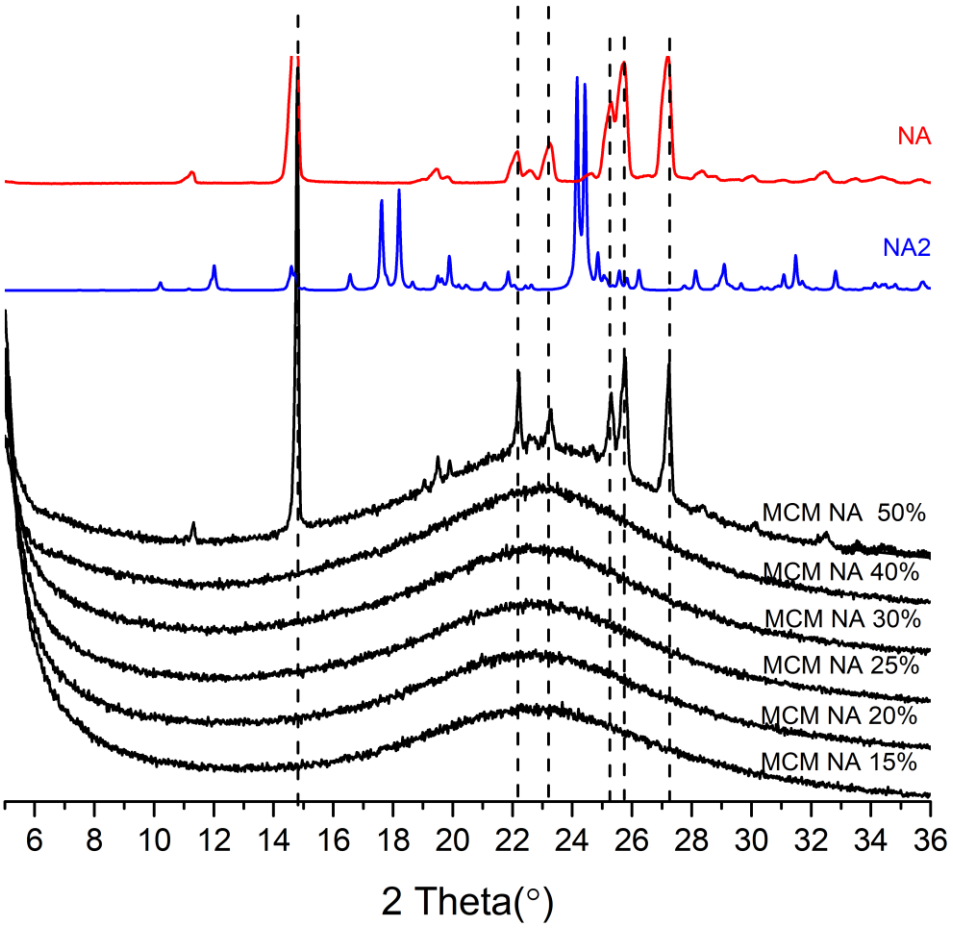

Figure 5-13 PXRD patterns of MCM-41 silica loaded with NA at various loading levels (black lines indicate matching NA form I, guest loading ratio (in wt%)

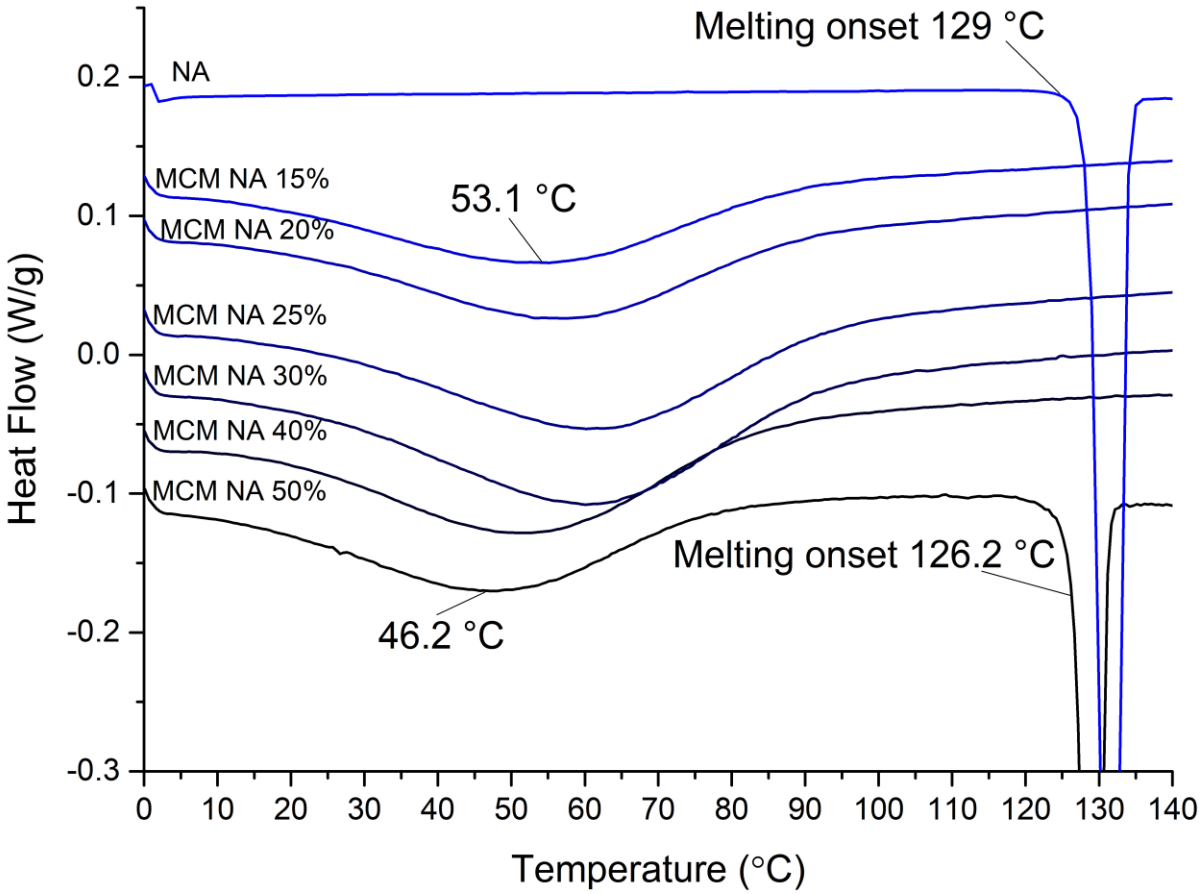

Figure 5-14 DSC thermogram of MCM-41 loaded with NA, guest loading ratio (in wt%)

A possible arrangement of molecules of NA form I is shown in the Figure 5-15. Contrasting with FFA/NA loaded into MCM-41, there is a greater number of molecules that are able to be packed into the space when we assume that the pores are fully saturated. From our data gathered above we would consider this to be at 40% and higher loadings. However, it does appear that even though there would be roughly double the number of molecules able to pack within the pores, at this pore size the molecules could still be considered amorphous in nature. This indicates that even if the arrangements of molecules inside the pores is that of perfect filling, there are not enough NA molecules arranged regularly in all three directions to give it the crystalline properties of form I's. Form II has not been considered here due to the size of the unit cells being four times that of form I and therefore its capability to pack inside a 3 nm size pore would be significantly reduced.

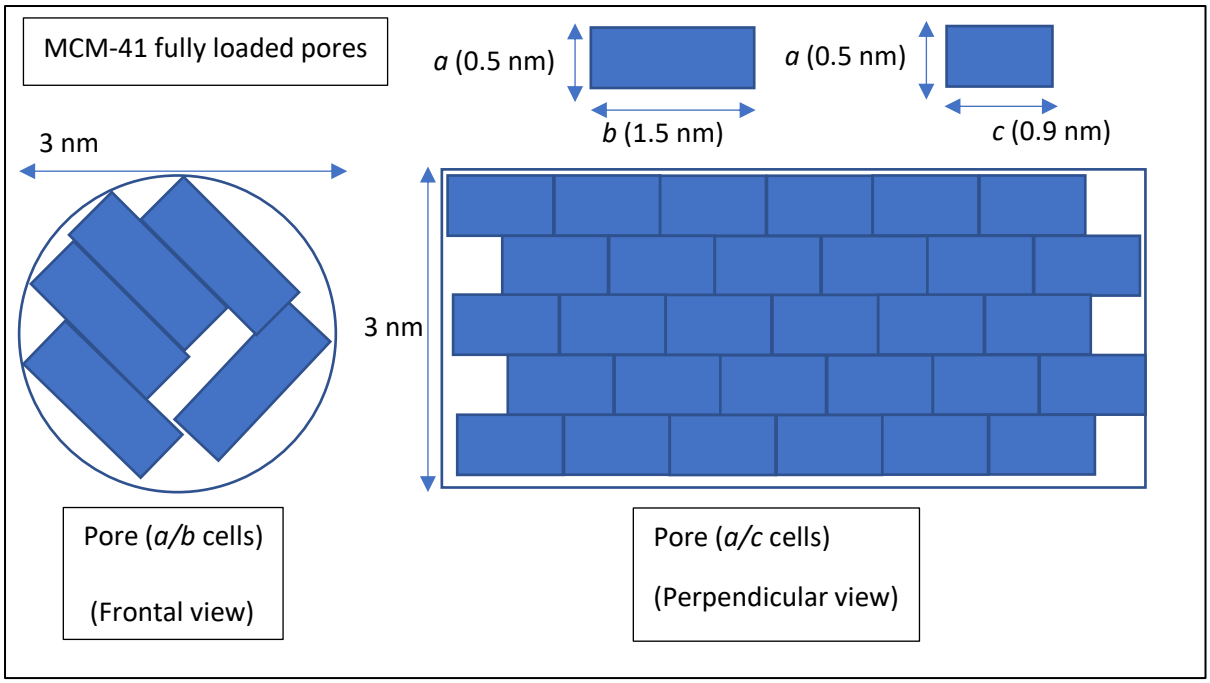

Figure 5-15 MCM-41 Fully Loaded Pore diagram of frontal and perpendicular view of pore space. Blue rectangles represent NA unit cells to scale with the pore dimensions.

At loading ratios of 30% and lower there is significant space that has been freed within the MCM-41's pore network for the movement of molecules. Figure 5-16 shows the possibility of space generated by reducing the loading ratio. From the sorption isotherms we know that space has been freed, the pore volume at 30% has increased to 343.747 m^2/g and the total pore volume three times higher at 0.24 cm^3/g than at 40% loading (Table 1—6). It is not surprising then to see the absence of melting peaks in DSC and crystal peaks in PXRD. However, the lack of these peaks does not mean that there is no material present. The state of these molecules of NA inside must be that of an aggregated mobile type that are not large enough to give indication of long-range ordering of any kind of polymorph.

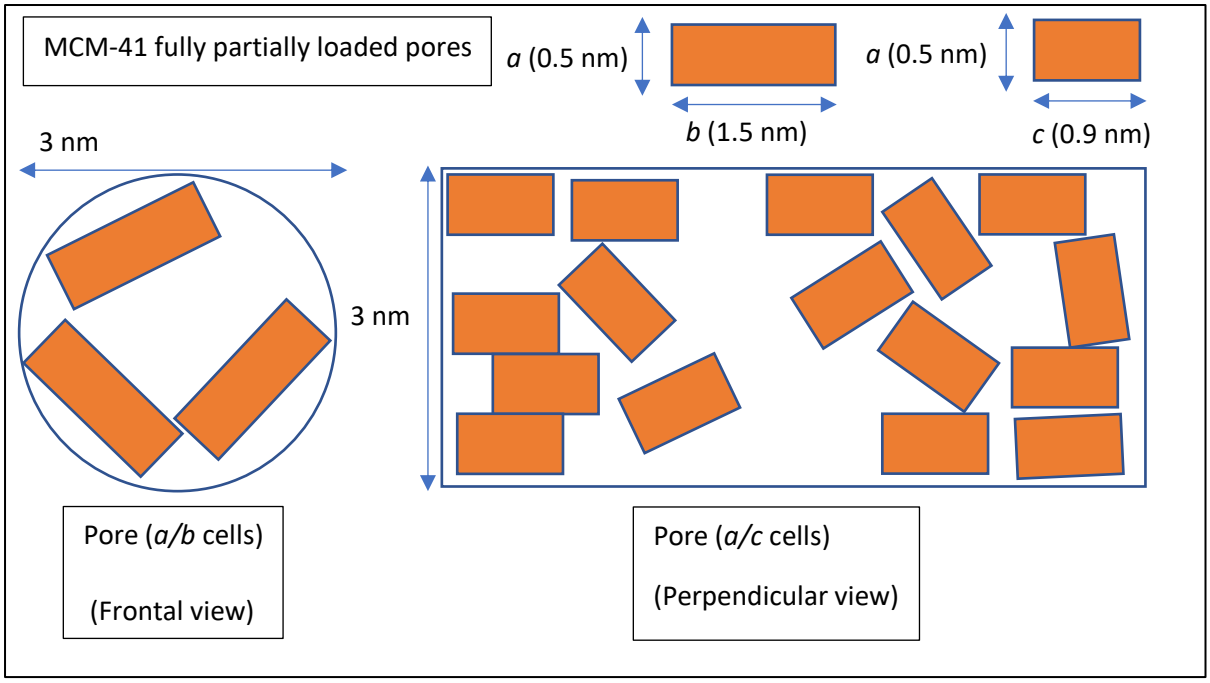

Figure 5-16 MCM-41 Partially loaded pore diagram of frontal and perpendicular view of pore space. Orange rectangles represent NA unit cells to scale with the pore dimensions.

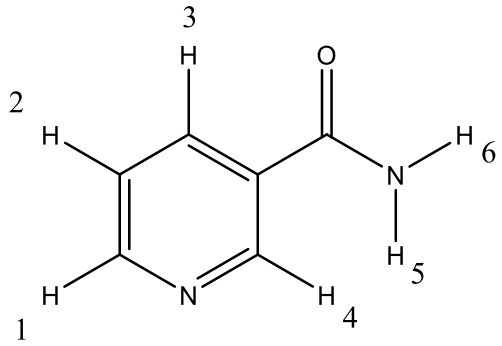

Figure 5-17 Proton site labelling of the nicotinamide molecule

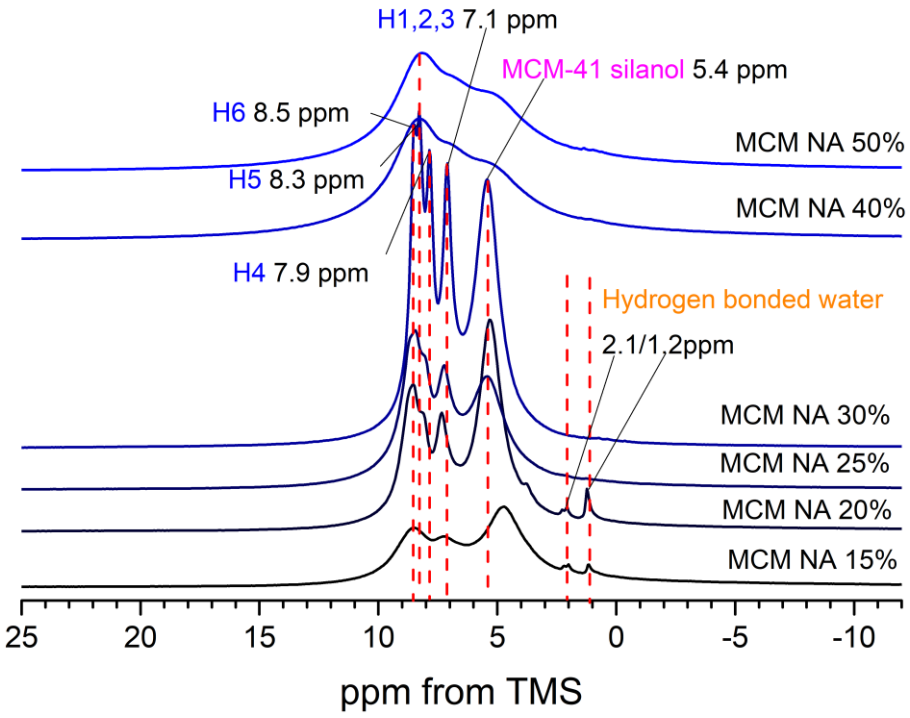

Figure 5-18 ^{1}H MAS solid-state NMR spectra of MCM-41 loaded with NA at 298 K, guest loading ratio (in wt%)

At room temperature the proton environments differ greatly when fully loaded and partially loaded MCM-41 is considered (Figure 5-18). At fully loaded ratios of 50 and 40% there is a much broader and less defined array of chemical shifts. NA by itself has four aromatic protons and two amidic protons. In the case of partial loading there are defined peaks corresponding to specific proton environments. Unlike in FFA/NA loaded MCM, where there were no distinguishable proton environments, here the two amidic protons (H6 and H5) can be identified at 8.5 and 8.3 ppm respectively. The next most identifiable proton environment is the proton located in between the pyridine nitrogen and carbon connecting the amide group (H4) due to the electron deshielding pushes the chemical shift downfield of the other aromatic protons at 7.8 ppm. The other three aromatic protons (H1-3) on the opposite side of ring are too close in chemical shift to distinguish from each other, resting at 7.1 ppm. The broader peak situated on 5.4 ppm at higher loadings, which then sharpens as the loading ratio decreases belongs to the silanol protons. At lower loadings there are some small chemical shifts consistent with MCM-41[140]. As stated previously this is most likely due to the effect of water molecules penetrating the pores. There are some low intensity chemical shifts present at 1 and 2 ppm which relate to different hydrogen bonding states of water protons with the silanol groups on the surface of

the pores. These chemical shifts are not present in higher loadings, most likely due to less space being available to allow water to penetrate and interact with the surface, whereas at lower loadings they are much more pronounced.

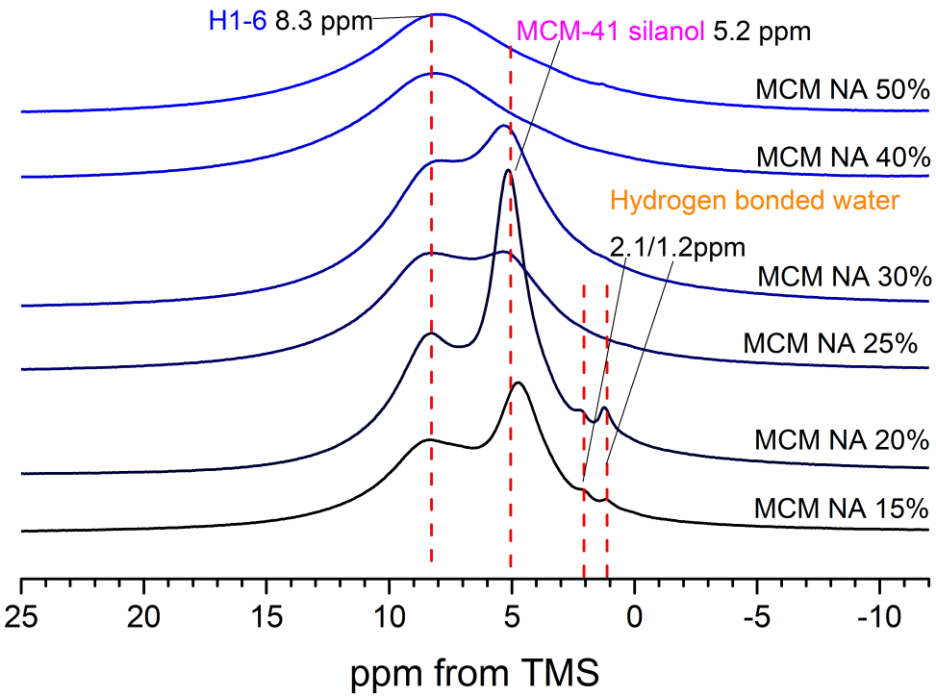

Figure 5-19 ^{1}H MAS solid-state NMR spectra of MCM-41 loaded with NA at 223 K, guest loading ratio (in wt%)

When the samples are cooled to 223 K there is significant broadening present when compared to the room temperature spectra. At 50-40% loadings, the spectra have now become an extremely broad singular peak stretching between 0-15 ppm, centred at about 8.3 ppm. Due to the reduction in temperature and MAS spin speeds, it not possible to distinguish any of the individual NA protons. As the loading ratio is decreased a second chemical environment is revealed at 5.2 ppm, which is most likely the silianol population. The reduction in temperature has reduced the mobility of NA molecules within the pores and has also had a freezing effect on the water that has entered the pores at lower loadings. At 20% loading the silanol water environments are now visible at 1 and 2 ppm. The increased intensity will most likely be from molecules of NA becoming more mobile and therefore more liquid-like. We observe the same behaviour at room temperature.

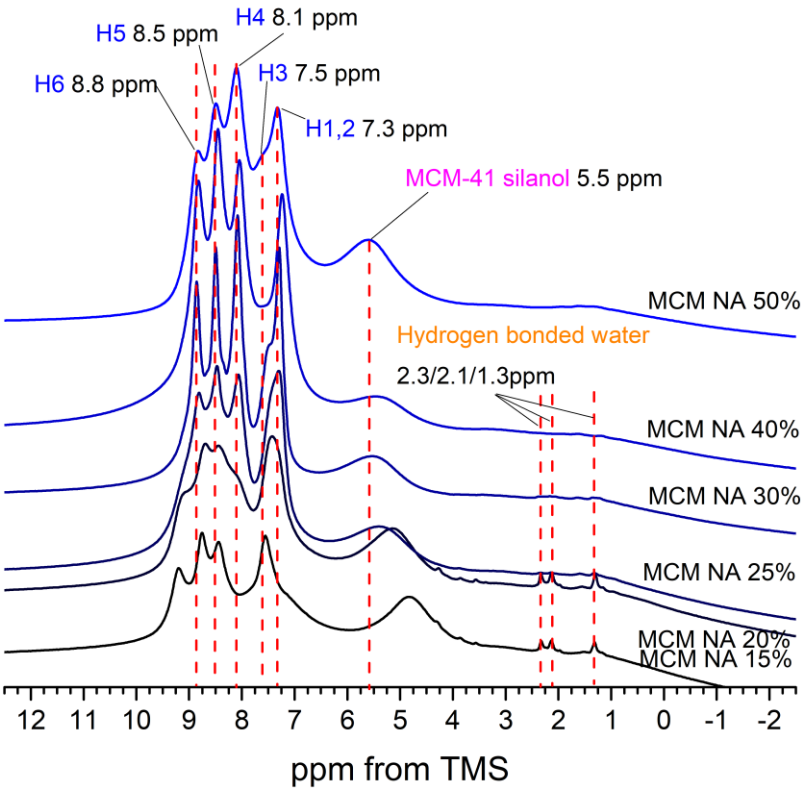

Figure 5-20 Highfield (19.96 T) at 55 KHz ^{1}H MAS solid-state NMR spectra of MCM-41 loaded with NA at 293 K, guest loading ratio (in wt%)

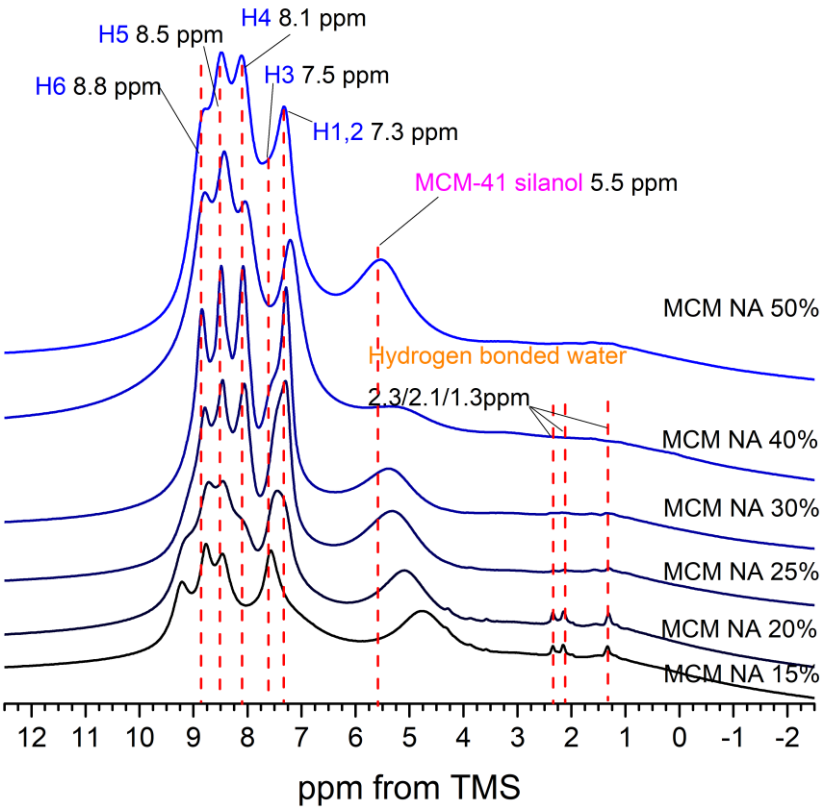

Figure 5-21 Highfield (19.96 T) at 55 KHz ^{1}H MAS solid-state NMR spectra of MCM-41 loaded with NA at 273 K, guest loading ratio (in wt%)

Figure 5-20 and 5-21 are ^{1}H spectra recorded at 19.96 T with a 1.3 mm rotor at fast MAS (55 KHz) on the loaded materials. This has reduced the effect of broadening due ^{1}H-^{1}H dipolar couplings in the samples and greatly improved the spectral resolution of the MCM-41 sample series. We can clearly label four of the proton environments of NA with the final two populations existing as a shoulder. This is most clearly indicated in the 30% loaded sample of MCM-41. The furthest left peak at 8.8 ppm and its closest neighbours belong to H6/H5 respectively, which are the amidic protons. Following these protons is H4 at 8.1 ppm which is the proton situated in between the pyridine nitrogen and the amide group. The final peak of NA consists of a main population at 7.3 ppm with a shoulder to its left situated on 7.5 ppm. These two peaks contain the final three aromatic protons of NA named H1, H2 and H3. The assignment of these three is more difficult. However, based on CASTEP predictions of NA form I, the most likely candidate for the shoulder peak at 7.5 ppm is H3, leaving the remaining two protons as the single larger peak centred on 7.3 ppm. The silanol group has been clearly separated from these proton environments, and appears to vary its chemical shift depending on the loading level of NA. The variation is close to 1 ppm, shifting from 5.5 ppm at 50% loading and then down to 4.75 ppm 15%. The strongest and sharpest peaks appear in the middle-ground loading levels of around 30%. Higher

loadings appear to possess broader components to their populations. As the loading ratio decreases under 30% the overall intensity of the NA peaks is falling significantly and the intensity of the silanol peak is increasing. We are also seeing development of the hydrogen bonding water peaks between 1-2 ppm as the loading ratio decreases further to 20-15%. We can therefore interpret that at a higher loading of NA the pores are filled by aggregated NA molecules, resulting in slightly broader peaks. As this loading ratio decreases there will be more space generated for molecules of NA to move freely. This can also mean that their inherent mobility makes them more liquid-like and therefore the signal increase we see is a more isotropic form of NA. Then as the loading ratio decreases further there is physically less NA present to generate that same mobile isotropic environment, our signal is decreasing and the silanol groups are taking up more of the individual spectra.

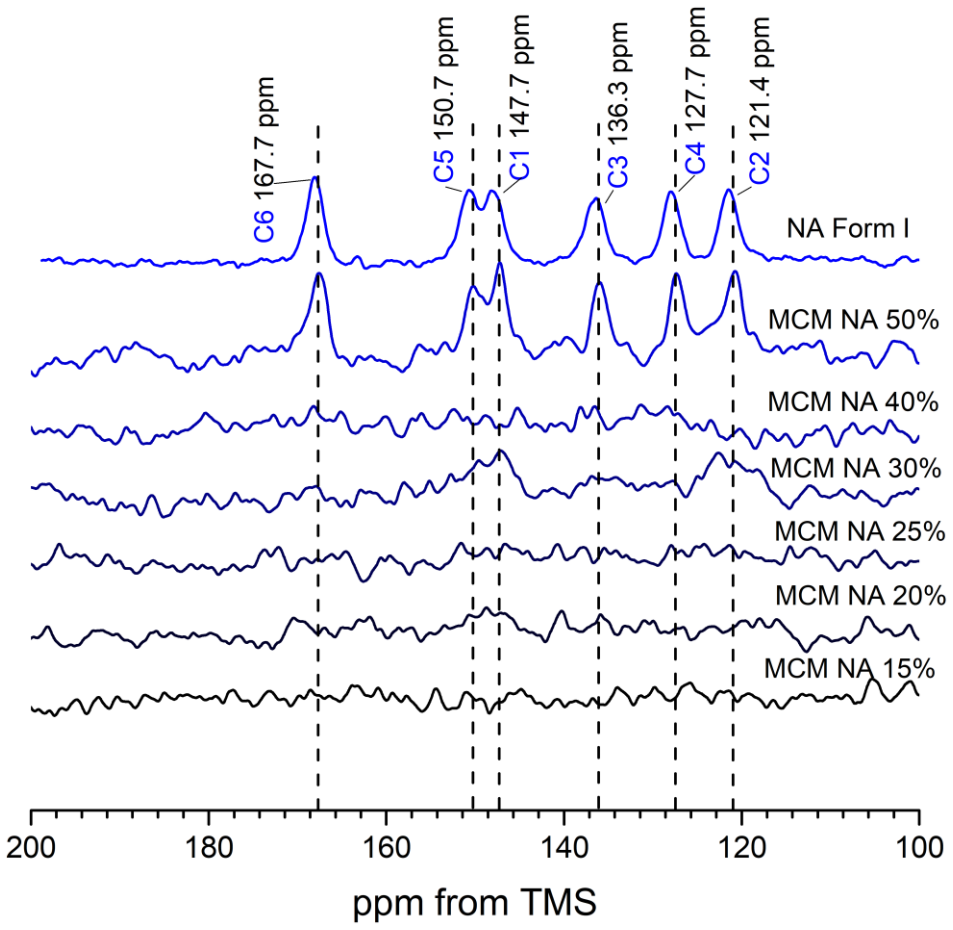

Figure 5-22 ^{1}H-^{13}C CP/MAS solid-state NMR spectra of MCM-41 loaded with NA cocrystal at 298 K at various loaded levels indicated by the percentage of loading of NA. Peak matching NA in black where appropriate

Figure 5-22 shows the room temperature ^{1}H-^{13}C CP-MAS spectra of the MCM loaded materials with NA form I for comparison. This was collected under MAS conditions and so we can identify the crystalline material as polymorph I. At high loading of 50% there is a set of peaks that correspond to NA form I. The corresponding peaks are not present at 40% loading. From sorption measurements we know that the pores are completely filled above 40% loading, therefore the peaks that we see at 50% loading are most likely that of NA form I that is loaded outside the pores of MCM-41. This would hence imply that the material loaded inside the pores is quite mobile as we are unable to detect any signal using carbon cross-polarization methods.

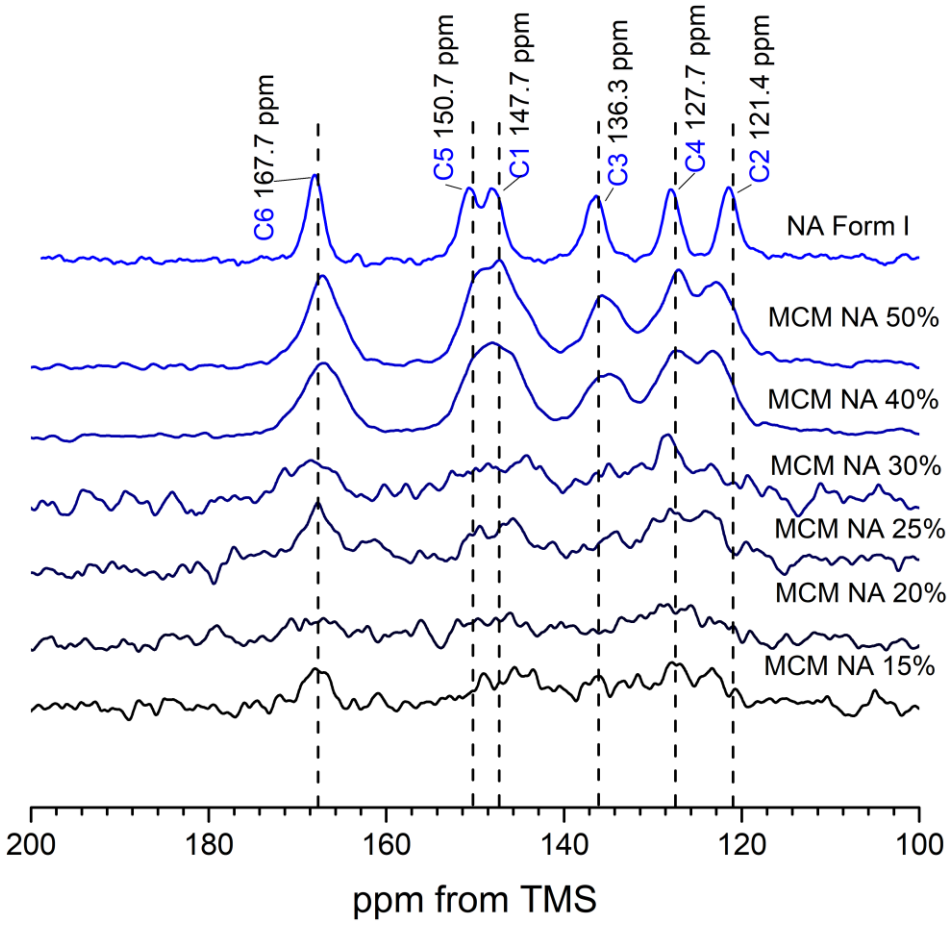

Figure 5-23 ^{1}H-^{13}C CP/MAS solid-state NMR spectra of MCM-41 loaded with NA cocrystal at 223 K at various loaded levels indicated by the percentage of loading of NA. Peak matching NA in black where appropriate

When the temperature is reduced there is a change in the intensities of the peaks in the loaded materials. When compared to the room temperature spectra, it can now be observed that peaks are present at 40% loading quite clearly. There are also small noise peaks, which are extremely broad, that have now appeared in low loaded materials. At room temperature we observed peaks related to NA

form I in the material loaded at 50%, but no peaks were observed at 40%. By freezing the system, we are slowing down the molecules of NA inside the pores to the point where the CP efficiency of the system is increased to where we begin to see signal. At 40% loading we know that MCM is fully loaded with NA material inside the pores from sorption isotherms, however the status of the molecules must be extremely mobile and disordered at room temperature because we do not see any crystallographic evidence of long-range order. The peaks observed at low temperature are extremely broad when compared to form I's profile. This would be expected if the pores are filled by an amorphous species, where the chemical shifts are more isotropic and do not resemble form I that much. There is some evidence to support this hypothesis from the shifting of the peaks here at low temperature. The C2 carbon of NA form I at 121.4 ppm shifts downfield in the loaded materials at 50 and 40%, while the C6 shifts upfield. All these peaks have then become extremely broad and it is difficult to distinguish C5 and C1, which now form one broad environment just under 150 ppm.

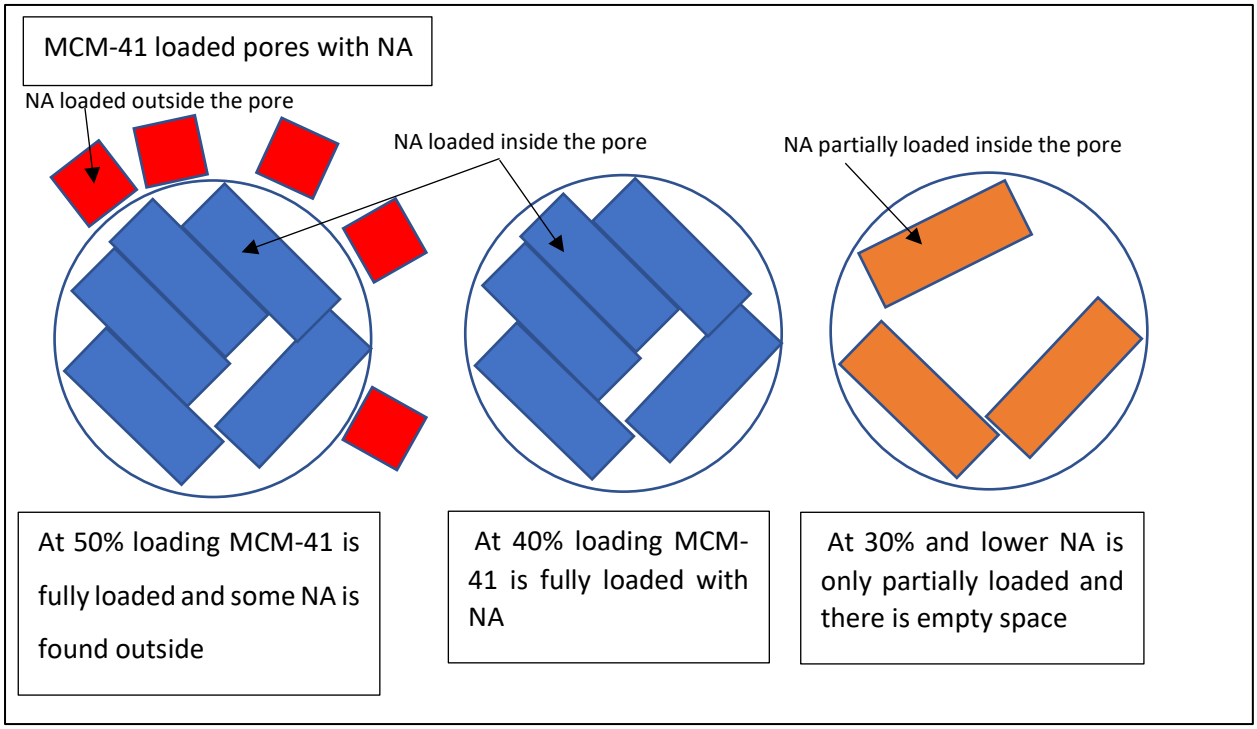

Figure 5-24 Pore arrangement of NA in MCM-41 at fully loaded and partially loaded ratios

5.4 Incorporation of NA into SBA-15 mesoporous silica

Of the mesoporous silicas selected, SBA-15[54,141] is an interesting candidate to compare to MCM-41. SBA-15 has pore dimensions roughly double the size of MCM-41 – around 6-7 nm depending on the produced batch of material. The limiting factor of diameter of the pore essentially restricts the possibility of creating and sustaining long-range order. By doubling that diameter with SBA-15 we

open up the small possibilities of allowing structurally ordered packing, however that possibility will most likely be influenced by cell dimensions of the material being loaded. Smaller cell dimensions such as Z'=1 structures are the most likely candidates, although smaller packed Z'=2 may also be a possibility. This in turn could result in different motifs and crystallisation pathways for NA to proceed on.

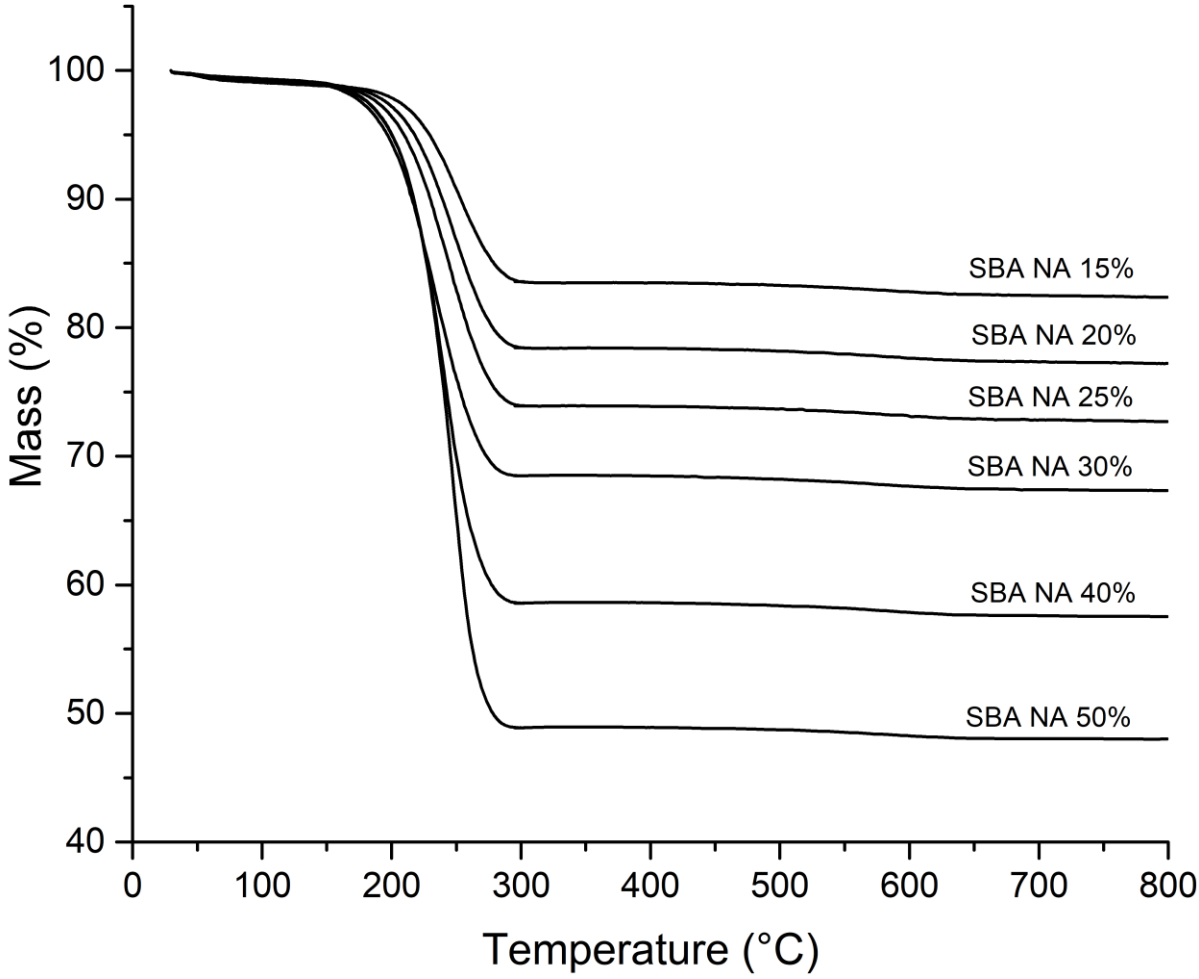

Figure 5-25 TG curves of SBA-NA. Loading levels indicated as wt% of silica to NA cocrystal.

Figure 5-25 is the TGA thermogram for the SBA loaded materials, showing very similar behaviour to that of MCM-41's analysis. Each sample of loaded material loses the organic component of NA it the loading level that has been reported. The only real difference between the SBA and MCM-41 curves is for the 50% loading, which in SBA-15 has a much smoother profile, similar to those of the other loaded materials. In MCM-41 there is a slight hump in the 50% loaded TGA curve.

Table 5-7 shows the BET surface areas and the calculated total pore volumes for each loading ratio. The BET surface area decreases with increasing loading ratio. The total pore volume, however, appears

to vary depending on sample. A lower loading ratio does give a higher pore volume, but the relationship is not a linear decrease with respect to loading ratio. This is contrary to SBA-15 loaded with FFA/NA. It appears that when loaded with NA at 50% the pores are not completely filled. With FFA/NA there is around 20 m^2/g available BET surface area, however with NA there is 102 m^2/g of available surface area. Likewise, when the pore volume is compared to SBA FFA/NA series of samples (0.07205 cm^3/g at 50%) against NA at 50% (0.239 cm^3/g) there is definitely physical volume left inside the SBA-15 loaded with NA.

Table 5-5 BET surface area (calculated as a multi-point BET in the linear region of the isotherms) and Pore Volume (calculated at *P/P_0 of 0.99)*, Pore Diameters calculated from BJH method[66]

Loading Ratio (% weight to SBA-15 weight)	BET Surface Area(m^2/g)	Total Pore Volume (cm^3/g)	Pore Diameter (nm)
0	902.8	0.744	7.60
15	398.2	0.770	8.09
20	376.5	0.806	7.39
25	295.2	0.622	7.38
30	270.2	0.624	6.78
40	167.3	0.391	6.80
50	102.5	0.239	6.79

The interesting difference between SBA and MCM is a change in the diffractogram from PXRD (Figure 5-26). In MCM-41 there is only evidence of diffraction peaks in the highest loaded sample at 50% loading. We also believe that the pores of MCM-41 at 50% loading are overloaded with NA material. Therefore, the peaks in PXRD we see as a match to form I are most likely from NA form I loaded outside the pore space. Here in SBA at 50% loading there is clearly a diffraction pattern, be it one that is quite broad without any sharp characteristics. However, there is a peak centred on 17°. This peak is very broad, but when compared to the PXRD pattern of NA form I, there are no peaks in that region that could match it. Likewise, with NA form II, even though there are two peaks nearby, at 17.6 and 18.2° respectively, they are most likely far enough away that they do not represent NA form II. This would

imply that the form that has recrystallised inside SBA is a new polymorph of NA. When the loading level is reduced to 40% and lower, the new peaks are not able to be separated or are not present, the amorphous background of the SBA-15 dominates the diffractogram.

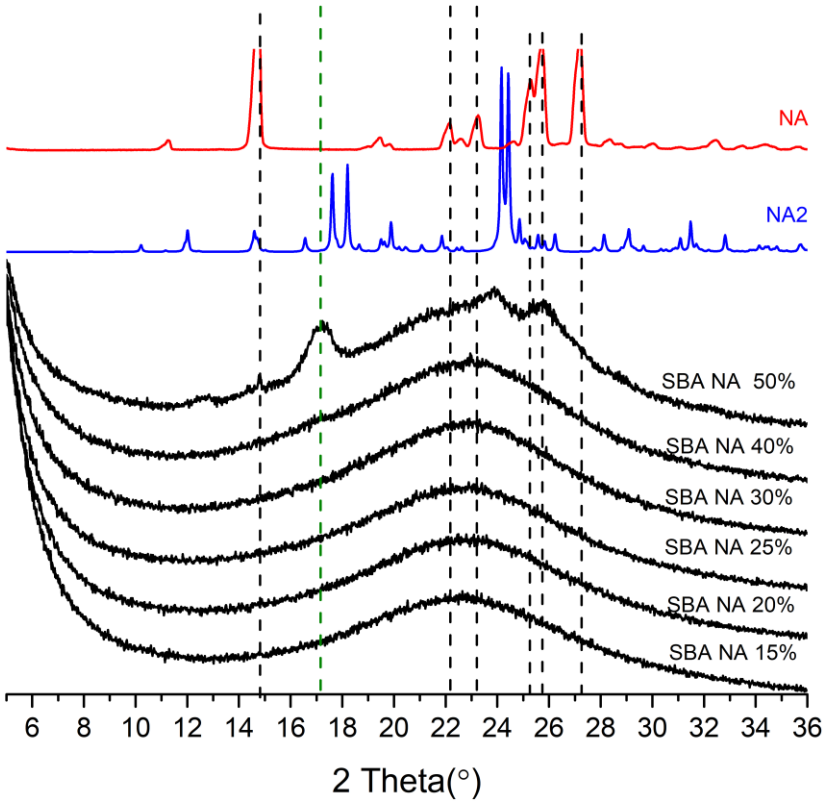

Figure 5-26 PXRD patterns of SBA-15 silica loaded with NA at various loading levels (black lines indicate matching NA form I, green line indicates a peak belonging to unknown polymorph, guest loading ratio (in wt%)

Further evidence to support the idea of a new polymorph inside is illustrated in the DSC thermogram (Figure 5-27). The highest level of loading, 50%, where the new PXRD peaks are found has a clear melting point at 60.5 °C which is not close to the melting point of NA form I at 129 °C. We have demonstrated before[65,72] that melting a crystalline compound inside the pores can have an effect on the melting point, usually causing a depression of around 10-20 °C from the bulk melting point. However, the melting point for NA in this sample is around 75 °C below the melting point of form I. This would further establish that at room temperature the polymorph that is inside the pores is not form I and from the paper where form II was published, we know it has a melting point 108 °C, therefore again showing it is most likely not form II either. The endothermic peak at 60.5 °C could be a transition from this unknown form to form I or II.

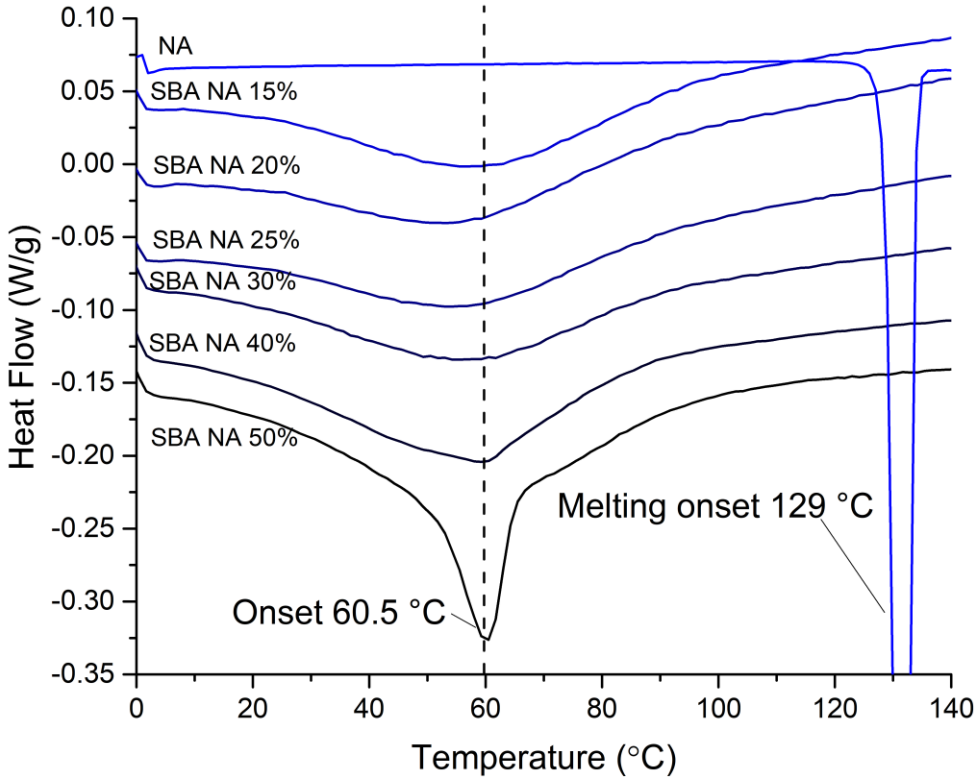

Figure 5-27 DSC thermogram of SBA-15 loaded with NA, guest loading ratio (in wt%)

From the data presented so far regarding SBA, there is a possibility that the NA inside is a different polymorph to that of form I and II. Therefore, it is difficult to present an accurate diagrammatic representation of the possibilities with regards to the packing of SBA because we do not have any cell parameters for this form to base repeat drawings on. The PXRD diffractogram is too broad and does not contain enough peaks in order to attempt a unit cell search and the DSC thermogram shows a melting point at only 50% loading. This form most likely only existed in characterizable quantity at this high loading, because when the sorption data is consulted, we can clearly see that a significant amount of space that has become available when the loading ratio is decreased to 40%. Therefore, the best assumption that can be made about the polymorph is that it most likely has a very small unit cell that has allowed it to stack across the diameter and length of the pores in a significant way that shows at property consistent with a crystallographic phase. The diagram of filled (Figure 5-28) and partially filled (Figure 5-29) pores have been drawn with the cell dimensions of form I for comparison, and when it is compared to the a fully loaded SBA with FFA/NA the number of repeating molecules is around three times larger. When compared to MCM fully loaded with NA, there is roughly double the number the cells present due to the fact that SBA has twice the diameter of MCM.

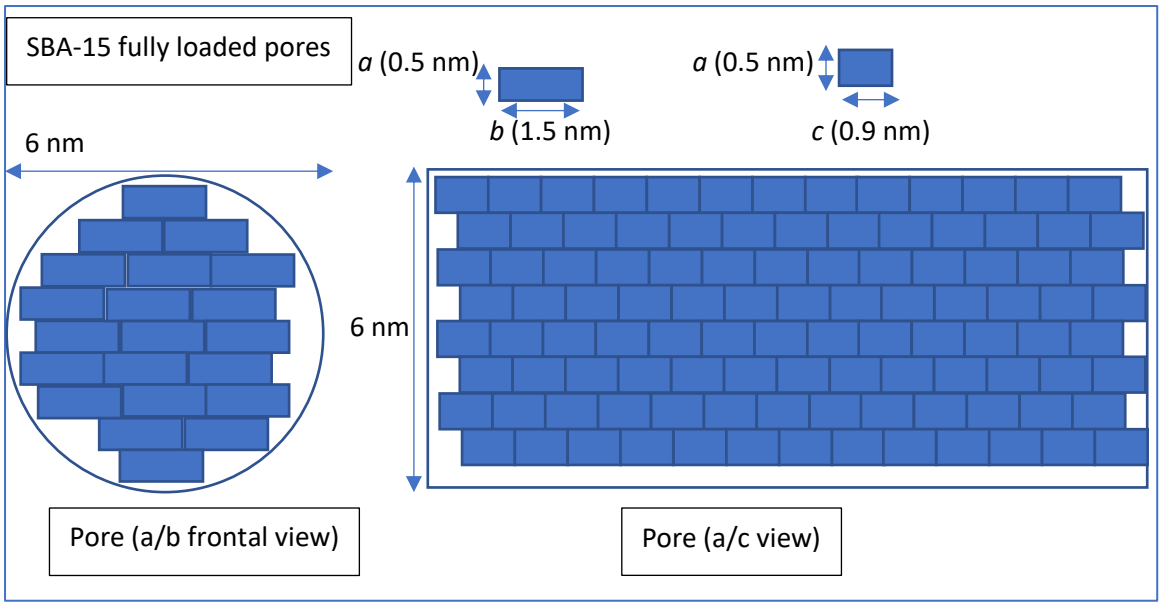

Figure 5-28 SBA-15 Fully Loaded Pore diagram of frontal and perpendicular view of pore space. Blue rectangles represent NA molecules to scale with the pore dimensions.

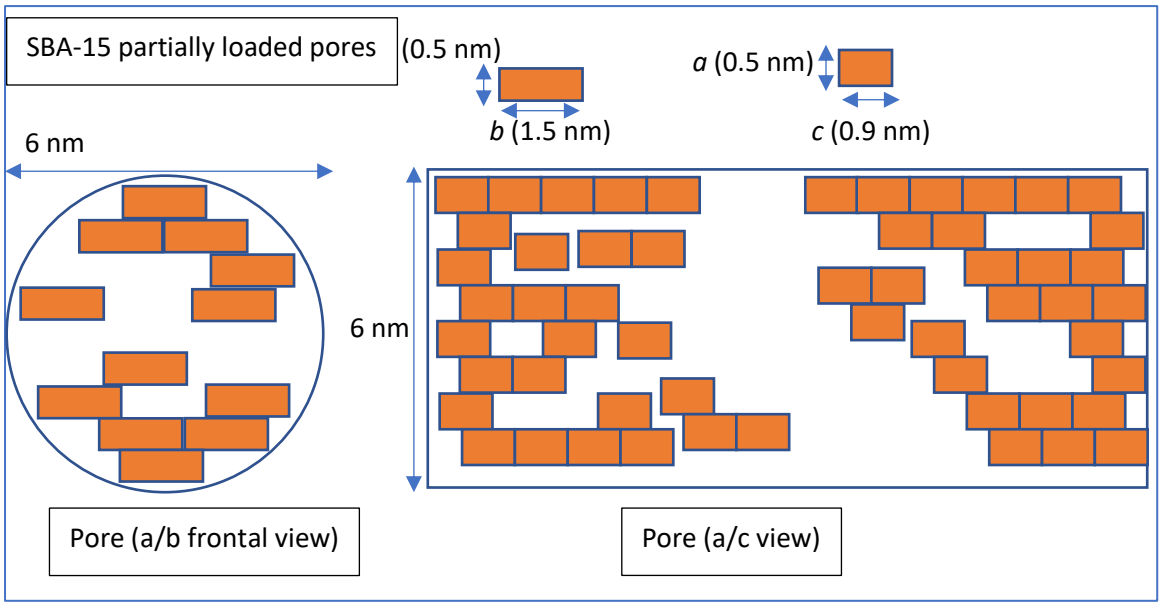

Figure 5-29 SBA-15 Partially loaded pore diagram of frontal and perpendicular view of pore space. Orange rectangles represent NA unit cells to scale with the pore dimensions.

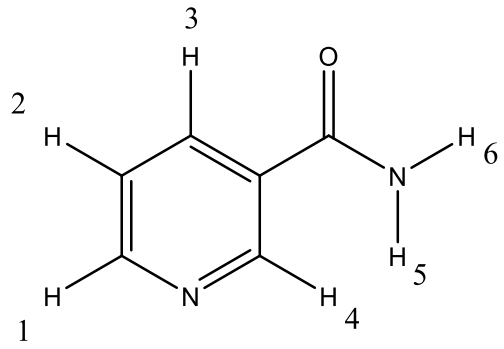

Figure 5-30 Proton site labelling of the nicotinamide molecule

The room temperature ^{1}H MAS NMR spectra (Figure 5-31) of the SBA series loaded with NA contrasts with MCM series when looking at the sharpness of peaks. In MCM-41 at the higher loading of 50-40% the proton peaks are relatively broad and undefined whereas in SBA at high loadings of 50-40% the ^{1}H peaks are much sharper. There are three populations centred on 8.15 ppm (8.5 (H6), 8.1 (H5) and 7.9 (H4) ppm). The three other proton populations (H1-3) at 6.9 ppm, which could not be resolved individually are the aromatic protons on the opposite side of the pyridine ring. The final peak at 5.1 ppm belongs to the silanol ^{1}H population on the surface of the pore. When the loading ratio is decreased the intensity falls sharply, and at 30% loading and lower it is difficult to distinguish and assign specific populations to individual peaks. The only peak to show a small increase in its intensity is at 15% loading just under 5 ppm when compared to the other environments.

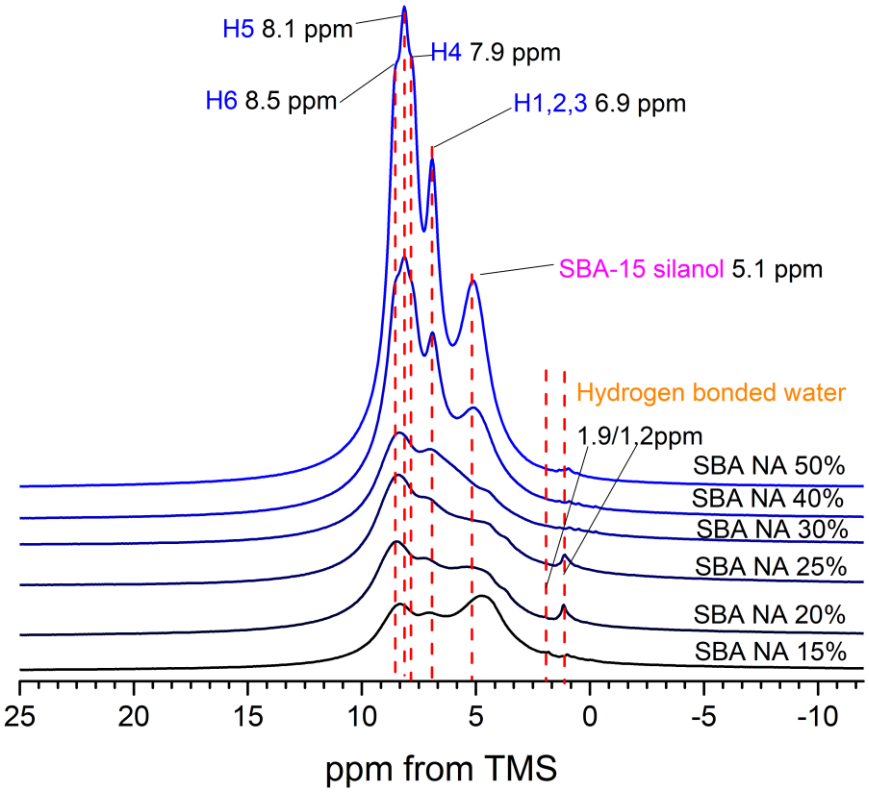

Figure 5-31 ^{1}H MAS solid-state NMR spectra of SBA-15 loaded with NA at 298 K, guest loading ratio (in wt%)

When the SBA samples are cooled to 223 K, we see a behaviour in the ^{1}H MAS NMR spectra (Figure 5-32) similar to other loaded silica samples. The peaks have significantly broadened, therefore assigning separate peaks to specific proton environments it much more difficult. The amidic protons and aromatic proton H5, H6 and H4 have mostly blended into one population centred on 7.9 ppm, whereas the silanol protons have a sharper more distinguished peak around 4.9 ppm. By cooling the system, we are reducing the mobility of nicotinamide. This means that a much broader range of chemical shifts becomes available due to different pockets of NA orientating in different ways. As we reduce the amount of NA inside the pores and increase the space, we are giving NA molecules less a lower probability of being able to stack and arrange themselves. This also increases the mobility of the NA molecules and sharpens the peaks more due to the NA molecules appearing more liquid-like and therefore more isotropic.

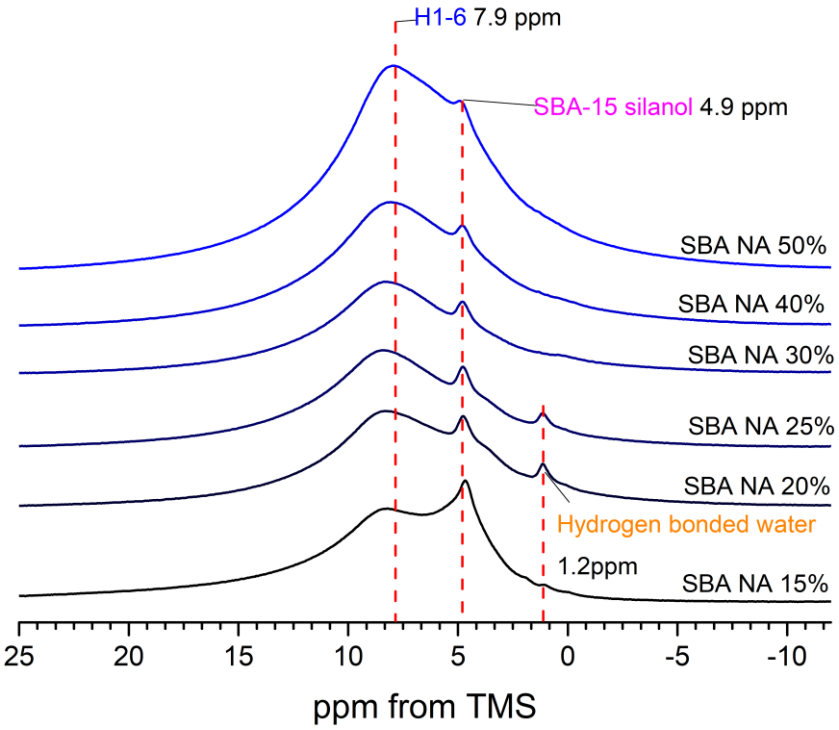

Figure 5-32 ^{1}H MAS solid-state NMR spectra of SBA-15 loaded with NA at 223 K, guest loading ratio (in wt%)

^{1}H spectra (Figure 5-33 and Figure 5-34) for NA loaded SBA were also recorded at 19.96 T using a 1.3 mm rotor at 55 KHz MAS rate. It should be noted that due to time constraints of the measurements, the 40% loaded sample was not studied. There are clearly four populations that can be attributed to NA, the resonances located at 8.6, 8.1, 7.8 and 6.9 ppm at 50% loading which differ in chemical shift to that of MCM-41. In MCM-41 we observed more of the aromatic protons, however in SBA-15 those are not possible to assign individually. However, there is enough resolution to distinguish the amidic protons H6 and H5 at 8.6 and 8.1 ppm, followed by the aromatic proton H4 at 7.8 ppm. There is a small silanol group peak also located at 5.1 ppm. One of the main differences in SBA's spectra is that the overall location of the chemical shifts appears to shift downfield as the loading ratio is decreased, most obviously for the aromatic protons H1, H2 and H3. These start at 6.9 ppm at 50% loading and then by the lowest loading of 15% are residing at 7.4 ppm. At lower loadings as with MCM-41 there are some hydrogen bonding populations occurring between 1-2 ppm as the amount of space that can be taken up by water from air moisture content is increased. We know that the pore diameter is roughly two times larger than MCM-41, and from PXRD the form that is present is most likely not that of form I or II. However, from the ^{1}H chemical shift there is no significant difference apart from slight broadening of peaks. There is a small contamination peak in the 25% loaded sample at around 1.5

ppm, we believe this to belong to a small amount of ethanol that was used to clean the rotors between different experiments.

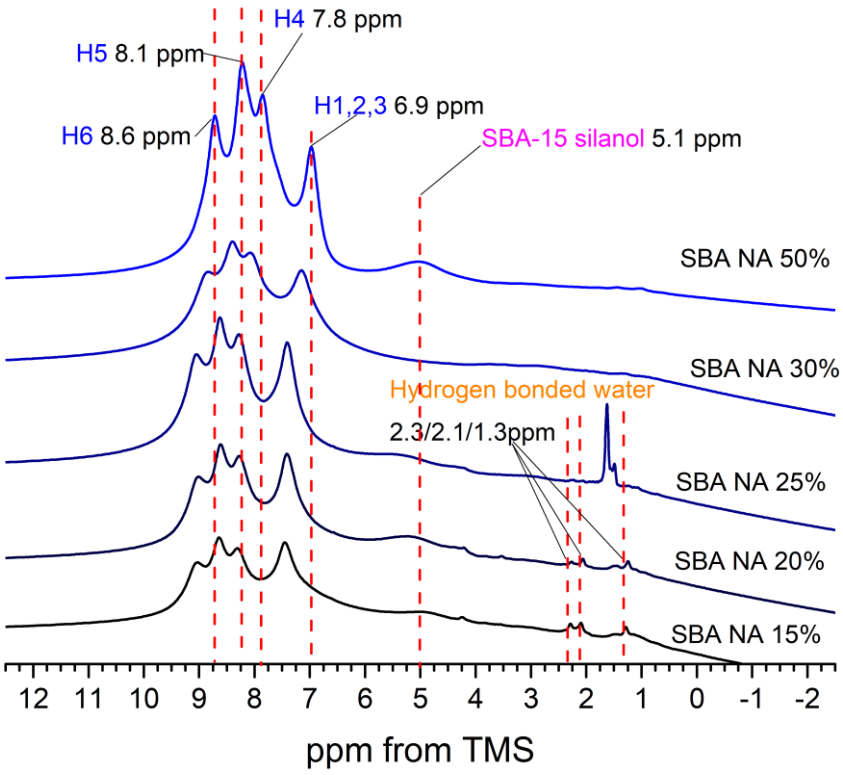

Figure 5-33 High-field (19.96 T) at 55 KHz ^{1}H MAS solid-state NMR spectra of SBA-15 loaded with NA at 293 K, guest loading ratio (in wt%), 40% loading is missing due to data not being collected

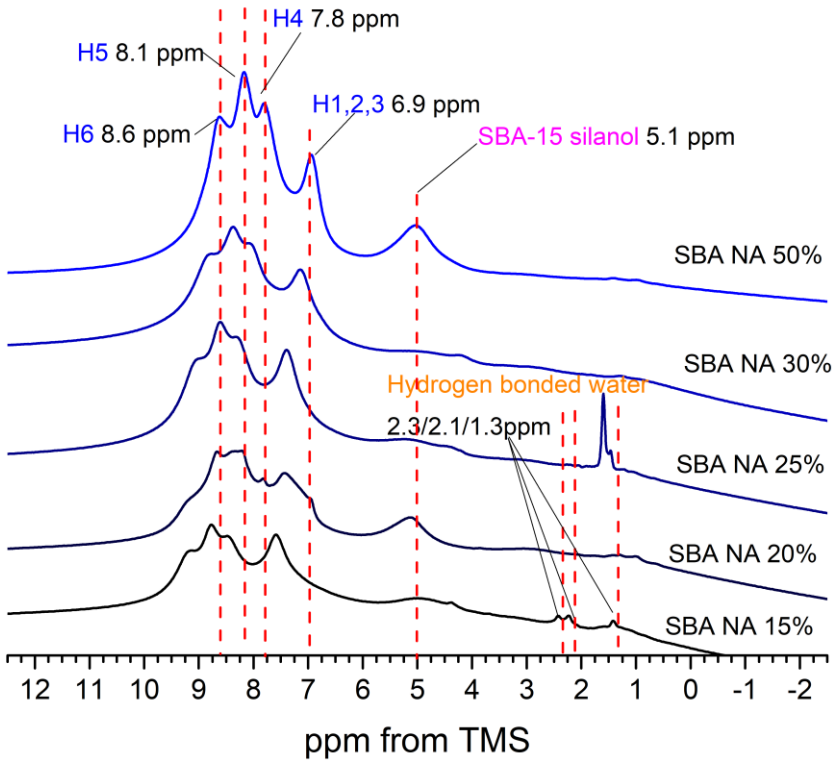

Figure 5-34 High-field (19.96 T) ^{1}H MAS solid-state NMR spectra of SBA-15 loaded with NA at 273 K, guest loading ratio (in wt%), 40% loading is missing due to data not being collected. MAS rate was 55 KHz.

The ^{1}H-^{13}C CP/MAS NMR spectra (Figure 5-35) provide the true insight into the characteristics of the polymorph in the pores. As previously shown, there are six carbon environments in nicotinamide, its form I structure being Z'=1, which should give six populations in the ^{1}H-^{13}C CP/MAS NMR spectra. However, it is clear that the polymorph inside the pores has seven carbon environments, some of which do not correspond with form I. At room temperature in SBA the NA form has seven clear peaks at a loading of 50%, which backs up the PXRD diffractogram's implication of a different polymorph. As the loading level drops to 40% there is some small indication of peaks that resemble those same populations, however they are only just above the baseline noise. There are two implications due to the extra peaks in the ^{1}H-^{13}C CP NMR spectra. The first is that after the melting and subsequent cooling of the molten NA inside the pores, there has been enough space for the form the crystallise and rigid enough to allow for effective magnetisation transfer through CP because we are able to see peaks. If the state of NA inside the pores was amorphous or extremely mobile, as in MCM-41, peaks would either be extremely broad or not present in the timescale of our measurements. The second implication is that the form that has crystallised inside SBA is most likely not form I or form II. The evidence present is that of the difference PXRD diffraction pattern. In DSC there is also a melting peak

evident much lower than expected of form I or form II. The melting peak is also lower than what we have come to expect from a depressed melting peak of a form, which is usually between 10-20 °C lower.

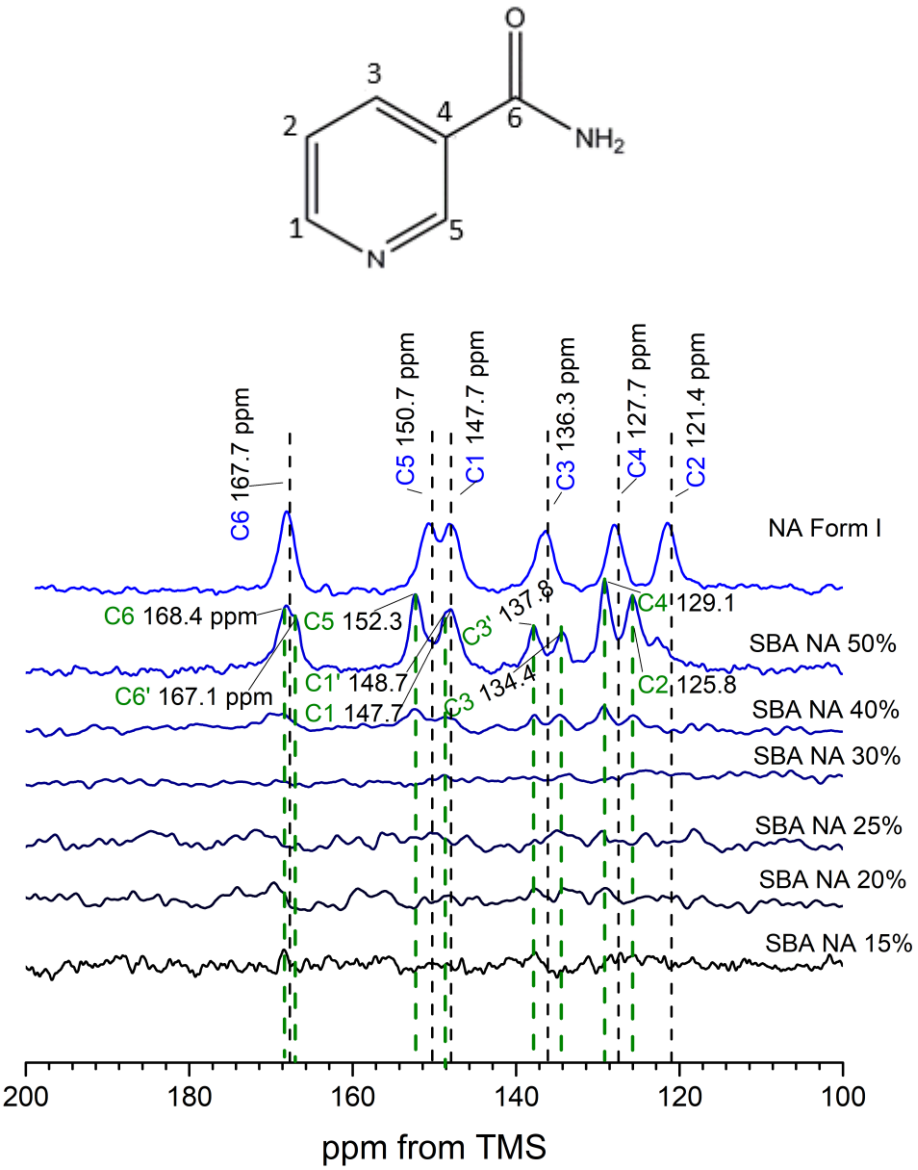

Figure 5-35 ^{1}H-^{13}C CP/MAS solid-state NMR spectra of SBA-15 loaded with NA at 298 K at various loaded levels indicated by the percentage of loading of NA. Peak matching NA in black where appropriate, unknown form peaks indicated in green.

Table 5-6 NMR assignment of ^{13}C spectra of NA

Carbon No.	C1	C2	C3	C4	C5	C6
NA Form I	147.7	121.4	136.3	127.7	150.7	167.7
Unknown polymorph	147.7 148.7	125.8	137.8 134.4	129.1	152.3	168.4 167.1

Additional resolution in the spectra of the polymorph is gained when the sample is cooled to 233 K (Figure 5-36). The peaks of this polymorph are clearly visible at 50% loading with clear line shape and different shifts when compared to form I. Also, there is evidence that at lower loading levels we are able to detect this polymorph all the way down to 20% loading. However, its peaks become extremely broad. This implies that the mobility of NA inside the pores is being directly affected by the cooling, the same affect we see with FFA/NA being loaded inside the pores. When considering the assignment of the peaks we have attempted to assign them based on chemical shift and which the assumption that the structure is Z'=2. This means that there will be two peaks for each carbon present in NA. The amide carbon C6 is most likely located at 168.4 ppm with an additional C6' at 167.1 ppm. The carbons next to the pyridine nitrogen, C5 and C1 are most likely be at 152.3 and 148 ppm. However, below these chemical shifts there is an extra peak and other peaks have shifted upfield. C2, which was present at 121.4 ppm in NA form I has most likely shifted over by 4.4 ppm in the unknown polymorph spectrum to 125.8 ppm.

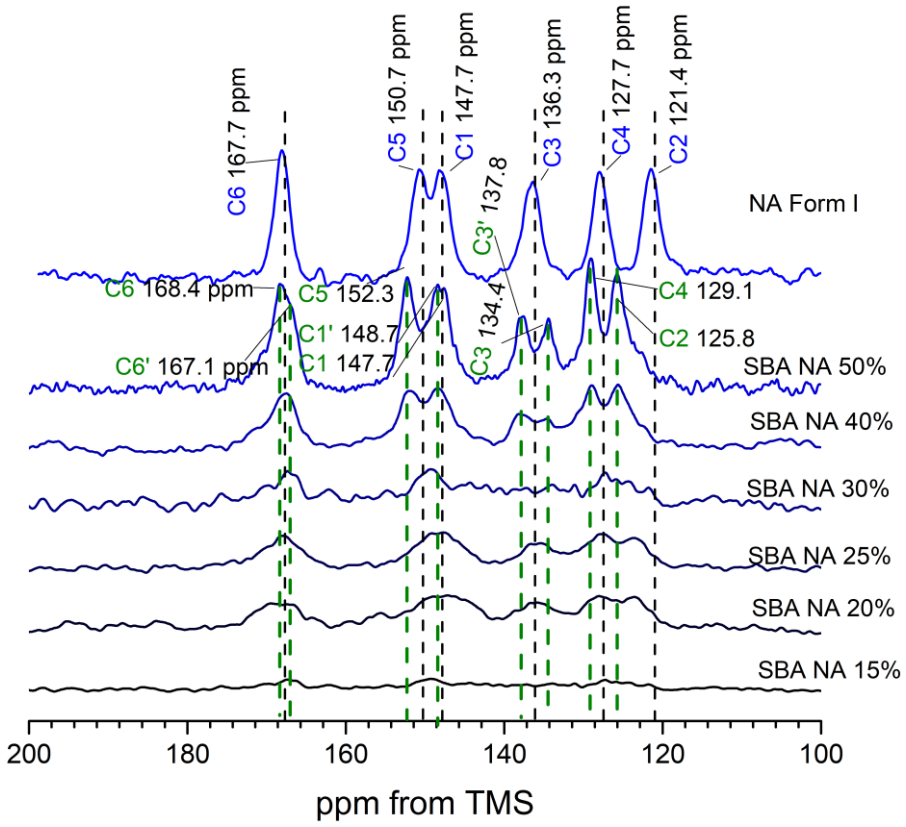

Figure 5-36 ^{1}H-^{13}C CP/MAS solid-state NMR spectra of SBA-15 loaded with NA at 223 K at various loaded levels indicated by the percentage of loading of NA. Peak matching NA in black where appropriate, unknown form peaks indicated in green.

Using this information, a series of experiments were designed in order to probe the crystallisation of this new polymorph by using a technique called CLASSIC[142] (Combined Liquid and Solid-State In-situ Crystallisation). This technique focuses on a series of time resolved experiments that probe the mobility and crystallinity of a sample using solid state NMR. Three experiments are performed to monitor the status of a compound that has been induced to crystallise. The first experiment is a standard proton spectrum in order to probe standard interactions. The second uses ^{13}C direct excitation (under High Powered Decoupling, HPDEC) with a low recycle delay and high number of scans. This serves to probe the most mobile and more liquid-like structures in the sample. Due to the short recycle time, the magnetisation is not able to fully recover except for in carbons that are able to relax through spin-lattice relaxation mechanisms to surrounding nuclei. The only nuclei that are capable of this will be the most mobile ones. The final experiment is a traditional ^{1}H-^{13}C CP/MAS NMR (cross-polarisation) experiment also on ^{13}C using ^{1}H as the polarisation source. This experiment serves to explore the more rigid and slow-moving components of the system, relying on efficient CP transfer to carbon nuclei. This is the best indicator of when the NA polymorph has fully recrystallised. By

repeating these three measurements over a time period it is possible to provide an insight into the crystallisation processes inside the pores. However, there are a few limiting factors that have to be considered. The primary issue that the process of crystallisation is a time-resolved mechanism, therefore if the method used to induce crystallisation results in crystallisation of the sample, we may not be able to detect any mechanistic components in the spectra we acquire. This problem also highlights the second issue with this methodology, which is the resolution of our experiments. After optimisation on a sample of SBA-15 with NA at 50% loading, the number of scans and recycle delays were selected for each experiment to allow both resolution of peaks but also the maximum number of experiments were recorded as a trade-off between time resolution and spectrum quality.

Table 5-7 Experimental conditions in the CLASSIC methodology for each experiment type

Experiment Type (CLASSIC)	Number of Scans	Recycle Delay (s)	Approximate time of experiment (minutes)
^{1}H	16	5	1.3
^{13}C {^{1}H} HPDEC	256	2	8.5
^{1}H-^{13}C CP	160	20	53.3

The result of this is that one individual segment of CLASSIC takes just over 63 minutes, accounting for the time taken by software/hardware to move onto the next experiment. The majority of this is spent performing the CP experiment. The advantage this experiment is that it allows us to track and monitor the progress of one form changing to another. From the DSC data performed on SBA we know that there is a melting peak present at around 60°C, therefore if we are firstly able to observe the melting of the polymorph in situ, we are able to know whether this affects the outcome of crystallisation. Therefore, before CLASSIC experiments we monitored the effect of higher temperatures. The sample chosen for these experiments was SBA-15 loaded at 50% with NA as this is the only sample in the SBA series that presented the unknown polymorph in a distinguishable manner. These were run using the same 4mm rotor at 10 KHz MAS rate as the previous experiments for a comparison, the only difference being the rotor cap which was switched from KEL-F to VESPEL, which allows the rotor to be spun at higher temperatures of up to 80°C. After the optimisation of recycle delays and number of scans were performed on the sample. The temperature of the probe was increased in 10°C increments and each of the stated experiments was performed on the sample. As DSC had shown a melting temperature of

60°C it was decided that 70°C would be a sufficient temperature to melt the NA component fully and not risk melting the rotor cap.

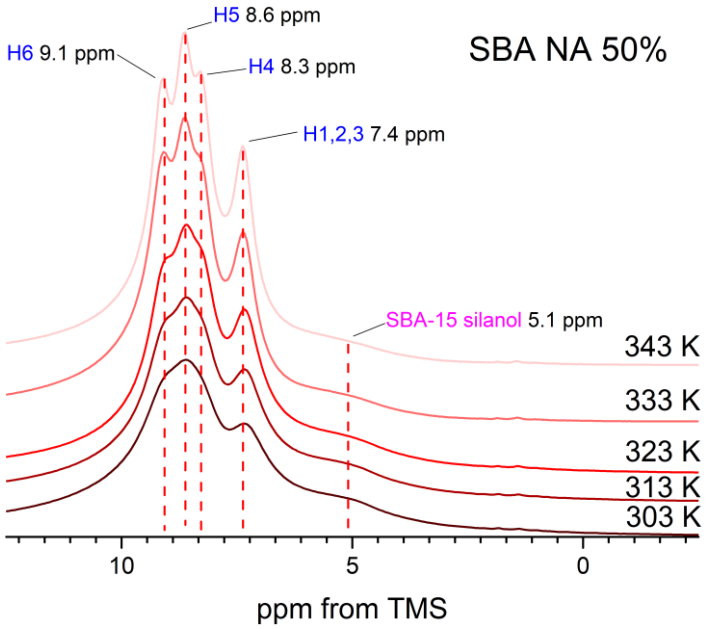

Figure 5-37 ^{1}H MAS solid-state NMR spectra of SBA-15 loaded at 50% with NA at temperatures between 303 K and 343 K

The ^{1}H spectra (Figure 5-37) show that as the temperature is increased the line widths of the peaks decreases. The silanol environment's overall intensity falls as the temperature increases. By the 333 K (60°C) the visibility of peaks increases significantly, possibility indicating the increased mobility of the polymorph or an interconversion to another polymorph though it is unclear which. The increase in mobility present could also be due to partial melting of the polymorph within the pores, this would be a plausible argument to make considering the sharpening of the peaks compared to room temperature.

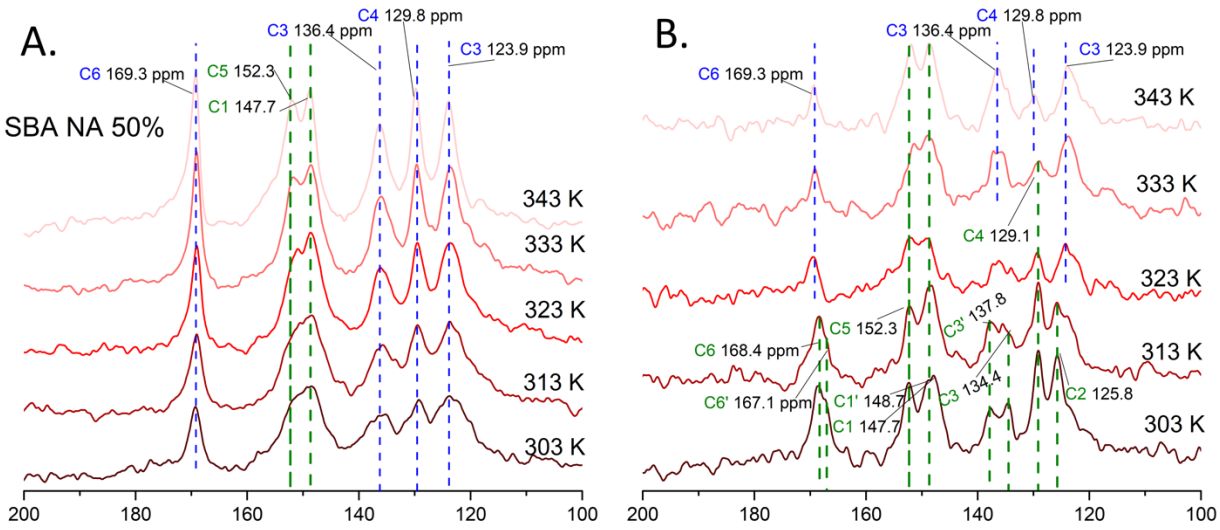

Figure 5-38 A. $^{13}C\{^{1}H\}$ HPDEC spectra at low recycle delay and **B.** ^{1}H-^{13}C CP/MAS solid-state NMR spectra of SBA-15 loaded at 50% with NA at between 303 K and 343 K. Peak NA unknown form in green, devolved as temperature was increased in blue.

The ^{13}C data from the HPDEC (Figure 5-38-A) and CP (5-38-B) spectra give a clearer indication of changes as the temperature increases. Initially the CP spectra show the unknown polymorph clearly with the seven carbon environment peaks present as opposed to the six that would be present for NA form I. The HPDEC spectrum initially is quite broad and does not have very clear environments that can be identified. Carbon sites at 150 ppm in the CP spectra clearly show two peaks whereas the HPDEC shows one extremely broad environment. Also, the lower portion of the spectrum in the HPDEC struggles to show definition in other peaks. This shows that within the SBA-15 sample the mobility of NA is quite limited, there is a good signal coming from CP which is more reliant on rigid ^{1}H-^{13}C interactions and the HPDEC signal is extremely broad for all the aromatic carbons except for the amidic carbon which can easily be distinguished around 170 ppm. As the temperature increases the CP signal intensities begin to fall until at 323K (50 °C) the populations that resemble the unknown polymorph have almost been lost to the baseline noise and the furthest upfield peak at 125.8 ppm moves further upfield to 123.9 ppm. In between these temperatures at 313K there appears to be a transitional population which begins evolving at 124 ppm. The HPDEC spectrum at 333K shows the exact opposite with regards to signal intensity and resolution. The ^{13}C environments at 150 ppm separate into distinguishable peaks at 152.3 and 147.7 ppm and the other carbon peaks have sharpened. At 343K it becomes very clear from the CP spectrum that the unknown polymorph has most likely melted or converted to another form as the peaks have broadened and shifted, the clearest example of this

being the previously discussed change of the most upfield population from 125.8 ppm to a much clearer peak centred on 124 ppm. Interestingly the pair of peaks at ca. 150 ppm have since become sharper as the temperature has changed from 50°C to 70°C once more. The duo set of populations at 137.8 and 134.4 ppm have also merged into a single population at 136.4 ppm. This experiment is not strictly a full CLASSIC because we are changing the temperature, however the primary purpose is to investigate the polymorph through heating in-situ because we are able to see that the polymorph melts either fully or partially around 60°C in our DSC experiment.

The second experiment performed, which does employ the CLASSIC methodology, used the same sample as the first experiment and immediately after the first experiment had concluded. Based on the conversion or melt of the polymorph inside the pores from the prior experiment, the setup for this experiment involved quenching the sample immediately after the final CP spectrum was acquired at 343 K. The sample was quenched to 298 K, tuned and matched, then repeating set of ^{1}H, ^{13}C{^{1}H} HPDEC and ^{1}H-^{13}C CP/MAS experiments were queued over a long period of time. This was to probe if the highly mobile NA in the pores was to back into the unknown polymorph. After a period of around 133 hours (5.5 days) the experiment was halted. We can see in the proton spectra (Figure 5-39) there is not that much of a visible change except for slight loss of intensity of the aromatic protons H1, H2 and H3 at around 7.4 ppm. The silanol group peak at 4.9 ppm is difficult to observe, however also loses some intensity of the signal. The amidic protons and final aromatic proton populations do not appear to change much. Compared to previous spectra performed on this sample, SBA loaded with NA at 50%, the spectra appear significantly broadened. There are not any real conclusions that can be drawn from the ^{1}H spectra.

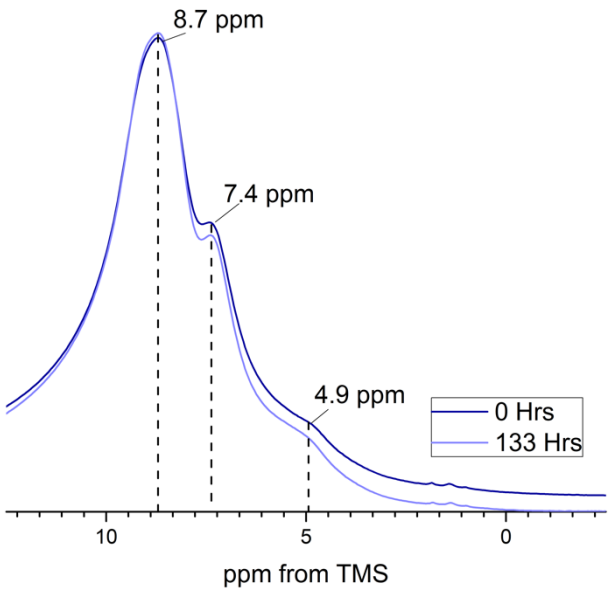

Figure 5-39 ^{1}H MAS solid-state NMR spectra of SBA-15 loaded at 50% with NA 0 hours after the quench to 298 K then 133 hours while being held at 298 K

The ^{13}C data from the HPDEC (Figure 5-40-A) and CP (5-40-B) spectra performed on the sample reveal that the sample has not recrystallised back into the unknown polymorph. The initial recorded CP spectrum has a lot of noise and is difficult to interpret. Previously at 343 K the CP recorded some broad populations, however the population at 150 ppm was clearly two distinct peaks, when quenched to room temperature this has now merged into one broad environment that could be interpreted as having multiple peaks present however due to the amount of noise it cannot be said with a degree of certainty. The HPDEC after quenching has broadened significantly, with the clear populations for each individual carbon now overlapping with each other and again the population at 150 ppm, C1 and C5, becoming one environment. Therefore, after the initial quench to room temperature it is difficult to state the exact form of NA as it may have just started recrystallisation from the melt or it has not fully converted to another polymorph. As time progressed the state of the CLASSIC was checked and additional time added as it had appeared that full recrystallisation had not occurred after 3 days. The final HPDEC has not changed much aside from some peak intensities changing slightly. The CP spectrum has finally resolved the carbons C1 and C5 at 150 ppm and other points of the spectrum have sharpened up to the point where populations are distinguishable. There is some background noise influencing the furthest upfield shift at 120 ppm, however it appears quite conclusive that the unknown polymorph that was in the pores prior to melting has not recrystallised. The conclusion we

can therefore draw from this melt-quench CLASSIC experiment of the unknown polymorph in SBA that it is more probable that polymorph interconversion occurred when the form melted above 60°C.

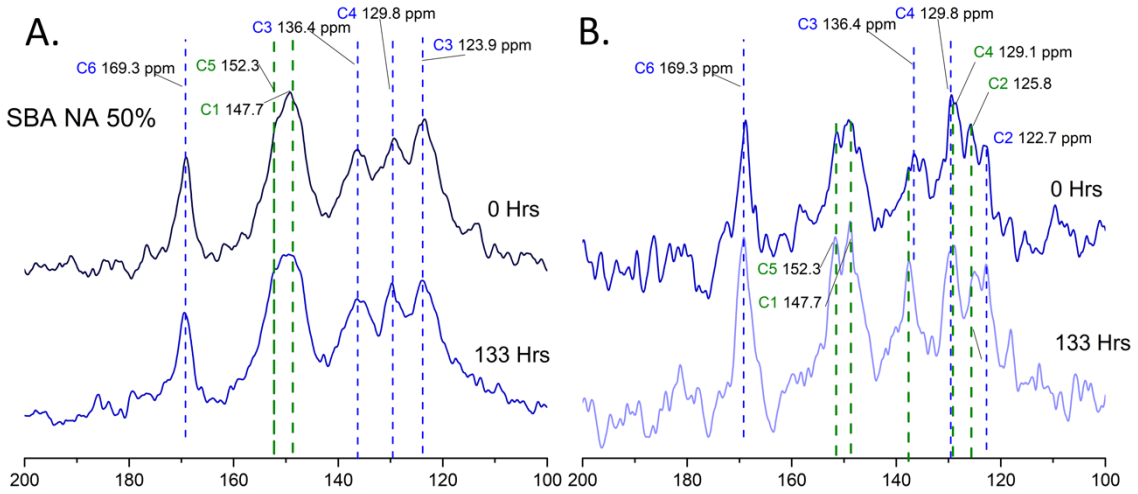

Figure 5-40 A. $^{13}C\{^{1}H\}$ HPDEC MAS NMR spectra at low recycle delay and **B.** ^{1}H-^{13}C CP/MAS NMR spectra of SBA-15 loaded at 50% with NA 0 hours after the quench to 298 K then at 133 hours while being held at 298 K. Peaks NA unknown form in green, other peaks labelled in blue.

A third CLASSIC experiment was performed on the SBA-15 sample at 50% loading but by following a closer procedure to that of how NA is loaded into the pores. The aim of this experiment was to effectively refresh a known sample of NA in SBA-15 (at 50% loading) by heating a sample above NA form I's melting point. The sample would then quickly be capped and placed into the NMR and the CLASSIC methodology implemented, holding a stable temperature of 298 K. By doing so we should be able to naturally observe the mechanism of the crystallisation process of the unknown polymorph, unless (as previously stated) it occurs in a timeframe less than the resolution of our CLASSIC segment times. Although continuous timepoints were recorded every hour, these representative spectra were chosen to display a start, midpoint and endpoint of the experiment. The specific time choices are more due to the results of the CP spectra which will be discussed shortly. The ^{1}H spectra (Figure 5-41) does not feature much change in the chemical shifts over the time period however. At the final end point there is some loss of intensity and small shifts in the aromatic protons. There is not much indication of what has occurred with regards to the state of the sample and whether or not it has recrystallised cannot be determined from the proton spectra alone.

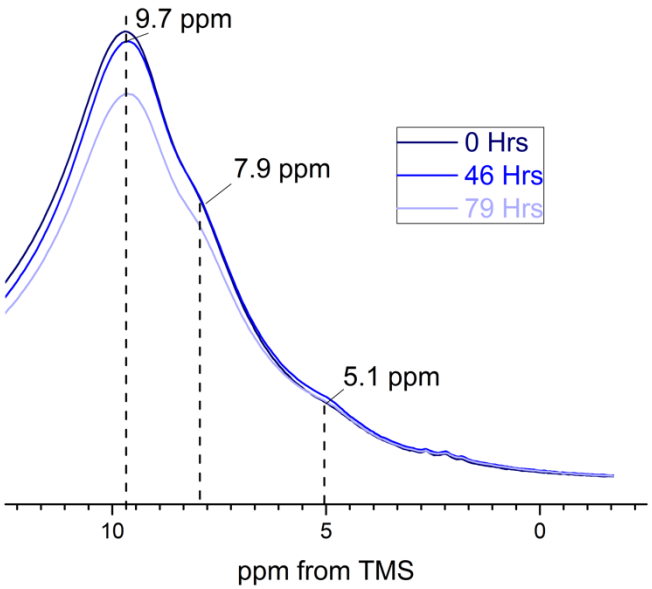

Figure 5-41 ^{1}H MAS NMR spectra of SBA-15 loaded at 50% with NA 0 hours at start of experiment, 46 hours then at 79 hours while being held at 298 K

The HPDEC and CP portions of the CLASSIC experiment (Figure 5-42-A/B) reveal a successful recrystallisation of the unknown polymorph within the pores. The HPDEC appears very broad and does not contain many environments that can be attributed to specific carbons of NA. This behaviour continues until the final spectrum is recorded showing no real difference happening. This must be considered with what has been physically done to the sample. By heating the rotor above the melting point of both the unknown polymorph and NA form I we know that a molten liquid melt is created. The sample was left in this heating state for around two hours, this also has an effect on the SBA by desorbing any water present on the surface of the pores. This simulates the melt-loading method used on the initial loading of NA into the pores, differing slightly on the physical mixing step because the sample is already pre-mixed and is unable to be stirred while packed into a rotor. The rotor itself was rapidly capped after the two-hour oven period and placed into the NMR to begin the CLASSIC experiment. Only around 7-8 minutes of recording time was lost due to transportation of the sample from the laboratory containing the oven, insertion of the rotor, spinning up the sample to 10 KHz MAS, stabilising the temperature to 25°C and tuning/matching the wobble curves for each nuclei. The result is that at the start of the experiment the CP spectrum does not show many sharp peaks that can be identified and at the conclusion of the experiment had recrystallised back into the unknown polymorph with its characteristic seven peaks (Z'>1) instead of the six peaks present in NA form I (Z'=1). This result shows clearly that the polymorph we have found within the pores is the preferential recrystallisation product inside the pores of SBA. This may be due to the silanol groups interacting

with the NA and influencing the initial crystallographic seeds, or it may be that the limited pore dimensions force this unknown polymorph to grow as a preferential product over form I or any other form.

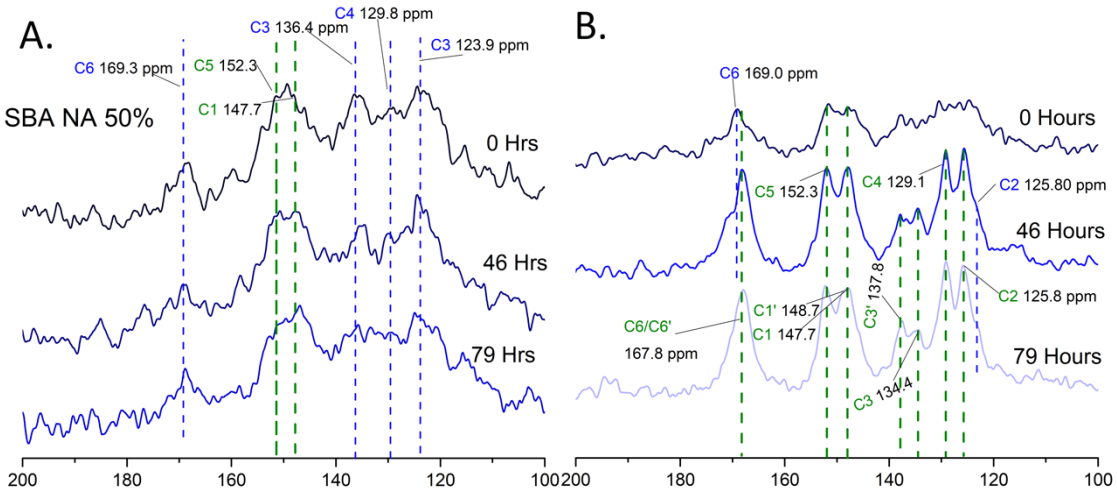

Figure 5-42 A. $^{13}C\{^{1}H\}$ HPDEC spectra at low recycle delay and **B.** ^{1}H-^{13}C CP/MAS solid-state NMR spectra of SBA-15 loaded at 50% with NA 0 hours at start of experiment, 46 hours then at 79 hours while being held at 298 K. Peaks NA unknown form in green, other peaks labelled in blue.

The kinetics of the CLASSIC study also has to be considered. Prior to these experiments when a sample was prepared it was generally left over a weekend period (48+ hours). Figure 5-43 is a pseudo-2D representation of the of the 1H-13C CP/MAS NMR spectra recorded in this third CLASSIC experiment. In total, 71 spectra were collected of the period of 79 hours. This view of the data shows that at the 46-hour mark was when the duo of peaks at 138 and 134 ppm begins to fully resolve and the other populations also begin to show increased resolution. This means that the polymorph took around 46 hours to fully recrystallise within SBA. However, there are some additional factors that should be considered before assuming this timeframe is taken a standard. The first being this recrystallisation took place under the influence of MAS at 10 KHz which exerts a certain amount of pressure on the sample while it is inside the NMR rotor, which could affect the speed of recrystallisation. This also means the sample is constantly moving, and while more traditional crystallisation experiments require a sample to be left vibration and movement free the effect of spinning may have negatively impacted the time it took for the sample to recrystallise.

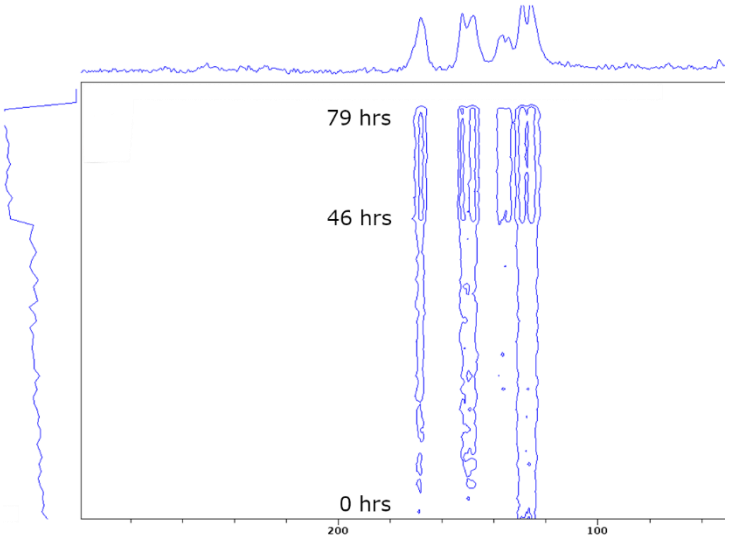

Figure 5-43 ^{1}H-^{13}C CP/MAS solid-state NMR spectra of SBA-15 loaded at 50% in pseudo-2D format for time resolution of when the unknown form recrystallised at the 46 hour mark.

Overall, the results of loading SBA with NA have resulted in the discovery of a new polymorph due to the recrystallisation of the melt of form I. This form appears to exist at loading capacities lower than 50%, however is most apparent at that loading level. The exact structure and orientation of NA molecules is currently undetermined due to lack of strong PXRD diffraction peaks not allowing for a unit cell to be computed. This form (when inside the pores) has a melting temperature of around 60 $°C$. When this form is melted at a temperature above 60 $°C$ but below the melting point of form I (129 $°C$) the polymorph does not appear to recrystallise, giving rise to the possibility of amorphization. The unknown polymorph is likely a Z'>1 type compound due to the extra carbon population discovered in the CP spectra, however it is difficult to speculate how many molecules are in the asymmetric unit as there may be significant chemical shift overlap because of the similarity of carbon environments. This is a curious difference to the cocrystal previously loaded into SBA-15 which is present in co-amorphous form in the pores.

5.5 Incorporation of NA into MCF mesoporous silica

When MCF[50] is considered as a pore space to load into we would have assumed from our previous work on the cocrystal FFA/NA that the size of the internal pores would possess the most interesting pores space to allow for unusual crystallization surfaces. The larger internal pores of 26 nm and its resultant increase in pore volume allows for significant stacking of molecules in all three crystallographic directions. Previous limitations in the vertical height of the pore stopped any thorough crystallization. However, as we have observed when loading SBA-15 with NA, this is very

much dependent of the size of the molecules that are being stacked as we have revealed a new and unknown polymorph forming within what we had previously regarded as pores that would be too small to allow recrystallisation of an API to occur. Therefore, the expectation of NA loaded inside the larger pores of MCF would be that we are able to recrystallize some kind of polymorph, whether this is a known form or for example the unknown form we found in SBA-15 cannot be predicted. It may be that the restrictive pore diameter of SBA-15 was the sole reason the polymorph was able to grow and not another form or a recrystallisation of form I. As shown previously, we have loaded six different loading percentages (w/w%) varying from 15% loading up to 50%. These were all conducted using the previously discussed melt-loading technique.

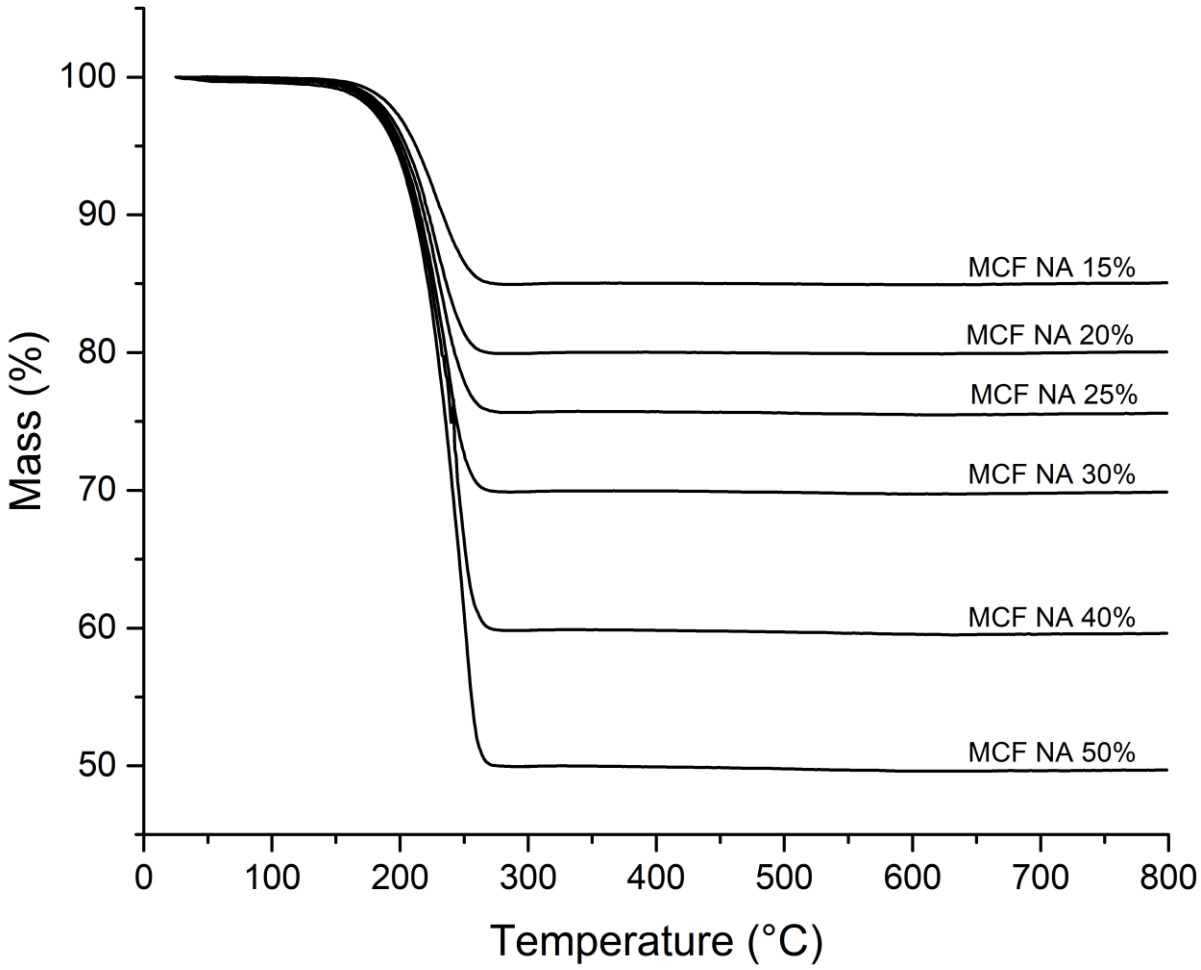

Figure 5-44 TG curves MCF-NA loaded materials. Loading levels indicated as wt% of silica to NA cocrystal.

Table 5-9 shows the BET surface area and total pore volume calculated from the sorption isotherms of the MCF loaded materials. BET surface area decreases upon loading of material and the total pore volume also decreases upon higher loadings. The apparent slightly anomalous result lies between 15-

20% loading where the sorption isotherms report almost the same BET surface area and pore volumes. It could be assumed that there has been an inconsistency with the physical loading of the samples with NA. However, when the TGA thermogram is referenced, it can clearly be seen that the two samples have the correct assigned weightings of NA compared to MCF material. An explanation for this could be that because of the larger pore size and the relatively small difference between the loading ratios the loading is not sufficient to cover the surface of the pore completely. The larger internal pore volume in MCF silica allows molecules to become mobile in the large space between the pore surfaces. Retrospectively, when the MCF data for the cocrystal FFA/NA are consulted it is seen that the 15-20% loading ratios BET surface area and total pore volume are very similar. It would therefore not be unreasonable to assume a similar situation occurring here, except with a much smaller unit cell and molecule emphasizing the discrepancy more.

Table 5-8 BET surface area (calculated as a multi-point BET in the linear region of the isotherms) and Pore Volume (calculated at *P/P_0 of 0.99)*, Pore Diameters for internal for MCF calculated using the BJH method from the adsorption branch of the isotherm, values in brackets indicate the pore windows calculated using BJH method from the desorption branch of the isotherm

Loading Ratio (% weight to MCF-17 weight)	**BET Surface Area(m^2/g)**	**Total Pore Volume (cm^3/g)**	**Pore Diameter (nm)**
0	372.6	1.275	23.50 (10.0)
15	169.3	0.753	23.96 (10.07)
20	172.1	0.764	23.96 (10.07)
25	153.3	0.702	23.98 (10.56)
30	134.8	0.615	23.96 (10.51)
40	123.5	0.561	24.22 (10.70)
50	89.3	0.411	23.96 (11.36)

The PXRD diffractograms (Figure 5-45) of the MCF samples reveal a much more resolved diffraction pattern that appears to have elements that do not match form I or II. Namely the two peaks at 16.9° and 17.3° do not match any of the peaks found in form I, and are shifted over too far to be the peaks

found in form II at 17.6 and 18.2°. Other peaks that appear to be different from these two forms include the small diffraction at 12.4° and a pair of diffraction peaks at 25.7 and 26.2°. There are some matching peaks for form I however, noted in loading ratios above 25% loading, the characteristic peak being the strong diffraction at 14.8°. This implies that there is a mixture of form I and the unknown polymorph inside MCF. The unknown polymorph appearing to be present at the lower loadings of 25%, as do the peaks matching form I. There are no matches to peaks in form II. The strongest diffraction occurs at the highest level of loading comparative to SBA-15's behaviour. This is also where the BET surface area is at its lowest (89.3 m^2/g). The calculated total pore volume at this loading ratio in MCF (0.41 cm^3/g) is around two times larger than SBA-15 (0.24 cm^3/g). This implies that there is some space still inside the pores in MCF and SBA-15. In contrast MCM-41 at 50% and 40% loading had extremely low pore volumes that were approaching the limit of detection of instrument. The much larger internal pores of MCF allow more space for multiple crystallization sites to occur, however it is not clear whether both polymorphs in MCF are located in the same pore space as each other.

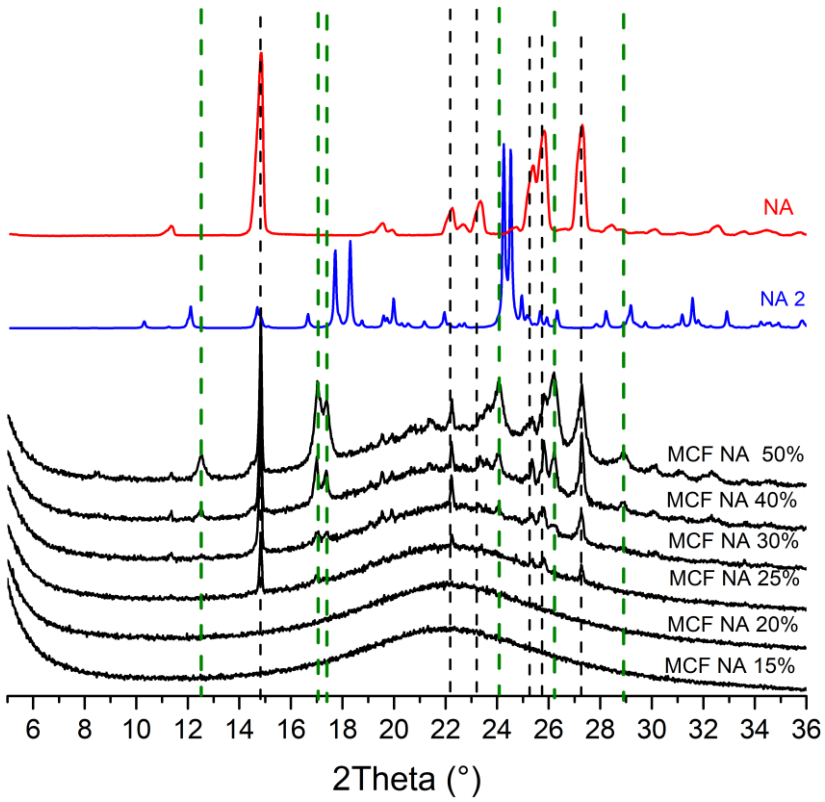

Figure 5-45 PXRD patterns of MCF silica loaded with NA at various loading levels (black lines indicate matching NA form I, green lines indicate a peak belonging to unknown polymorph, guest loading ratio (in wt%)

When the PXRD patterns (Figure 5-46) of MCF and SBA loading at 50% are compared there is an indication that the more sharply resolved peaks in MCF are that of the same unknown polymorph. The main indication is the diffraction peak at 17.2 ° in SBA-15 which matches up well with the two split diffraction peaks in MCF at 17 and 17.4°. There is a small diffraction matching the strong NA form I peak at 14.8°, however this does not appear to be a significant component of the diffractogram and also does not appear to be present in a distinguishable way in the other data collected on SBA.

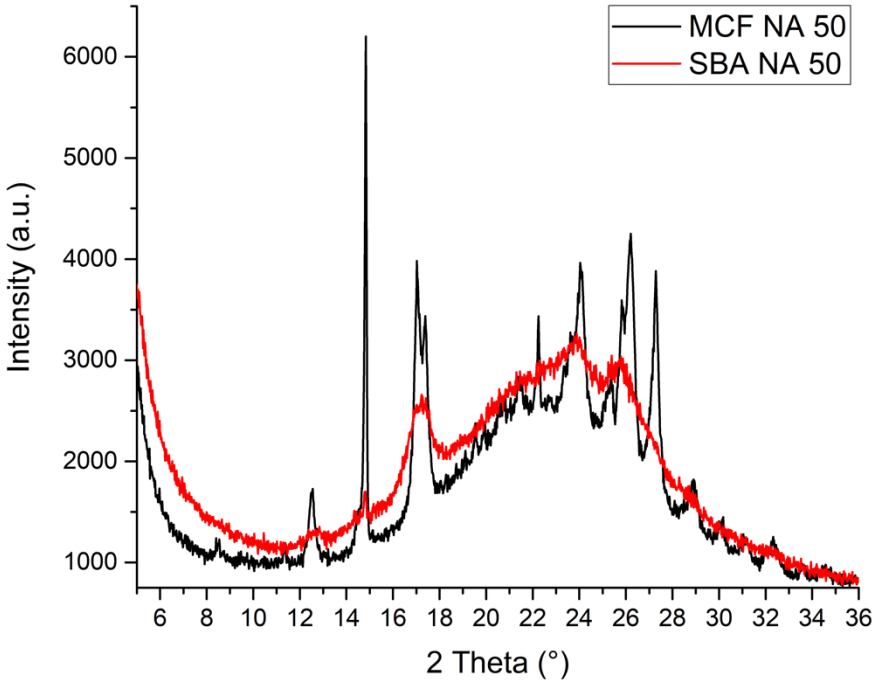

Figure 5-46 PXRD patterns comparing MCF and SBA-15 loaded NA at 50% loading level

A preprint publication by Li *et al*[143]. shows promising new set of polymorphs of nicotinamide. In total seven new polymorphs of nicotinamide have been found using a combination of melt crystallization and computational methods of crystal structure prediction. Of these seven new polymorphs discovered; two are Z'=1, three are Z'=2, one is Z'=4 and one is Z'=20. This is significant when considering our previous data collected on this unknown polymorph of NA inside SBA-15 and MCF. From the ^{13}C spectra, there are a total of seven peaks implying a Z'>1. This allows a narrower field of search when comparing these new polymorphs to our existing data. The authors of this paper supplied us with an image of the predicted PXRD patterns of each of these new polymorphs (Figure 5-47). It was then possible to match the unknown polymorph inside MCF. Looking towards Figure 5-47, the diffraction patterns in the highest loading of 50%, there is most likely a mixture of polymorphs at room temperature. The lines in purple indicate the presence of some form I, while the lines in green match to polymorph δ. There are no other close matches that feature the duo of peaks at 17 and 17.3°, even

when accounting for the small shift in unit cell size due to the single crystal x-rays being recorded at 100 K. When the single crystal x-ray diffraction data are consulted, we can see that polymorph δ is a Z'=2 structure and also carries interesting unit cell parameters when we take into consideration the way the pores in silica are structurally arranged. Form δ has unit cell lengths of a = 7.35, b = 20.7, c = 7.4 Å. The a and c lengths are of interest here as they are extremely close to each other in value. A similar ac packing means that the crystal structure can be built fairly uniformly inside the pore space using the ac packing direction as the diameter of the pore and then the much longer c direction can grow and pack in the longitudinal direction of that the pore is constructed in.

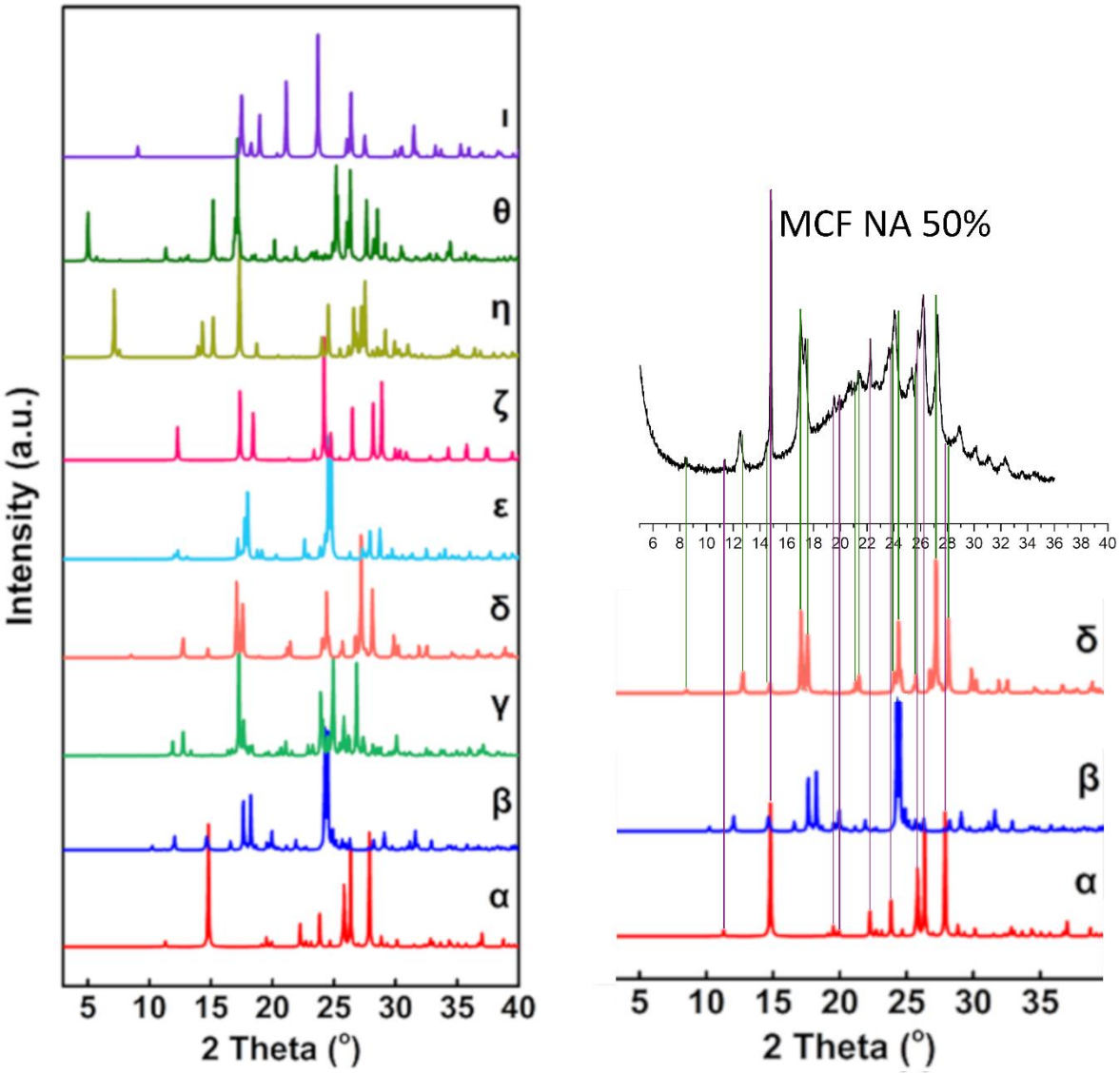

Figure 5-47 PXRD patterns of the new forms provided by Li *et al*. pre-publication and a comparison between peaks found in MCF NA loaded at 50% showing a match to form $\boldsymbol{\alpha}$ and form $\boldsymbol{\delta}$ inside MCF

The DSC thermograms (Figure 5-48) of the MCF samples loaded with NA show a lot of differences when compared with SBA-15's data. From the PXRD we can see that MCF most likely contains a mixture of the δ polymorph and form I. In SBA-15 the δ polymorph has a melting point of around 60°C therefore we would expect a similar melting point to be present here in MCF alongside a depressed melting point slightly below the melting temperature of form I. This however is not the case, with the MCF NA 50% presenting a much higher first melting point around 92.7°C then a further melting point at 112.2°C. As the loading level decreases these peaks decrease in their intensity until there is only a slight melt detectable at 25% loading. All the loaded samples exhibit the characteristic broad component between 20 and 70°C. The highest melting peak is consistent with what we expect with a depressed melting point from the material we know to be form I inside the pores. When we compare to FFA/NA loaded inside MCF, the 50% loaded material had a melting peak at 117.2°C which is around 19 °C lower than its melting point at 136.6 °C. With regards to NA inside MCF at 50% that peak difference is 16.8 °C from form I's melting point at 129 °C.

The anomalous result here is the difference between NA when loaded at 50% in MCF and SBA-15. The discrepancy between melting points of 59.3 °C and 92.7 °C is a difficult question to address. We know that MCF most likely has both form δ and form I present inside the pores, and from the CLASSIC data collected on SBA we know it is possible to melt form δ around 70 °C. The reduction in pore size may have an influence on this depressed melting point, however in larger pore space of MCF it may result in further polymorph interconversion as there may be room for other polymorphs to be accessed during the melt. There are many possibilities of what could be occurring during the melt, however without access to thermal data on the other newly discovered polymorphs it is difficult to assign exact melting points. What can be safely assumed is that complete melting of both the form δ and form I occurs when the temperature exceeds that of 112.2 °C (which is most likely a depressed melting point of form I), and that most likely form δ is being converted into form I when it does melt at 92.7 °C

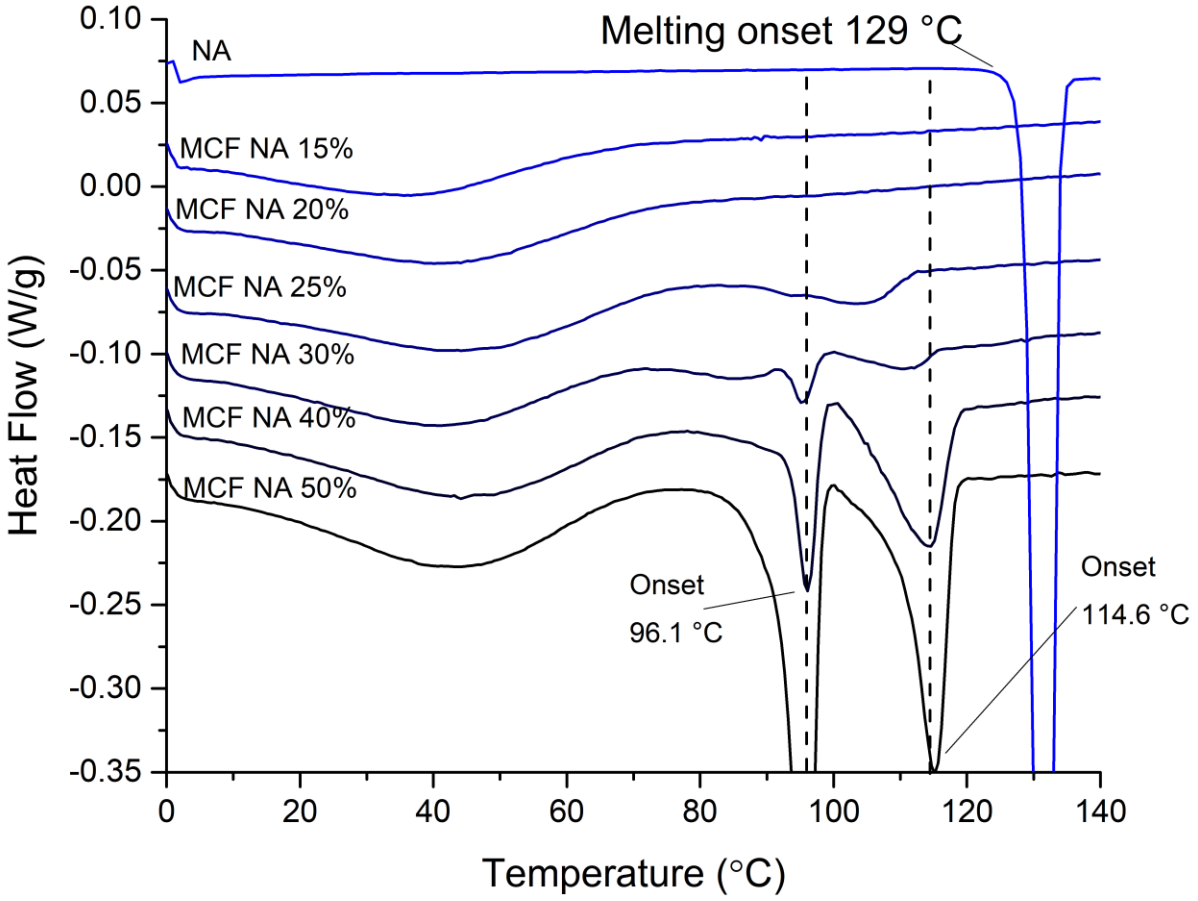

Figure 5-48 DSC thermogram of MCF loaded with NA, guest loading ratio (in wt%)

Figure 5-49 and 5-50 are a representation of what the possible orientation and arrangement of NA molecules might look like inside MCF. As can be seen in fully loaded pores at 50% loading level there is most likely a mixture of form δ and form I. The difference in unit cell dimensions is not visualised however should be considered that form δ has a much more uniform packing arrangement because two of its crystallographic length parameters are extremely close in value (a = 7.35 Å, b = 20.7 Å, c = 7.4 Å) whereas form I has entirely different abc lengths. The partially loaded MCF materials can also be seen to host both polymorphs, albeit in much less proportions to that of 50% loading, however both forms can be still visualised and distinguished down to around the 25% loading ratio. This implies that the much larger pores are allowing for more discrete pockets of the different polymorphs to grow. This possibility further corroborated by the fact that MCF possesses windows to these internal pores. Hence there might be a possibility of crystallographic separation of materials in order to seed certain polymorphic growth, or could be a mixture of both the below interpretations. Due to the fact that PXRD shows the entire sample it is not possible to distinguish between these two scenarios.

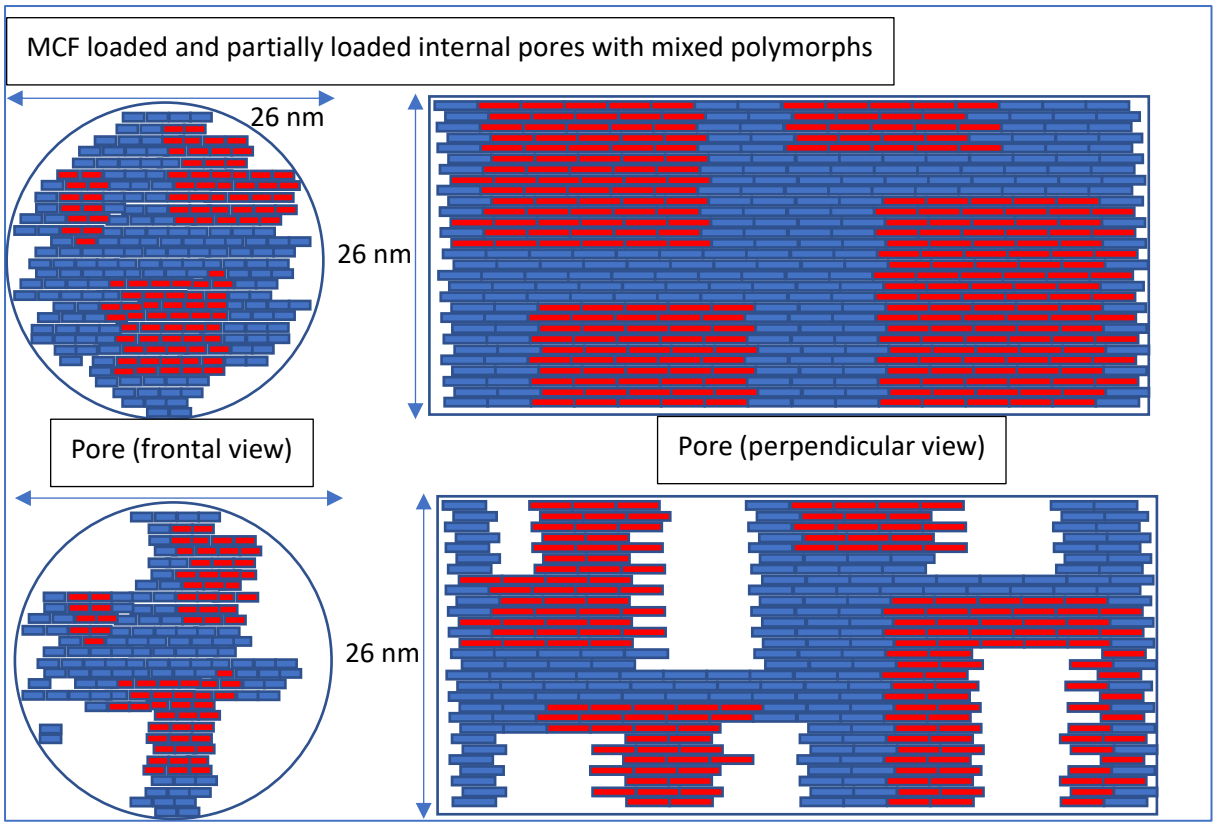

Figure 5-49 MCF-NA Fully Loaded Pore diagram of frontal and perpendicular view of pore space. Different polymorphs of NA are indicated by blue/red.

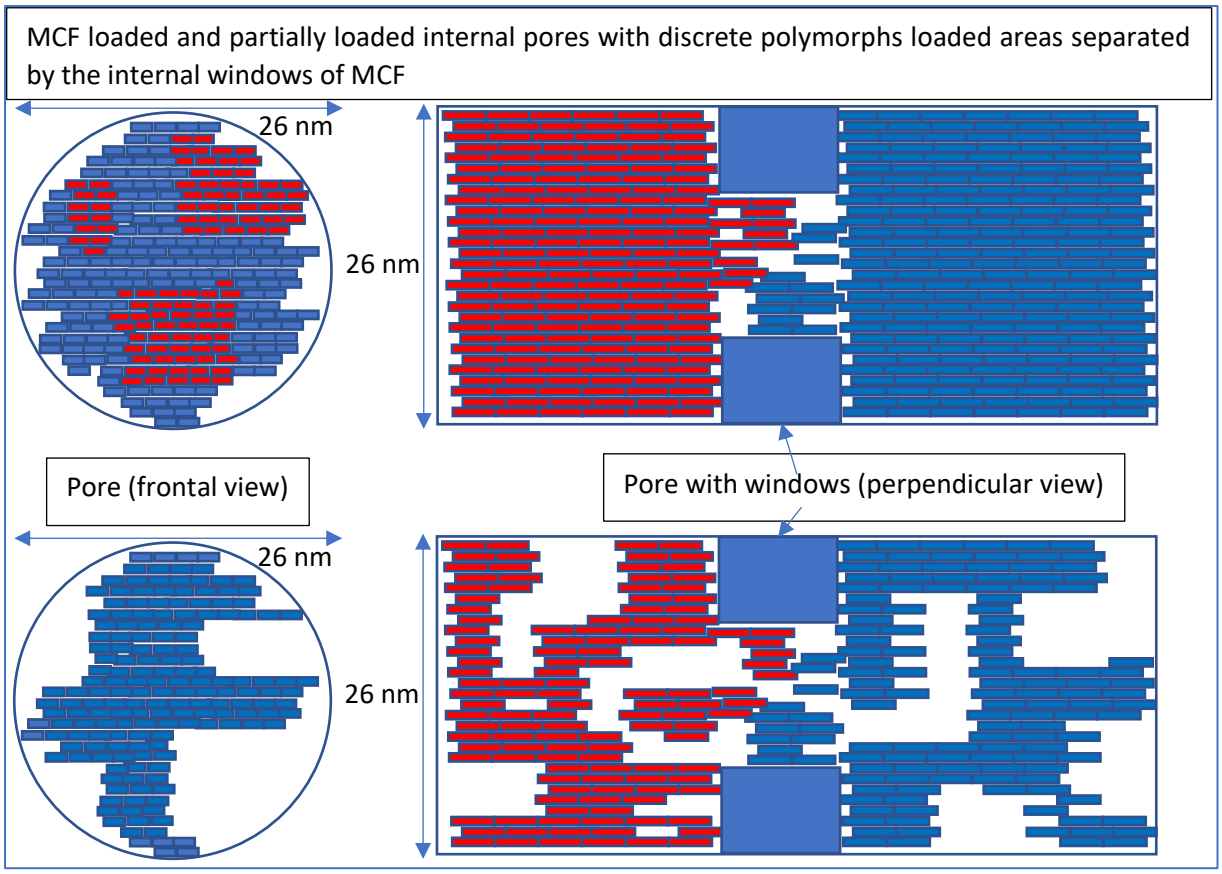

Figure 5-50 MCF Partially loaded pore diagram of frontal and perpendicular view of pore space. Different polymorphs of NA are indicated by blue/red.

The ^{1}H NMR spectra the MCF loaded materials (Figure 5-52) have some similarities to the spectra produced by the SBA series, with the highest level of loading exhibiting the most intense and sharpest peaks. When directly compared the ^{1}H spectra at 50% loading, MCF has much sharper peaks of NA than in SBA-15. A similar assignment is possible of these proton environments whereby the peak furthest shifted downfield at 8.6 ppm and its closest neighbour at 8.1 ppm refer to the amidic protons H6 and H5 respectively. Following this, the aromatic proton H4 in between the pyridine nitrogen and the amide group can be found at 7.8 ppm. The remaining cluster of aromatic protons H1-3 can then be assigned to the next population at 6.9 ppm. The silanol ^{1}H sites from MCF silica are observed at 5.1 ppm. From the PXRD and DSC profile of this series of MCF loaded with NA, we would not have expected to be able to distinguish individual protons so clearly. On the assumption that we have a mixture of form δ and form I inside pores, that would be a mixture of a Z'=1 and Z'=2 systems together in the same spectra. As the loading level decreases, the population intensities also decrease according to the loading level differences.

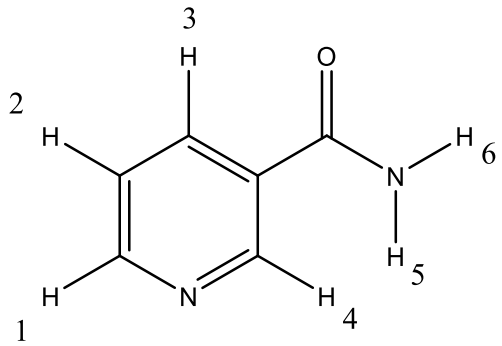

Figure 5-51 Proton site labelling of the nicotinamide molecule

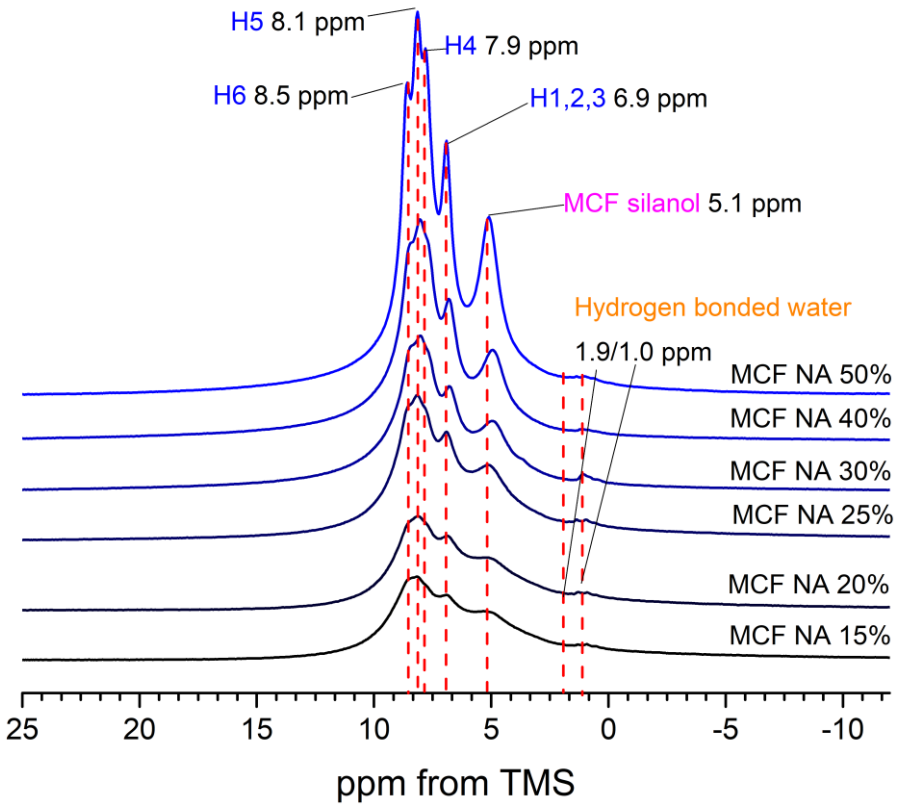

Figure 5-52 ^{1}H MAS solid-state NMR spectra of MCF loaded with NA at 298 K, guest loading ratio (in wt%)

It is clear that when the loaded samples of MCF are cooled down to 223 K there are distinguishable features in the ^{1}H spectra (Figure 5-53) present aside from the broad peak that takes up most of the aromatic region of the chemical shift scale. The mobility of NA in MCF samples has been severely affected by the reduction in temperature, implying that many different orientations of NA are currently inside the pores. The curious effect at room temperature of having such sharp and clear environments is greatly contrasted here, and also is quite comparable with the SBA series loaded with

NA. The only difference is that with the SBA series, a much clearer population representing the silanol peaks of SBA was present at *ca*. 4.7 ppm. In MCF however the silanol peak present at room temperature is not present at 223 K. This could be due to the fact that MCF is not uniform in the same way SBA is and the existence of separate pores and windows creates less defined silanol groups that may have different chemical shifts associated with them. Regardless of this hypothesis, it now is clear that the crystalline material that was quite mobile at room temperature exhibits much broader spectra.

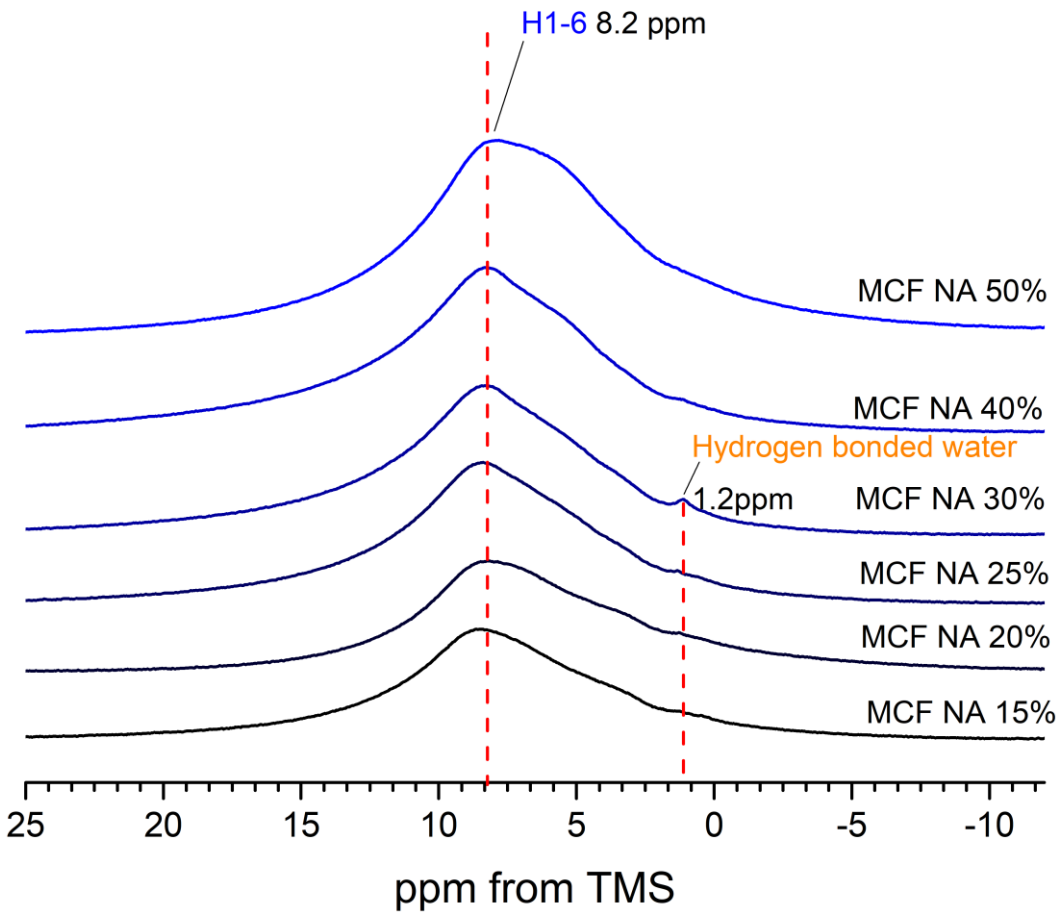

Figure 5-53 ^{1}H MAS solid-state NMR spectra of MCF loaded with NA at 223 K, guest loading ratio (in wt%)

As with our previous NA loaded samples, we performed ^{1}H NMR on them at high field of 19.96 T and fast MAS. The result (Figure 5-54 and 5-55) was a similar enhancement of resolution allowing us to clearly separate more of the aromatic protons from each other. Based on previous assignments, we can observe the amidic protons H6 and H5at 8.8 ppm and 8.3 ppm are. This is followed by the aromatic proton H4 lying between the pyridine nitrogen and the amide group at 7.9 ppm. The fast MAS and

extra resolution at 19.96 T show the next closest aromatic proton H3 as a shoulder of H4 at a chemical shift of 7.7 ppm. This is then followed by the remaining aromatic protons H1 and H2 centred at 7.1 ppm. The silanol groups are present at 5.2 ppm. When the loading ratio is reduced below 50% the populations shift downfield, with some of the peaks sharpening and some losing intensity. Below 50% loading the silanol group's intensity is less than half that of its intensity at 50% loading. Following this, the spectra appear to have extra peaks and shoulders present, to the point where the complexity of the spectra results in the assignment of specific chemical shifts to become extremely difficult. This could be a result of the ratio of NA form I and the unknown polymorph inside the pores changing as loading level is decreasing.

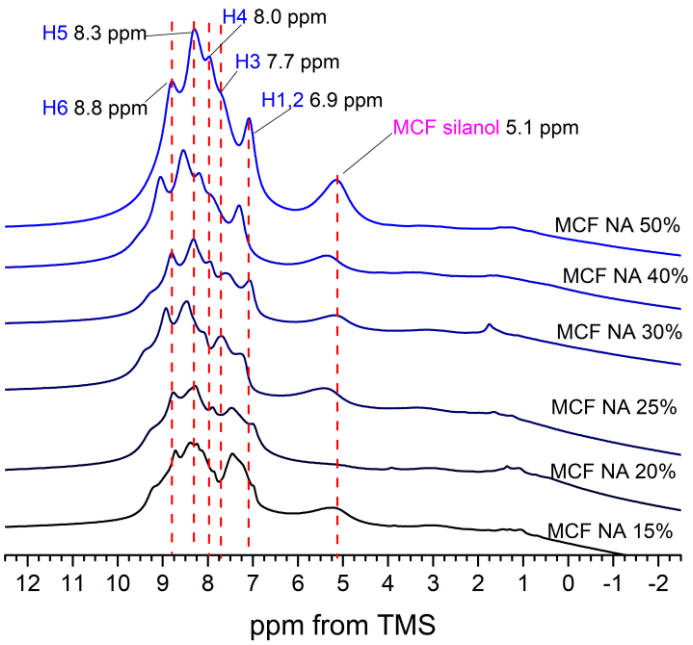

Figure 5-54 Highfield (19.96 T) at 55 KHz ^{1}H MAS solid-state NMR spectra of MCF loaded with NA at 293 K, guest loading ratio (in wt%)

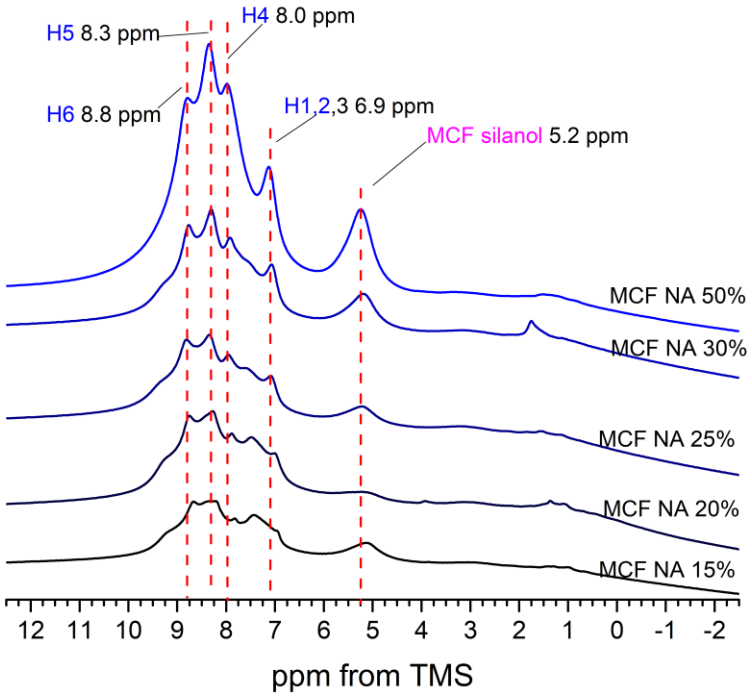

Figure 5-55 Highfield (19.96 T) ^{1}H MAS solid-state NMR spectra of MCF loaded with NA at 273 K, guest loading ratio (in wt%). The spectra were recorded at MAS rate of at 55 KHz.

The ^{1}H-^{13}C CP/MAS NMR spectra (Figure 5-56) were recorded for MCF loaded with NA at various loading levels at 298 K. When compared to SBA-15 there is a clear comparison to be drawn with the extra population present and the chemical shift changes that are indicative of not being related to NA form I. The spectrum for NA-MCF with the highest loading of 50% is slightly broader than that of NA/SBA-15, however the indications of the presence of form δ in MCF can clearly be seen at 40% loading and some hints are present at 30% loading in MCF. This implies that there is still some long-range order as the loading ratio decreases at room temperature, which is also confirmed by the presence of diffraction peaks. As loading level decreases to 25% there is not any evidence of any peaks in the spectra.

There is a small shoulder present at 50% NA loading at 122.1 ppm that has some agreement to match C2 in the NA molecule. A possible reason why form I is not detected may be due to the recycle delay used in the experiment. During optimisation of the recycle delay and other pulse program parameters the optimisation was carried out, unknowingly, on form δ. The CP spectrum of pure NA form I has an extremely long recycle delay of about 200 seconds, therefore it could be that the NA form I does not have sufficient time for magnetisation to reset in between scans. However, as the same experiments performed on MCM-41 loaded with NA at 50% do clearly show populations that match form I. As stated prior to this section, we believe that the structure belonging to these peaks is located outside

the pore space, due to the limiting pore dimensions not allowing a number of NA molecules to stack in all three crystallographic directions. The other possibility is that the PXRD diffractograms which imply form I is present do not represent the true ratio of the mixture of forms.

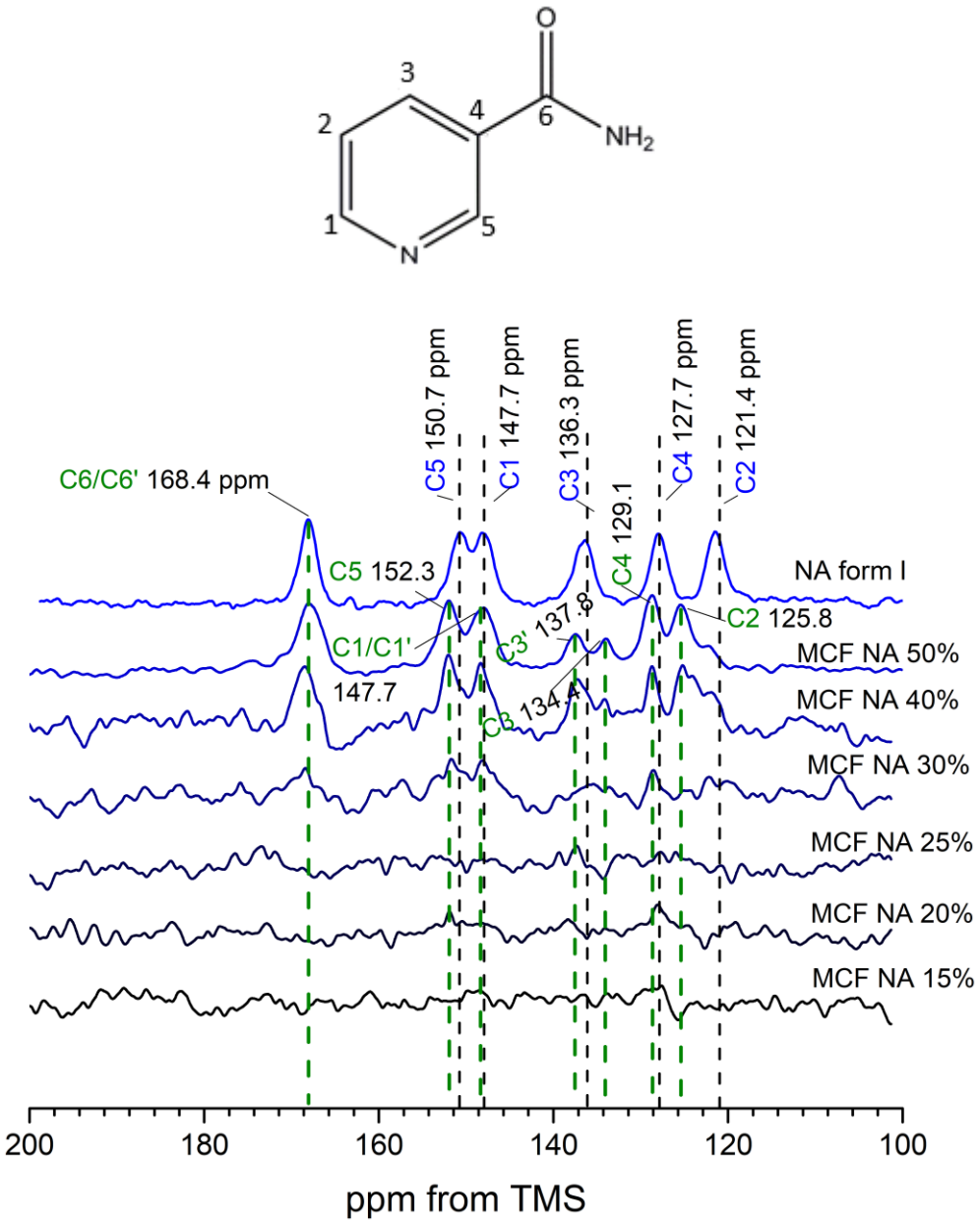

Figure 5-56 ^{1}H-^{13}C CP/MAS solid-state NMR spectra of MCF loaded with NA at 298 K at various loaded levels indicated by the percentage of loading of NA. Peak matching NA in black where appropriate, unknown form peaks indicated in green.

Table 5-9 ^{13}C assignment of MCF NA materials

Carbon No.	**C1**	**C2**	**C3**	**C4**	**C5**	**C6**
NA Form I	149.2	122.6	137.5	129.1	151.9	169.2
Form δ	147.7 148.7	125.8	137.8 134.4	129.1	152.3	168.4 167.1

When the low temperature ^{1}H-^{13}C CP/MAS spectra (Figure 5-57) are consulted this similar situation becomes clear. The peaks that could be assigned to form δ are still quite broad, however they become also detectable at lower loading levels. This broad nature does imply that a number of orientations have been assumed by NA inside MCF resulting in a greater range of chemical shifts. Due to the possibility that there is a mixture of polymorphs inside MCF, this broadening would not be a completely unexpected result. As the loading ratio decreases further, several NMR peaks were detected, although it is difficult to assign these specific carbons.

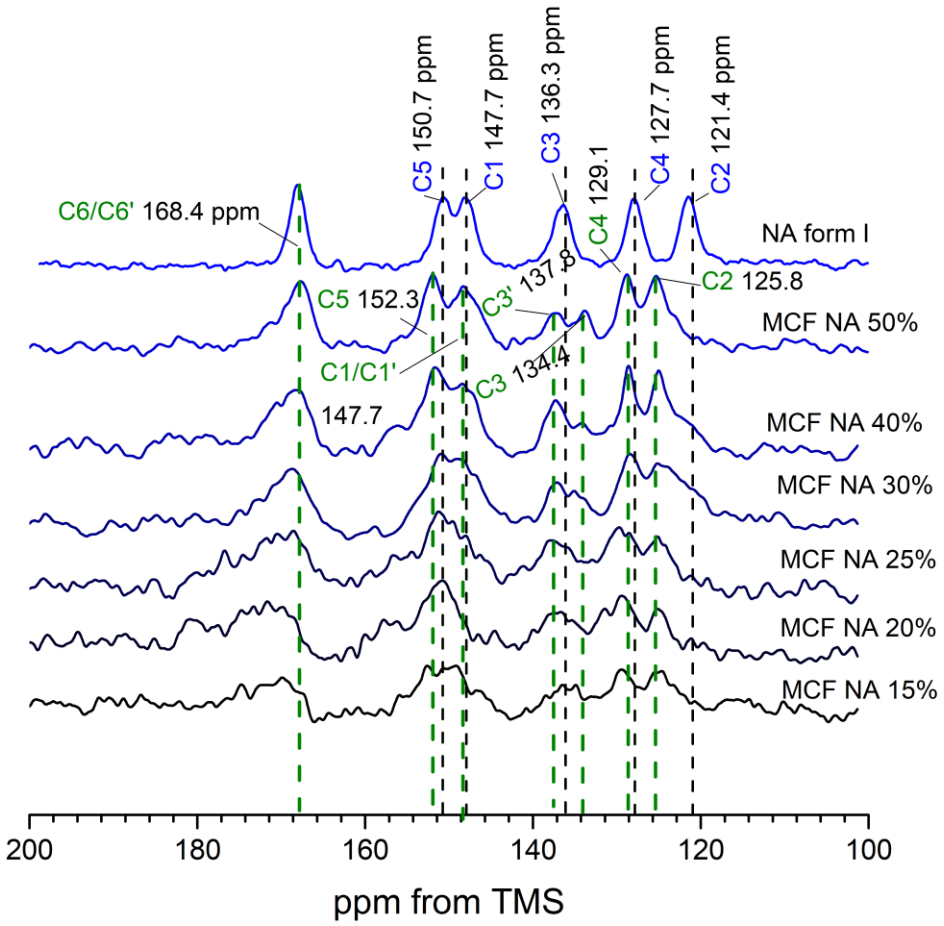

Figure 5-57 ^{1}H-^{13}C CP/MAS solid-state NMR spectra of MCF loaded with NA at 223 K at various loaded levels indicated by the percentage of loading of NA. Peak matching NA in black where appropriate, unknown form peaks indicated in green.

We acquired some ^{1}H-^{13}C CP/MAS data on MCF NA 50% at 19.96 T (Figure 5-58). The increase in resolution allows us to distinguish peaks due to C6' at 169.9 ppm and C3/C3' at 137.7/134.3 ppm respectively.

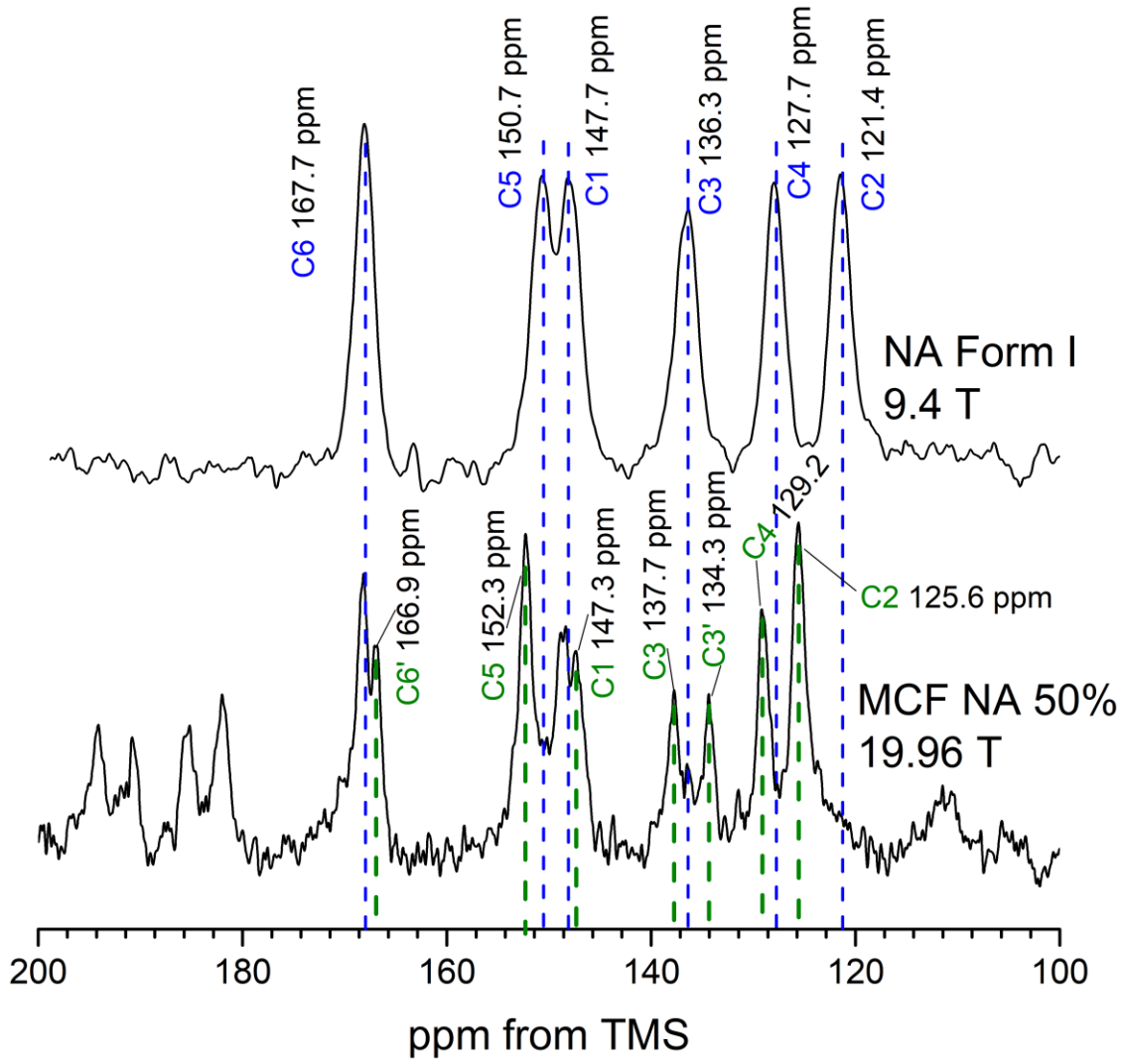

Figure 5-58 Comparison of ^{1}H-^{13}C CP/MAS spectra of NA form I at 9.4 T against MCF NA 50% at 19.96 T

5.6 Conclusions

In this chapter we have demonstrated the phase transition of NA form I into a previously unknown NA form when encapsulated in large enough pores in SBA-15 and MCF mesoporous hosts (6 and 26 nm respectively).

We systematically loaded NA using a melt-loading method into mesoporous silica with different pore sizes in order to explore its behaviour when encapsulated. Through variable temperature solid-state NMR experiments we have studied the effect of the mobility of NA molecules inside the pores. Combined with other characterisation techniques of DSC, TGA and PXRD we are able to offer some explanations as to the state of NA in pores and demonstrate a difference when loading different loading ratios. Prior to our work we knew of form I (CSD code: NICOAM, NICOAM01-03, NICOAM05-

09) and II (CSD code: NICOAM04) with form II being discovered through accidental co-crystallisation experiments by Li *et al.*[135].

In MCM-41 we believe that NA is fully loaded inside the pore space at loadings above 40% is in an aggregated amorphous state and that at 50% loading some NA material is crystalline outside the pore space. At 50% loading the DSC data has a melting peak matching that of form I and PXRD shows diffraction matching form I. At loadings of 40% and below there is no melting peak present nor diffraction peaks aside from the amorphous background provided by MCM-41. ^{13}C NMR also corroborates that at 50% the material is similar to that of form I, and at 40% and lower peaks appear extreme broad suggesting the absence of long-range ordering. Combining this with our knowledge of the pore dimensions of MCM-41 we believe the NA material inside the pores to be a mobile species that does not possess crystalline characteristics.

SBA-15 differs to MCM-41 with the present of PXRD peak in the highest level of loading (50%) which does not correspond to form I. There is also a melting point in the DSC curves at around 60 °C that is present in most loading levels, but in reduced intensity. ^{13}C NMR data further suggested that the polymorph inside the pores did not match that of form I or a predicted pattern of form II. Through use of the CLASSIC[142,144] methodology we were able to monitor the kinetics of recrystallisation of this unknown polymorph inside SBA pores.

MCF showed the clearest PXRD diffraction patterns of which we were able to get a partial identification of the unknown polymorph. However, there also appears to be diffraction peaks matching those of form I pointing to a mixture of polymorphs of NA inside MCF. The DSC melting points differed greatly to SBA-15, with multiple endotherms on the curves making it difficult to explain what which is a melting process and which is a polymorphic interconversion because of the possibility of a mixture of polymorphs. ^{13}C NMR data corroborated the presence of the unknown polymorph inside MCF.

A preprint publication[143] offered some insight at the end of the project with limited data as to the identity of the unknown polymorph found in SBA-15 and MCF. In SBA-15 the unknown polymorph was found by itself, whereas in MCF there appeared to be a mixture of the unknown form and form I. We believe the polymorph to match that of the described form δ, a Z'=2 structure newly discovered.

Table 5-10 Crystallographic parameters of the nine polymorphs of nicotinamide. Adapted from [143]. Yellow highlights are forms already characterised and present in CSD. Pink highlight are forms with a large Z' for asymmetric unit. Red highlights are forms without two similar crystallographic lengths.

Green highlights are forms that possess unfavourable angles to allow stacking in a perpendicular direction. Blue highlight is form which matches closely to PXRD and other parameters.

Polymorph	Form α (I)	Form β (II)	Form γ	Form δ	Form ϵ	Form ζ	Form η	Form θ	Form ι
Crystal System	Monoclinic	Monoclinic	Monoclinic	Monoclinic	Triclinic	Monoclinic	Triclinic	Monoclinic	Monoclinic
Space group	P21/c (14)	P2/n (13)	P21/c (14)	P21/c (14)	P-1(2)	P21 (4)	P-1(2)	P21 (4)	P 21/c (14)
a / Å	3.882666(15)	14.9915 (3)	15.3671(7)	7.3525(3)	7.5564(2)	3.81231(4)	3.7525(3)	10.70050(10)	9.9011(3)
b / Å	15.6453(5)	10.6814 (2)	7.3847(5)	20.7383(9)	7.9413(2)	14.38794(19)	12.3229(7)	35.1874(2)	5.87732(19)
c / Å	9.3836(3)	15.1888 (4)	21.1950(10)	7.4058(4)	10.7974(4)	5.11942(6)	13.0618(6)	15.82560(10)	10.2784(5)
α / °	90	90	90	90	108.100(3)	90	71.499(5)	90	90
β / °	98.394(4)	101.955(2)	104.650(5)	91.044	102.596(2)	94.2560(10)	85.676(6)	102.5800(10)	100.003
γ / °	90	90	90	90	98.293(2)	90	85.202(5)	90	90
Volume / Å3	563.904(4)	2379.43(9)	2327.0(2)	1129.04	585.137	280.032	570.013	5813.37	589.028
Z	4	16	16	8	4	2	4	40	4
Z'	1	4	4	2	2	1	2	20	1

When the structural parameters of NA form δ are consulted against other polymorphs (Table 5-12), some of the behaviour we see of NA inside the silica pores makes more logical sense. Among the seven new discovered polymorphs; there are two Z'=1, three Z'=2, one Z'=4 and one Z'=20 structures. Inside our silicas we have limited space to allow molecules to stack in all three crystallographic directions. Therefore, both larger Z' structures and larger unit cell dimensions are less likely to be candidates, especially for being present in SBA-15 which has pore size of 6-7 nm. This most likely eliminates the Z'=4 and Z'=20 structures of forms γ and ι. These structures are also unlikely due to sharp peaks in ^{1}H-^{13}C CP-MAS data.

When molecules of a particular polymorph are stacked in all three crystallographic dimensions within a cylindrical pore, we assume that the diameter remains constant along the perpendicular surface of the silanol walls. We could therefore infer that a unit cell which contains two similar crystallographic lengths could stack in the *xy* plane of the diameter of the pore evenly, where the third crystallographic length would result in stacking in the *z* direction of the length of the pore. Stacking and growth of an ordered structure would also favour angles within the unit cell to be close to cubic parameters ($\alpha = \beta = \gamma = 90°$) because the pores run in channels, therefore any polymorph with angles extremely outside of this range would be less likely.

By process of elimination, we can see in Table 5-12 that form δ is the only form which fulfils these assumptions. Alongside the PXRD data identifying this form as being present inside SBA-15 and MCF, it becomes more reasonable to assume that part of the reason this form appeared is due to those

crystallographic parameters. The encapsulation of NA by melt loading inside mesoporous silica has revealed that by restricting the space in which molecules are able to arrange themselves can lead to the growth of other polymorphic forms that are better able to stack, grow and show a semblance of long-range order.

Overall, the purpose of this chapter was to attempt to complete the picture of the previous chapter on FFA/NA cocrystal. We had previously loaded FFA[72] into the pore space and wanted to explore further the cocrystal/coamorphous relationships. Therefore, loading NA into the mesoporous silicas was the next logical step to understanding the interactions and phase transitions, and through it we have discovered a polymorphic transition of NA form I into a different form.

6 Solvent driven phase transitions of acyclovir – the role of water and solvent polarity

6.1 Introduction

Acyclovir (ACV) is a derivative of guanine and is present on the World Health Organisation's Model List of Essential Medicines. Its structure is detailed in the Figure 6-1 below. It features guanine base with a functional group added to the imidazole ring. ACV is analogous to the nucleoside guanosine. Its antiviral mechanism works by competing with guanosine for DNA polymerase and therefore slows down the production of viral DNA[145]. ACV is also present on the Biopharmaceutical Classification System as a class III drug. This indicates that the drug is soluble in water but has limited permeability[146]. Acyclovir is used in a variety of medical settings and in dosage formats; ranging from tablets, gels, creams and suspensions in treatments.

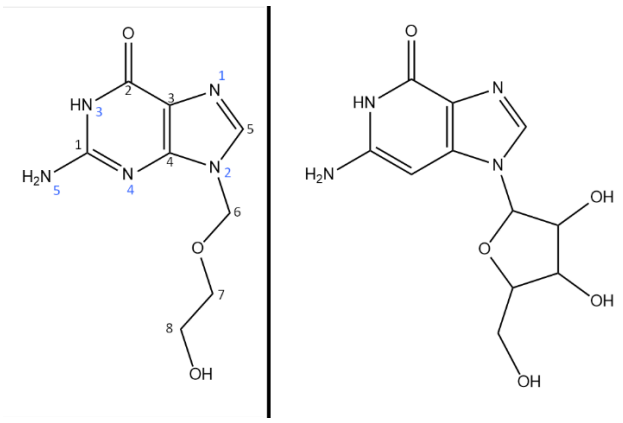

Figure 6-1 Structure of ACV (left) and Guanosine (right), carbon atoms highlighted in black, nitrogen atoms highlighted in blue.

Due to variety of hydrogen bonding donors/acceptors (eight in total) in ACV there are a variety of ways in which hydrogen bonding motifs can be formed. This has resulted in the discovery of six forms of ACV, two of which are hydrates. The crystalline phases of ACV were obtained by Lutker *et al.*[120] through polymer-induced heteronucleation (PIHn) and increased temperatures, and also by Terada *et al.*[122] through the use of dynamic vapour sorption methods. The conversions between these forms are shown in Figure 6-2 below.

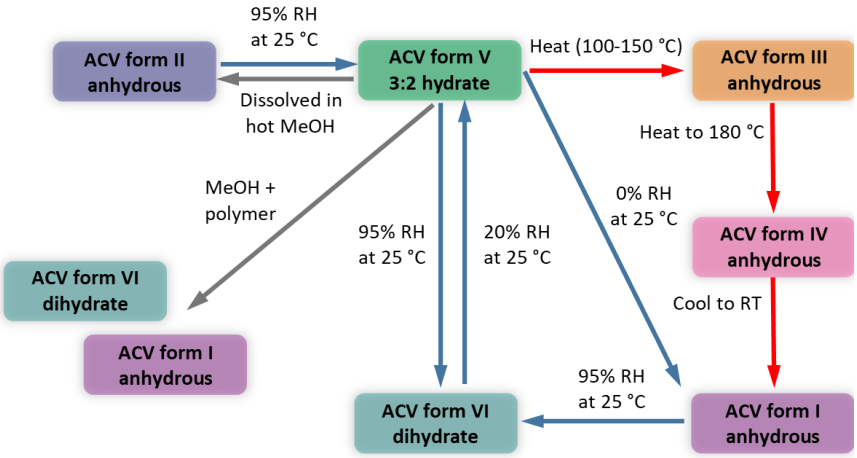

Figure 6-2 Phase transitions between different forms of ACV as described by Terada *et al.* and Lutker *et al.* Blue arrows indicate humidity driven phase transitions, red arrows indicate temperature driven phase transitions and grey arrows indicate solvent or PIHn crystallisation.

These studies (Figure 6-2) show that a variety of forms of ACV may be accessed through the use of the commercially available 3:2 (ACV:H_2O) hydrate form V. Forms III and IV are noted as metastable high temperature forms existing only above their transition temperature. ACV form V was first reported by Birnbaum *et al.*[147] in 1981 and further characterised by Birnbaum *et al.*[148] in 1984. ACV form I (anhydrous) was obtained by Lutker *et al.*[120] through the heating of form V to 180 °C and its subsequent cooling to room temperature. It can also be obtained through the recrystallisation of ACV form V from methanol in the presence of/ Nylon 6. ACV form II (the second anhydrous form) was obtained through the solution crystallisation of ACV form V in methanol at 68 °C inside a sealed vial, then through evaporation of the solvent by continuous heating. Form II could also be obtained by precipitation from N,N-dimethylformamide using an antisolvent of acetonitrile. The different arrangement of the molecules of ACV in these structures appears to result in different pathways in

which phase transitions can occur. Anhydrous form I transforms into the high temperature form IV at 180 °C prior to melting whereas form II does not undergo any phase changes prior to melting.

The dynamic vapour studies conducted by Terada *et al.*[122] have demonstrated that the anhydrous form I is able to transform into the dihydrate form VI at 90% Relative Humidity (RH). They also showed that form II is able to transform into the commercial form V (3:2 hydrate) at RH of above 95%. The third anhydrous form (metastable form III) is obtained through the heating of form V to between 130-150 °C. Upon cooling form III converts back to form V using atmospheric water to form the 3:2 water stoichiometry. The extended heating of the metastable form III to *ca*. 180 °C results in the conversion to a fourth anhydrous form (form IV) only stable at high temperature. Upon cooling form IV transforms back into form I which then remains stable at room temperature. Form VI (dihydrate) was first discovered when a polymorph screening was undertaken by Terada *et al.*[122] during polymer induced heteronucleation of ACV with poly(ethyleneterephthalate) and polypropylene.

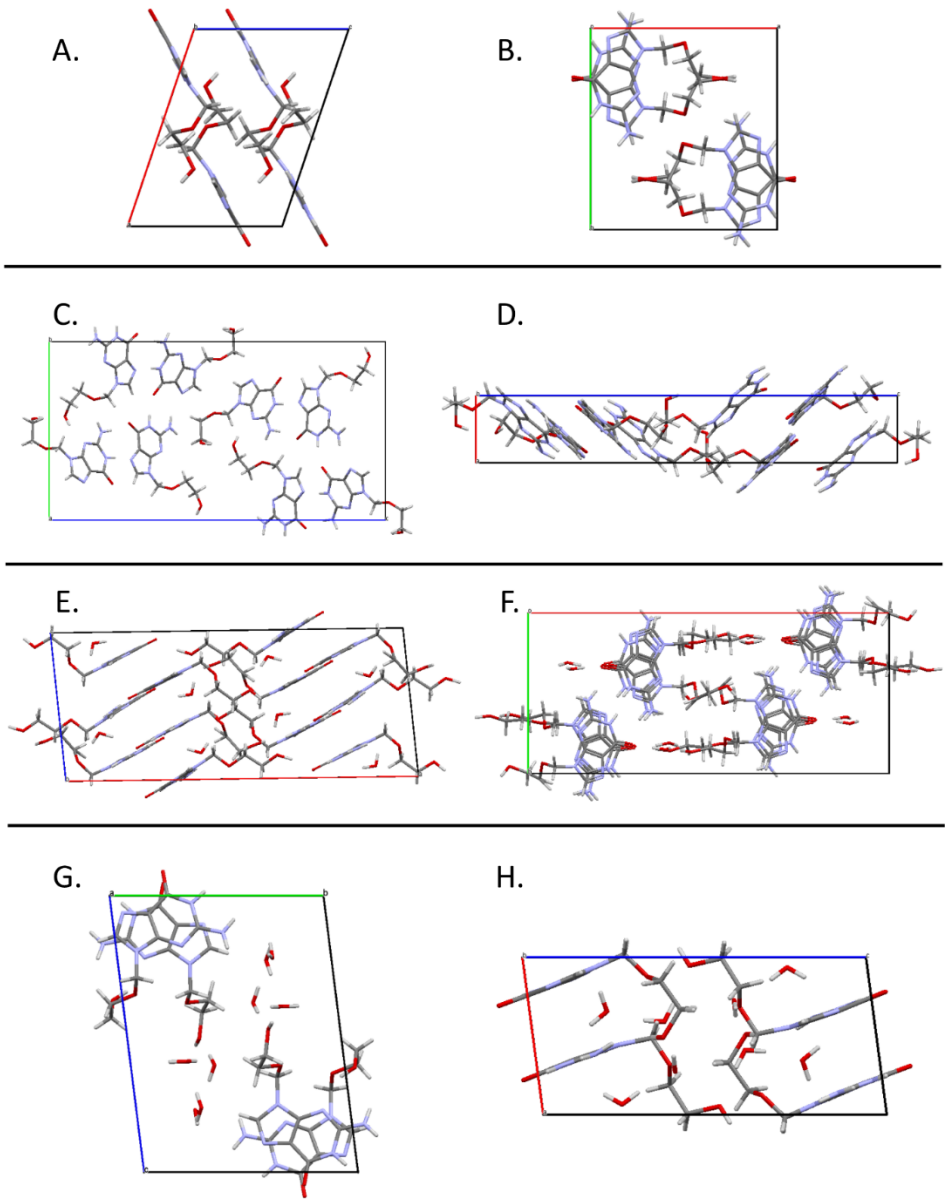

Figure 6-3 Packing of ACV form I (A., B., CSD ref. code MECWIC01); form II (C., D., CSD ref. code MECWIC03); form V (E., F, CSD ref. code CEHTAK10); form VI (G., H., CSD ref. code WOZPAE).

Terada *et al.* analysed the purine ring arrangements of the ACV crystal structures in order to investigate the mechanisms of transformation from the hydrated to anhydrous forms and vice-versa. Through the use of crystal structures and the studies carried out with dynamic water sorption, a proposal of explanation for these transformations was suggested. It was shown through the RH studies (0-95% RH at 25 °C) that form V did not directly convert to anhydrous form II. Similarly, anhydrous form I did not directly convert to the 3:2 commercial form V. Form I would convert to form V through the formation of the dihydrate (form VI) at 95% RH which would then transform to form V when the

RH was lowered to 20%. They attributed this transformation to the similar stacking arrangement present in the purine rings of forms I and VI. On the other hand, forms I and V have a much more apparent difference in their stacking (Figure 6-3). It was therefore hypothesised by Terada *et al.* that the anhydrous forms I and II are not able to undergo direct polymorphic interconversion due to the significant structural differences in the arrangement of the purine rings[122].

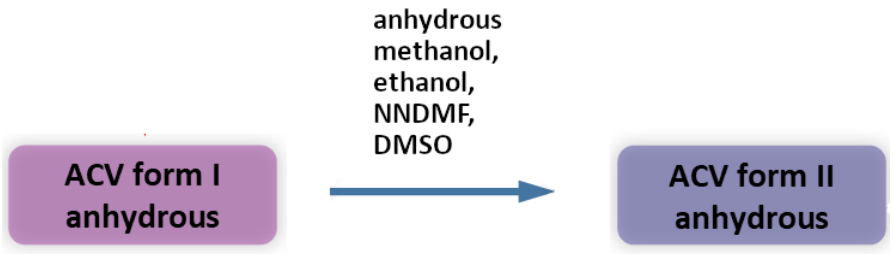

Figure 6-4 Proposed scheme of ACV form I to form II transformation by solvent mediated methods

In this chapter we show that ACV form I can convert into to ACV form II via solvent induced phase transformation (Figure 6-4) through use of anhydrous solvents such as methanol, ethanol, N,N-dimethylformamide and dimethylsulfoxide. From the knowledge gathered on the subject, there does not appear to be much that is known about ACV solvent mediated phase transformations. ACV is a good candidate to represent purine based derivates of a whole group of known biologically active pharmaceuticals.

With regards to the polymorphic screening of compounds, this is usually carried out following the modification of the conditions of crystallisation. This can range from temperature, pressure, humidity or use of different solvents in order to recrystallise or precipitate the ordered formation and assembly of molecules[149]. Solution mediated phase transformation (SMPT) is an effective method for polymorphic screening of new solvates or cocrystals[150,151], the process by which crystallisation or slurrying of the starting material/s in solvents with different polarities or by using different amounts of water and mixtures of organic solvents[152–156]. In this chapter we will explore the different solvent induced phase transitions that can occur with ACV. Though there is not much knowledge present on its polymorphism with regards to solvent driven changes. Through use of 15 different solvents, hydration experiments and temperature driven phase changes, this chapter will explore the possibilities ACV can offer. These possibilities the use of previously described techniques such as solid-state NMR as a spectroscopic and polymorph identification tool. These NMR studies will be supported

through computational methods for DFT calculations of chemical shift tensors. Thermal methods such as DSC and TGA for decomposition and polymorph interconversion studies and PXRD methods for phase identification of solids.

6.2 Results and Discussion

6.2.1 Characterisation of the Solid forms of ACV

ACV is an N-substituted purine derivative, featuring six different crystalline structures to date. The fact that ACV possesses this rich polymorphism suggests that other purine derivatives could also feature many different polymorphs that have not been discovered as of yet. Through the characterisation of the crystallographic packing and arrangement of the ACV molecules and the water molecules that make up the hydrates similar methodologies of crystal engineering could be applied to other biologically active compounds.

Table 6-1 Unit cell parameters of ACV forms I, II, V and VI from the Cambridge Structural Database

	Form I	**Form II**	**Form V**	**Form VI**
CSD code	MECWIC01	MECWIC03	CEHTAK10	WOZPAE
Space group	P 2_1/c	P 2_1 2_1 2_1	P 2_1/n	P-1
Unit cell parameters				
a/Å	10.9402	4.5518	25.459	6.8386
b/Å	11.1854	15.0481	11.282	11.3679
c/Å	8.1167	28.3857	10.768	14.942
α/°	90.0	90.0	90	82.85
β/°	108.63	90.0	95.16	82.42
γ/°	90.0	90.0	90	89.33
Volume, Å^3	941.206	1944.31	3080.34	1142.47
Z	4	8	4	4
Z'	1	2	3	2

Of the six crystalline species discovered of ACV, four are present in the CSD. Two are the anhydrous forms, ACV form I and II (CSD ref. codes: MECWIC01 and MECWIC03 respectively) and the other two forms are the hydrates, ACV form V (3:2) and the dihydrate form VI (CSD ref. codes: CEHTAK10 and WOZPAE respectively). Their crystallographic data are shown in Table 6-1. The structural arrangement is shown in Figure 6-3. In order to fully structurally characterise all of the polymorphic forms of ACV at room temperature we explored the PXRD and solid-state NMR methods of characterisation as we can fully track phase changes. This may also give us insight into the mechanism of structural rearrangement from one form to another.

Published alongside the XRD data by Terada *et al.* were solid state NMR studies of the ACV polymorphs. ^{1}H-^{13}C CP/MAS NMR spectra reported by Terada *et al.* exhibited some artefacts and significant line broadening. This presented us with a difficult assignment of carbon sites available and reduced the information we could interpret regarding any structural information. Therefore, we undertook the task of collecting our own ^{1}H-^{13}C CP/MAS NMR measurements on each of the room temperature crystalline polymorphs, and backed that assignment with computational DFT characterisation methods. The full assignment of ^{13}C environments of the ACV forms is shown in our own data is shown in Figure 6-5-A and the calculated isotropic chemical shifts are shown in Table 6-2.

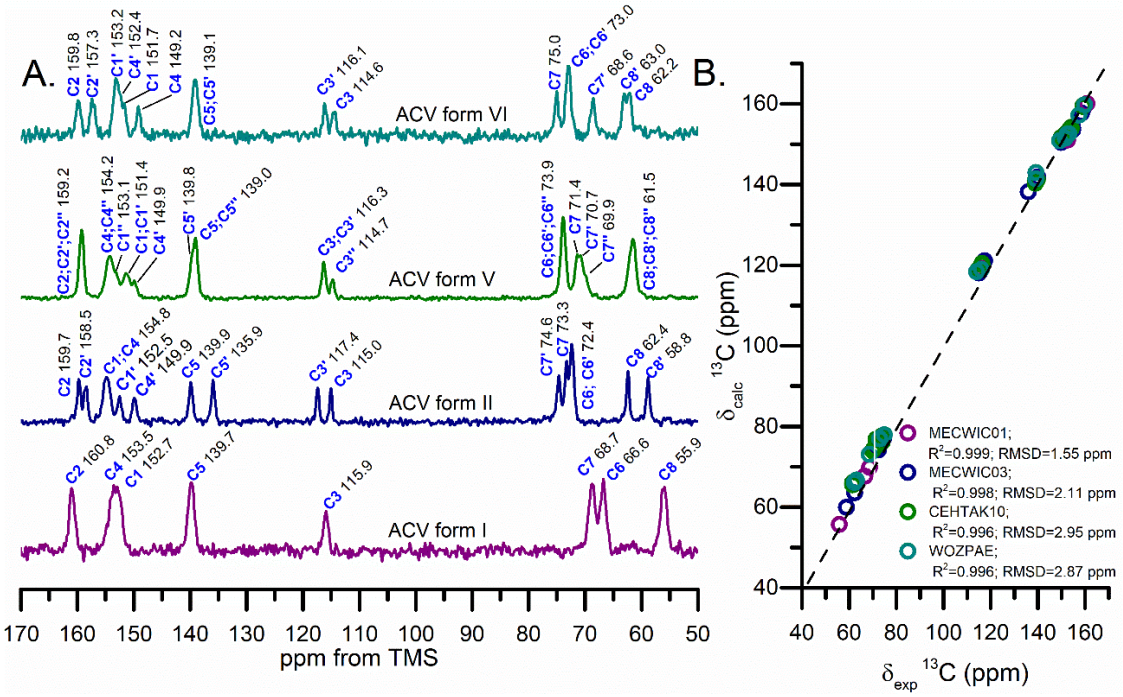

Figure 6-5 A. ^{1}H–^{13}C CP/MAS NMR spectra of ACV forms I, II, V and VI. B. Comparison of experimental and CASTEP calculated ^{13}C chemical shifts for ACV forms I (CSD ref. code MECWIC01), II (CSD ref. code MECWIC03), V (CSD ref. code CEHTAK10) and VI (CSD ref. code WOZPAE).

6.2.2 ACV form V

ACV by itself has eight carbon atoms, form V is a Z'=3 structure and therefore it is expected that a total of 24 peaks would be present in the ^{1}H-^{13}C CP/MAS NMR spectrum. However, as it can be seen in Figure 6-5-A, there are only around 15 peaks present – some of which exist as small shoulders to main peaks. The calculated chemical shifts using CASTEP are also in good agreement with a RMSD of 2.95 ppm, shown in Figure 6-5-B and in Table 6-2. The reason explaining that there is a lower number of peaks present is most likely due to the similar carbon local environments in the crystal structure, and therefore similar ^{13}C chemical shifts in the solid-state NMR. There are three distinct groups on the spectrum, one belonging to the aliphatic tail represented by carbons C6, C7 and C8. Out of these carbons C6 (75.0 ppm) and C8 (61.5 ppm) are not separated into any additional peaks due to similar shifts. However, C7, C7' and C7'' have some separation, appearing as a broader resonance of three overlapping peaks between 69.9 and 71.4 ppm. The next distinct group of carbons belong to the purine ring; C3, C3' and C3''. These are located between 114.7 and 116.3 ppm. With the latter, C3'' peaks separate into a more distinct line at 114.7 ppm while the others remain a broader resonance on 116.3 ppm. The final group of carbons present belong to the rest of aromatic carbons in the purine

ring; C1, C2, C4 and C5. These are grouped in the region between 160-140 ppm and despite the Z' = 3 nature of the polymorph has some small separation in their chemical shift allowing a better than expected assignment of the peaks. This may be due to the different layering of the purine rings in the crystal system. Alongside the ^{1}H-^{13}C CP/MAS data acquired is the PXRD diffraction, both experimental and simulated (CSD ref. code CEHTAK107), of ACV form V (Figure 6-6). The two patterns are in good agreement with each other with characteristic reflections at *d*(200) = 12.63 Å; d(210) = 8.44 Å; *d*(321) = 4.22 Å and *d*(30−3) = 3.40 Å.

6.2.3 ACV form I

The anhydrous form I of ACV is has one molecule of ACV in the asymmetric unit (Z'=1) and possesses an antiparallel purine ring arrangement. The ^{1}H-^{13}C CP/MAS NMR spectrum of it (Figure 6-5-A) was acquired after dehydrating the commercial form V hydrate at 180 °C and allowing it to cool and crystallise at room temperature. The calculated chemical shifts using CASTEP are also in good agreement with a RMSD of 1.55 ppm, shown in Figure 6-5-B and in Table 6-2. There is a significant difference between its chemical shifts and those of the starting material (ACV form V). There are eight peaks, one for each carbon environment (Z'=1) in good agreement with crystallographic data shown in Table 6-1. The second difference between the form I and Vs NMR spectra is the apparent shift in the aliphatic carbon tail of C8 and C6, which shift 5 and 6 ppm upfield at 55.9 and 66.6 ppm respectively. This can be explained through the involvement of the side chain in form V in hydrogen bonding with water molecules in the crystal structure. The oxygens present in water in a crystal system are more electronegative than the carbons and therefore will polarise nearby electron clouds in nuclei, resulting in a deshielding effect causing a downfield shift. This was described by Spiess *et al.*[157] when using experimental solid-state NMR methods combined with the computational aid of DFT calculations. Meanwhile, ACV form I does not have any other hydrogen bonding close contacts in its structure around the aliphatic tail. As with ACV form V, the PXRD diffraction pattern (Figure 6-6) of form I is in good agreement with the simulated pattern with characteristic reflections at *d*(100) = 10.41 Å; *d*(210) = 4.71 Å; *d*(20−2) = 3.71 Å and *d*(30−2) = 3.12 Å.

6.2.4 ACV form II

ACV form II is the second anhydrous form with two molecules of ACV in its asymmetric unit (Z'=2). As it can be seen in the ^{1}H-^{13}C CP/MAS NMR spectrum (Figure 6-5-A), there are two of each ^{13}C site in agreement with the crystallographic data. The calculated chemical shifts using CASTEP are also in good agreement with a RMSD of 2.11 ppm, shown in Figure 6-5-B and in Table 6-2. There are some notable

differences between the two anhydrous forms, on being a significant downfield shift in C8. In ACV form II C8 and C8' lie at 58.8 and 62.4 ppm respectively which is quite far from ACV form I's C8 carbon at 55.9 ppm. This could be a result of hydrogen bonding between N1 nitrogen on the imidazole ring and the OH attached to the C8 of the second ACV molecule. Another change between the two anhydrous forms is that of C5 and C5' shift downfield by *ca*. 5 ppm, possibly due to three short contact interactions occurring between C5 of one ACV molecules and N3 of the second ACV molecule in the asymmetric unit. The PXRD pattern of ACV form II displays characteristic reflections with *d*(002) = 14.33 Å; *d*(021) = 7.26 Å and *d*(101) = 4.57 Å.

6.2.5 ACV form VI

Similarly, to ACV form II, the second hydrate (form VI) has two ACV molecules in its asymmetric unit (Z'=2), giving two peaks for each ^{13}C in the ^{1}H-^{13}C CP/MAS NMR spectrum (Figure 6-5-A). The calculated chemical shifts using CASTEP are also in good agreement with a RMSD of 2.87 ppm, shown in Figure 6-5-B and in Table 6-2. Form VI has similarities with form V with C1, C4, C3 and C5. Some differences appear. For instance, C6 and C7 have swapped their order such that in form VI C7 is shifted downfield below C6-C6', and C7' is shifted upfield of the C6-C6' cluster. The ACV molecules in form VI form hydrogen bonds through their carbonyl oxygens. C2 on one of the ACV molecules is hydrogen bonded to two water molecules through three hydrogen bonding. The other, C2', forms a hydrogen bond with one water molecule and the hydrogens on amine group. This results in an upfield shift for C2 and a downfield shift for C2', 159.7 and 158.5 ppm respectively. In the unit cell there are four molecules (Z=4) of ACV, these are stacking such that the purine rings are in an alternating orientation. There are eight water molecules present in the unit cell, which are arranged into two channels nearby the aliphatic chain. This arrangement of antiparallel purine rings was first suggested by Terada *et al* as an explanation for the transformation of anhydrous form I into form VI through water sorption. The experimental PXRD pattern, with characteristic peaks *d*(001) = 15.04 Å; *d*(011) = 9.7 Å; *d*(012) = 6.63 Å and *d*(210) = 3.30 Å is in good agreement with the simulated pattern.

Table 6-2 Experimental and CASTEP calculated ^{13}C chemical shifts of ACV forms I, II, V and VI.

^{13}C Site	ACV form I (Z'=1)		ACV form II (Z'=2)		ACV form V (Z'=3)		ACV form VI (Z'=2)	
	δ_{exp}	δ_{calc}	δ_{exp}	δ_{calc}	δ_{exp}	δ_{calc}	δ_{exp}	δ_{calc}
C2	160.8	160.0	159.7	159.2	159.2	159.5	159.8	159.7
C2'	-	-	158.5	157.7	159.2	159.5	157.4	157.1
C2''	-	-	-	-	159.2	159.3		
C1	153.5	153.5	154.8	154.0	151.4	151.9	151.7	151.4
C1'	-	-	152.5	153.0	151.4	152.3	153.2	152.5
C1''	-	-	-	-	153.1	153.4		
C4	152.7	151.0	154.8	153.5	154.2	153.8	149.2	150.9
C4'	-	-	149.9	150.4	149.9	151.6	152.4	152.4
C4''	-	-	-	-	154.2	154.2		
C5	139.7	141.4	139.9	141.8	139.0	141.3	139.1	143.0
C5'	-	-	135.9	138.2	139.8	141.2	139.1	141.4
C5''	-	-	-	-	139.0	140.9		
C3	115.9	119.1	115.0	118.1	116.3	120.4	114.6	118.3
C3'	-	-	117.4	121.1	116.3	120.1	116.1	118.9
C3''	-	-	-	-	114.7	118.9		
C7	68.7	69.9	73.3	77.0	73.9	76.1	75.0	77.9
C7'	-	-	74.6	77.5	70.7	74.6	68.8	73.1
C7''	-	-	-	-	69.9	74.0		
C6	66.6	67.7	72.4	75.0	73.9	77.6	73.0	76.9
C6'	-	-	72.4	74.2	73.9	77.6	73.0	77.0
C6''	-	-	-	-	71.4	76.8		
C8	55.9	55.7	62.4	63.6	61.5	65.6	62.2	66.7
C8'	-	-	58.8	60.0	61.5	65.8	63.0	66.1
C8''	-	-	-	-	61.5	66.1		

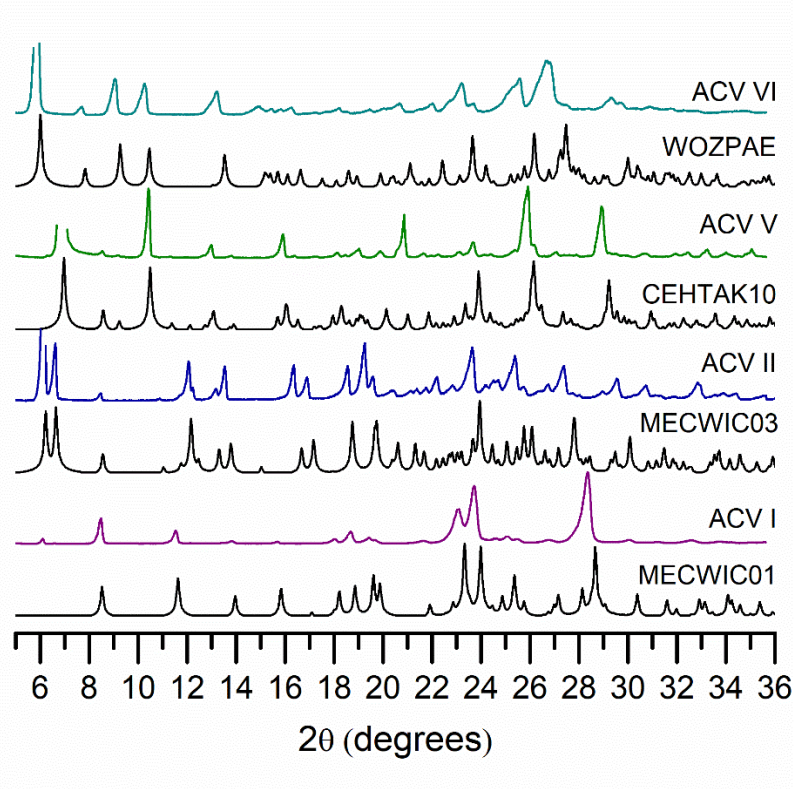

Figure 6-6 Experimental and calculated PXRD patters of synthesised ACV forms I (CSD ref. code: MECWIC01), II (MECWIC03), V (CEHTAK10), VI (WOZPAE).

6.2.6 Thermally Induced Phase Transitions of ACV

The first investigations into the temperature induced phase transitions of the ACV forms were carried out by Lutker *et al*.[120] and further studies by Terada *et al*.[122]. The subsequent dehydration and solvation processes that will allow the phase transformation from one polymorph to another are not readily accessible otherwise. Our group had demonstrated previously that it is possible to form a metastable form of indomethacin (form V) by the careful removal of methanol from the indomethacin solvate[65]. It is also known that when solvent is removed from a crystal lattice, depending on the method of removal, the process can result in the subsequent generation of disorder, for example in the removal of water from orotic acid[155].

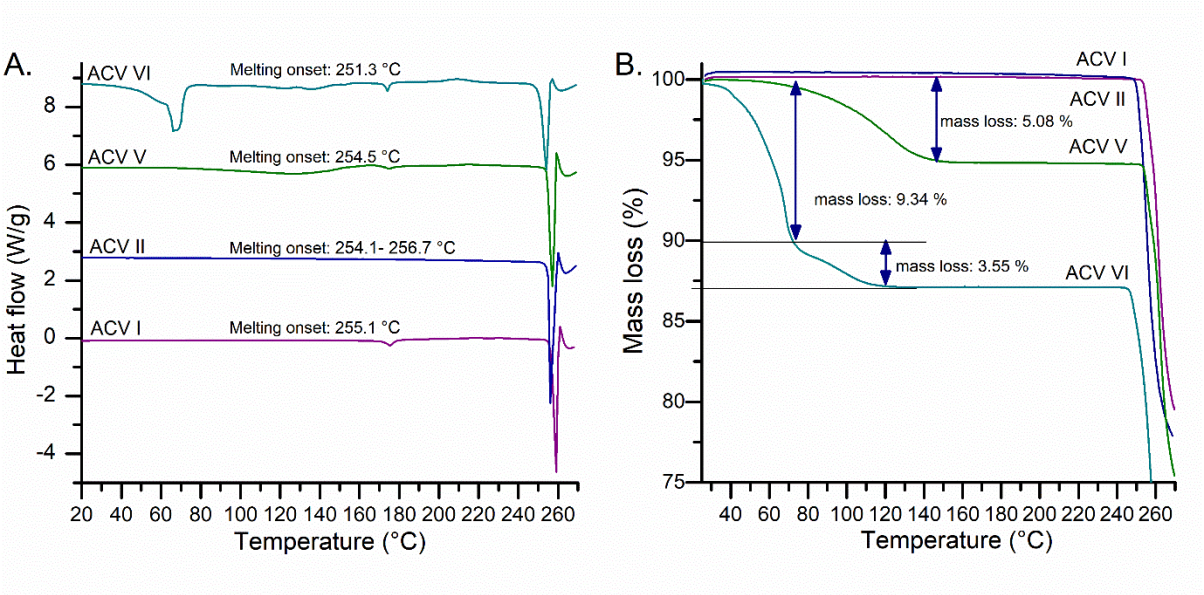

Figure 6-7 A. DSC thermograms and **B.** TGA curves of ACV forms I, II, V and VI

Table 6-3 DSC thermal parameters of transformations of ACV forms I, II, V and VI

ACV form	Unit	Dehydration	Phase transition	Melting onset
ACV I	T [°C]	-	171.0 (ACV form I → IV)	255.1 (ACV form IV)
	ΔH [kJ/mol]	-	2.3	33.5
ACV II	T [°C]	-	-	254.1-256.7 (ACV form II)
	ΔH [kJ/mol]	-	-	33.3-39.5
ACV V	T [°C]	58-155	168.9 (ACV form III → IV)	254.5 (ACV form IV)
	ΔH [kJ/mol]	28.9	2.0	36.3
ACV VI	T [°C]	50-90	173.0 (ACV form V → IV); 200.0 (ACV form IV → VII)	251.3 (ACV form VII)
	ΔH [kJ/mol]	62.4	1.8 4.8	32.3

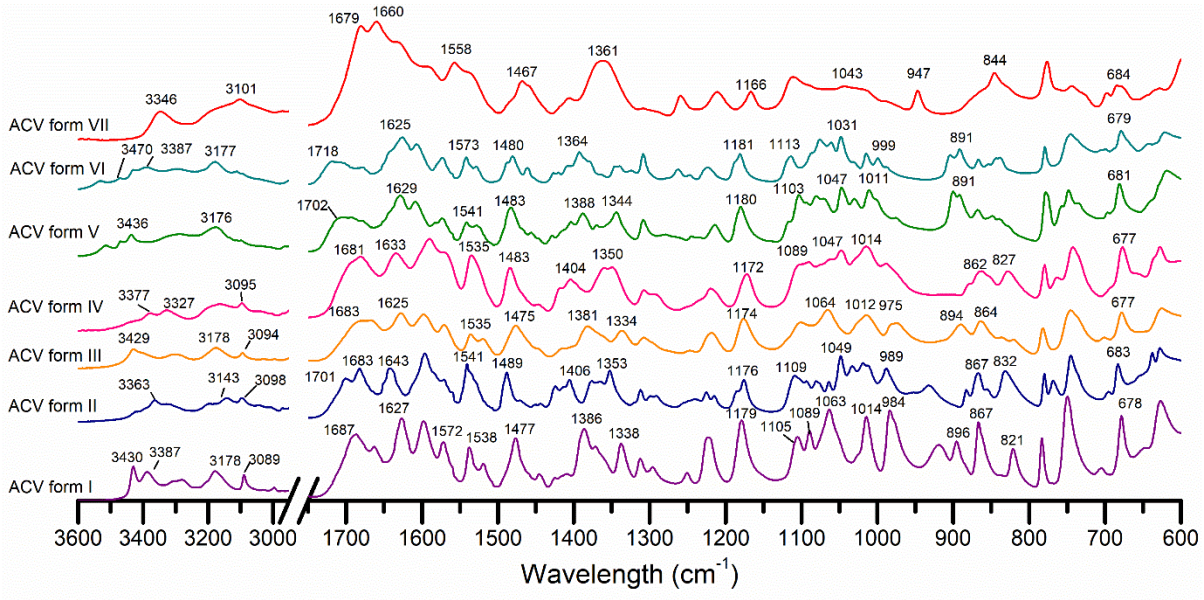

Figure 6-8 FT-IR spectra of ACV forms I, II, V, VI at room temperature, and extracted from variable temperature experiments for ACV form III (175 °C), form IV (230 °C) and VII (250 °C).

The DSC and TGA curves of the four room temperature stable crystalline forms are shown in Figure 6-7. Form V presents a broad endothermic peak in its DSC curve ranging from 58 to 155 °C (Figure 6-7-A), which corresponds with the 5.08% weight loss (w/w) of the two water molecules in the 3:2 (ACV:H_2O) form V indicated by its TGA curve (Figure 6-7-B). The thermally induced dehydration of the 3:2 hydrate results in its subsequent transformation into the metastable high temperature ACV form III between 100-170 °C. This is then followed by a second endothermic transition at 170.3 °C into the second high temperature form, ACV form IV as previously described by Lutker *et al*[120]. These high temperature forms were also confirmed through variable temperature FT-IR studies (Figure 6-8) which showed peaks indicative of the form transformation. The further heating of this form results in the melting and decomposition of ACV at 257.1 °C shown in the TGA curve. When ACV form IV is allowed to cool to room temperature it will convert from the high temperature form into the anhydrous form I, this is shown in Figure 6-9. In each heating/cooling cycle there is a transition present at *ca.* 170 °C consistent with reversible transition to form I.

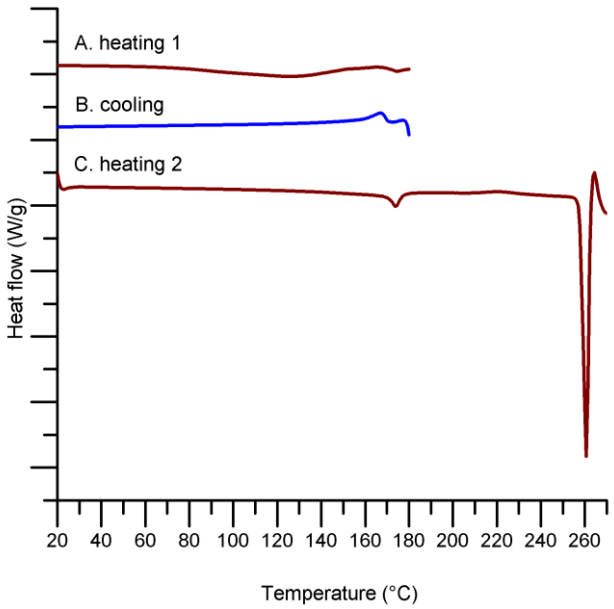

Figure 6-9 DSC thermograms of ACV form V showing **A.** the heating to 170 °C where the reversible transition can occur. **B.** The cooling from 180-20 °C **C.** Second heating to the point where melting and decomposition happens

ACV form I shows similar behaviour to form V upon heating (Figure 6-7-A) where an endothermic transition at 171.2 °C is present. This transition is the formation of the high temperature form IV which is found above ca 170 °C in form Vs DSC thermogram. Interestingly, form I does not convert to the other high temperature form III before the form IV transition, as seen in the DSC curve which has no features in the region from 100-170 °C. The transition from I to IV is also shown in the variable temperature FT-IR studies that were performed on each of the room temperature crystalline phases which are shown in Figure 6-10. In contrast to form I, the other anhydrous form II does not appear to undergo any temperature induced phase transitions until the melt and decomposition at *ca*. 250 °C.

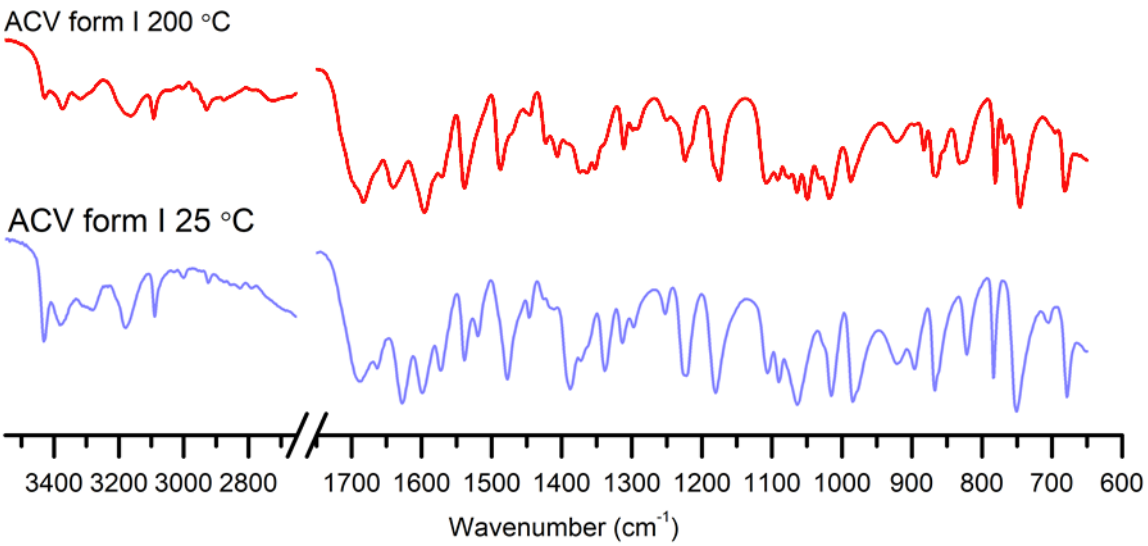

Figure 6-10 FTIR spectra of ACV form I (blue) at 25 °C and the same sample at 200 °C (red) showing transformation into the high temperature form IV

The dihydrate form VI shows complex behaviour in the DSC thermogram with many different thermal events occurring. Figure 6-7-A of form VI firstly shows an asymmetric endothermic event between 45-70 °C which when the TGA curve is consulted (Figure 6-7-B) can be seen corresponding to the weight loss of around 10% (w/w) consistent with the loss of two water molecules in the asymmetric unit compared to the one molecule of ACV present. There is then a second broad endothermic event between 90-160 °C resulting in around a 4 % loss of weight, which we associate with another loss of water. In order to confirm whether the dihydrate was following a two-step water loss mechanism upon dehydration, the TGA was performed at multiple heating rates. Figure 6-11 demonstrates a two-step curve distinctly between 5-20 °C/min heating rates, with 2 °C/min exhibiting an extremely smooth dehydration step. This implies that form VI recrystallises into the 3:2 commercially available hydrate form V. Stoichiometrically the dihydrate is at a ratio of 1:2 ACV to water molecules, whereas the form V has a ratio of 1:0.67. Therefore, the dehydration of form VI into form V prior to complete dehydration is a process that mechanistically makes sense. Further heating follows the same pathway as form V also, following DSC curve the endothermic event at 173.0 °C signifies the transformation into the high-temperature form IV. However, there is a contrasting exothermic event occurring at *ca*. 210 °C that does not appear in any DSC curves for the other forms. This is then followed by its subsequent melting at 251.3 °C.

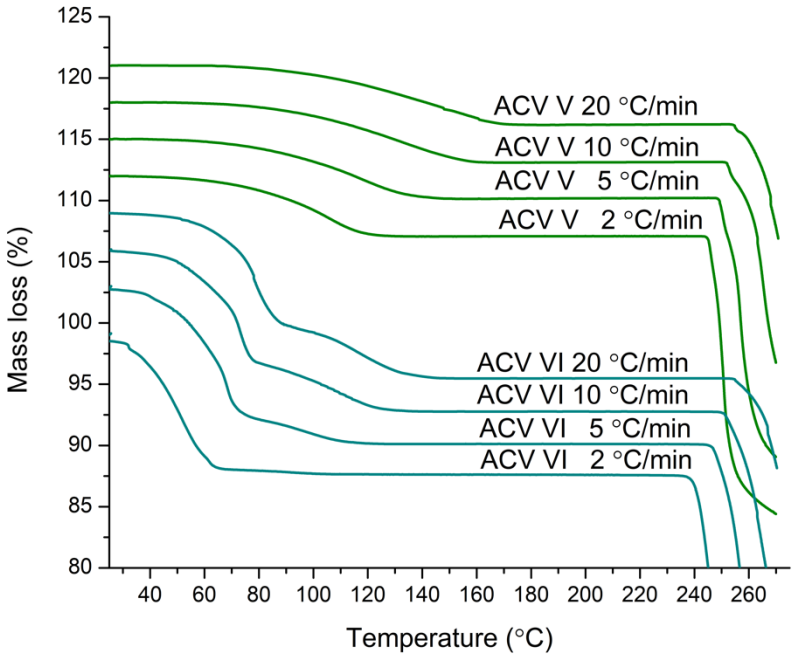

Figure 6-11 TGA thermograms of ACV form V and form VI at different heating rates ranging from 2 to 20 °C/min. A two-step dehydration can be observed in ACV form VI.

In order to observe transformation of the hydrate forms V and VI and their dehydration steps we used variable temperature FT-IR to complement the thermal techniques of DSC and TGA. Lutker *et al.*[120] published FT-IR spectra of ACV forms I, II and V giving us a reference to compare our spectra to. In addition to this, the use of variable temperature FT-IR allowed us to record spectra of form VI and of the high-temperature polymorphs of ACV III, IV and a newly discovered form VII. Form VII was obtained from the dihydrate form VI where the exothermic transition occurred at *ca.* 210 °C. There are three regions where changes in IR spectra present the different characteristics for each polymorph. The first is the NH vibrational bands between 3600-3300 cm^{-1}, the second between 1750-1650 cm^{-1} where the characteristic carbonyl stretches occur and thirdly the region between 1650-1250 cm^{-1} where NH/CH bending, carbon-double bond and carbonyl stretching occur which can be seen in Figure 6-8 for each polymorph. The anhydrous ACV form I possesses four strong vibrational bands at 3430, 3387, 3187 and 3089 cm^{-1}, whereas the other anhydrous form II has less intense bands in this region (3500-3000 cm^{-1}). The hydrated ACV forms feature extremely complex spectra, with many low intensity peaks in that same range. Separating form V (3:2 hydrate) from form VI (dihydrate) can be seen through the characteristic peaks at 3530 (form V), 3513 (form VI) and 3089 cm^{-1} (both V and VI). The vibrational bands belonging to the carbonyl groups are found to be less intense for the hydrated forms (1750-1650 cm^{-1}) and also shifted towards higher wavenumbers when compared to anhydrous

forms I and II (1702 and 1718 cm^{-1}). An explanation for this was suggested by Lutker *et al*.[120] that water molecules in the hydrated structures form stronger hydrogen bonds with carbonyl group on which in turn causes a peak shift towards higher frequencies. The hydrated forms also have a much more complex region between 1650-1250 cm^{-1} when compared to the anhydrous forms which may be due to presence of multiple molecules in the asymmetric unit of these forms.

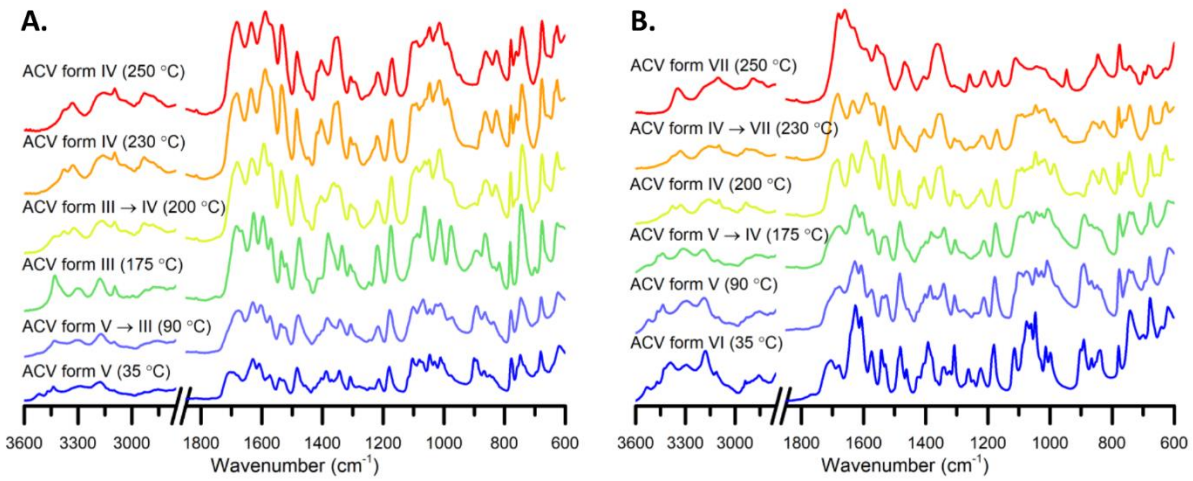

Figure 6-12 Variable temperature of the thermally induced transformations between 30-250 °C of **A.** ACV form V **B.** ACV form VI

Variable temperature FT-IR spectroscopy experiments were performed on ACV form V and VI and are shown in Figure 6-12-A/B respectively. ACV form V shows the dehydration into the first metastable form III at around 90 °C and then its subsequent transformation into form IV at around 200 °C, which is in agreement with the DSC studies performed and with previous research[120,122] of ACV form V (Figure 6-7-A). Form III has a FT-IR spectrum similar to that of form I, which is further corroborated by the PXRD patterns from Lutker *et al.*[120] and Terada *et al.*[122] Form III does show more broadened peaks than form I, however there is enough difference between the two spectra to distinguish them and hence exclude the formation of form I upon dehydration of form V shown in Figure 6-13. After subsequent further heating form III converts into the high-temperature form IV at *ca.* 200 °C. This is marked by a significant change in the FT-IR spectra with much sharper and distinct bands present. After this there are no more thermally induced transitions. In contrast, the heating of the dihydrate (form VI) results in a different behaviour from the 3:2 hydrate (form V). The first step is the initial dehydration converting to form V at around 60 °C which is corroborated through DSC and TGA (Figure 6-7-A/B). Terada *et al*.[122] reported a similar dehydration step when performing RH measurements on

the water desorption of form VI. The stark difference then between the spectra is that at this higher temperature form V does not undergo any further transformations until around 170 °C. This is contrast to DSC thermograms that show two distinct transitions in the temperature range from 100 to 160 °C. As indicated in the DSC for form VI, there is an exothermic transition at *ca*. 210 °C which we now know has resulted in a further phase change due to the indicated difference in FT-IR spectra into the new high temperature form VII.

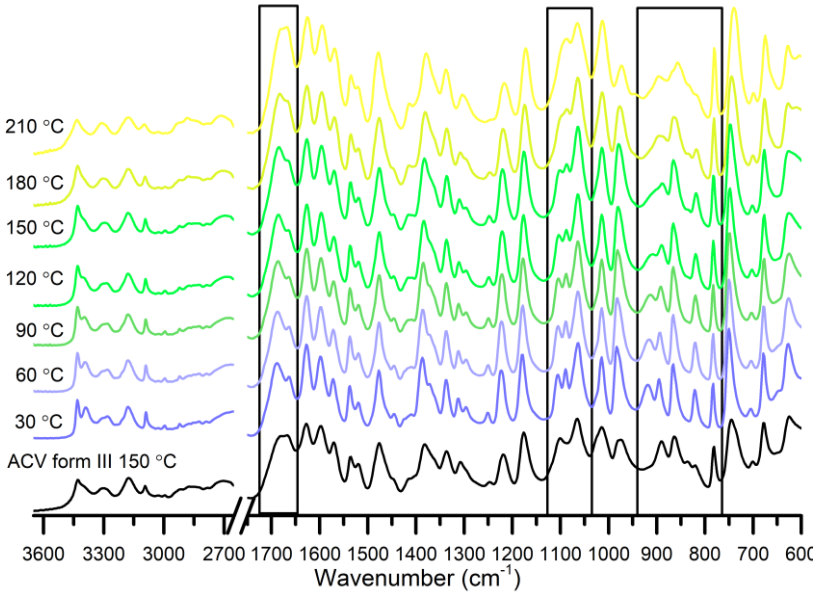

Figure 6-13 Variable temperature FT-IR spectra of ACV form I (coloured) compared high temperature metastable form III (black). Regions showing difference between the spectra are indicated by black frames.

6.2.7 Solvent mediated phase transformations of ACV forms

The process of SMPT occurs in three-steps. The first being a dissolution of a less stable (metastable) form of a crystal system, followed secondly by the nucleation of a more stable (thermodynamically) form and the subsequent third step is growth of that form[156,158]. Gu *et al.*[156] indicated that given a specific solvent medium there is always a preferential polymorphic form that will crystallise out, even when this form is not seeded. This is due to the solvent interactions with the solute and forms the basis of SMPT as a method of crystal engineering.

Lutker *et al.*[120] and Terada *et al.*[122] provide the basis for ACV's polymorphism through the effects of temperature induced phase transitions and examples of humidity affecting the hydration and dehydration of ACV forms. However, to our knowledge (and prior to our research) there were no SMPT type studies carried out on ACV in order to explore any possible new solvates or polymorphic interconversion methods. By carrying out this study we aimed to gain insight into more of the rich polymorphism exhibited by ACV through solvate and hydrate formation, but also explore and explain more mechanistically transformations from one known polymorph to another. This also allowed us to explore dissolution kinetics of ACV as it is known to be fairly soluble[146].

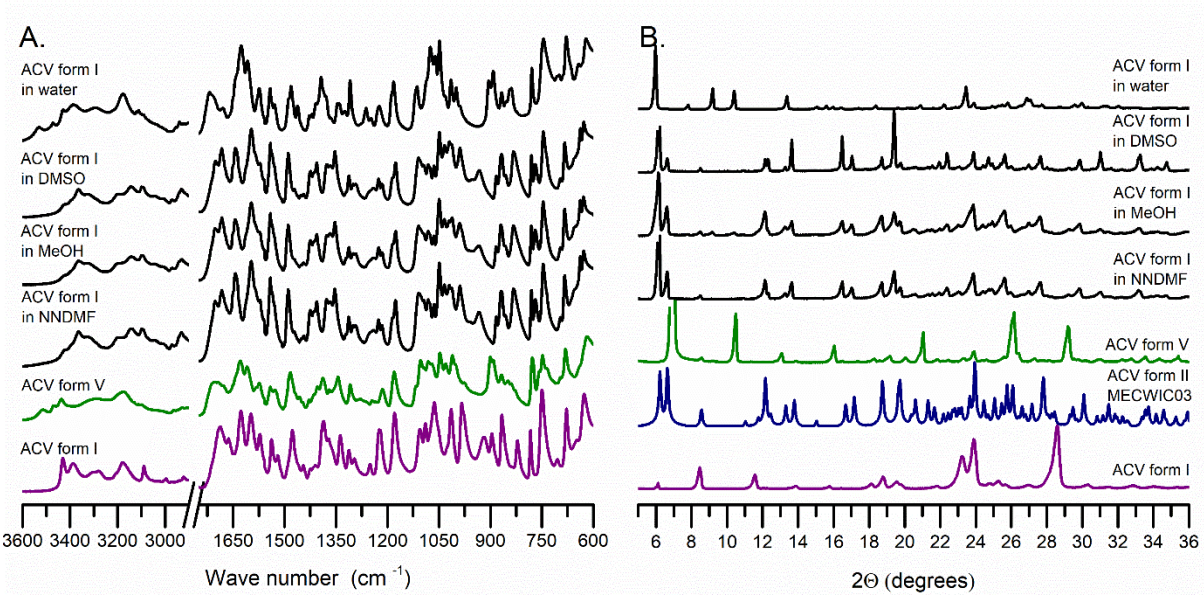

Figure 6-14 A. FTIR spectra and **B.** PXRD patterns of ACV form I slurried for four weeks in NNDMF, MeOH, DMSO and water. The FTIR spectra and PXRD traces of ACV form I and form V along with the calculated PXRD pattern of ACV form II (CSD ref. MECWIC035) are given for comparison.

When the anhydrous ACV form I was slurried in dry methanol ($a_w \leq 0.14$), NNDMF and DMSO for a period of four weeks at room temperature, the formation of form II was identified (Figure 6-14). 11 other solvents were slurried with ACV form I and did not give any discernible phase change. It can be seen in the FT-IR spectra and PXRD patterns that the resultant data match that of the comparative spectrum of ACV form II, except for the case of when form I was slurried in water which converted into the dihydrate form VI. The DMSO slurry of form I resulted in the formation of an opaque gel-like substance which contained well-formed crystalline form II. It was also discovered that the dryness of the solvent affected the ability for the phase change to occur, which we related to the water activity of the given solvent. For example, when the water activity was increased in methanol, a mixture of

forms I, II and V were found. When the water activity was increased further, an increasing content of ACV form V was found.

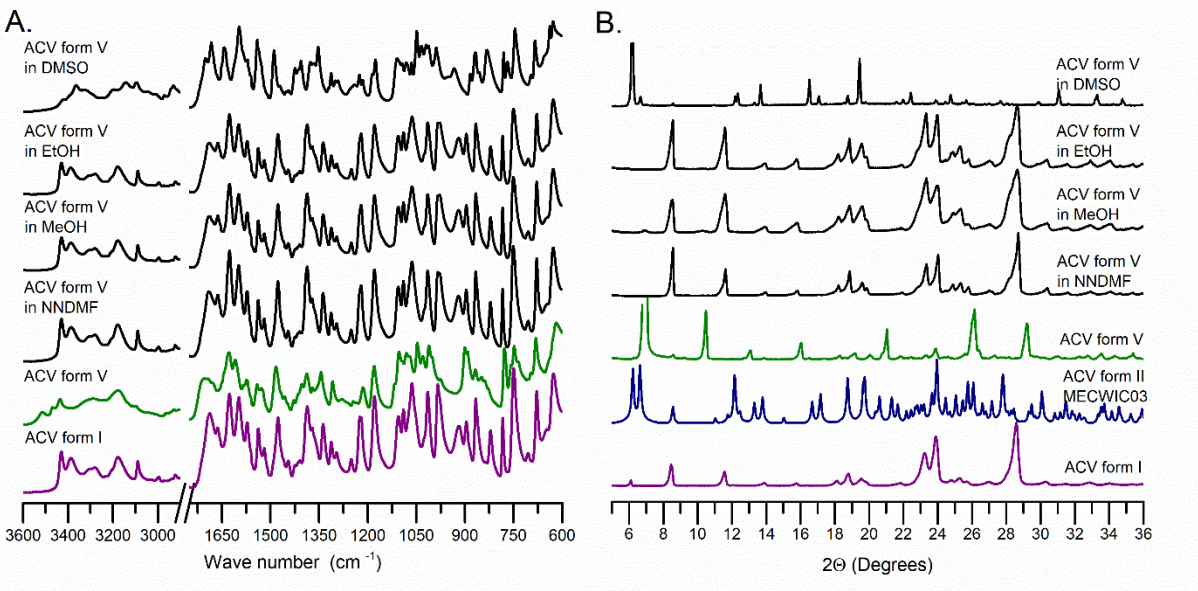

Figure 6-15 FTIR spectra and **B.** PXRD patterns of ACV form V slurried for four weeks in NNDMF, MeOH, DMSO and water. The FT IR spectra and PXRD traces of ACV form I and form V along with the calculated PXRD pattern of ACV form II (CSD ref. MECWIC03) are given for comparison.

When the 3:2 commercial hydrate form V was slurried with the same solvents, there was a difference in the outcome of crystallisation. From ethanol, methanol and NNDMF form I was obtained as shown in Figure 6-15. This phase change from hydrate form V to anhydrous form I was only observed when using extremely dry solvents (stored at humidities below 40%) where the water activity in the given solvent was also low ($a_w \leq 0.1$ in methanol and $a_w \leq 0.22$ in NNDMF). When the water activity reached a certain level, it stopped the transformation of form V into form I. Once form I is formed produced using a dry solvent, the subsequent addition of water content tends to drive the transition towards the dihydrate (form VI) rather than form V. This was also the case when ACV form I was slurried in water, implying that the arrangement of the purine rings favours that polymorphic conversion due to the way it is dissolved in the solvent. Water molecules could influence the transition due to the way they interact with ACV molecules in solution through hydrogen bonding. This in turn could cause the nucleation of form V. This could also be due to presence of water being in such high quantities compared to the amount of ACV. In terms of timing, the dehydration of ACV form V was observed after only one week when crystallising from NNDMF whereas dry ethanol and methanol took four times longer. This could be due to NNDMFs affinity towards water being greater than that for ethanol

and methanol – it is commonly used as a drying agent in organic synthesis[159]. The ability for the solvent to pull the water molecules from the ACV hydrate is the key limiting step to form a more thermodynamically stable product, just as with thermally induced dehydrations the temperature at which the polymorph is kept determines the energy of the system being able to remove water molecules and then subsequently rearrange into a more favourable crystallographic form. A summary of these transformations is shown in Figure 6-16.

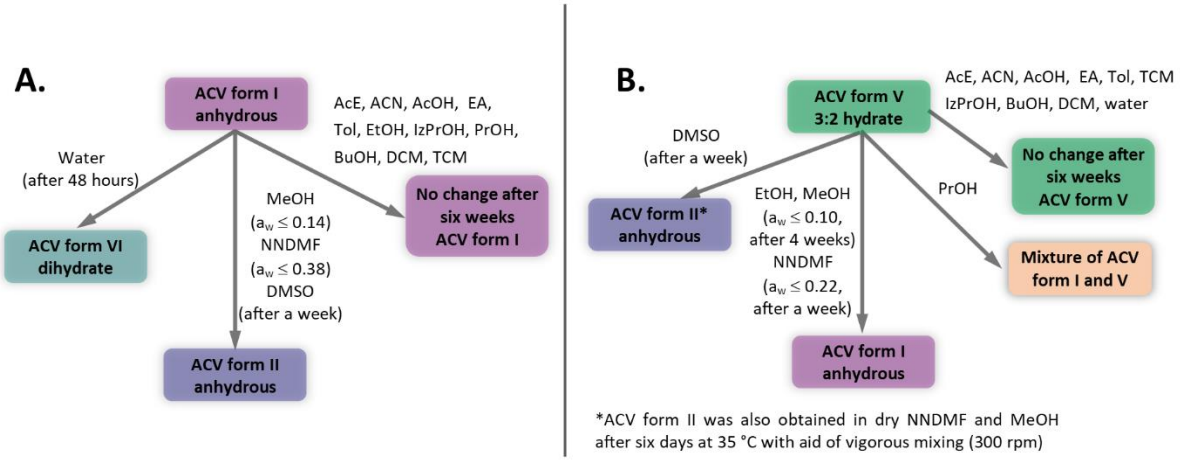

Figure 6-16 The SMPT of ACV **A.** Anhydrous form I **B.** 3:2 Hydrate form V

6.2.8 The structural changes of the polymorphic forms of ACV

ACV form V (3:2 hydrate, commercially available form) is able to be dehydrated into ACV form I (Z'=1, anhydrous form) by either a thermally induced phase transition or by using dry organic solvents such as NNDMF, ethanol and methanol. As shown in Figure 6-17, form V has two distinct water molecules in its unit cell that form channels along the *b* axis. Of these two water molecules, one (pictured in blue) hydrogen bonds with two ACV molecules that are aligned in parallel through their purine ring bases. The final ACV molecule present has an antiparallel alignment of its purine ring to the other two, allowing stacking interactions to alternate between the opposite ends of the purine bases. The previous water molecule also donates a hydrogen towards the carbonyl group of an ACV (yellow) molecule whilst accepting a hydrogen from the amino group of a different ACV molecule. The second water molecule (red) possesses three hydrogen bonds with three different ACV molecules that are stacked together. Each of the ACV molecules in the crystal structure forms hydrogen bonded dimers with two adjacent molecules through the amides and carbonyl groups present of the purine base. The

three remaining aliphatic chains point out in alternating directions depending on the orientation of the ACV molecule.

When these water molecules are completely removed from the structure, the result is ACV form I (Z'=1). ACV form I presents the same dimer alternate stacking arrangement found in ACV form V but does not possess the space for water channels to be present. The fact that it is a $P2_1/c$ space group means that the alternate stacking of the purine bases is to be apparent because it possesses a two-fold screw axis with a translation along the *c* axis. The fact that the structures are that different from each other indicates that it is not simply an isomorphic dehydration form of V (missing the water).

The second anhydrous polymorph of ACV (form II) is formed through SMPT when form I is dissolved in methanol, NNDMF and DMSO. It is also able to from when the commercial 3:2 hydrate (form V) is dissolved in DMSO. This structure shows a different hydrogen bonding pattern to all the other polymorphs, where each of the ACV molecules forms seven hydrogen bonds with three adjacent neighbouring molecules. Ring stacking is still partially present through the amine and carbonyl on the purine base. These extreme structural differences to the other ACV forms show that it is not surprising that this form is not able to be accessed through thermally induced phase transitions, be it heating or cooling. It requires some form of solvent mediation in order to allow the structural rearrangement of the molecules of ACV through breaking and reformation of hydrogen bonding. Even from the previous research by Lutker *et al*. [120] when put into the perspective of our studies support this. They had previously achieved the transformation of form I into form II through the use of hot methanol in a sealed vial. Form II was also made through by precipitation, by mixing form I with Nylon-6 and an antisolvent of acetonitrile.

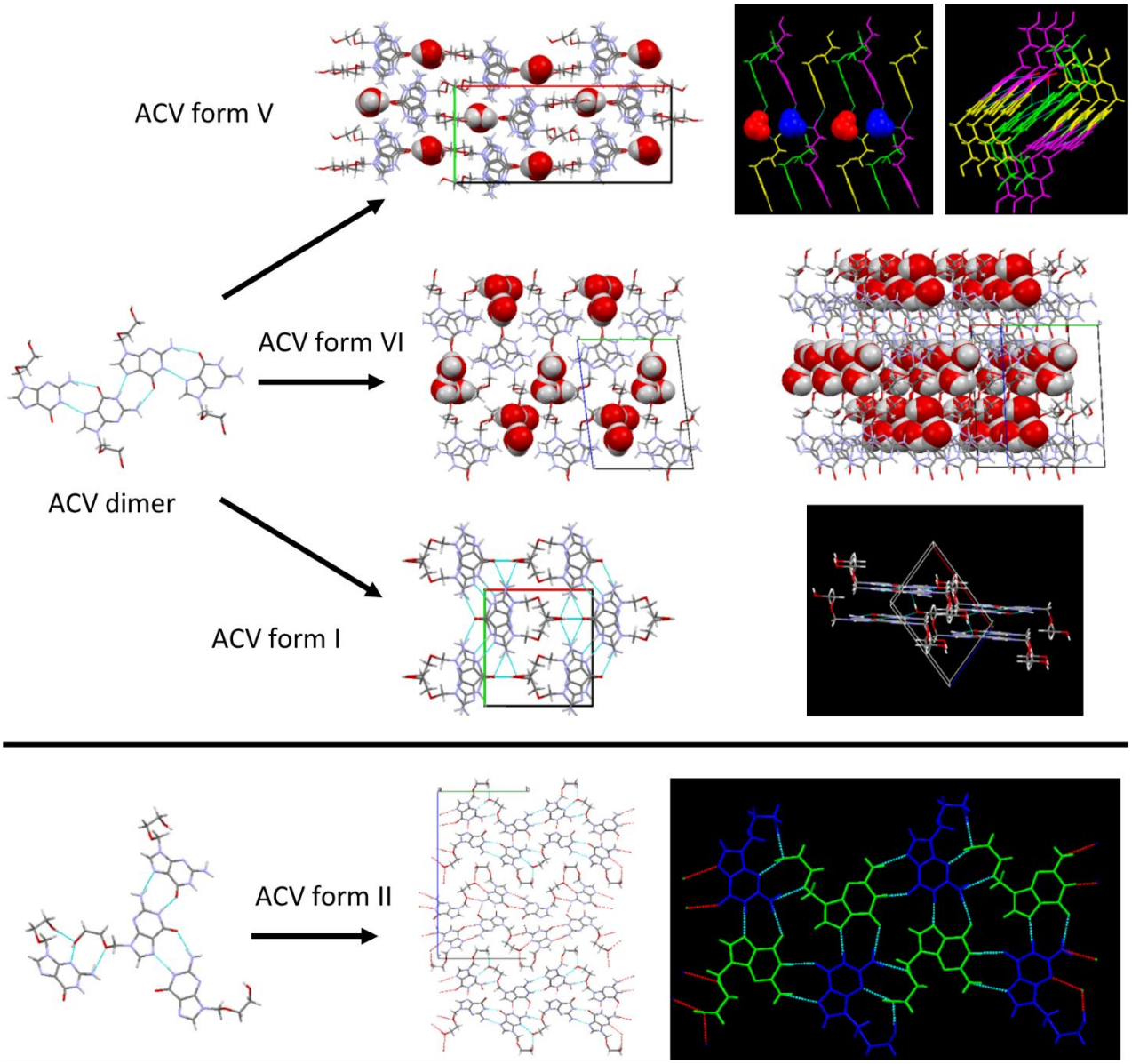

Figure 6-17 The structural difference between the stable polymorphs of ACV. Form I and V are shown down the *c* axis whereas form VI and II are shown down the *a* axis.

6.2.9 Conclusions

Through the use of solvent mediated phase transformations, the antiviral drug acyclovir has been investigated in 15 different organic solvents. These have shown that it is possible to dehydrate the commercially available 3:2 hydrate (form V) into the anhydrous form I, when the solvent is of high polarity (methanol and ethanol) or a good organic drying agent (NNDMF). The slurrying of form V in DMSO formed gel-like material that matched the structurally interesting anhydrous form II. This anhydrous form II was also able to be formed by slurrying of form I in dry solvents like methanol and NNDMF. DMSO, as with form V, formed a gel-like substance containing the crystalline form II

polymorph. When the water activity of the solvent was increased it stopped the SMPT to these forms occurring. Through combination of solid-state NMR analysis, computational calculations, variable temperature FT-IR spectroscopy, PXRD and thermal methods such as DSC and TGA we have gained insight into the structural transformations and mechanisms that ACV has to offer and the discovery of a new metastable high temperature form VII through VT-FTIR.

6.3 Contributions

This chapter formed a paper[160] published in *CrystEngComm* in 2019 in collaboration with Karol P. Nartowski, Julia Karabin, Maciej Nowak, László Fábián, Bożena Karolewicz and Yaroslav Khimyak. My overall contribution to this paper included:

- Solid-state NMR characterisation of ACV forms
- CASTEP calculation of NMR chemical shifts
- PXRD characterisation of ACV forms
- FT-IR measurements and VT FT-IR studies

7 General discussion and Conclusions

7.1 Showing interactions between phases of FFA/NA by ^{19}F-^{19}F NOESY NMR

^{19}F MAS NMR demonstrated the existence of three separate phases of FFA/NA when loaded into the MCF host, which possesses the largest pores at 26 nm. Two phases were found in SBA-15 (6 nm pores), and one phase was found in MCM-41 (3 nm pores). Correlating these phases with the size of the pores led to the development of a hypothesis regarding the structural arrangement of FFA/NA inside the pores. PXRD and DSC showed that MCF contained a phase that was crystalline inside the pore space. The smaller pores of SBA-15 and MCM-41 showed an absence of any crystalline phase. The ^{19}F NMR spectra at 19.96 T at 55 KHz MAS of MCF pointed to the hosts with the largest pores having a mixture of crystalline, aggregated and mobile phases of FFA/NA, however, they did not definitively show that they existed in the same pore space. It would also be beneficial to perform more measurements on the sample of MCF loaded with at 35% with FFA/NA focussing on understanding of the nature of interfaces between different components in the pore space. The sample was made extremely late in the PhD as an investigation into the point between complete loading and partial loading. Both thermal and PXRD measurements may greatly aid the understanding why evidence of crystallinity falls off rapidly below 40% loading. If the state at 35% is more of a mixture of co-amorphous and co-crystalline phases it would possibly be a good starting point of attempting to quantify the ratios of these.

The high-field ^{19}F-^{19}F NOESY NMR spectra are the key piece of information that proves the hypothesis that these phases exist and interact in the same pore space. By showing both the existence and absence of cross-peaks in that NOESY NMR data, we could demonstrate the spatial proximity of the species with different degree of ordering. The evolution of the intensity of the peaks corresponding to ordered co-crystalline, aggregated and liquid-like mobile components could be followed from the in-situ crystallisation experiments. This has subsequently allowed us to hypothesise the arrangement of FFA/NA molecules within each of the mesoporous silicas we have loaded them into. The ^{19}F NMR data for encapsulated species indicate an increase in less ordered species from both a decrease in the size of the pores (MCF > SBA-15 > MCM-41) but also the ratio of loading of the FFA/NA (50 – 15%). This gradient in the degree of ordered species implies that there is a critical nucleus size required to

form what resembles a crystalline species. However, this has been just from this study of one system and further studies are needed on different APIs in order to fully explore different phases that can exist within the pores. This is not the first example of loading drug APIs into the MSMs. Moreover, it is not the first time cocrystals have been loaded for example ibuprofen/nicotinamide[161] were loaded into 16 nm MSMs and were characterised for their ability to stabilize the poorly soluble ibuprofen into a co-amorphous state, whilst simultaneously achieving a better dissolution profile for the drug. Studies on BA/FBA[70] cocrystals have been previously conducted similarly using techniques of NMR and exploring thermal properties. The 2D NMR studies showed the structure and dynamics of the cocrystal inside the pores to a good extent when combined with molecular dynamics simulations. This, to our knowledge, is the first-time multiple environments have been detected inside differing sizes of MSMs, and furthermore shown proof that these phases exist in close proximity to each other. The implication of this being that the properties of a loaded co-crystal system can be influenced and affected by changing the composition, loading ratio and size of the pores. This could be used to tune the point at which a particular drug will either crystallise or form the co-amorphous state within pores as a vehicle of drug delivery, depending on the dissolution profile and kinetics required.

7.2 Determination of a new polymorph of nicotinamide

Our group's previous work on FFA loaded inside silica[72] and subsequent work in this thesis on the cocrystal of FFA/NA left a gap in the full extent of our characterisation. Naturally, loading NA into each of the pore spaces was the next step in order to have a more complete picture. The hope also was that resolution in the ^{1}H-^{13}C CP-MAS NMR spectra of NA loaded material would aid the assignment and understanding of the cocrystal. However, we then discovered that NA behaved differently to FFA/NA inside SBA-15. In SBA-15 loaded with the FFA/NA cocrystal, we do not observe what we would characterise as a structurally ordered species. We had thought this would apply to NA also due to SBA-15's pore diameter of only 6-7 nm. The resulting ^{1}H-^{13}C CP-MAS spectra of SBA-15 loaded with NA revealed a different polymorph to that of what was initially loaded, form I (Z'=1), and different PXRD patterns to that of the second polymorph in the CSD, form II (Z'=4)[135].

During the course of the project, we attempted to characterise and solve the structure of this NA polymorph to no avail. It was only in the late stages of the write-up that a preprint paper detailed the structures of seven new polymorphs of NA[143]. The paper detailed the SCXRD results of each polymorph with the crystallographic structural parameters, however the raw data was not available at this point. Upon reaching out to the authors of the paper we were supplied with an image containing a PXRD overlay of the new forms that allowed for a possible match to be made. Our highest resolved PXRD

diffractogram was that of MCF loaded NA, which features diffraction peaks that we could not identify and some that we characterised as form I. We subsequently characterised our unknown NA polymorph from the PXRD data supplied to us as matching polymorph δ due to the fact that we believe the cell parameters are suitable for the growth of nano-needles inside the pores. The prospect of directed polymorphic growth of nano-needles by encapsulation is a field we look to explore further with similar APIs to NA such as isonicotinamide.

7.3 Solvent mediated phase transitions of ACV

The solubility properties of acyclovir are the essential characteristics that have allowed for the discovery of the phase changes between the anhydrous and hydrated forms. The mechanism for the dissociation of water from a crystalline hydrate by thermal decomposition is difficult to model and is not well understood[162]. Computational models have attempted to describe the dehydration of specific crystal systems, e.g. naproxen sodium hydrates by Larsen *et al.*[163], Fujii *et al.*[164] used variable temperature PXRD for structure determination of the hydrates and anhydrous forms of pharmaceuticals, in which has had some success with describing dehydration mechanism of specific crystal hydrates.

This is what has allowed ACV to be an interesting candidate for studies into the phase transitions between its anhydrous and hydrated forms. By first fully characterising each of the forms thermally using solid-state NMR, DSC, PXRD and TGA we were able to build a picture of the possible interconversions between forms that were first suggested by Lutker *et al.*[120] and Terada *et al.*[122] By comprehensively characterising each sample, we were able to detect the presence of a new high temperature metastable form VII by adding VT-FTIR to the list of characterisation techniques. The new aspect to this study was use of the solution mediated transformations in order to bring about a phase transition and explore the pathways of hydration and solvation of the drug.

Tanaka, Koga and Galwey[165] used microscopy in order to study the kinetics of decomposition of different hydrates, outlining different nucleation behaviours, and rate determining steps that depend on the dimensionality of the crystal growth. Comparative to these pathways is the model developed by Petit and Coquerel[166], termed the Rouen 96 model, which describes the process of dehydration of water giving the result of formation of new anhydrous material (NAM). Two classes of this pathway are described; class I assuming that the NAM produced has a crystal structure different to its hydrate, or class II where the anhydrous and hydrate structures are topotactical in nature. However, these pathways have been based on inorganic crystalline materials. The nature of organic dehydration could

be described as a more imperfect process, with class I and II pathways intersecting each other resulting in mixed dehydration products.

The initial characterisation has then allowed us to fully explore the dehydration process through the use of solvents. Of the 14 organic solvents we have identified those which are able to cause a solvent mediated phase transformation, noting that the solvents with the higher polarities and greater water activities are able to drive that solid form change. The subsequent pairing with thermal dehydration data help to broaden the understanding and gains us insight into the possible mechanisms at work. Additional work that shows the influence of SMPT is by Bobrovs[167] with the effect of different solvents on the polymorphic behaviour of the chemotherapeutic tegafur. In the paper, the transition from the α to β forms of tegafur are influenced by supersaturation ratio of the drug given a specific solvent. From this a mechanism was proposed as to the nucleation pathway; showing that through different nucleation rates, a second-order power function was evident on a particular face of the given polymorph of tegafur. The arrangement of the purine rings in each polymorph of ACV appears to be a key factor towards water channels being accessible by the dry solvents in order to pull them away and cause a polymorphic change.

7.4 Overall conclusions and further work

We have demonstrated both the presence and spatial relationship between the components with different degree of ordering of FFA/NA inside mesoporous silicas. There has also been demonstrated a dependence on the type of phase of FFA/NA accordingly to the size of the pores it is encapsulated in. The assignment of these phases has required application of different characterisation techniques. We believe we have captured evidence of three distinct phases of FFA/NA. Through variable temperature experiments and 2D NMR we have shown that these phases are present in the same pore space. In-situ NMR studies have enabled us to monitor the changes in the populations of these components during crystallisation. Our next steps in this area of research are to model the API/silica interface to determine orientations and energies. We also plan to further optimise the 2D correlation experiments, such as NOESY, with functionalised silica surfaces (hydrophobic surfaces such as the addition of fluorine) and different cocrystal systems from similar families of the fenamic acids. This would allow us to see if these discrete phases also exist in different silica systems but also if more interactions point to a greater number of phases.

This aspect of molecular landscape of crystallography has been explored by others groups. The work of Roger Davey into how polymorphism can be affected by conformation and hydration kinetics on fluconazole is similar to this thesis's experiments on both the FFA API and hydration profiles of ACV[168].

The choices of API we have made are similar across the discipline for the kind of model drugs that have some predictable behaviour i.e. simple small organic molecules such as nicotinamide, isonicotinamide, p/o/m-benzene derivates. This is especially important for the development of pharmaceuticals and their polymorphic behaviour as Grant *et al*.[169] comments on emphasising the greatest areas of interest to be the determination and subsequent prediction of polymorphic species in order to further understand the mechanism of phase transformations present.

The loading of NA into the different silicas has shown that the melt loading method of encapsulating materials within a mesoporous silica can cause polymorphic transformation. The question being, are we able to find new polymorphs of old APIs by performing this technique. The important lesson we have learnt, which can be implied to other APIs, is that nucleation of specific polymorphs can be controlled through restricting the dimensions in which a structure is able to grow. This could mean that routes towards polymorphs that appear inaccessible or have yet to be reported could be discovered. Roger Davey *et al*.[170] highlighted some of the primary issues with organic crystalline polymorphism, namely questioning why some polymorphs are more difficult to access than others and also highlighting the stabilities of those polymorphs under different conditions. Prior to our work nicotinamide had been explored thoroughly, and it was only recently that new NA polymorphs were discovered. Had we been able to characterise the unknown polymorph we discovered quicker we may have been able to derive its structure. Hindsight has thus allowed us to give a partial assignment of this polymorph to the most likely structure. However, we did have further work planned to explore and characterise the unknown polymorph further. We had hoped to isotopically label nicotinamide with ^{15}N in the pyridine nitrogen position which would have allowed us to discover the number of molecules in the asymmetric unit. A good potential future aspect to this work would be to perform Crystal Structure Prediction of this polymorph through and combine its findings with the data from PXRD and solid-state NMR. It is clear that a wealth of different polymorphs could be discovered due to their encapsulation in silica, however more methods of both the characterisation and interpretation of data are required to fully understand the dynamics and structures that exist.

Another aspect that should be explored further is the interactions of the various phases with each other by attempting to characterise the type of interactions, the lifetime of the interactions of the phases with each other and also to show if exchange of molecules is occurring between those phases. This would be assisted by further variable temperature studies to help to answer the question of the dynamics of these phases. Our previous evidence shows that the phases exchange magnetisation with each other, therefore if we could explore the range of this interaction, we could begin to evaluate the possible size and shapes that the co-amorphous forms are taking in the pore space. Also, by mapping

out possible silanol surface interactions with loaded guests at various temperatures we may be able to quantify the mobility of the surface phase inside the pores. This would then allow us to further develop our understanding of the growth, decay and quantity of different phases. This would allow us to understand why some phases (like the crystalline or disordered) only appear at specific loading levels, or whether the liquid-like phase on the surface of the silanol is always present. Answers to these questions could serve to further our understanding of mechanics of crystallisation and thus predict how a specific structure will react to being encapsulated as a vehicle of drug delivery.

The pharmaceutical implications of multiple phases existing in the same drug delivery vehicle must also be considered. The use of these silica devices is dependent on understanding what happens to the APIs within their pore space. As we show, there is a significant difference between the size of the pores and the types of API environments that become present after loading. To further this we must consider how the drug will be accessed inside the body. Different sizes and complexities of the phases of the drug will break down at different rates, these rates can be highly dependent on environment. Park *et al.*[171] showed the effect of pH on cisplatin release from MSNs while simultaneously showing that the drug actively killed different cancer cells more effectively than pristine cisplatin, whilst still having comparable toxicity levels. The further application of the biological properties needs to be explored, but also considered from a pharmaceutical engineering standpoint. What would help this is furthering the predictions of what kind of phases a drug will exhibit when placed in a pore with a specific size, and thus how those phases will affect its release profile. This may one day allow an even greater programming of drug release into the body.

8 References

1 B. C. Hancock and G. Zografi, *J. Pharm. Sci.*, 1997, **86**, 1–12.

2 B. Vessal, in *Computer Modeling in Inorganic Crystallography*, Elsevier, 1997, pp. 295–332.

3 G. G. Z. Zhang and D. Zhou, in *Developing Solid Oral Dosage Forms: Pharmaceutical Theory and Practice: Second Edition*, Elsevier Inc., 2017, pp. 23–57.

4 J. Haleblian and W. McCrone, *J. Pharm. Sci.*, 1969, **58**, 911–929.

5 W. Z. Ostwald, *Phys. Chem.*, 1879, **22**, 289.

6 D. W. Van Krevelen and K. Te Nijenhuis, in *Properties of Polymers*, eds. D. W. Van Krevelen and K. B. T.-P. of P. (Fourth E. Te Nijenhuis, Elsevier, Amsterdam, 2009, pp. 703–746.

7 A. G. Pinkus, J. S. Kim, J. L. Mcatee, C. R. Concilio, J. L. Mcatee and C. R. Concilio, *J. Am. Chem. Soc.*, 1959, **81**, 2652–2654.

8 P. G. Vekilov, in *Handbook of Crystal Growth: Second Edition*, ed. T. B. T.-H. of C. G. (Second E. Nishinaga, Elsevier, Boston, 2015, vol. 1, pp. 795–871.

9 R. J. Davey, S. L. M. Schroeder and J. H. Ter Horst, *Angew. Chemie - Int. Ed.*, 2013, **52**, 2166–2179.

10 R. J. Davey, K. R. Back and R. A. Sullivan, *Faraday Discuss.*, 2015, **179**, 9–26.

11 C. W. Lan, *Chem. Eng. Sci.*, 2004, **59**, 1437–1457.

12 S. Karthika, T. K. Radhakrishnan and P. Kalaichelvi, *Cryst. Growth Des.*, 2016, **16**, 6663–6681.

13 M. Volmer and A. Weber, *Z. Phys. Chem.*, 1925, **119**, 277–301.

14 J. W. Gibbs and J. Tyndall, *Equilib. Heterog. Subst. first [-second] part*, 2020, **3**, 108–248.

15 P. G. Vekilov, *Cryst. Growth Des.*, 2010, **10**, 5007–5019.

16 J. J. De Yoreo, P. U. P. A. Gilbert, N. A. J. M. Sommerdijk, R. L. Penn, S. Whitelam, D. Joester, H. Zhang, J. D. Rimer, A. Navrotsky, J. F. Banfield, A. F. Wallace, F. M. Michel, F. C. Meldrum, H. Cölfen and P. M. Dove, *Science (80-.).*, 2015, **349**, aaa6760.

17 A. F. Wallace, L. O. Hedges, A. Fernandez-Martinez, P. Raiteri, J. D. Gale, G. A. Waychunas, S. Whitelam, J. F. Banfield and J. J. De Yoreo, *Science (80-.).*, 2013, **341**, 885–889.

18 F. Zhang, F. Roosen-Runge, A. Sauter, M. Wolf, R. M. J. Jacobs and F. Schreiber, *Pure Appl. Chem.*, 2014, **86**, 191–202.

19 A. Sauter, F. Roosen-Runge, F. Zhang, G. Lotze, A. Feoktystov, R. M. J. Jacobs and F. Schreiber, *Faraday Discuss.*, 2015, **179**, 41–58.

20 M. A. Vorontsova, D. Maes and P. G. Vekilov, *Faraday Discuss.*, 2015, **179**, 27–40.

21 A. Bhatia, S. Chopra, K. Nagpal, P. K. Deb, M. Tekade and R. K. Tekade, in *Dosage Form Design Parameters*, ed. R. K. B. T.-D. F. D. P. Tekade, Academic Press, 2018, vol. 2, pp. 31–65.

22 M. Mirmehrabi and S. Rohani, *J. Pharm. Sci.*, 2005, **94**, 1560–1576.

23 S. L. Price and L. S. Price, *Polymorph. Pharm. Ind.*, 2018, 133–157.

24 F. Cao, G. L. Amidon, N. Rodriguez-Hornedo and G. E. Amidon, *Mol. Pharm.*, 2016, **13**, 1030–

1046.

25 S. J. Bethune, N. Huang, A. Jayasankar and N. Rodríguez-Hornedo, *Cryst. Growth Des.*, 2009, **9**, 3976–3988.

26 U. Likhitha, B. Narayana, B. K. Sarojini, A. G. Lobo, G. Sharma, S. Pathania and R. Kant, *J. Mol. Struct.*, 2019, **1195**, 827–838.

27 C. B. Aakeröy, M. E. Fasulo and J. Desper, *Mol. Pharm.*, 2007, **4**, 317–322.

28 A. Gunnam, K. Suresh, R. Ganduri and A. Nangia, *Chem. Commun.*, 2016, **52**, 12610–12613.

29 D. Shekhar Reddy, Y. E. Ovchinnikov, O. V. Shishkin, Y. T. Struchkov and G. R. Desiraju, *J. Am. Chem. Soc.*, 1996, **118**, 4085–4089.

30 M. C. Etter, *J. Phys. Chem.*, 1991, **95**, 4601–4610.

31 S. Saha and G. R. Desiraju, *J. Am. Chem. Soc.*, 2018, **140**, 6361–6373.

32 G. Patrick Stahly, *Cryst. Growth Des.*, 2009, **9**, 4212–4229.

33 Z. J. Li, Y. Abramov, J. Bordner, J. Leonard, A. Medek and A. V. Trask, *J. Am. Chem. Soc.*, 2006, **128**, 8199–8210.

34 D. P. McNamara, S. L. Childs, J. Giordano, A. Iarriccio, J. Cassidy, M. S. Shet, R. Mannion, E. O'Donnell and A. Park, *Pharm. Res.*, 2006, **23**, 1888–1897.

35 P. J. Barnes, *Am. J. Respir. Crit. Care Med.*, 2013, **188**, 901–906.

36 A. V. Trask, W. D. S. Motherwell and W. Jones, *Int. J. Pharm.*, 2006, **320**, 114–123.

37 D. Yang, J. Cao, L. Jiao, S. Yang, L. Zhang, Y. Lu and G. Du, *ACS Omega*, 2020, **5**, 8283–8292.

38 A. V. Trask, W. D. Samuel Motherwell and W. Jones, *Cryst. Growth Des.*, 2005, **5**, 1013–1021.

39 P. A. Wright, in *Encyclopedia of Materials: Science and Technology*, eds. K. H. J. Buschow, R. W. Cahn, M. C. Flemings, B. Ilschner, E. J. Kramer, S. Mahajan and P. B. T.-E. of M. S. and T. Veyssière, Elsevier, Oxford, 2001, pp. 1–6.

40 J. D. F. Ramsay and S. Kallus, in *Membrane Science and Technology*, ed. N. K. B. T.-M. S. and T. Kanellopoulos, Elsevier, 2000, vol. 6, pp. 373–395.

41 A. L. Morritt, J. R. Lopez, T. J. Blundell, E. Canadell, H. Akutsu, Y. Nakazawa, S. Imajo and L. Martin, *Inorg. Chem.*, 2019, **58**, 10656–10664.

42 L. Martin, A. L. Morritt, J. R. Lopez, Y. Nakazawa, H. Akutsu, S. Imajo, Y. Ihara, B. Zhang, Y. Zhang and Y. Guo, *Dalt. Trans.*, 2017, **46**, 9542–9548.

43 L. Martin, A. L. Morritt, J. R. Lopez, H. Akutsu, Y. Nakazawa, S. Imajo and Y. Ihara, *Inorg. Chem.*, 2017, **56**, 717–720.

44 M. M. L. Ribeiro Carrott, F. L. Conceição, J. M. Lopes, P. J. M. Carrott, C. Bernardes, J. Rocha and F. Ramôa Ribeiro, *Microporous Mesoporous Mater.*, 2006, **92**, 270–285.

45 Y. Xia and R. Mokaya, *Microporous Mesoporous Mater.*, 2004, **74**, 179–188.

46 H. K. Christenson, *J. Phys. Condens. Matter*, 2001, **13**, R95–R133.

47 G. Graubner, G. T. Rengarajan, N. Anders, N. Sonnenberger, D. Enke, M. Beiner and M. Steinhart, *Cryst. Growth Des.*, 2014, **14**, 78–86.

48 M. Hussain, S. K. Song and S. K. Ihm, *Fuel*, 2013, **106**, 787–792.

49 C. Li, Y. Wang, Y. Guo, X. Liu, Y. Guo, Z. Zhang, Y. Wang and G. Lu, *Chem. Mater.*, 2007, **19**, 173–178.

50 Y. Han, S. S. Lee and J. Y. Ying, *Chem. Mater.*, 2007, **19**, 2292–2298.

51 J. S. Beck, J. C. Vartuli, W. J. Roth, M. E. Leonowicz, C. T. Kresge, K. D. Schmitt, C. T. W. Chu, D. H. Olson, E. W. Sheppard, S. B. McCullen, J. B. Higgins and J. L. Schlenker, *J. Am. Chem. Soc.*, 1992, **114**, 10834–10843.

52 C. T. Kresge, M. E. Leonowicz, W. J. Roth, J. C. Vartuli and J. S. Beck, *Nature*, 1992, **359**, 710–712.

53 M. Colilla and M. Vallet-Regí, in *Comprehensive Biomaterials*, ed. P. B. T.-C. B. Ducheyne, Elsevier, Oxford, 2011, vol. 4, pp. 497–514.

54 D. Zhao, J. Feng, Q. Huo, N. Melosh, G. H. Fredrickson, B. F. Chmelka and G. D. Stucky, *Science (80-.).*, 1998, **279**, 548–552.

55 S. Ruthstein, V. Frydman, S. Kababya, M. Landau and D. Goldfarb, *J. Phys. Chem. B*, 2003, **107**, 1739–1748.

56 J. L. Blin and M. Impéror-Clerc, *Chem. Soc. Rev.*, 2013, **42**, 4071–4082.

57 R. Mokaya, in *Encyclopedia of Physical Science and Technology*, ed. R. A. B. T.-E. of P. S. and T.

(Third E. Meyers, Academic Press, New York, 2003, pp. 369–381.

58 Y. Zhang, T. Jiang, Q. Zhang and S. Wang, *Eur. J. Pharm. Biopharm.*, 2010, **76**, 17–23.

59 N. Zheng, J. Li, C. Xu, L. Xu, S. Li and L. Xu, *Artif. Cells, Nanomedicine, Biotechnol.*, 2018, **46**, 1132–1140.

60 K. E. Bremmell and C. A. Prestidge, *Drug Dev. Ind. Pharm.*, 2019, **45**, 349–358.

61 J. Florek, R. Caillard and F. Kleitz, *Nanoscale*, 2017, **9**, 15252–15277.

62 Y. Zhou, G. Quan, Q. Wu, X. Zhang, B. Niu, B. Wu, Y. Huang, X. Pan and C. Wu, *Acta Pharm. Sin. B*, 2018, **8**, 165–177.

63 M. Vallet-Regí, M. Colilla, I. Izquierdo-Barba and M. Manzano, *Molecules*, 2018, **23**, 47.

64 E. C. L. Jones and L. M. Bimbo, *Pharmaceutics*, 2020, **12**, 214.

65 K. P. Nartowski, J. Tedder, D. E. Braun, L. Fábián and Y. Z. Khimyak, *Phys. Chem. Chem. Phys.*, 2015, **17**, 24761–24773.

66 E. P. Barrett, L. G. Joyner and P. P. Halenda, *J. Am. Chem. Soc.*, 1951, **73**, 373–380.

67 S. Egodawatte, S. Dominguez and S. C. Larsen, *Microporous Mesoporous Mater.*, 2017, **237**, 108–116.

68 M. Bouchoucha, R. B. Van Heeswijk, Y. Gossuin, F. Kleitz and M. A. Fortin, *Langmuir*, 2017, **33**, 10531–10542.

69 T. Nakamura, F. Sugihara, H. Matsushita, Y. Yoshioka, S. Mizukami and K. Kikuchi, *Chem. Sci.*, 2015, **6**, 1986–1990.

70 E. Skorupska, P. Paluch, A. Jeziorna and M. J. Potrzebowski, *J. Phys. Chem. C*, 2015, **119**, 8652–8661.

71 E. Skorupska, S. Kaźmierski and M. J. Potrzebowski, *Mol. Pharm.*, 2017, **14**, 1800–1810.

72 K. P. Nartowski, D. Malhotra, L. E. Hawarden, J. Sibik, D. Iuga, J. A. Zeitler, L. Fábián and Y. Z. Khimyak, *Angew. Chemie - Int. Ed.*, 2016, **55**, 8904–8908.

73 V. López-Mejías, J. W. Kampf and A. J. Matzger, *J. Am. Chem. Soc.*, 2012, **134**, 9872–9875.

74 X. Chen, T. Li, K. R. Morris and S. R. Byrn, *Mol. Cryst. Liq. Cryst. Sci. Technol. Sect. A Mol. Cryst. Liq. Cryst.*, 2002, **381**, 121–131.

75 H. Li, H. Wen, J. G. Stowell, K. R. Morris and S. R. Byrn, *J. Pharm. Sci.*, 2010, **99**, 3839–3848.

76 M. Karimi-Jafari, L. Padrela, G. M. Walker and D. M. Croker, *Cryst. Growth Des.*, 2018, **18**, 6370–6387.

77 S. J. Clark, M. D. Segall, C. J. Pickard, P. J. Hasnip, M. I. J. Probert, K. Refson and M. C. Payne, *Zeitschrift fur Krist.*, 2005, **220**, 567–570.

78 I. I. Rabi, J. R. Zacharias, S. Millman and P. Kusch, *Phys. Rev.*, 1938, **53**, 318.

79 J. Keeler, *Understanding NMR spectroscopy*, John Wiley and Sons, 2006, vol. 43.

80 F. A. Bovey, *Nuclear magnetic resonance*, Oxford University Press, 1965, vol. 43.

81 W.S.B, *Nuclear magnetic resonance spectroscopy. A physicochemical view*, Longman Scientific & Technical, 1984, vol. 57.

82 P. D. Lickiss, *Modern NMR Techniques for Chemistry Research*, Pergamon Press, 1987, vol. 329.

83 T. D. W. Claridge, *High-Resolution NMR Techniques in Organic Chemistry: Third Edition*, Elsevier, 2016.

84 E. L. Hahn, *Phys. Rev.*, 1950, **80**, 580–594.

85 H. Y. Carr and E. M. Purcell, *Phys. Rev.*, 1954, **94**, 630–638.

86 N. Bloembergen, E. M. Purcell and R. V. Pound, *Phys. Rev.*, 1948, **73**, 679–712.

87 R. R. Ernst, *Angew. Chemie Int. Ed. English*, 1992, **31**, 805–823.

88 R. R. Ernst and W. A. Anderson, *Rev. Sci. Instrum.*, 1966, **37**, 93–102.

89 M. J. Duer, Ed., *Solid-State NMR Spectroscopy Principles and Applications*, Blackwell Science Ltd, Oxford, UK, 2007.

90 D. D. Laws, H. M. L. Bitter and A. Jerschow, *Angew. Chemie - Int. Ed.*, 2002, **41**, 3096–3129.

91 Y. J. Jiang and J. K. Harper, *Concepts Magn. Reson. Part A*, 2009, **34A**, 249–263.

92 S. Penzel, A. Oss, M. L. Org, A. Samoson, A. Böckmann, M. Ernst and B. H. Meier, *J. Biomol. NMR*, 2019, **73**, 19–29.

93 R. Jiménez-Gallegos, L. Téllez-Jurado, L. M. Rodríguez-Lorenzo and J. San Román, 2009.

94 W. Kolodziejski and J. Klinowski, *Chem. Rev.*, 2002, **102**, 613–628.

95 R. Kimmich and R. Kimmich, in *Nmr*, ed. R. Kimmich, Springer Berlin Heidelberg, Berlin, Heidelberg, 1997, pp. 360–366.

96 A. Pines, M. G. Gibby and J. S. Waugh, *J. Chem. Phys.*, 1973, **59**, 569–590.

97 S. R. Hartmann and E. L. Hahn, *Phys. Rev.*, 1962, **128**, 2042–2053.

98 L. E. Smart and E. A. Moore, *Solid State Chemistry*, CRC Press, 2016.

99 S. M. Brekhovskikh and J. S. Rez, *Cryst. Res. Technol.*, 1990, **25**, 1219–1233.

100 V. I. Simonov, in *Physics of Laser Crystals*, eds. J.-C. Krupa and N. A. Kulagin, Springer Netherlands, Dordrecht, 2003, pp. 1–21.

101 S. Gates-Rector and T. Blanton, *Powder Diffr.*, 2019, **34**, 352–360.

102 M. Baias, C. M. Widdifield, J. N. Dumez, H. P. G. Thompson, T. G. Cooper, E. Salager, S. Bassil, R. S. Stein, A. Lesage, G. M. Day and L. Emsley, *Phys. Chem. Chem. Phys.*, 2013, **15**, 8069–8080.

103 C. E. Hughes, G. N. M. Reddy, S. Masiero, S. P. Brown, P. A. Williams and K. D. M. Harris, *Chem. Sci.*, 2017, **8**, 3971–3979.

104 R. E. Dinnebier and S. J. L. Billinge, Eds., *Powder Diffraction*, Royal Society of Chemistry, Cambridge, 2008.

105 M. Saunders, *Thermal Analysis of Pharmaceuticals*, CRC Press/Taylor & Francis, 2008.

106 J. Abraham, A. P. Mohammed, M. P. A. Kumar, S. C. George and S. Thomas, in *Characterization of Nanomaterials: Advances and Key Technologies*, eds. S. Mohan Bhagyaraj, O. S. Oluwafemi, N. Kalarikkal and S. B. T.-C. of N. Thomas, Woodhead Publishing, 2018, pp. 213–236.

107 O. Koshy, L. Subramanian and S. Thomas, in *Thermal and Rheological Measurement Techniques for Nanomaterials Characterization*, eds. S. Thomas, R. Thomas, A. K. Zachariah and R. K. B. T.-T. and R. M. T. for N. C. Mishra, Elsevier, 2017, vol. 3, pp. 109–122.

108 S. Loganathan, R. B. Valapa, R. K. Mishra, G. Pugazhenthi and S. Thomas, in *Thermal and Rheological Measurement Techniques for Nanomaterials Characterization*, eds. S. Thomas, R. Thomas, A. K. Zachariah and R. K. B. T.-T. and R. M. T. for N. C. Mishra, Elsevier, 2017, vol. 3, pp. 67–108.

109 M. Thommes, K. Kaneko, A. V. Neimark, J. P. Olivier, F. Rodriguez-Reinoso, J. Rouquerol and K. S. W. Sing, *Pure Appl. Chem.*, 2015, **87**, 1051–1069.

110 K. S. W. Sing, D. H. Everett, R. A. W. Haul, L. Moscou, R. A. Pierotti, J. Rouquerol and T. Siemieniewska, *Pure Appl. Chem.*, 1985, **57**, 603–619.

111 K. S. W. Sing, *J. Porous Mater.*, 1995, **2**, 5–8.

112 G. Leofanti, M. Padovan, G. Tozzola and B. Venturelli, *Catal. Today*, 1998, **41**, 207–219.

113 A. Corma, *Chem. Rev.*, 1997, **97**, 2373–2419.

114 S. Brunauer, P. H. Emmett and E. Teller, *J. Am. Chem. Soc.*, 1938, **60**, 309–319.

115 E. P. Barrett, L. G. Joyner and P. P. Halenda, The Determination of Pore Volume and Area Distributions in Porous Substances. I. Computations from Nitrogen Isotherms, https://www.scienceopen.com/document?vid=09eccecf-c30b-47cf-a952-44a4334e43be, (accessed 31 August 2020).

116 V. Chashchikhin, E. Rykova and A. Bagaturyants, *J. Phys. Chem. Lett.*, 2013, **4**, 2298–2302.

117 M. Gierada, I. Petit, J. Handzlik and F. Tielens, *Phys. Chem. Chem. Phys.*, 2016, **18**, 32962–32972.

118 L. Fábián, N. Hamill, K. S. Eccles, H. A. Moynihan, A. R. Maguire, L. McCausland and S. E. Lawrence, *Cryst. Growth Des.*, 2011, **11**, 3522–3528.

119 M. Grün, K. K. Unger, A. Matsumoto and K. Tsutsumi, *Microporous Mesoporous Mater.*, 1999, **27**, 207–216.

120 K. M. Lutker, R. Quiñones, J. Xu, A. Ramamoorthy and A. J. Matzger, *J. Pharm. Sci.*, 2011, **100**, 949–963.

121 M. H. Abraham, *Chem. Soc. Rev.*, 1993, **22**, 73–83.

122 K. Terada, H. Kurobe, M. Ito, Y. Yoshihashi, E. Yonemochi, K. Fujii and H. Uekusa, *J. Therm. Anal. Calorim.*, 2013, **113**, 1261–1267.

123 J. P. Perdew, K. Burke and M. Ernzerhof, *Phys. Rev. Lett.*, 1996, **77**, 3865–3868.

124 D. Vanderbilt, *Phys. Rev. B*, 1990, **41**, 7892–7895.

125 C. J. Pickard and F. Mauri, *Phys. Rev. B - Condens. Matter Mater. Phys.*, 2001, **63**, 2451011–2451013.

126 J. R. Yates, C. J. Pickard and F. Mauri, *Phys. Rev. B - Condens. Matter Mater. Phys.*, 2007, **76**, 024401.

127 B. M. Fung, A. K. Khitrin and K. Ermolaev, *J. Magn. Reson.*, 2000, **142**, 97–101.

128 N. A. Seaton, J. P. R. B. Walton and N. quirke, *Carbon N. Y.*, 1989, **27**, 853–861.

129 J. Trébosc, J. W. Wiench, S. Huh, V. S. Y. Lin and M. Pruski, *J. Am. Chem. Soc.*, 2005, **127**, 3057–3068.

130 A. Datt, I. El-Maazawi and S. C. Larsen, *J. Phys. Chem. C*, 2012, **116**, 18358–18366.

131 P. D'Orey, T. Cordeiro, M. A. O. Lourenço, I. Matos, F. Danède, J. C. Sotomayor, I. M. Fonseca, P. Ferreira, N. T. Correia and M. Dionísio, *Mol. Pharm.*, 2021, **18**, 898–914.

132 B. Grünberg, T. Emmler, E. Gedat, I. Shenderovich, G. H. Findenegg, H. H. Limbach and G. Buntkowsky, *Chem. - A Eur. J.*, 2004, **10**, 5689–5696.

133 W. H. Organization, M. C. Stuart, M. Kouimtzi and S. Hill, 2009, Earlier version published in 2004.

134 S. Ventegodt, *World health organization model list of essential medicines*, World Health Organization, Geneva PP - Geneva, 2015.

135 J. Li, S. A. Bourne and M. R. Caira, *Chem. Commun.*, 2011, **47**, 1530–1532.

136 C. Y. Chen, S. L. Burkett, H. X. Li and M. E. Davis, *Microporous Mater.*, 1993, **2**, 27–34.

137 M. Vallet-Regí, L. Ruiz-González, I. Izquierdo-Barba and J. M. González-Calbet, *J. Mater. Chem.*, 2006, **16**, 26–31.

138 M. Vallet-Regi, A. Rámila, R. P. Del Real and J. Pérez-Pariente, *Chem. Mater.*, 2001, **13**, 308–311.

139 E. Skorupska, A. Jeziorna, P. Paluch and M. J. Potrzebowski, *Mol. Pharm.*, 2014, **11**, 1512–1519.

140 J. Trébosc, J. W. Wiench, S. Huh, V. S. Y. Lin and M. Pruski, *J. Am. Chem. Soc.*, 2005, **127**, 3057–3068.

141 W. W. Lukens, P. Schmidt-Winkel, D. Zhao, J. Feng and G. D. Stucky, *Langmuir*, 1999, **15**, 5403–5409.

142 C. E. Hughes, P. A. Williams, V. L. Keast, V. G. Charalampopoulos, G. R. Edwards-Gau and K. D. M. Harris, *Faraday Discuss.*, 2015, **179**, 115–140.

143 X. Li, X. Ou, B. Wang, H. Rong, B. Wang, C. Chang, B. Shi, L. Yu and M. Lu, ,

DOI:10.26434/chemrxiv.12387452.

144 C. E. Hughes, P. A. Williams and K. D. M. Harris, *Angew. Chemie - Int. Ed.*, 2014, **53**, 8939–8943.

145 J. J. O'Brien and D. M. Campoli-Richards, *Drugs*, 1989, **37**, 233–309.

146 A. Parr, I. J. Hidalgo, C. Bode, W. Brown, M. Yazdanian, M. A. Gonzalez, K. Sagawa, K. Miller, W. Jiang and E. S. Stippler, *Pharm. Res.*, 2016, **33**, 167–176.

147 G. I. Birnbaum, M. Cygler, J. T. Kusmierek and D. Shugar, *Biochem. Biophys. Res. Commun.*, 1981, **103**, 968–974.

148 G. I. Birnbaum, M. Cygler and D. Shugar, *Can. J. Chem.*, 1984, **62**, 2646–2652.

149 H. G. Brittain, *Polymorphism in Pharmaceutical Solids: Second edition*, 2016.

150 G. G. Z. Zhang, R. F. Henry, T. B. Borchardt and X. Lou, *J. Pharm. Sci.*, 2007, 96, 990–995.

151 C. H. Gu, H. Li, R. B. Gandhi and K. Raghavan, *Int. J. Pharm.*, 2004, **283**, 117–125.

152 H. Zhu, C. Yuen and D. J. W. Grant, *Int. J. Pharm.*, 1996, **135**, 151–160.

153 H. Zhu and D. J. W. Grant, *Int. J. Pharm.*, 1996, **139**, 33–43.

154 Y. Li, P. S. Chow, R. B. H. Tan and S. N. Black, *Org. Process Res. Dev.*, 2008, **12**, 264–270.

155 D. E. Braun, K. P. Nartowski, Y. Z. Khimyak, K. R. Morris, S. R. Byrn and U. J. Griesser, *Mol. Pharm.*, 2016, **13**, 1012–1029.

156 C. H. Gu, V. Young and D. J. W. Grant, *J. Pharm. Sci.*, 2001, **90**, 1878–1890.

157 L. Mafra, S. M. Santos, R. Siegel, I. Alves, F. A. Almeida Paz, D. Dudenko and H. W. Spiess, *J. Am. Chem. Soc.*, 2012, **134**, 71–74.

158 E. H. Lee, *Asian J. Pharm. Sci.*, 2014, **9**, 163–175.

159 S. Ding and N. Jiao, *Angew. Chemie - Int. Ed.*, 2012, **51**, 9226–9237.

160 K. P. Nartowski, J. Karabin, A. L. Morritt, M. Nowak, L. Fábián, B. Karolewicz and Y. Z. Khimyak, *CrystEngComm*, 2019, **21**, 2180–2192.

161 Y. Bi, D. Xiao, S. Ren, S. Bi, J. Wang and F. Li, *J. Pharm. Sci.*, 2017, **106**, 3150–3155.

162 N. Z. Lyakhov and V. V Boldyrev, *Russ. Chem. Rev.*, 1972, **41**, 919–928.

163 A. S. Larsen, M. T. Ruggiero, K. E. Johansson, J. A. Zeitler and J. Rantanen, *Cryst. Growth Des.*, 2017, **17**, 5017–5022.

164 K. Fujii and H. Uekusa, in *Advances in Organic Crystal Chemistry: Comprehensive Reviews 2015*, eds. R. Tamura and M. Miyata, Springer Japan, Tokyo, 2015, pp. 299–316.

165 H. Tanaka, N. Koga and A. K. Galwey, *J. Chem. Educ.*, 1995, **72**, 251–256.

166 S. Petit and G. Coquerel, *Chem. Mater.*, 1996, **8**, 2247–2258.

167 R. Bobrovs, L. Seton and A. Actiņš, *CrystEngComm*, 2014, **16**, 10581–10591.

168 P. A. Basford, K. R. Back, M. Cram, R. Docherty, R. J. Davey and A. J. Cruz-Cabeza, *Cryst. Growth Des.*, 2019, **19**, 7193–7205.

169 D. J. W. Grant and S. R. Byrn, *Adv. Drug Deliv. Rev.*, 2004, **56**, 237–239.

170 A. J. Cruz-Cabeza, N. Feeder and R. J. Davey, *Commun. Chem.*, 2020, **3**, 1–4.

171 S. S. Park, M. H. Jung, Y. S. Lee, J. H. Bae, S. H. Kim and C. S. Ha, *Mater. Des.*, 2019, **184**, 108187.